Investigating the Role of High Endothelial Venules in Cancer Immunity

Stefan Milutinović

Cardiff University

Doctor of Philosophy (Ph.D.)

November 2020

Acknowledgements

I am very grateful for being offered the opportunity to work on such an interesting and cutting-edge research project. I would first like to express my enormous gratitude to my supervisors, Professor Awen Gallimore and Dr Emma Jones for their continued advice, guidance and support. My ability to overcome challenges and take full ownership and responsibility has undoubtably come from your supervision and I am forever grateful to you for this. I would also like to thank Professor Andrew Godkin for his key insights and helpful advice offered during lab meetings.

I am grateful to all members of the Gallimore Godkin lab group who have been incredibly supportive during my PhD. I am very grateful to Dr Emma Jones for teaching me all the key laboratory skills that I needed to begin my project and whose office door was always open to me for any question I may have had. I would also like to thank Kathryn Smart and Dr Sarah Lauder for all their help with mouse work and Michelle Somerville for all her help and advice related to imaging and IHC.

Completion of this project was very much the product of an internationally collaborative effort. As such I would like to thank Professor Jens Stein for all his advice and for allowing me to visit his lab in Bern. I am very grateful to Dr Jun Abe for performing all SPIM imaging and for teaching me key image processing skills. I would also like to thank Dr Gib Bogle and Dr Inken Kelch for all their help and patience whilst teaching me how to build and use the vessel tools. I was made to feel very welcomed during my one month stay in Auckland and it is undoubtably an experience I will cherish for the rest of my life.

I would like to thank all members of office 3F02 both present and past. Our office undoubtably served as a key source of support during this PhD. I was incredibly lucky to meet several people whose friendship I will cherish forever. As such I would like to thank Dr Ruban Rex Peter and Abdullah S Alanzi. Our Turkish coffee meetups and restaurant outings were very much needed. I would also like to thank Prags (we made it!). A special thanks to Jake Scott (G Ye) for his continued friendship and support.

Outside of the lab I would like to thank Stefan Dz (momci). Our kafas and gym workouts kept me going through the toughest of times. I would also like to thank my flatmate Jason who kept me sane during the first lockdown.

Lastly, I would like to thank my incredibly supportive and loving parents Ariana and Nikola who have always been there for me since the beginning. A special thanks to my loving grandfather Novak Todorovic. Without you I would never have been able to complete my PhD studies in the UK and I remain forever grateful to you.

Summary

The extent of T-cell infiltration is a key parameter that dictates cancer immunity and response to immunotherapy. The depletion of $Foxp3^+$ regulatory T cells (Tregs) in a 3-methylcholanthrene (MCA) carcinogenesis model was previously shown to lead to the formation of high endothelial venules (HEVs) in approximately 50% of treated mice. Importantly, HEV formation was found to correlate both with the extent of T cell infiltration and control of tumour growth. To examine how intra-tumoral HEVs are globally distributed and whether they can be augmented to improve control of tumour growth, a 3-dimensional (3D) imaging technique known as light sheet fluorescence microscopy (LSFM) was used.

In-vivo labelling, auto-fluorescence reducing, and organic solvent clearing protocols were successfully optimized for imaging blood vessel and HEV networks by LSFM. *In-silico* vessel quantification tools were further optimized to process LSFM acquired datasets of discrete HEV networks. These tools were validated by mapping the topology of naïve popliteal and inguinal lymph node (LN) HEV networks and were used to show that LN HEVs expand following Treg depletion and following the establishment of a fibrosarcoma tumour.

LSFM imaging of a non-treated fibrosarcoma revealed the presence of HEVs in a small subset of vessels suggesting Treg depletion may not be an essential pre-requisite for intra-tumoral HEV formation. Furthermore, LSFM imaging of a regressor fibrosarcoma revealed a heterogenous global distribution and structural organization of HEVs. Lastly, LSFM imaging was used to show that combinatory Treg depletion with LTβR agonist or anti-IL-27 neutralizing antibody treatment augments intratumoural HEVs. Such changes were not accompanied by an increase in immune cell infiltrate or improved control of tumour growth.

Whilst LSFM imaging has demonstrated the plasticity of HEVs, the relationship between their presence, T cell infiltrate and tumour control is complex and requires further investigation before they can be harnessed for immunotherapy.

Table of Contents

List of Figures

List of Tables

List of Abbreviations

ACT Adoptive T-cell Transfer

AF Alexa Fluor

ANGPT2 Angiopoietin-2

APC Antigen Presenting Cell

β_2M Beta-2-Microglobulin

BABB Benzyl Alcohol and Benzyl Benzoate

Batf3 Basic Leucine Zipper Transcriptional Factor ATF-Like 3

BEC Blood Endothelial Cell

BMP-4 Bone Morphogenetic Protein-4

BSA Bovine Serum Albumin

c-FLIP Anti-Apoptotic FADD-Like IL-1β–Converting Enzyme-Inhibitory Protein

CAF Cancer Associated Fibroblast

CAR Chimeric Antigen Receptor

CCL C-C Motif Chemokine Ligand

CD Cluster of Differentiation

CD62L L-selectin

CLEC-2 C-Type Lectin Receptor 2

CTLA-4 Cytotoxic T Lymphocyte Associated Antigen 4

CUBIC Clear, Unobstructed Brain/Body Imaging Cocktails and Computational analysis

CXCL C-X-C Motif Chemokine Ligand

CXCR C-X-C Motif Chemokine Receptor

DAB 3, 3'-diaminobenzidine

DAPI 4, 6-diamidino-2-phenylindole

DC Dendritic Cell

DKK1 Dickkopf-1

DLN Draining Lymph Node

DOF Depth of Focus

DOL Degree of Labelling

DPX Dibutylphthalate Polystyrene Xylene

DSS Disease Specific Survival

DT Diphtheria Toxin

EBI3 Epstein-Barr Virus Induced 3

EC Endothelial Cell

ECi Ethyl Cinnamate

EGFR Epidermal Growth Factor Receptor

ELS Ectopic Lymphoid-like Structure

ET_BR Endothelin B Receptor

EVIS Extended Volume Confocal Imaging

FAP Fibroblast Activation Protein-α

FasL Fas Ligand

FDA US Food and Drug Administration

fDC Follicular Dendritic Cell

FFPE Formalin Fixed Paraffin Embedded

FIJI FIJI is just ImageJ

FITC Fluorescein isothiocyanate

FOV Field of View

FRC Fibroblastic Reticular Cell

GBM Glioblastoma

GC Germinal Centre

GFP Green Fluorescent Protein

GM-CSF Granulocyte-Macrophage Colony Stimulating Factor

HEC High Endothelial Cell

HEV High Endothelial Venule

HSV Herpes Simplex Virus

HSV-2 Herpes Simplex Virus Type 2

HVEM Herpes Virus Entry Mediator

ICAM-1 Intercellular Adhesion Molecule 1

ICB Immune Checkpoint Blockade

ICI Immune Checkpoint Inhibitor

IF Immunofluorescence

IFN-γ Interferon-gamma

IHC Immunohistochemistry

IL Interleukin

IV Intravenous

LCMV Lymphocytic Choriomeningitis Virus

LIGHT Homologous to LT, Exhibits Inducible Expression and Competes with HSV Glycoprotein D for Binding to Herpesvirus Entry Mediator, a Receptor Expressed on T Lymphocytes

LMP Low Melting Point

LN Lymph Node

LSCM Laser Scanning Confocal Microscopy

LSFM Light Sheet Fluorescence Microscopy

LT Lymphotoxin

LTi Lymphoid Tissue Inducer

LTβR Lymphotoxin Beta Receptor

MAdCAM-1 Mucosal Addressin Cell Adhesion Molecule-1

MAGEA1 Melanoma-Associated Antigen 1

MCA Methylcholanthrene

MDSC Myeloid-Derived Suppressor Cell

MHC Major Histocompatibility Complex

MIP Maximum Intensity Projection

MSC Mesenchymal Stem Cell

NA Numerical Aperture

NBFS Neutral-Buffered Formalin Solution

NDLN Non-Draining Lymph Node

NK Natural Killer

NKT Natural Killer T Cell

OCT Optimum Cutting Temperature

OPT Optical Projection Tomography

OSCC Oral Squamous Cell Carcinoma

OPSCC Oral and Pharyngeal Squamous Cell Carcinoma

OVA Ovalbumin

CFA Complete Freund's Adjuvant

PAC Preoperative Neoadjuvant Chemoradiotherapy

PBS Phosphate Buffer Saline

PD-1 Programmed Cell Death-1

PD-L1 Programmed Cell Death-Ligand 1

PD-L2 Programmed Cell Death-Ligand 2

PDAC Pancreatic Ductal Adenocarcinoma

PDPN Podoplanin

PFA Paraformaldehyde

PGE2 Prostaglandin E2

PMN Pre-Metastatic Niche

PNAd Peripheral Node Addressin

PNET Pancreatic Neuroendocrine Tumour

RA Rheumatoid Arthritis

RAG Recombination Activation Gene

RAM Random-Access Memory

RBC Red Blood Cell

RNAi RNA Interference

ROI Region of Interest

RT Room Temperature

SCC Squamous Cell Carcinoma

SCID Severe Combined Immunodeficient

sCMOS Scientific Complementary Metal–Oxide–Semiconductor

shRNA Short Hairpin RNA

SLN Sentinel Lymph Node

SLO Secondary Lymphoid Organ

S/N Signal to Noise

SPIM Selective Plane Illumination Microscopy

SS Sjögren's Syndrome

STAT Signal Transducer and Activator of Transcription

T-VEC Talimogene Laherparepvec

TAA Tumour Associated Antigen

TCGA The Cancer Genome Atlas

TCR T Cell Receptor

Tfh T Follicular Helper

TGF-β Transforming Growth Factor-Beta

TIFF Tagged Image File Format

TIL Tumour Infiltrating Lymphocyte

TLS Tertiary Lymphoid Structure

TME Tumour Microenvironment

TNC Tenascin

TNFR Tumour Necrosis Factor Receptor

TNM Tumour, Node and Metastasis

Treg $Foxp3^{+}$ Regulatory T cell

VCAM-1 Vascular Cell Adhesion Molecule 1

VE-cadherin Vascular Endothelial Cadherin

VEGF Vascular Endothelial Growth Factor

VEGFR-2 Vascular Endothelial Growth Factor Receptor 2

VTR Vascular Targeting Peptide

WGA Wheat Germ Agglutinin

WT Wild-Type

1. Introduction

1.1 Cancer Development

Cancer is the second leading cause of mortality in the world and can arise in almost any tissue found in the body (World Health Organisation). Currently it is predicted that one out of every two people in the UK will develop cancer (Cancer Research UK).

In their seminal paper entitled “Hallmarks of cancer”, Hanahan and Weinberg described six essential alterations that neoplastic cells display which in turn dictates their malignant growth (Hanahan and Weinberg, 2000). The ability of neoplastic cells to have indefinite replicative potential is driven by the following acquired traits: achieving growth signalling autonomy, becoming insensitive to anti-growth signals and becoming capable of evading apoptosis (Hanahan and Weinberg, 2000). The ability to induce and sustain angiogenesis is necessary for proliferating neoplastic cells to acquire the necessary nutrients and oxygen in order to expand to a larger size (Hanahan and Weinberg, 2000). Cancer cells eventually acquire the ability to invade surrounding tissue and metastasise to other parts of the body (Hanahan and Weinberg, 2000). Importantly metastasis is the leading cause of cancer related death (Sporn, 1996). In 2011, Hanahan and Weinberg expanded the list of emerging hallmarks to include the deregulation of cellular energetics as a means of supporting cell growth and division as well as the ability to avoid immune destruction (Hanahan and Weinberg, 2011). The latter hallmark was added in light of emerging evidence that implicates the immune system in actively identifying, eradicating and sculpting the immunogenic phenotype of tumour cells as discussed below.

1.2 Cancer Immunosurveillance

1.2.1 History of Cancer Immunosurveillance

Paul Ehrlich was the first to predict in 1909 that the immune system could repress the growth of carcinomas that would otherwise form with “overwhelming frequency” (reviewed in Dunn *et al.*, 2002). However, the concept that the immune system is actively involved in identifying and eliminating or inactivating transformed cells was put forward half a century later by Sir Macfarlane Burnet and Lewis Thomas (Burnet, 1957). This hypothesis postulated that a mechanism of immunological character evolved as a necessity to prevent the outgrowth of transformed cells and that lymphocytes could serve to carry out this role (Burnet, 1957). In response to this several studies aimed to challenge an important implication this hypothesis carried; namely that immunocompromised hosts should have an increased incidence of either spontaneous or chemically induced tumours (reviewed in Dunn *et al.*, 2002). Whilst an increase incidence of spontaneous lymphomas was reported in mice with induced immunodeficiencies, this was largely attributed to an increased susceptibility to transforming viruses (reviewed in Dunn *et al.*, 2002). Whether cancer immunosurveillance mediates protection against chemically induced tumour formation was examined extensively by Oasis Stutman in the 1970s, who utilized immunodeficient CBA/H strain nude mice which do not form a functional thymus and possess fewer T cells than wild-type (WT) mice (Stutman, 1975). Exposure to the chemical carcinogen MCA did not result in an increased tumour incidence in these mice (Stutman, 1975). As a result, the cancer immunosurveillance hypothesis was very much abandoned at this point (reviewed in Dunn *et al.*, 2002).

Interest in the cancer immunosurveillance process was rekindled in the mid-1990s when two key components of the immune system: IFN-γ and perforin were found to mediate protection against MCA induced tumour formation (Dighe *et al.*, 1994; van den Broek *et al.*, 1996; Kaplan *et al.*, 1998; Street, Cretney and Smyth, 2001; Dunn *et al.*, 2002). First the importance of IFN-γ release by lymphocytes and its control of tumour growth was demonstrated by early experiments conducted by the Schreiber group (Dighe *et al.*, 1994). IFN-γ insensitive tumour cells expressing a truncated form of the IFN-γ receptor α chain, were found to be

more tumorigenic than WT tumour cells when implanted into BALB/C mice (Dighe *et al.*, 1994). Furthermore, when transplanted into severe combined immunodeficient (SCID) mice which lack lymphocytes, the tumour growth kinetics mirrored those of WT transplanted tumour cells suggesting the presence of lymphocytes was an important factor in the control of tumour growth (Dighe *et al.*, 1994). This anti-tumour role of IFN-γ was subsequently confirmed by the same group which demonstrated increased development of both MCA induced and spontaneously arising tumours in IFN-γ receptor deficient mice as well as mice lacking STAT-1; a key transcription factor which drives IFN-γ responses (Kaplan *et al.*, 1998). Following on from this, mice lacking perforin; a key component of cytolytic granules released by cytotoxic T cells and natural killer (NK) cells, were shown to form significantly more MCA induced tumours than WT mice (van den Broek *et al.*, 1996; Street, Cretney and Smyth, 2001). The importance of lymphocytes in mediating control of tumour growth was previously put in question by work performed by Oasis Stutman (Stutman, 1975). However, in retrospect, the athymic mice utilized by Stutman actually possessed functional $\alpha\beta$ T-cells as well as lymphocytes that are known to develop extrathymically including natural killer cells and a subset of $\gamma\delta$ T-cells (Dunn *et al.*, 2002). As a result, cancer immunosurveillance was not truly defective in these mice (Dunn *et al.*, 2002). In contrast, the development of recombination activation gene (RAG) knockout mice which lack natural killer T cells (NKT), T cells and B cells could now be used to properly address this question (Shinkai *et al.*, 1992). Experiments conducted by Shankaran and colleagues demonstrated that RAG-2$^{-/-}$ mice were more susceptible to MCA induced tumour formation as well as spontaneous epithelial tumour formation (Shankaran *et al.*, 2001). Work culminating from several groups now support the involvement of both the innate and adaptive arms of immunity since the targeted genetic ablation of NKT cells, NK cells, $\alpha\beta$ T cells, $\gamma\delta$ T cells, IFN-γ and interleukin-12 (IL-12) were all shown lead to an increased incidence of MCA-induced sarcomas (Dunn *et al.*, 2002).

1.2.2 Cancer immunosurveillance in humans

Increased tumour incidence in immunocompromised humans is difficult to attribute to defective cancer immunosurveillance given that tumours can form as a result of failure to control endemic virus infections, pathogens and viral reactivation (reviewed in Dunn *et al.*, 2002). However higher incidences of several cancers including cancers of the colon, larynx, lung and bladder, have been previously reported in Norwegian recipients of renal transplants as compared to the same reference population (Engberg *et al.*, 2016). Direct evidence for the involvement of the immune system in eliminating transformed cells in humans is difficult to measure (as discussed by Gallimore and Godkin, 2008). This is because the successful elimination of malignant cells by the immune system would take place undetected as the patient would not present clinically (Gallimore and Godkin, 2008). Those that do present clinically have by definition failed to control their tumour through cancer immunosurveillance (Gallimore and Godkin, 2008). Lastly, in contrast to infections, there are currently no established immunological markers that mark the occurrence or resolution of a successful anti-tumour response (Gallimore and Godkin, 2008). However, there are several lines of indirect evidence that support the involvement of the immune system in tumour control. In particular the extent of lymphocyte infiltration (particularly T cells) has been found to correlate with good prognosis in several cancers including breast cancer, melanoma, ovarian cancer, non-Hodgkin's lymphoma and head and neck cancer (Pages *et al.*, 2010). In colorectal cancer, the presence of tumour infiltrating $CD8^+$ T cells within cancer cell nests was found to be associated with improved patient survival (Naito *et al.*, 1998). Subsequently, a seminal study led by Galon and colleagues demonstrated that the type, density and localization of $CD3^+$ and $CD45RO^+$ memory T cells was a more powerful predictor of patient outcome than histopathological tumour, node and metastasis (TNM) staging (Galon *et al.*, 2006).

1.2.3 Cancer Immunoediting

Cancer immunosurveillance is now recognized as being part of a broader process termed cancer immunoediting which was first described by the Schreiber

group in 2002 (reviewed in Dunn *et al.*, 2002). Immunoediting encompasses both the host-protecting aspects of cancer immunosurveillance as well as the tumour-promoting aspects which includes sculpting of the immunogenic phenotype of the tumour (reviewed in Dunn *et al.*, 2002). Early evidence of such tumour sculpting effects came from tumour transplantation experiments which showed that MCA-induced sarcomas forming in RAG-$2^{-/-}$ mice were more immunogenic than those which formed in immunocompetent mice (Shankaran *et al.*, 2001). Immunoediting is composed of three separate phases (elimination, equilibrium and escape) which can progress sequentially or occur independently (reviewed in Dunn *et al.*, 2002). The elimination phase describes the identification and eradication of tumour cells by the innate and adaptive arms of the immune system as described earlier. Tumour cells that are not completely eradicated progress to the equilibrium phase whereby tumour cell outgrowth is suppressed but sculpting of the immunogenic phenotype takes place (reviewed in Dunn *et al.*, 2002). The escape phase is defined as the outgrowth of sculpted tumour cells that have evaded the immune system and can now grow into solid tumours that become visible and clinically apparent (Dunn *et al.*, 2002).

Immunogenic sculpting of tumours by the adaptive immune response was experimentally demonstrated by Koebel and colleges whereby mice exposed to MCA were shown to develop late stage tumours following the administration of neutralizing antibodies for $CD4^+$ cells, $CD8^+$ cells and IFN-γ (Koebel *et al.*, 2007). This late stage tumour latency was not mirrored in RAG-$2^{-/-}$ mice exposed to the same MCA dose, arguing against *de novo* transformation as a mechanism of late stage tumour outgrowth following immunodepletion (Koebel *et al.*, 2007). Instead, small tumour masses with stabilized growth kinetics were found to form in MCA injected immunocompetent mice (Koebel *et al.*, 2007). When transferred into RAG-$2^{-/-}$ mice the tumour cells grew progressively larger suggesting tumour outgrowth was immunologically restrained (Koebel *et al.*, 2007). Lastly tumour cells that had maintained equilibrium or had formed following the administration of neutralizing antibodies were found to be more immunogenic than tumour cells isolated from late stage forming sarcomas as the latter were not rejected when transferred into WT mice (Koebel *et al.*, 2007). This study showed that tumour cells that had escaped the equilibrium phase were less immunogenic as a direct consequence of immunoediting. In the same MCA model, the equilibrium phase

was subsequently found to be maintained by the opposing effects of interleukin-23 (IL-23) which promotes tumour persistence and IL-12 which supports tumour elimination (Teng *et al.*, 2012).

The escape phase can be mediated by the direct sculpting effects of the immune system or as a consequence of cancer driven immunosuppression (as reviewed by Schreiber, Old and Smyth, 2011). Mechanisms driving escape include reduced expression or presentation of immunogenic tumour associated antigens and overexpression of antiapoptotic factors providing resistance to cytotoxic mediated cell killing (Schreiber, Old and Smyth, 2011; Mittal *et al.*, 2014). The establishment of an immunosuppressive microenvironment can be achieved through the release of immunosuppressive cytokines such as vascular endothelial growth factor (VEGF) and transforming growth factor-beta (TGF-β) as well as through the recruitment of immunosuppressive Treg cells and myeloid-derived suppressor cells (MDSCs) which inhibit effective anti-tumour immune responses (Schreiber, Old and Smyth, 2011). The recognition that the immune system has an active role in control of tumour growth but that it can also be actively suppressed by a tumour, sets the basis for the use of immune-based cancer treatments (termed cancer immunotherapy) (Mittal *et al.*, 2014).

1.3 Cancer Immunotherapy

1.3.1 Adoptive T-cell transfer

Adoptive T-cell transfer (ACT) is a form of immunotherapy that involves the removal of lymphocytes with anti-tumour activity from tumour bearing patients so that they can subsequently be expanded *ex-vivo* (in the presence of various growth factors including IL-2) and reinfused back into the patient (as reviewed by Makkouk and Weiner, 2015). ACT therefore aims to bypass the requirement for *in-vivo* activation and immune cell proliferation (as reviewed by Makkouk and Weiner, 2015). Rosenberg and colleagues were the first to report a method for the expansion and adoptive transfer of TILs into several murine tumours which resulted in significant anti-tumour activity (Shinkai *et al.*, 1992). Pooled data from three separate ACT clinical trials for the treatment of metastatic melanoma showed overall response rates reaching 50% and complete response rates in

20% of patients of which 95% had durable responses (Hinrichs and Rosenberg, 2014). In cases where tumour biopsies are not readily available or the numbers of TILs are reduced, it is also possible to genetically engineer circulating lymphocytes with tumour reactive T cell receptors (TCRs) (Vacchelli *et al.*, 2013; Makkouk and Weiner, 2015). Genetic engineering can also be used to endow T-cells with increased proliferative potential, *in-vivo* persistence and enhanced trafficking capabilities (Vacchelli *et al.*, 2013). Furthermore, the use of chimeric antigen receptors (CARs) instead of TCRs allows for the direct recognition of tumour associated antigens (TAAs) without the need for MHC-peptide complex recognition (Makkouk and Weiner, 2015). CARs T-cells targeting the CD19 B cell costimulatory receptor have demonstrated therapeutic efficacy in the treatment of B-cell malignancies in particular, with a reported 81% of patients achieving remission rates in patients with relapsed or refractory B-cell acute lymphoblastic leukemia (ALL) (Maude *et al.*, 2018). There are currently two US Food and Drug Administration (FDA) approved CD19 targeting CAR therapies: tisagenlecleucel and axicabtagen ciloleucel (Kruger *et al.*, 2019). Tisagenlecleucel is used for the treatment of ALL and diffuse-large B cell lymphoma whilst axicabtagen ciloleucel is used in the treatment of the latter (Kruger *et al.*, 2019). However, CAR therapies have also been associated with considerable off-target toxicities as they are readily activated by low levels of antigen expressed by normal cells (Makkouk and Weiner, 2015; Maude *et al.*, 2018). Bispecific T cell engagers (BiTEs) have also shown therapeutic efficacy in B-cell leukaemias. BiTEs are small proteins whose antibody binding domains recognize distinct antigens that can in turn lead to the cross linking of tumour cells and T cells. Blinatumomab is the only currently approved BiTE which is bispecific for CD3 and CD19 and has shown to significantly improve overall survival as compared to chemotherapy in patients with relapsed or refractory B-cell ALL (Kantarjian *et al.*, 2017).

1.3.2 Cancer Vaccines

Whilst vaccination to prevent infection which drives cancer development (as with human papilloma virus) has proven successful, the use of therapeutic cancer vaccines composed of tumour antigens or even whole tumour cells has proven challenging (as discussed by Makkouk and Weiner, 2015). As opposed to viral antigens which are foreign, cancer immunoediting and suppression of peptide

processing and presentation makes it more difficult to elicit and sustain immune responses to TAAs (Makkouk and Weiner, 2015). One of the first TAAs that was shown to elicit T-cell responses was the melanoma antigen MAGE-A1 (van der Bruggen *et al.*, 1991). Early vaccination efforts were initially focused on targeting such TAAs as they can be shared by several patients (as discussed by Makkouk and Weiner, 2015). However, as a result of self-tolerance, a failure to induce effective immune responses resulted in poor clinical outcomes (Makkouk and Weiner, 2015; Hollingsworth and Jansen, 2019). Targeting cancer mutated antigens (termed neoantigens) instead is more promising as these are not subject to self-tolerance and can elicit strong $CD4^+$ and $CD8^+$ T cell responses (Hacohen *et al.*, 2013; Schumacher and Schreiber, 2015). Such neoantigens were identified as early as 1994, following the purification of mutated connexin 37 from a murine lung carcinoma that was capable of inducing cytotoxic T-cell responses (Mandelboim *et al.*, 1994). Whilst neoantigen vaccines have to be tailor made for each patient, early clinical work using a vaccine targeting up to 20 neoantigens showed that all patients had activation and expansion of both $CD4^+$ and $CD8^+$ T cells with four out of six patients having had no disease recurrence (Ott *et al.*, 2017). Similarly, the use of RNA neo-epitope vaccines encoding expression of up to 10 neoantigens, elicited T-cell responses to at least 3 neoantigens in all vaccinated melanoma patients (Sahin *et al.*, 2017). Whilst encouraging, larger trials and further development and optimization is required to make neoantigen vaccination production more scalable and cost effective (Dougan, Dranoff and Dougan, 2019; Hollingsworth and Jansen, 2019).

Instead of targeting single TAAs, the use of whole cell-based vaccines which can potentially elicit immune responses to a multitude of TAAs has also been explored. One such example is GVAX, a vaccine composed of two irradiated prostate cancer cell lines that secrete granulocyte-macrophage colony stimulating factor (GM-CSF) (Chiang, Kandalaft and Coukos, 2011). GVAX has however failed to provide an enhanced survival benefit in randomized clinical trials (Chiang, Kandalaft and Coukos, 2011). The most promising systemic cell-based vaccination strategy involves the use of autologous DCs pulsed with TAAs. Sipuleucel T (a DC vaccine pulsed with prostatic acid phosphatase fused to GM-CSF) was FDA approved following three separate phase 3 clinical trials showing

marked improvements in prostate cancer patient survival (Small *et al.*, 2006; Higano *et al.*, 2009).

As opposed to delivering selected neoantigens or whole tumour cells systemically, *in-situ* vaccination involves the delivery of immunomodulatory agents directly to the tumour microenvironment (as reviewed by Dougan, Dranoff and Dougan, 2019). The aim here is to induce tumour cell death leading to the release and uptake of TAAs by DCs and subsequent antigen presentation and immune activation (as reviewed by Dougan, Dranoff and Dougan, 2019). Oncolytic viruses specifically target tumour cells leading to their lysis whilst simultaneously activating DCs through the recognition of viral proteins by innate sensing pathways (including toll like receptors and activation of stimulator of interferon genes) (as reviewed by Dougan, Dranoff and Dougan, 2019). The first oncolytic therapy to demonstrate improved durable response rates in melanoma and to be FDA approved was talimogene laherparepvec (T-VEC), a modified herpes simplex virus (HSV) type-1 engineered to target tumour cells and to induce GM-CSF production (Andtbacka *et al.*, 2015).

1.3.3 Immune Checkpoint Inhibitors

The development of immune checkpoint inhibitors (ICIs) as a new form of cancer treatment has been recognized as an immense breakthrough in cancer therapeutics (as reviewed by Sharma and Allison, 2015; Kruger *et al.*, 2019). As a reflection of this, the 2018 Nobel prize in Physiology or Medicine was awarded to James P. Allison and Tasuku Honjo for their discovery of this novel cancer treatment (Altmann, 2018). ICIs work by targeting co-inhibitory molecules which are involved in the negative regulation of T-cell activity (as discussed by Sharma and Allison, 2015). The goal of immune checkpoint blockade (ICB) therapy therefore is to unleash effective anti-tumour responses that would otherwise be supressed by such inhibitory signalling pathways (as discussed by Sharma and Allison, 2015). The development of ICIs was based on the notion that naïve T cell activation is more complex than TCR recognition of cognate antigen-MHC complexes alone, but that it is in fact regulated by both co-stimulatory and co-inhibitory signalling pathways (Townsend and Allison, 1993; Greenwald,

Freeman and Sharpe, 2005; Sharma and Allison, 2015). More specifically naïve T cell activation proceeds following the additional engagement of CD28 (expressed on the surface of T cells) with the B7 molecules CD80 and CD86 expressed by antigen presenting cells (APCs) (Greenwald, Freeman and Sharpe, 2005; Schumacher and Schreiber, 2015). Following T cell activation, inhibitory pathways were shown to be induced leading to the attenuation and eventual termination of this response, pointing to an endogenous homeostatic role for control of excessive T cell responses (Greenwald, Freeman and Sharpe, 2005). One such pathway involves the co-inhibitory molecule Cytotoxic T lymphocyte associated antigen 4 (CTLA-4) which is expressed following T cell activation. CTLA-4 expression was found to oppose CD28 co-stimulation by binding with higher affinity to B7 molecules leading to an inhibition of T-cell activity (Walunas *et al.*, 1994; Krummel and Allison, 1995). Based on these findings, it was hypothesised that the use of anti-CTLA4 targeting antibodies could unleash effective anti-tumour responses even without prior knowledge of specific TAAs involved in such responses (as discussed by Sharma and Allison, 2015). Anti-CTLA-4 targeting antibodies were first shown to elicit anti-tumour responses in mice inoculated with colon carcinoma or fibrosarcoma cell lines (Leach, Krummel and Allison, 1996). This eventually led to the development of ipilimumab; a human anti-CTLA4 antibody which showed significant improvement in overall survival in metastatic melanoma patients undergoing phase 3 clinical trials (Hodi *et al.*, 2010; Robert *et al.*, 2011). Importantly, a follow up study showed durable responses with 20% of patients living more than 4 years and a subset of patients living past 10 years (Schadendorf *et al.*, 2015). However, Immune related adverse events were recorded in 60% of treated patients with 10-15% experiencing grade 3 to 4 adverse events and 7 patients dying (Schadendorf *et al.*, 2015).

In 2000, a separate immune checkpoint called Programmed cell death-1 (PD-1) was found to limit T-cell responses (Freeman *et al.*, 2000). As opposed to CTLA-4, PD-1 does not interfere with co-stimulatory signalling but rather with TCR signalling following activation by its ligands PD-L1 and PD-L2 (as discussed by Sharma and Allison, 2015). PD-L1 exhibits broad expression on many different cell types including resting and activated B cells, T cells, myeloid cells, and DCs whilst PD-L2 is expressed by activated macrophages and DCs (Greenwald,

Freeman and Sharpe, 2005). The fact that IFN-γ induces PD-L1 expression on several nonhematopoietic cells including endothelial cells, epithelial cells and tumour cells suggests that the PD-1-PD-L1 pathway is involved in mediating protection from T-cell attack as opposed to regulating early T-cell activation (Greenwald, Freeman and Sharpe, 2005; Sharma and Allison, 2015). The first anti-PD-1 antibody to be FDA approved was pembroluzimab following promising clinical trials that showed response rates reaching 38% in patients with advanced melanoma as well as response rates of 26% in patients that were refractory to prior ipilimumab treatment (Hamid *et al.*, 2013; Robert, Ribas, *et al.*, 2014). Soon after a different anti-PD-1 antibody called nivolumab showed improved response rates compared to chemotherapy alone and was as a result approved by the FDA for the treatment of both metastatic melanoma and non-small cell lung cancer (Robert, Long, *et al.*, 2014). Recently, the FDA approved the anti-PD-1 antibody avelumab as a first line treatment for advanced Merkel cell carcinoma following promising durable response rates reaching 70% in the phase 2 JAVELIN Merkel 200 trial (Kaufman *et al.*, 2018; Samimi, 2019). Combinatory ICB therapy consisting of nivolumab plus ipilimumab treatment has shown improved objective response rates reaching 50% with more than 80% tumour reduction in patients with advanced melanoma (Wolchok *et al.*, 2013). Combining ICI with other immunotherapies such as vaccination has also been explored. The use of T-VEC with ipilimumab was associated with significantly improved objective response rates (ORR) reaching 39% as compared to ipilimumab alone (ORR of 18%) in a phase 2 study in patients with advanced melanoma (Chesney *et al.*, 2018).

Whilst ICIs have shown to be effective in patients with advanced disease, only a proportion of treated patients have measurable responses and even less so have durable responses (Mellman *et al.*, 2016). ICIs are also largely ineffective in several tumour types including prostate, colorectal and pancreatic tumours (Mellman *et al.*, 2016). Understanding why only a proportion of patients are responsive and what makes select tumour types susceptible to treatment is currently being investigated (Darvin *et al.*, 2018; Kruger *et al.*, 2019). This in turn will drive the development of predictive biomarkers that could be used to select patients for ICI treatment (Darvin *et al.*, 2018; Kruger *et al.*, 2019). Resistance to both anti-PD-1 and anti-CTLA-4 treatment, has been linked to loss of MHC class I antigen presentation with only non-responding patients displaying a loss of both

beta-2-microglobulin (β_2M) copies (Sade-Feldman *et al.*, 2017). Defects in genes associated with IFN-γ pathways have also been linked to ICB resistance (Gao *et al.*, 2016; Zaretsky *et al.*, 2016).

1.3.4 Current Bottlenecks to Successful Immunotherapy

Analysis of pre-treatment biopsies have revealed that a lack of baseline T cell infiltrate within tumours prior to ICB or cancer vaccine administration, is associated with poor responses (Gajewski, Meng and Harlin, 2007; Harlin *et al.*, 2009; Ji *et al.*, 2012; Topalian *et al.*, 2012; Tumeh *et al.*, 2014; Ayers *et al.*, 2017). Given that most solid tumours can be characterized as having a non-T cell inflamed phenotype (Rooney *et al.*, 2015; Spranger *et al.*, 2016), it is of great interest to uncover the mechanisms that prevent anti-tumour T cell priming and T-cell trafficking (as discussed by Joyce and Fearon, 2015; Spranger and Gajewski, 2018b, 2018a) in an effort to expand currently available immunotherapy treatment to the majority of non-responsive cancer patients. Several tumour cell intrinsic pathways have been found to be associated with non-T cell inflamed tumours (Spranger and Gajewski, 2018a, 2018b).

1.3.4.1 WNT-β-catenin Signalling and T-cell Trafficking

The WNT-β-catenin signalling pathway was found to be activated in 48% of human metastatic melanoma lesions that were non-T cell inflamed (Spranger, Bao and Gajewski, 2015). A lack of T cell infiltration and response to ICB was subsequently recapitulated in melanoma mouse models expressing active β-catenin (Spranger, Bao and Gajewski, 2015). The presence of β-catenin in tumours was found to lead to a reduction of CCL4 expression; a chemokine involved in the recruitment of basic leucine zipper transcriptional factor ATF-like 3 lineage dendritic cells (Batf3 DCs) (Spranger, Bao and Gajewski, 2015). Batf3 DCs are capable of cross-presenting tumour derived antigens (Hildner *et al.*, 2008) and are required for the rejection of immunogenic tumour variants (Fuertes *et al.*, 2011). Further work by Spranger and colleagues revealed that a lack of T-cell infiltration in β-catenin positive tumours was a result of defective effector T cell trafficking (Spranger *et al.*, 2017). Batf3 DCs were shown to be the main producers of CXCL9 and CXCL10 which are required for the recruitment of

effector T-cells (Spranger *et al.*, 2017). Recently an integrative analysis of the Cancer Genome Atlas (TCGA) revealed that 28 out of 31 tumour types that were non-T cell inflamed had activated β-catenin signalling (Luke *et al.*, 2019) suggesting that this tumour intrinsic pathway is a broad and relevant therapeutic target for promoting T cell infiltration. Indeed the use of RNA interference (RNAi) targeting the CTNNB1 gene encoding β-catenin in several syngeneic tumour mouse models led to an increase in T cell infiltration and established sensitivity to ICB (Ganesh *et al.*, 2018).

1.3.4.2 The Tumour Microenvironment and Immune Cell Exclusion

Local factors within the tumour microenvironment (TME) have also been linked to a lack of T cell infiltrate. TGF-β signalling in fibroblasts was found to be associated with poor responses to the anti-PD-L1 drug atezolizumab in a patient cohort with metastatic urothelial cancer (Mariathasan *et al.*, 2018). A high TGF-β signature was also associated with an immune excluded phenotype whereby $CD8^+$ T cells were localized to the peritumoral stroma and excluded from the tumour parenchyma (Mariathasan *et al.*, 2018). Using an EMT6 mouse mammary carcinoma model which recapitulates an immune excluded phenotype, the combined use of anti-TGF-β and anti-PD-L1 antibodies facilitated T cell infiltration into the tumour parenchyma resulting in tumour regression (Mariathasan *et al.*, 2018). Similarly, TGF-β was found to be associated with a poor prognosis in human colorectal cancer (Calon *et al.*, 2015) and was later identified as the primary mechanism responsible for T cell exclusion from the tumour parenchyma in mice bearing four main colorectal cancer driver mutations in the WNT, EGFR, p53 and TGF-β signalling pathways (Tauriello *et al.*, 2018). By Inhibiting TGF-β through the use of galunisertib (TGFBR1 inhibitor), effective anti-tumour T cell responses were unleashed that in turn prevented metastasis to the liver (Tauriello *et al.*, 2018). Concurrent administration of galunisertib with anti-PD-L1 antibodies had a synergistic effect, leading to an increase in the number of infiltrating lymphocytes and a prolonged recurrence-free survival for over a year after treatment cessation (Tauriello *et al.*, 2018).

T cell exclusion and accumulation in the stroma can also be mediated by cancer associated fibroblasts (CAFs) which express the membrane protein

fibroblast activation protein-a (FAP) and are capable of producing matrix proteins such as collagen and fibronectin (as discussed by Joyce and Fearon, 2015). T cell motility was found to be particularly restricted in matrix dense areas as assessed by live cell imaging of 60 µm thick human lung tumour tissue slices (Salmon *et al.*, 2012) suggesting FAP^+ CAFs are capable of physically excluding T cells from the tumour parenchyma (as discussed by Joyce and Fearon, 2015). CXCL12 expression in human pancreatic ductal adenocarcinoma (PDAC) is associated with worse survival (Liang *et al.*, 2010) and in a mouse model of PDAC FAP^+ CAFs were found to be the main tumoral source of this chemokine (Feig *et al.*, 2013). Inhibition of the CXCL12/CXCR4 axis through the use of plerixaflor (a CXCR4 antagonist) together with anti-PD-L1 administration, potentiated T cell infiltration and control of tumour growth (Feig *et al.*, 2013). This combinatory therapy was also recently showed to be effective in a syngeneic mouse model of ovarian cancer (Zeng *et al.*, 2019). Whilst the mechanism of immunosuppression exerted by CXCL12 is not fully understood (as discussed by Joyce and Fearon, 2015), targeting of the CXCL12/CXCR4 axis provides an alternative therapeutic target that does not rely on the systemic depletion of FAP^+ CAFs which have essential roles in normal tissues (Roberts *et al.*, 2013).

1.3.4.3 Tumour Endothelium: A Barrier to Effective T Cell Trafficking

The TME may also regulate T cell entry into tumours during initial interactions between circulating T cells with local tumour blood vessels which can act as a tumour endothelial barrier (as discussed by Joyce and Fearon, 2015). For example, the analysis of over 600 tissue microarrays from several human tumour types including breast, colon and ovarian, revealed the selective expression of the death mediator Fas ligand (FasL) on tumour vasculature but not on normal tissue (Motz *et al.*, 2014). Tumours with high FasL expression had few $CD8^+$ T cells but abundant Treg cells (Motz *et al.*, 2014). This resistance by Tregs to FasL killing was found to be mediated by the expression of the anti-apoptotic FADD-like IL-1β–converting enzyme-inhibitory protein (c-FLIP) (Motz *et al.*, 2014). Importantly, in FasL expressing mouse tumours, blockade of FasL facilitated T cell influx which was further synergised by ACT therapy (Motz *et al.*, 2014). Several immunosuppressive factors which are found within the TME including VEGF, prostaglandin E2 (PGE2), and interleukin-10 (IL-10) were found

to induce FasL expression (Motz *et al.*, 2014). In human ovarian cancer the vascular expression of endothelin B receptor (ET_BR) as well as the immune regulatory ligand B7H3 was also associated with an absence of TILs and shorter patient survival times (Buckanovich *et al.*, 2008; Zang *et al.*, 2010).

Given that tumours rely on angiogenesis to grow and metastasize, the development of anti-angiogenic agents were initially developed to prune tumour vessels thereby starving them of oxygen and nutrient delivery (as discussed by Martin, Seano and Jain, 2019). However, the use of the anti-vascular endothelial growth factor (anti-VEGF) antibody bevacizumab showed no apparent improvement in survival as a monotherapy whilst improving the outcome of chemotherapy (Hurwitz *et al.*, 2004). In response to this observation, Rakesh Jain first coined the term vessel normalization which refers to the use of anti-angiogenic agents with the aim of normalizing tumour vessel structure and function leading to improved treatment outcomes through increased oxygen and drug delivery (Jain, 2005). Indeed, most types of tumours have poorly structured blood vessels that are compressed, leaky and poorly perfused giving rise to hypoxia which further supports an immunosuppressive TME, increased tumour malignancy and aggressiveness (as discussed by Jain, 2014).

Sustained expression of vascular endothelial growth factor-A (VEGF-A) in angiogenic tumours has also been shown to downregulate the expression of the adhesion molecules ICAM-1 and VCAM-1 on tumour vessels leading to an impairment of T cell extravasation (Gabrilovich *et al.*, 1996; Dirkx *et al.*, 2003). Several groups have examined whether the normalization of blood vessels through the judicious use of anti-angiogenic treatment can improve T cell infiltration as well as enhancing the response to established immunotherapies. For example, Rosenberg and colleagues demonstrated that a single dose of VEGF-neutralizing antibody was sufficient to significantly enhance T-cell infiltration into vascularized B16 melanoma tumours following the adoptive transfer of antigen specific T cells (Shrimali *et al.*, 2010). The use of low dose anti-VEGF receptor 2 (VEGFR-2) antibody was shown to lead to a more homogenous distribution of functionalized tumour blood vessels (with enhanced pericyte coverage and improved perfusion) in a mouse model of breast cancer, which in turn facilitated $CD4^+$ and $CD8^+$ T cell infiltration (Huang *et al.*, 2012).

Importantly higher doses of anti-VEGFR-2 antibody were inversely correlated with T cell infiltration (Huang *et al.*, 2012) supporting the vessel normalization hypothesis which argues against the use of high doses of anti-angiogenic agents which lead to vessel pruning (Jain, 2005). In addition to improving T cell extravasation, anti-VEGF treatment may also improve anti-tumour responses by preventing the inhibition of precursor DC maturation (Gabrilovich *et al.*, 1996). Whilst the impact of anti-VEGF treatment on vessel normalization is transient (as discussed by Jain, 2014; Rivera and Bergers, 2015), the inhibition of angiopoietin-2 (ANGPT2) can stably induce vessel normalization leading to improved drug delivery and enhanced T-cell infiltration (as discussed by Schmittnaegel and De Palma, 2017). ANGPT2 is a negative regulator of Tie-2; a stabilizer of tumour vasculature (as discussed by Martin, Seano and Jain, 2019). The ectopic expression of ANGPT2 was shown to counteract the benefits of anti-VEGF therapy in a mouse model of glioblastoma (GBM) (Chae *et al.*, 2010) and an increase in circulating ANGPT2 has been reported in GBM patients receiving cediranib (a pan-VEGFR tryrosine kinase inhibitor) (Batchelor *et al.*, 2010). Furthermore, in mouse pancreatic neuroendocrine tumours (PNET), ANGPT2 overexpression was identified as a mechanism of resistance to anti-VEGFA therapy (Rigamonti *et al.*, 2014). The combined use of anti-ANGPT2 and anti-VEGF therapy led to vessel normalization and reduction of GBM burden (Peterson *et al.*, 2016) and also suppressed PNET progression (Rigamonti *et al.*, 2014). Such dual therapy has also been shown to potentiate ICB therapy in several mouse models including models of metastatic breast cancer and colorectal adenocarcinoma (Schmittnaegel *et al.*, 2017). The use of a dual anti-ANGPT2 and anti-VEGFA targeting antibody (A2V) led to an increased perivascular accumulation of activated IFN-γ expressing CTLs which when combined with anti-PD-1 blockade further improved control of tumour growth (Schmittnaegel *et al.*, 2017).

The use of agents of which induce the development of specialized immune cell recruiting blood vessels termed HEVs has also been explored. HEVs are post-capillary venules confined to all secondary lymphoid organs (SLOs) except the spleen. HEVs have however been found to form at the site of chronic inflammatory diseases (Aloisi and Pujol-Borrell, 2006), infection (Neyt *et al.*, 2012) as well as cancer (Martinet *et al.*, 2011). HEVs can be found in isolation or

as parts of lymphoid like tissue termed tertiary lymphoid structures (TLSs) which vary in their respective organizational capacity but are not encapsulated like SLOs (as reviewed in Colbeck *et al.*, 2017). The role of TLS in cancer has been reviewed extensively elsewhere (Colbeck *et al.*, 2017; Sautes-Fridman *et al.*, 2019) but in general and with the information available to date, their presence in solid malignancies is associated with favourable prognosis (Cabrita *et al.*, 2020; Helmink *et al.*, 2020).

The correlation between HEV formation, increased lymphocyte infiltration and more favourable prognosis in various cancer types (Martinet *et al.*, 2011, 2012; Wirsing *et al.*, 2016) provides a rational for therapeutically inducing HEV formation in tumours. Several studies have implicated vessel normalization and stabilization as an important pre-requisite for TLS formation (Allen *et al.*, 2017; Johansson-Percival *et al.*, 2017; He *et al.*, 2018). The combined use of checkpoint inhibitors (anti PD-L1) with anti-angiogenic therapy has been shown to lead to the induction of HEVs in murine models of breast and pancreatic neuroendocrine mouse tumours but not in GBM (Allen *et al.*, 2017). This poor response in GBM was attributed to a lack of activated cytotoxic T cells within the tumour; a prerequisite for ICB efficacy (Tang *et al.*, 2016). However, administration of a lymphotoxin β receptor (LTβR) agonist together with anti-PD-L1 and anti-VEGF/VEGFR led to the induction of HEVs and a reduced tumour burden (Allen *et al.*, 2017). Similarly, the selective targeting of LIGHT (a ligand which signals through LTβR and HVEM) to tumour vasculature via vascular targeting peptides (VTPs) also results in vessel normalization and HEV induction (He *et al.*, 2018). VTPs are short peptides (5-9 amino acids long) which were first identified by in-vivo phage display to home specifically to neovessels found in either dysplastic lesions or in malignant tumours (Hoffman et al., 2003). When combined with antiangiogenic therapy and ICB, LIGHT-VTP triple therapy was effective against GBM, permitting the induction of HEVs and recruitment of $CD3^+$ tumour-infiltrating T cells leading to a reduction in tumour growth burden (He *et al.*, 2018). Normalized vasculature may therefore permit immune cell trafficking whilst immune cell activation through ICB leads to the release of cytokines which stimulate HEV formation. This points to a reciprocal interaction between adaptive immunity and tumour vasculature resulting in a positive feedback loop similar to the one described in a fibrosarcoma tumour model whereby the depletion of

Tregs leads to roughly 50% of tumours developing HEVs which was in turn found to be driven by TNFR signalling (Hindley *et al.*, 2012; Colbeck *et al.*, 2017).

In addition to modulating primary tumour vessels, LIGHT-VTP therapy has also been shown to normalize blood vessels in the pre-metastatic niche (He *et al.*, 2020). In a subcutaneous Lewis lung carcinoma mouse model, LIGHT-VTP therapy prevented metastatic lung colonization by limiting both cancer cell intravasation into the systemic circulation from the primary tumour as well as extravasation into pre-metastatic sites (He *et al.*, 2020). Furthermore, in a B16 metastatic melanoma mouse model, established metastatic blood vessels were normalized following LIGHT-VTP therapy (He *et al.*, 2020). This led to HEV formation, immune effector infiltration as well as sensitization to anti-PD-1 administration (He *et al.*, 2018). This work therefore provides a rationale for using LIGHT-VTP therapy for the prevention of metastasis as well as in the treatment of established metastatic disease (He *et al.*, 2020).

HEVs were also shown to be induced by the targeted delivery of lymphotoxin α (LTα) in a B78-D14 melanoma syngeneic tumour model (Schrama *et al.*, 2001). In addition to increased T cell infiltration and eradication of the primary tumour and pulmonary metastases, LTα therapy also led to the induction of TLSs composed of T cell, B cell and APC aggregates (Schrama *et al.*, 2001). This is consistent with the ability of LTα, which signals through TNFR1, TNFR2 and herpes virus entry mediator (HVEM) as a homotrimer as well as through LTβR as a heterotrimeric complex with LTβ, to induce TLS under chronic inflammation as first demonstrated by Kratz and colleagues who reported the development of organized lymphoid tissue at kidney and pancreas sites where expression of LTα was driven by the tissue specific rat insulin promoter (Kratz *et al.*, 1996).

In addition to HEV induction, the exploitation of spontaneously formed HEVs as a means of selectively delivering chemotherapeutic drugs is a promising avenue that has recently been explored. Pancreatic Ductal Adenocarcinoma (PDAC) is a lethal disease characterized by a dense stroma and extensive desmoplastic reaction which limits efficient drug delivery (Bahmani *et al.*, 2018). By targeting ectopic HEVs with MECA79-Taxol-nanoparticles Bahmani et al.

showed improved Taxol responses through PDAC growth suppression (Bahmani *et al.*, 2018). Furthermore, it was recently reported that preoperative neoadjuvant chemoradiotherapy (PAC) leads to a higher density of TLO containing HEVs which are associated with a more favourable prognosis (Kuwabara *et al.*, 2019). This provides a rational to both induce HEVs and exploit them for effective chemotherapeutic drug delivery in PDAC treatment.

1.4 High Endothelial Venules

1.4.1 HEV structure and function

HEVs are readily distinguished from other blood endothelial cells (BECs) by their characteristic plump, cuboidal morphology which was first described in the late 19th Century (Thomé, 1898). Whilst they share common pan-endothelial cell (EC) markers such as CD31 and VE-cadherin (Pfeiffer *et al.*, 2008), HEVs preferentially express genes that are important in the regulation of lymphocyte recruitment and immunological defence (Lee *et al.*, 2014). This includes the expression of several enzymes involved in the synthesis of mucin-like glycoproteins termed peripheral node addressins (PNAd) which act as adhesion molecules for CD62L (L-selectin) expressing lymphocytes (Lee *et al.*, 2014). Whilst mouse high endothelial cells (HECs) express CCL21 (an arrest chemokine required for transendothelial migration), human HECs rely on the perivascular delivery of CCL21 via transcytosis (Carlsen *et al.*, 2005). The interaction between L-selectin and PNAd mediates the tethering and rolling of lymphocytes along HEVs which marks the initial stages of the multistep adhesion cascade ultimately leading to lymphocyte extravasation into the LN parenchyma (Miyasaka and Tanaka, 2004; Girard, Moussion and Förster, 2012). Neutrophils and mononuclear phagocytes have also been shown to use L-selectin to roll across HEVs (Warnock *et al.*, 1998). Furthermore, activated platelets can use P-selectin to provide an alternative pathway for lymphocyte rolling across HEVs by forming a bridge between lymphocytes and HEVs (Diacovo *et al.*, 1998).

HEVs express PNAd both apically (thus allowing for lymphocyte recruitment) and basolaterally although the precise role of the latter is not well understood (Ager and May, 2015). In LNs, HEVs are localized to the cortical–

paracortical junction and paracortex (where the T-cell zone is located) and form part of the venular tree; a distinct hierarchy of venules which branch out from the largest collecting vein (order I) to the smallest post capillary venules (order V) (Figure 1.1) (von Andrian, 1996). Intravital microscopy studies performed by Ulrich von Andrian and colleagues revealed that the major sites of lymphocyte recruitment occur in venule branches that are of the order III-V which constitutes all HEVs (von Andrian, 1996). Single-cell RNA sequencing has revealed that HECs under homeostatic conditions display heterogenous gene expression profiles within the same tissue (Veerman *et al.*, 2019). This includes the heterogenous expression of CCL21 which may reflect specialized functions of individual HECs within the same tissue (for example LN paracortex vs medulla) (Veerman *et al.*, 2019). Individual HECs found lining the HEV wall at preferential sites for immune cell transmigration (termed “exit ramps”) may reflect such specialized functions (Bajenoff *et al.*, 2006). Furthermore, important differences in the regulation of genes controlling lymphocyte trafficking were also revealed by single-cell RNA sequencing (Veerman *et al.*, 2019). Several genes involved in the synthesis of the 6-sulfo sLeX epitope which decorate PNAd including the fucosyltransferase FucT-VII (Fut7) and core 2 branching enzyme Core2 GlcNAcT (Gcnt1) were found to require higher levels of LTβR-dependent signalling for expression than the sulfotransferase GlcNAc6ST-2 (Chst4) (Veerman *et al.*, 2019). Such differential sensitivity of HEV genes to LTβR-dependent signalling may in part explain the cellular and spatial heterogeneity of peripheral LN HEVs (Veerman *et al.*, 2019).

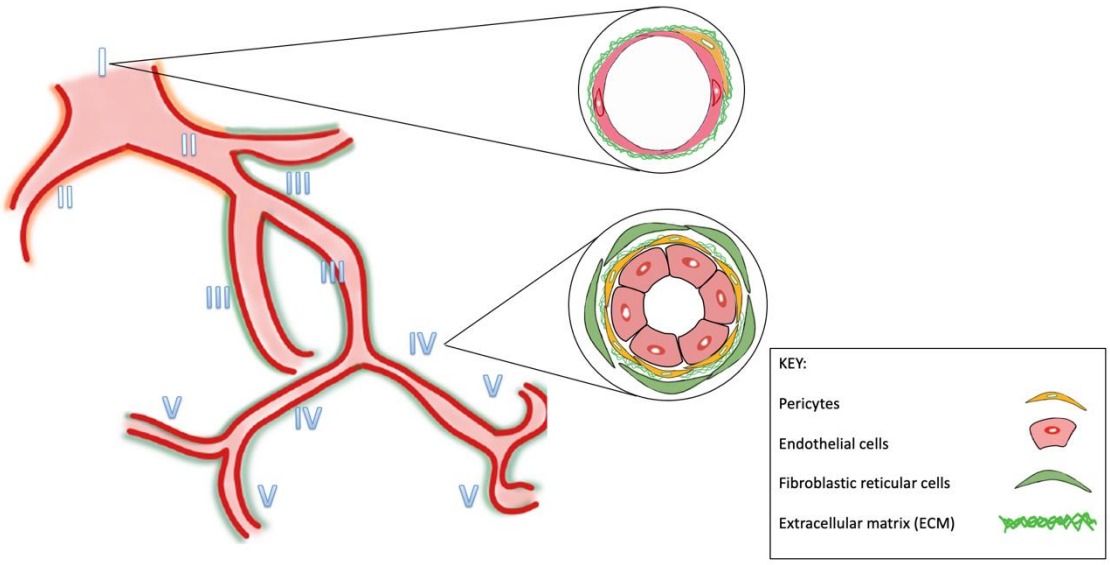

Figure 1.1 | HEV structure and function.
The venular tree found in lymph nodes (LNs) is organised into a distinct hierarchy of branches that branch out from the collecting venule (order I) until the smallest postcapillary venules (order V). HEVs constitute all venules found on the order of III–V and have a distinct cuboidal morphology composed of plump high endothelial cells. HEVs display a thickened basal lamina surrounded by overlapping pericytes and are ensheathed by concentric layers of fibroblastic reticular cells. This is in contrast to normal venules, which consist of flat endothelial cells surrounded by a thin basal lamina and ensheathed by pericytes. Figure adapted from (Girard, Moussion and Förster, 2012; Ager, 2017).

Mouse studies have shown that HEVs arise perinatally and can be identified by their distinct morphology, lack of PNAd expression and expression of MAdCAM-1 and CD34 at 18.5 days post coitum (d.p.c) (Hayasaka *et al.*, 2010). Since MAdCAM-1 is also expressed on lymphatic vessels (Cupedo *et al.*, 2004) the lack of an HEV-specific marker prevents the study of early HEV development. Consistent with the idea that HEVs differentiate from BECs, DNA microarray analysis on HECs isolated from new-born and adult mesenteric LNs showed that new-born HECs differentially express genes associated with angiogenesis as well as genes expressed by immature ECs and progenitor ECs (Hayasaka *et al.*, 2010). Whilst the factors which drive the differentiation of BECs to HECs have not been elucidated (Ager and May, 2015) several studies support the notion that mature HEVs require constant signalling in order to maintain their mature phenotype (Lacorre *et al.*, 2004; Browning *et al.*, 2005; Moussion and Girard, 2011). The downregulation of MAdCAM-1 and upregulation of PNAd marks the maturation of HEVs (Mebius *et al.*, 1996). That HECs rapidly de-differentiate when isolated from human tonsils points to a requirement for the LN microenvironment in maintaining HEVs (Lacorre *et al.*, 2004). More specifically LTβR activation on ECs (Onder *et al.*, 2013) maintains the expression of enzymes responsible for synthesis of PNAd and other scaffolding proteins required for supporting lymphocyte trafficking (Browning *et al.*, 2005). $CD11c^+$ DCs are known to express ligands for LTβR and when depleted the ability of HEVs to recruit immune cells is lost (Moussion and Girard, 2011).

1.4.2 Reactive LN HEV Remodelling

The functional and structural plasticity of HEVs in response to LN stimulation is well documented in the literature. Several studies performed in the 1970s utilized alcian blue dye infusion together with angiography to show extensive LN expansion and HEV remodelling (Herman, Yamamoto and Mellins, 1972; Anderson, Anderson and Wyllie, 1975). This was characterized by both HEV lengthening and increased branching patterns (Herman, Yamamoto and Mellins, 1972; Anderson, Anderson and Wyllie, 1975). This vascular expansion was also accompanied by increased blood flow and lymphocyte trafficking (Hay and Hobbs, 1977) reflecting functional changes in response to vascular remodelling. Whilst autoradiographic studies revealed increases in HEV

endothelial cell proliferation (Anderson, Anderson and Wyllie, 1975), the mechanisms governing HEV remodelling in response to immunization have only recently begun to be elucidated.

HEVs are suspended in a reticular network characterized by collagen rich fibrils ensheathed by reticular cells termed fibroblastic reticular cells (FRCs). The FRC network is important for providing chemokine and survival cues for T cells (Link *et al.*, 2007) as well as a platform that supports effective dendritic cell migration (Acton *et al.*, 2012) and facilitating T cell migration possibly contributing to a higher propensity for DC-T cell encounter (Bajenoff *et al.*, 2006). In addition to these roles, FRCs have been found to be important in mediating HEV remodelling following OVA/CFA immunization, given that they are one of the main producers of VEGF mRNA (Chyou *et al.*, 2008). VEGF production is driven by LTβR signalling on FRCs (Chyou *et al.*, 2008). In addition to regulating the blood vessel compartment, the close proximity of FRCs to lymphatic vessels and the reduction in $PNAd^-$ endothelial cells (of which 20% constitute lymphatic endothelial cells) following VEGF blockade suggests FRCs also play a role in regulating the lymphatic vessel compartment (Chyou *et al.*, 2008). LN B-cells play a key role in the expansion of the lymphatic network required for effective dendritic cell migration from the periphery and provide a source of VEGF-A (Angeli *et al.*, 2006).

The vascular-stromal compartment is therefore involved in HEV remodelling and cues provided by immune cells stimulate the expansion of both compartments in order to accommodate the development of an immune response (Figure 1.2). Specifically, $CD11c^+$ cells are important in the initiation and resolution of this response whilst T cells and B cells are important drivers of HEV and FRC expansion (Webster *et al.*, 2006; Tzeng *et al.*, 2010; Chyou *et al.*, 2011). Therefore, the cells which make up the LN are also actively involved in its remodelling in response to LN stimulation. $CD11c^+$ DCs play an important role in modulating HEV expansion and maintaining HEV function (Moussion and Girard, 2011).

HEV remodelling is thought to support the initiation of an adaptive immune response by increasing the pool of naïve lymphocytes which can detect cognate

antigen. For example, intravaginal infection of mice with herpes simplex virus type 2 (HSV-2) results in LN hypertrophy and an accumulation of non-dividing lymphocytes with a naïve resting phenotype (Soderberg *et al.*, 2005). Furthermore, the rate of lymphocyte entry into draining LNs is enhanced and is mediated by an increase in HEV numbers as well as the expansion of the primary feed vessel (Soderberg *et al.*, 2005). Similar increases in trafficking efficiency have been documented following OVA/CFA immunization (Chyou *et al.*, 2008). Importantly, inhibiting the remodelling of the vascular-stromal compartment through VEGF inhibition reduces the frequency of lymphocytes that enter into the draining LN (Chyou *et al.*, 2008).

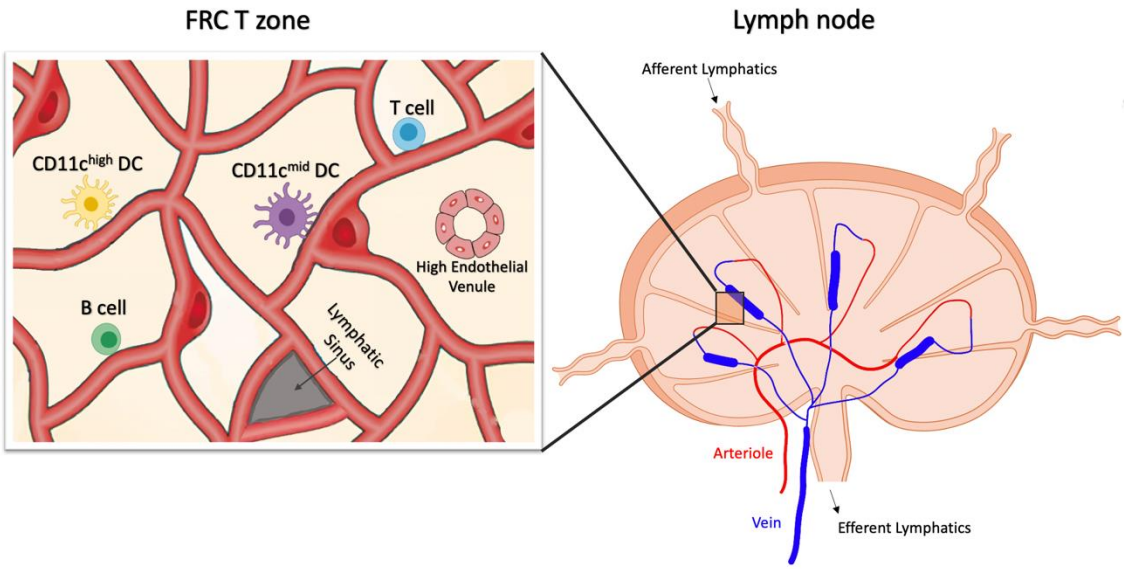

Figure 1.2 | Vascular-stromal elements involved in LN HEV remodelling.
The LN feeding arteriole branches into capillaries, which in turn branch into postcapillary HEVs (thickened blue segment). Cross-section of vascular-stromal elements found in the T zone are depicted. HEVs are suspended in a reticular network characterised by collagen-rich fibrils ensheathed by reticular cells, termed fibroblastic reticular cells (FRCs), which form a network supporting immune cell migration and survival. In addition to FRCs, T cells, B cells, and dendritic cells (DCs) are involved in mediating HEV remodelling in response to ovalbumin in complete Freund's adjuvant (OVA/CFA) immunisation. The initiation phase is driven by $CD11c^{Med}$ DCs (purple), whilst the expansion phase is driven by T and B cells. $CD11c^{High}$ DCs (yellow) are important in the resolution of this response. FRCs are also in close proximity to lymphatic vessels and may have a role in the regulation of this compartment as well. Figure adapted from (Fletcher, Acton and Knoblich, 2015; Dasoveanu *et al.*, 2016).

HEV remodelling in response to experimental OVA/CFA immunization has been extensively studied and is a well-regulated process which occurs in three distinct phases (Webster *et al.*, 2006; Chyou *et al.*, 2008, 2011; Tzeng *et al.*, 2010; Kumar *et al.*, 2012; Benahmed *et al.*, 2014). The initiation phase lasts for 2 days and is driven by $CD11c^+$ cells (Webster *et al.*, 2006). The initiation phase is also T cell and B cell independent and therefore occurs in the absence of antigen presentation (Chyou *et al.*, 2011). Upregulation of VEGF by FRCs is in part stimulated by the release of IL-1β from $CD11c^+$ cells (Benahmed *et al.*, 2014). The initiation phase is marked by increased endothelial cell proliferation, FRC proliferation and a modest increase in HEV EC numbers (Webster *et al.*, 2006; Chyou *et al.*, 2011). FRCs which are normally tightly wrapped around vessels begin to detach to allow for vascular expansion to occur (Tzeng *et al.*, 2010). The ability of FRCs to stretch and allow for LN expansion to occur is driven by the delivery of C-type lectin receptor 2 (CLEC-2) by $CD11c^+$ cells which leads to the uncoupling of podoplanin (PDPN) from RhoA/C, resulting in the relaxation of the actomyosin cytoskeleton (Acton *et al.*, 2014). PDPN expression by FRCs is also critical in the maintenance of overall HEV integrity during LN expansion and lymphocyte homing through its interaction with CLEC-2 expressing platelets (Herzog *et al.*, 2013).

In addition to EC and FRC proliferation, the expansion phase marks extensive increases in total HEV length and branching patterns (Kumar *et al.*, 2012) and lasts between days 2-5 (Chyou *et al.*, 2011). Recently multi-coloured fluorescent fate-mapping models which enable labelling of adult LN ECs with specific colours to allow for subsequent progeny tracking at the single cell level, have revealed that HECs act as local progenitors to create both capillaries and HEV neo-vessels during vascular expansion (Mondor *et al.*, 2016). This phase is strongly dependent on T cells and B cells which are required for the expansion of both the vascular and stromal compartment (Chyou *et al.*, 2011). HEV expansion may therefore reflect an effort to support the development of an adaptive immune response (Dasoveanu *et al.*, 2016). In addition to structural HEVs changes that occur during this phase there are also marked changes in HEV phenotype. HEVs revert to an immature phenotype (MAdCAM-1^{high}HEC-$6ST^{low}$) coinciding with impaired afferent lymphatic vessel function characterized by a lack of tracer dye accumulation within the reactive LN (Liao and Ruddle,

2006). This in turn leads to the dilution of LTβR derived DC ligands (Moussion and Girard, 2011). It has been suggested that this impairment in lymphocyte recruitment serves to prevent the dilution of lymphocytes that have already established contact with antigen presenting DCs (Ager and May, 2015).

The vascular-stromal quiescence phase can last for several weeks and is mediated by $CD11c^{hi}$ DCs (Tzeng *et al.*, 2010). This phase marks a reduction in HEV and FRC proliferation, reduction in HEV trafficking efficiency and stabilization of vessels by FRC reassembly around vessels (Tzeng *et al.*, 2010). HEVs also revert back to a mature phenotype during this period (Liao and Ruddle, 2006). LN vascular expansion is then thought to eventually result in vascular regression following the resolution of the immune response (Dasoveanu *et al.*, 2016). Whilst partial lymphatic vessel regression has been documented (Mumprecht, Roudnicky and Detmar, 2012) complete reversion of the vascular-stromal compartment has not been shown. Both pre-existing and neo-vessels have been found to be pruned at the same pace during LN quiescence (Mondor *et al.*, 2016). The factors that induce such pruning remain to be identified and likely involve a combination of both active signalling pathways and withdrawal of survival factors (Mondor *et al.*, 2016).

Several questions regarding vascular-stromal expansion remain including delineating specific DC subsets involved in HEV remodelling regulation as well as the identification of additional mediators stimulating VEGF expression (as discussed by Dasoveanu *et al.*, 2016). However, insights gained from OVA/CFA induced HEV remodelling have revealed important regulatory mechanisms that can be examined under different LN stimulation settings. For example, in MRL-lpr/lpr mice, a chronic model of spontaneous lupus, the continually expanding vasculature is a result of the re-establishment of quiescence driven by above base-line EC proliferation (Chyou *et al.*, 2012).

1.4.3 Global Lymph Node HEV Remodelling

The development of mesoscopic imaging techniques such as optical projection tomography (OPT) and LSFM have allowed for the global analysis of HEV network remodelling in response to infection (Kumar *et al.*, 2010),

immunization and autoimmune lymphadenopathy (Kumar *et al.*, 2012). Such studies have proven useful for mapping progressive changes to all HEVs and have revealed key similarities and differences between different LN stimulation settings. The total number of vessels and branching points including each individual vessel length and diameter can be extracted from LSFM/OPT acquired datasets (Figure 1.3). Since vessel elongation and a reduction in diameter may also result from vessel stretching as opposed to an increase in number of HECs (reflecting expansion), flow cytometric analysis and enumeration of HEC populations can be performed following 3D imaging by rehydration of organic solvent cleared LN samples (Kumar *et al.*, 2010, 2012).

Lymphocytic choriomeningitis virus (LCMV) is a widely used mouse model for examining immune responses during viral infection due to it being non-cytolytic and capable of inducing a wide range of immune responses depending upon which LCMV strain is used (Oldstone, 2016). LCMV has a strong tropism for SLOs and the resulting structural changes that LN HEV networks undergo following LCMV infection were examined by Kumar and colleagues using OPT (Kumar *et al.*, 2010). In this work similarities were found between LCMV and OVA/CFA immunization in terms of total HEV network length and extent of HEV branching (arborization) which likely reflect shared regulatory mechanisms underpinning HEV remodelling (Kumar *et al.*, 2010, 2012). On the other hand, differences such as vessel arborization preceding elongation during LCMV infection (Kumar *et al.*, 2010) likely reflect stimuli specific differences. Indeed, LCMV induced HEV remodelling is primarily driven by LT-$\alpha_1\beta_2$ expressing B cells and not by VEGF-A stimulation (Kumar *et al.*, 2010). The impact of targeting vessel remodelling in an attempt to modulate immune activity can also be assessed by 3D imaging. For example, mesenchymal stem cells (MSCs) are well established inhibitors of inflammation and immunity and show therapeutic efficacy in several mouse models of human disease (Zanotti *et al.*, 2016). Previous work by Zannotti et al. explored whether MSC mediated immunosuppression is driven by modulation of the LN vascular compartment using OPT (Zanotti *et al.*, 2016). Following MSC administration a reduction in HEV elongation and arborization in response to OVA/CFA immunization was noted resulting in impaired immune cell trafficking (Zanotti *et al.*, 2016). Understanding how HEV remodelling progresses during different disease states

will provide useful information for elucidating the factors controlling such changes and provide common targets for therapeutic targeting. By inducing HEV expansion it may be possible to promote immune activation by enhancing immune cell recruitment. Conversely inhibiting HEV remodelling may prove useful for the treatment of diseases driven by excessive immune activation.

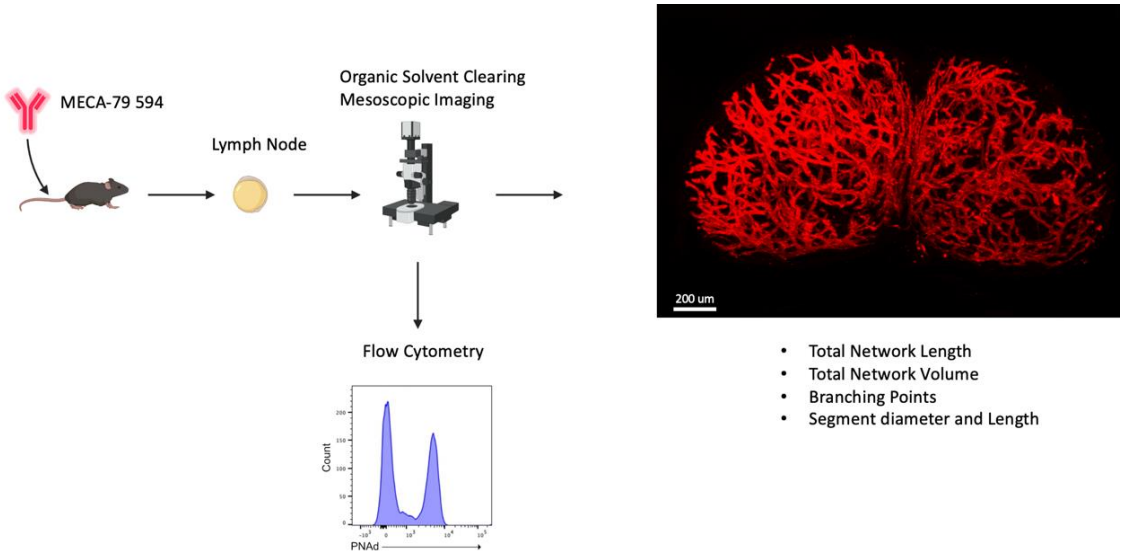

Figure 1.3 | 3D Imaging of HEV Networks with OPT and LSFM.
Whole lymph node (LN) HEV networks can be labelled intravenously using the fluorescently labelled MECA-79 antibody, which recognises the 6-sulpho sialyl Lewis X epitope presented on peripheral node addressin (PNAd). Labelled lymph nodes are optically cleared using organic solvents and imaged either by OPT or LSFM. Extended volume confocal imaging (EVIS imaging) can also be used to reconstruct the 3D structure of HEVs. Through the use of vessel tracing tools, several numerical parameters, including individual segment lengths and diameters, can be extracted from the 3D datasets. Following 3D imaging, samples can be rehydrated for flow cytometric analysis. Figure adapted from (Kumar *et al.*, 2010).

1.4.4 Sentinel LN HEV Remodelling and Tumour Cell Dissemination

Regional LNs which drain established tumours and are the first to receive metastatic cells (referred to as sentinel LN (SLN)) are known to undergo tumour-reactive lymphadenopathy accompanied by both lymphatic and vascular expansion (Qian *et al.*, 2006; Chung *et al.*, 2012; Lee *et al.*, 2012). SLN vessels studied in the context of mouse models and human breast, squamous cell cancer and melanoma, are described as enlarged, thin-walled vessels engorged with red blood cells (RBCs); a transition which precedes the ability to detect metastatic tumour cells in the SLN (Figure 1.4) (Qian *et al.*, 2006; Chung *et al.*, 2012; Lee *et al.*, 2012; Maeda *et al.*, 2018). For this reason, it is conceivable that tumours may "prime" SLN vessels via lymph-borne tumour-specific or inflammatory mediators to prepare for the arrival of malignant cells.

Whilst there may be some commonality between lymph borne factors driving remodelling of tumour reactive and immune reactive LNs, overall the mechanisms driving such changes are likely to be largely distinct. In support of this, it has been shown that nude mice are susceptible to SLN remodelling but resistant to endotoxin induced LN remodelling suggesting a lack of immune cell involvement in the former (Qian *et al.*, 2006).

The functional consequences of SLN HEV remodelling have been described. Real-time ultrasonography studies have revealed SLNs have increased blood flow to large blood vessels (Qian *et al.*, 2006). Furthermore, 2D histological examination of SLNs in human and murine tumours showed red RBCs localized within the HEV lumen and a loss of the functional HEV marker PNAd (Qian *et al.*, 2006; Chung *et al.*, 2012; Lee *et al.*, 2012). SLN HEV remodelling is therefore thought to represent a switch in functionality from immune cell carrier to blood flow carrier (Qian *et al.*, 2006). Importantly, in human tongue squamous cell carcinoma, the patient's overall survival risk was progressively worse as more HEVs were identified per high power field with the highest risk seen in patients with dilated HEVs with RBCs localized to the lumen (Lee *et al.*, 2012). Therefore, SLN HEV remodelling towards a blood flow carrier is associated with a worse prognosis regardless of whether LN metastasis is established (Lee *et al.*, 2012).

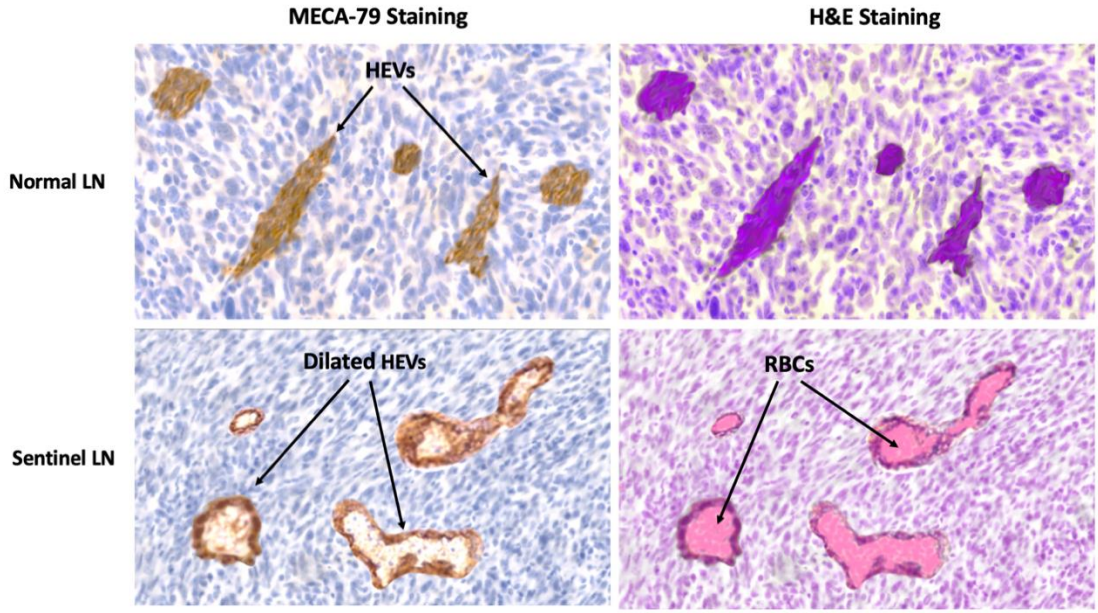

Figure 1.4 | Sentinel LN HEV Remodelling.
Both murine and human sentinel LNs undergo extensive HEV remodelling. This is characterised by a thinning of the vessel wall and an increase in vessel diameter. A higher density of HEVs as well as the accumulation of red blood cells (RBCs) in the HEV lumen is associated with more aggressive disease and poorer survival. Functional changes to sentinel LN HEVs include reduced peripheral node addressin (PNAd) and CCL21 expression, leading to defective immune cell trafficking. Figure was illustrated in Adobe Photoshop 21.2 using an LN nuclear counterstain, which served as the background layer. All other objects, including the H&E stain, RBCs, and MECA-79 stain were illustrated using the background layer as a graphical template. Figure adapted from (Qian *et al.*, 2006).

In addition to structural changes in SLN HEVs, intravital microscopy of LNs draining B16 melanoma tumours also revealed impaired HEV function (Carriere *et al.*, 2005). Lymphocyte adhesion in HEVs was found to be reduced along with a decrease in expression of the chemokine CCL21 (Carriere *et al.*, 2005). which mediates lymphocyte arrest on the HEV endothelium (Girard, Moussion and Förster, 2012). Again, this occurred irrespective of LN metastasis suggesting a disruption of HEV function in response to the establishment of a tumour (Carriere *et al.*, 2005)).

The involvement of LNs as a gateway for further dissemination of tumour cells is supported by correlative evidence from mouse models of breast and prostate cancer (Chen *et al.*, 2005; Roberts *et al.*, 2006; Burton *et al.*, 2008) as well as human breast cancer patients who have worse outcomes if they present with lymphovascular invasion and nodal metastasis (Jatoi *et al.*, 1999; Clarke *et al.*, 2005; Mohammed *et al.*, 2007; Nathanson *et al.*, 2010). Therapeutic intervention by means of irradiating regional LNs has also been associated with improved outcomes in early-stage breast cancer patients (Poortmans *et al.*, 2015; Whelan *et al.*, 2015). The ability of HEVs to provide a lymphatic-venous shortcut for metastasizing cells to directly access the blood circulation has been suggested previously (Qian, Resau and Teh, 2007) and is supported by the finding that 20% of women with node-negative breast cancer still develop metastasis (Lee *et al.*, 2012).

Tumour cell dissemination via HEVs was confirmed recently by two studies. By microinfusing 4T1 mammary carcinoma tumour cells intralymphatically, Brown et al. showed that 4T1 cells accumulated within the subcapsular sinus of the draining LN (Brown *et al.*, 2018). Three days post-infusion, 4T1 cells were found closely associated with HEVs and were also found to have intravasated the HEV lumen (Brown *et al.*, 2018). By infusing mCherry$^+$ luciferase$^+$ 4T1 cells it was possible to detect metastasis in the lungs through the use of whole-animal *in-vivo* bioluminescence imaging (Brown *et al.*, 2018). Importantly lung metastasis and the presence of mCherry$^+$ 4T1 cells in the blood circulation were only detectable 3 days after intra-lymphatic infusion coinciding with the time taken for the tumour cells to intravasate HEVs (Brown *et al.*, 2018). Furthermore, the ligation of downstream efferent lymphatics did not compromise the ability of 4T1 cells to

seed the lungs (Brown *et al.*, 2018), confirming the role of HEVs as an active gateway for tumour cell dissemination. A separate study by Pereira and colleagues used several cancer cell lines (including 4T1, B16-F10 melanoma and SCCV2 squamous cell carcinoma) engineered to express the photoconvertible protein Dendra2 (Pereira *et al.*, 2018). Dendra2 is a green-light emitting protein that upon excitation with a 405-nm laser diode is converted to a red-light emitting protein. Using this technology, it is therefore possible to track the migratory fate of cells photoconverted at tissue specific sites. By orthotopically implanting Dendra2 expressing tumour cells and photoconverting cells within the metastatic draining LN following tumour establishment, the presence of red-light emitting cells was detected in the systemic blood circulation and in the lungs (Pereira *et al.*, 2018). The directed migration of photoconverted tumour cells towards LN blood vessels and subsequent migration within vessels was also confirmed by two-photon microscopy (Pereira *et al.*, 2018). These two key studies therefore showed that HEVs are the main exit route by which tumour cells gain entry to the blood circulation.

The study by Brown et al. did not require tumour establishment in order for HEVs to disseminate intralymphatic infused 4T1 cells (Brown *et al.*, 2018). The implication of this is that HEVs in their basal state (in the absence of tumour driven SLN remodelling) are able to support tumour cell dissemination. Given that SLN HEV remodelling is known to occur and precede tumour cell colonization of the LN (Qian *et al.*, 2006) and that increased HEV density along with the presence of RBCs is associated with reduced overall survival (Lee *et al.*, 2012), it would be of interest to examine the impact this remodelling has on tumour cell dissemination efficiency.

The mechanisms governing SLN HEV remodelling require further investigation since currently no clinicopathological factors have been found to correlate with SLN HEV remodelling in humans (Chung *et al.*, 2012). Furthermore, changes to the stromal compartment have not been examined in this context and it is not known whether FRCs expand and/or disassemble around HEVs (Qian, Resau and Teh, 2007) as is the case in other types of LN stimulation settings (Tzeng *et al.*, 2010; Chyou *et al.*, 2011). It is likely that lymph-borne factors as opposed to blood-borne factors stimulate HEV remodelling as injecting

dead tumour cells and plasma from tumour bearing mice does not induce systemic LN HEV remodelling (Qian, Resau and Teh, 2007). In a murine model of VEGF-D driven tumour metastasis, bone morphogenetic protein-4 (BMP-4) expressed by LN endothelial cells was identified as a negative regulator of HEV remodelling (Farnsworth *et al.*, 2011). In this model, HEV EC dilation and proliferation were induced by VEGFR-2 signalling whilst BMP-4 downregulation was not rescued by VEGFR-2 inhibition suggesting additional regulatory pathways (Farnsworth *et al.*, 2011).

What is currently lacking is a global analysis of SLN HEV remodelling using the aforementioned 3D imaging techniques. Whilst HEV diameters are increased in SLNs (Qian *et al.*, 2006; Qian, Resau and Teh, 2007; Chung *et al.*, 2012; Lee *et al.*, 2012), it is unclear what the relative contribution of HEV elongation and arborization is to the reported increases in HEV densities which have been identified by 2D histology. Such information can only be established by performing 3D imaging and mapping changes in total vessel length/diameter distribution and number. Therefore, characterizing the tumour driven progression of HEV remodelling and comparing this to previously characterized HEV changes may reveal shared features that could be therapeutically targeted if such changes are indeed found to be important mediators of tumour metastasis.

1.4.5 Ectopic HEVs in the Tumour Microenvironment

The extent of lymphocyte infiltration is associated with favourable clinical outcome in several cancers including ovarian carcinoma, lung and colon cancer (Pages *et al.*, 2005, 2009; Galon *et al.*, 2006). However, the formation of HEVs in primary human solid tumours and its association with lymphocyte infiltration was first reported by Martinet et al. (Martinet *et al.*, 2011). In this work, cuboidal HEVs were reportedly found in several tumour types including breast, lung, ovarian, colon and melanoma (Martinet *et al.*, 2011). Importantly in a retrospective cohort of 146 invasive breast cancer patients, HEVs were found to correlate with disease-free, metastasis-free and overall survival (Martinet *et al.*, 2011). In addition to tumour regression, the expression of both naïve T cell and Th1 genes correlated with HEV density in human melanoma further supporting the role of HEVs as active sites of lymphocyte recruitment and activation (Martinet *et al.*, 2012). In patients with oral squamous cell carcinoma (OSCC) the presence of HEVs was associated with 5-year longer disease specific survival (DSS) (Wirsing *et al.*, 2016). Interestingly higher-grade tumours (T3 and T4 stage) had less HEVs than lower grade tumours and the complete absence of HEVs was associated with worse DSS (Wirsing *et al.*, 2016).

In keeping with their function in SLOs (von Andrian and Mempel, 2003), several murine studies further support the role of intratumoral HEVs as active sites of lymphocyte recruitment (Schrama *et al.*, 2008; Hindley *et al.*, 2012; Di Caro *et al.*, 2014; Peske *et al.*, 2015; Colbeck *et al.*, 2017). For example, intravenously injected GFP^+ splenocytes can be recruited to spontaneously induced TLS in a model of inflammation-driven carcinogenesis (Di Caro *et al.*, 2014). Furthermore, in a B16 melanoma model, the induction of TLS in splenectomized $LT\alpha^{-/-}$ mice which lack all peripheral LNs leads to the recruitment and induction of specific T cell responses suggesting in-situ priming at TLS sites (Schrama *et al.*, 2008). Even in the absence of supporting TLSs, HEVs have been implicated in recruiting and initiating specific T cell responses (Hindley *et al.*, 2012; Peske *et al.*, 2015; Colbeck *et al.*, 2017). Unlike in SLOs however (von Andrian and Mempel, 2003), the functional consequence of HEV formation in tumours remains to be determined by intravital *in-vivo* microscopy (as discussed by Colbeck *et al.*, 2017). HEVs may simply be a by-product of an ongoing immune

response or actively involved in shaping the immune response through immune cell recruitment (as discussed by Colbeck *et al.*, 2017). In the fibrosarcoma tumour model where HEVs can form following Treg depletion, HEV development was completely abrogated by blockade of TNFR signalling (Hindley *et al.*, 2012; Colbeck *et al.*, 2017). As a result, the TIL frequency was comparable to those tumours which do not develop HEVs following Treg depletion (Colbeck *et al.*, 2017) suggesting an active role of HEVs in immune cell recruitment. Lastly, not all TLS/HEVs may result in improved anti-tumour immunity. Shields et al., have showed that B16-F10 melanoma tumours engineered to express CCL21 form TLS that have an immunosuppressive role through the recruitment of Tregs (Shields *et al.*, 2010). Similarly, immunosuppressive activated Tregs were found localized to TLS in a mouse model of lung adenocarcinoma (Joshi *et al.*, 2015). However, robust anti-tumour T cell responses and tumour destruction was achievable following local Treg depletion in the lung (Joshi *et al.*, 2015), suggesting that the role of TLS in tumour progression can be modulated by therapeutic intervention.

1.5 Aims and Hypotheses

There were two main hypotheses that were tested within this study:

1) Intra-tumoral HEVs exhibit a heterogenous structural organization and asymmetric distribution pattern which is distinct from that of HEVs found in SLOs such as LNs.
2) Intra-tumoral HEVs can be augmented through the use of LTβR agonist and neutralizing anti-IL-27 antibodies to further enhance the extent of T-cell infiltration and further improve control of tumour growth.

In order to test these hypotheses the following aims were used:

1) Optimize fluorescent labelling, clearing and LSFM imaging protocols that allow for a global 3D characterization of blood vessels and HEVs found in fibrosarcoma tumours and LNs.

2) Further develop, implement and validate 3D vessel quantification tools that can be used to generate topological descriptors of continuous blood vessel networks acquired by LSFM imaging.

3) To implement the aforementioned techniques to examine features of tumours and SLN vessels and how this relates to tumour growth.

2. Methods

2.1 Mouse Work

2.1.1 Mice

Genetically engineered Foxp3^{DTR} mice first described by Kim and colleagues (Kim, Rasmussen and Rudensky, 2007) were gratefully received from Professor Alexander Rudensky and backcrossed with C57BL/6 mice in-house for more than 5 generations. Mice were housed in accordance with UK Home Office regulations and isolator-bred before being housed in filter-top cages for the duration of experiments.

2.1.2 Tumour Induction and Growth Monitoring

Foxp3^{DTR} mice aged 8 to 15 weeks were injected subcutaneously into the left hind leg with 400 µg of 3-methylcholanthrene (Sigma-Aldrich) in 100 mL of olive oil under general anaesthetic as described previously (Hindley *et al.*, 2012). Mice were then monitored for tumour development weekly for up to 18 weeks. Tumour-bearing mice were culled before their tumours reached 1.5 cm in diameter or if tumours caused apparent discomfort.

Tumour size and growth were monitored every other day using calipers. Measurements of the tumour leg width, non-tumour leg width, tumour width and tumour height were recorded in millimetres. Subsequently the tumour growth rate (k, days^{-1}) was derived by taking the difference between the tumour and non-tumour leg diameters and using the equation for exponential growth: $Y=Y0 \times exp(k \times X)$, which was performed in the statistical package Prism 7 (Graphpad).

2.1.3 In-vivo Treg depletion and Administration of Anti-LTβR Agonist and Anti-IL-27 Antibodies

Following the detection of a palpable tumour, 0.1 µg of diphtheria toxin (DT) diluted in 100 µl of phosphate buffer saline (PBS, Gibco Life Technologies) was administered intraperitoneally (i.p.) every other day for at least 3 treatments to deplete Tregs *in-vivo*.

Anti-LTβR agonist (4H8) was kindly gifted by Professor Carl Ware (Sanford-Burnham-Prebys Medical Discovery Institute, La Jolla, San Diego, California). 100 µg of this agent was diluted in 100 µl of sterile PBS and administered i.p. to $Foxp3^{DTR}$ mice every 3 days for a total of 14 days.

20 µg of anti-IL27 (R&D systems) was prepared in a 100 ul of sterile PBS and injected i.p. every 3 days for a total of 3 treatments before tumour harvest. All i.p. injections were performed by Kathryn Smart.

2.1.4 Tissue Dissection

Tumours were carefully dissected and separated from muscle and other normal tissue including the local popliteal LN. The inguinal lymph node found in close proximity to the tumour bearing hind leg was designated as the tumour draining LN (dLN) and the contralateral inguinal lymph node was designated as the non-draining LN (ndLN). *In-vivo* labelled tumours and LNs were excised and immediately fixed in 4% paraformaldehyde (PFA, ThermoFischer) at 4^0C overnight whilst tumours and LNs that were used for standard 2D immunohistochemistry (IHC) and immunofluorescence (IF) were placed in either optimum cutting temperature (OCT, CellPath) and stored at -80ºC or fixed in 4% neutral-buffered formalin solution (NBFS) and embedded in paraffin.

2.2 Immunofluorescence

2.2.1 Frozen Sections

5 µm thick sections of a naïve inguinal LN frozen in OCT compound and stored at -80ºC were cut using a cryostat. Sections were fixed in 4% PFA for 10 minutes then washed 3x 5 minutes in PBS. Sections were then washed in 0.3M glycine in PBS for 10 minutes to quench free aldehydes. Sections were washed for 3x 5 minutes in PBS after which they were blocked with 2.5% normal horse serum (VectorLabs) for 30 minutes at room temperature (RT). Sections were washed 3x 5 minutes in PBS before being incubated with 250 µl of primary antibody diluted in 1% Bovine serum albumin (BSA)/PBS overnight at 4ºC. A list of antibodies used is found in Table 2.1. Sections were then washed 3x 5 minutes in PBS and post-fixed in 1% PFA for 10 minutes. Sections were washed in 0.3M glycine for 10 minutes and washed for 3x 5 minutes in PBS before being mounted in Vectashield containing 4, 6-diamidino-2-phenylindole (DAPI) after which they were covered with a glass coverslip and sealed with nail varnish. Sections were then imaged using a Zeiss LSM 800 confocal microscope.

2.3 Immunohistochemistry

2.3.1 Formalin Fixed Paraffin Embedded (FFPE) Sections

5 µm thick sections of tumours, dLNs and ndLNs were cut on a microtome and mounted on glass slides. The slides were then left to dry overnight at 37ºC before being baked at 60ºC for 45 minutes. Baked sections were then dewaxed in xylene (3x 3 minutes) before being rehydrated in descending concentrations of ethanol (2x 3 minutes in 100% ethanol, 3 minutes in 90% ethanol and 3 minutes in 70% ethanol) before being placed under running tap water for 5 minutes. After a brief wash in distilled water, the sections were placed in Tris-EDTA antigen retrieval buffer (10 mM Tris Base, 1 mM EDTA, 0.05% Tween 20, pH 8.0) and heated for 20 minutes inside a pressure cooker. The slides were left to cool down for 30 minutes before being washed for 3x 3 min in PBS and blocked for 10 minutes in 0.3% hydrogen peroxide/PBS to block endogenous peroxidase activity. Non-specific antibody binding was blocked by incubating slides in 2.5%

horse serum for 30 minutes at RT. Slides were then incubated overnight at 4^{o}C with 250 µl of primary antibody diluent prepared in 1% BSA/PBS. A list of antibodies used is found in Table 2.1. The following day the sections were washed 3x 3 minutes in PBS and incubated with the relevant ImmPRESS^{TM} horseradish peroxidase (HRP) polymer detection kit (VectorLabs) for 30 minutes. Slides were then washed 3 x 3 minutes in PBS before being incubated with the HRP substrate (both VectorLabs) Impact DAB (3, 3'-diaminobenzidine, brown) for 7 minutes. After a brief wash in distilled water, slides were counterstained in Mayer's Hematoxylin for 4.5 minutes before being incubated in bluing reagent (Sigma) for 1 minute to detect nuclei. Slides were then dehydrated in 100% ethanol 2x 3 minutes followed by 3x 3-minute incubations in xylene. Slides were mounted in DPX (dibutylphthalate polystyrene xylene) and covered with glass coverslips. Slides were left to dry overnight in a fume hood before being imaged with a Zeiss slide scanner (Zeiss Axioscan Z.1).

Table 2.1 | List of antibodies used in immunohistochemistry and immunofluorescence staining

Target Antigen	Isotype	Clone	Conjugate	Sample Type	Supplier	Final Concentration (µg/ml)
Primary Antibodies						
CD3	Rabbit IgG	Polyclonal	Purified	FFPE	Dako	0.24
CD4	Rat IgG2a	RM4-5	Purified	OCT	eBioscience	1
CD8a	Rat IgG2a	4SM15	Purified	OCT	eBioscience	1
CD31	Rat IgG2a	SZ31	Purified	FFPE	Dianova	2
Lyve-1	Rat IgG1	ALY-7	Purified	FFPE	eBioscience	15
PNAd	Rat IgM	MECA-79	Alexa Fluor® 488 and 594 (ThermoFischer)	OCT	BD Pharmigen	2.5
PNAd	Rat IgM	MECA-79	Purified	FFPE	BD Pharmigen	0.25
Isotype Control Antibodies						
Rat IgM	-	eBRM	Purified	FFPE	Invitrogen	Matched to Primary
Rat IgM	-	eBRM	Alexa Fluor 488 and 594	OCT	Invitrogen	Matched to Primary
Rat IgG1	-	eBRG1	Purified	FFPE	Invitrogen	Matched to Primary
Rat IgG2a	-	eBR2a	Purified	FFPE	Invitrogen	Matched to Primary
Rabbit IgG	-	Polyclonal	Purified	FFPE	Abcam	Matched to Primary
Secondary Antibodies						
Anti-Rabbit IgG	Donkey IgG	Polyclonal	Alexa Fluor 488	OCT	Invitrogen	1
Anti-Rat IgG	Donkey IgG	Polyclonal	Alexa Fluor 594	OCT	Invitrogen	1

2.4 Quantification of T cell infiltration in Tumour Tissue

Frozen tumour sections were stained for either $CD3^+CD4^+$ or $CD3^+CD8^+$ T cells by immunofluorescence. Sections were then imaged using a Zeiss slide scanner. Enumeration of double positive cells per high power field of view (area covering 0.13 mm^2) was performed manually using Zen software. For each sample, 10 high power fields of view were enumerated and averaged.

2.5 Quantification of HEV formation

FFPE tumour sections were stained with the anti-mouse PNAd (clone MECA-79) Rat IgM antibody and imaged using a Zeiss slide scanner. Measurements tools found in Zen software were used to draw around individual $PNAd^+$ vessels across whole tumour sections in order to derive the area in square microns (μm^2). Similarly, the total tumour area (μm^2) was derived using the same approach. Subsequently several numerical parameters pertaining to HEV formation could be derived as previously described (Colbeck, 2015). This included the total HEV area (expressed as a percentage of the total tumour area), HEV density (number of HEV vessels per unit area (10^6 μm^2) of tumour) and average HEV area.

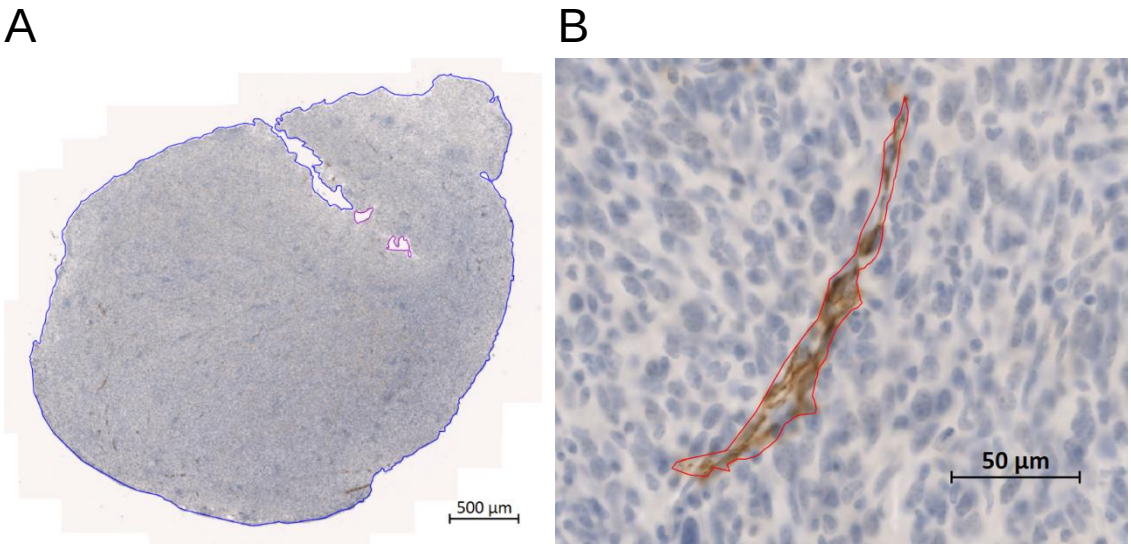

Figure 2.1 | HEV and tumour area quantification
High endothelial venules (HEVs) stained in paraffin embedded tumour sections were quantified using Zen software. (**A**) The total tumour area was quantified by drawing around the tumour region using the contour (polygon tool) which is depicted by the blue perimeter. Parts of the section that were not tumour tissue were excluded from the analysis (purple perimeter). (**B**) Similarly, the HEV area was derived for each vessel using the contour (polygon) tool as depicted by the red line drawn around the HEV vessel.

2.6 In-vivo Tumour and Lymph Node Blood Vessel Labelling

2.6.1 MECA-79 IgM Fluorescent Labelling

1 milligram (mg) of MECA-79 IgM (BD Pharmigen) was conjugated to Alexa Fluor (AF) dyes using the AF labelling kits 488 and 594 (ThermoFisher) as per manufacturer's instructions with slight modifications. Briefly 500 µl of a 2 mg/ml solution of MECA-79 IgM was incubated with either the AF 488 or 594 reactive dye for 1 hour at RT with gentle stirring. To ensure optimal labelling reactions, the antibody fluorophore mixture was incubated for an additional hour at 4^{o}C before being subjected to column elution. Protein concentration and absorbance was measured using the Nandorop 2000 (Thermofischer Scientific). Subsequently the degree of labelling (DOL) was calculated using the following equations:

$$1)\ Mole\ AF\ 488\ Dye\ per\ protein = \frac{Absorbance\ (494)}{71{,}000\ x\ Protein\ concentration\ (M)}$$

$$2)\ Mole\ AF\ 594\ Dye\ per\ protein = \frac{Absorbance\ (590)}{73{,}000\ x\ Protein\ concentration\ (M)}$$

where 71,000 $cm^{-1}M^{-1}$ is the approximate molar extinction co-efficient of the AF 488 dye at 494 nm and 73, 000 $cm^{-1}M^{-1}$ is the molar extinction coefficient of the AF 594 dye at 590 nm. Labelled MECA-79 IgM with a DOL between 4-9 (as deemed optimal by the manufacturer's instructions) was used for all subsequent *in-vivo* labelling experiments.

2.6.2 In-vivo HEV and Blood Vessel Labelling

To remove toxic sodium azide, solutions of Lycopersicon esculentum dylight 594 and 649 (Vectorlabs) and MECA-79 Alexa Fluor 488 and 594 were buffer exchanged with PBS twice by spinning at 12G for 10 minutes using Vivaspin 500 protein concentrators (GE healthcare). To label blood vessels and HEVs, tumour bearing mice were placed in an incubator set at 37^{o}C for 30 minutes to dilate blood vessels. Mice were then injected intravenously into the tail vein with 100-

150 µg of Lycopersicon esculentum to label blood vessels and 12-50 µg of MECA-79 to label HEVs. All tail vein injections were performed by Professor Awen Gallimore. 12-15 minutes post-injection mice were culled and the dLN, ndLN and tumour were excised and fixed in 4% PFA at 4^{o}C overnight. For confirmation of fluorescent labelling, lymph nodes and tumours were embedded in 4% UltraPure™ Low Melting Point Agarose/PBS (LMP, Invitrogen) after which 50 µM thick sections were cut using a vibratome (Leica VT1200 S). Sections were mounted in Vectashield, covered with a glass coverslip and sealed with nail varnish. Sections were then imaged with a Zeiss LSM 800 confocal microscope.

2.6.3 Bleaching

To reduce endogenous autofluorescence fixed labelled tissues were washed in PBS for 30 minutes before being stepwise dehydrated in increasing concentrations of methanol (33%, 66% and 100% methanol) for 15 minutes each as previously described (Alanentalo *et al.*, 2006). This was done to preserve the specimen for subsequent bleaching. Specimens were then incubated in modified Dent's bleach (2:1:3 ratio of methanol, dimethyl sulfoxide and 30% hydrogen peroxide) for 24 hours which lead to tissue decolourization, improved optical clearing and an enhanced signal to noise ratio.

2.7 Agarose Embedding and Organic Solvent Optical Clearing

For selective plane illumination microscopy (SPIM) imaging, fixed labelled and bleached lymph nodes were directly embedded in 1.5% LMP agarose whilst tumours were cut into 5 mm sized diameter pieces prior to embedding. Agarose blocks were cut into a cuboidal shape with the following dimensions: 8 mm x 8 mm x 25 mm. Such dimensions are imposed by the quartz cuvette into which the specimen is introduced to for SPIM imaging (Abe *et al.*, 2016). Agarose embedded specimens were dehydrated in 100% methanol for three days (methanol replenished every 24 hours) to ensure complete removal of extracellular water. Specimens were then transferred to 60 mls of the organic clearing solvent benzyl alcohol and benzyl benzoate (BABB, 1:2 ratio) until complete transparency was achieved. Tumour specimens that were imaged with the LaVision Ultramicroscope 2 were cut into 6 mm diameter sized pieces as this

is the maximum working distance of the detection objective (Ariel, 2018). Tumour pieces were then directly dehydrated in methanol and cleared in a 1:2 ratio of BABB as described above.

2.8 LSFM Imaging and Analysis

2.8.1 SPIM Imaging

A custom built SPIM set up described by Abe and colleagues was used to image cleared agarose embedded specimens (Abe *et al.*, 2016). SPIM imaging was kindly performed by Dr Jun Abe. All images were recorded using an N-PLAN EPI 5×/0.12 objective and a 12-bit digital CCD camera. Between 800-1000 images with a z-spacing of 5 µm were acquired for each tumour piece and LNs at each field of view (FOV). Multi-channel 3D stacks obtained at overlapping FOVs were exported in the tagged image file format (TIFF) format.

2.8.2 LaVision Ultramicroscope 2 Imaging

The LaVision Ultramicroscope 2 (Milteny) was used to image tumours with a maximum diameter of 6 mm. Cleared tumour samples were fixed in position using a screw mounting cap. The sample was lowered into the imaging chamber which was filled with 250 mls of a 1:2 ratio of BABB. In the absence of a fume extractor, ethyl cinnamate (ECi) was used instead of BABB as it is a non-toxic organic solvent that has a similar refractive index to BABB (Klingberg *et al.*, 2017). All images were recorded using a 2x detection objective with a working distance of 6 mm and a zoom ratio of 0.63x - 6.3x (1:10). A zoom factor of 1.25x was used for all tumour imaging as this was deemed sufficient for performing a qualitative overview of tumour blood vessels as discussed in Chapter 3. A left-handed only light sheet with a thickness of 25.27 µm was chosen as this was sufficient to illuminate the entire sample homogenously. Multi-colour image acquisition spanning 6-9 FOVs was performed and detected with a 16-bit scientific complementary metal–oxide–semiconductor (sCMOS) camera. The Z-step size was 10 µm and the resulting imaging times lasted between 2-5 hours depending on the total diameter of the specimen as well as the total number of

FOVs required. Multi-channel 3D stacks obtained at overlapping FOVs were exported in the TIFF format.

2.8.3 Post Imaging Processing and Analysis

Post image acquisition stitching, visualization and analysis required the use of specialised commercial software including additional open-source plugins which are all summarised in Table 2.2. All image data processing and analysis was performed on a dedicated image analysis personal computer workstation equipped with 128 GB of random-access memory (RAM) and an NVIDIA Quadro P4000 graphics card with 8 GB of GDDR5 memory.

All LSFM acquired data sets were exported as multi-channel images in the TIFF file format. Prior to stitching multi-channel images were first split into individual channels in FIJI. SPIM acquired images were subsequently stitched together using the pairwise stitching plugin. FOVs located in the same row were stitched together first before separate rows were stitched together. In some cases, individual TIFF files were converted to IMS files using Imaris file converter and subsequently stitched together simultaneously using IMARIS stitcher. Stitched image files were rendered and viewed as maximum intensity projections (MIPs) using IMARIS software following the input of set voxel properties: dX = 1.29 µm, dY= 1.29 µm and dZ = 5 µm. Image datasets acquired by the LaVision Ultramicroscope 2 were stitched together simultaneously using BigStitcher in FIJI. Stitched image files were rendered and viewed as MIPs using IMARIS software. Voxel properties were automatically set based on the information contained in the TIFF metadata.

Table 2.2 | List of software and plugins used to process and analyse LSFM data.

Name	Type	Description	Supplier/Developer	Use in this study	File formats
Amira 6.7.0	Commercial software	2D-5D visualisation and image analysis software	ThermoFischer	3D visualization of HEV network topology	TIFF AM (3D mesh file format) PNG
BigStitcher	Open-source FIJI plugin	Terabyte sized 3D multi-tile, multi-view dataset stitcher	Horl et al. (Horl *et al.*, 2019)	Stitching of LaVision Ultramicroscope 2 acquired 16-bit datasets	TIFF XML
FIJI is just ImageJ (FIJI)	Open-source software	Scientific image analysis software with preinstalled plugins	National Institutes of Health (NIH), USA	TIFF formatting, multi-channel separation and vessel hole filling	TIFF PNG
Imaris 9.5	Commercial software	3D-4D visualisation and image analysis software	BitPlane	Multi-channel maximum intensity projections of LSFM acquired datasets	TIFF IMS PNG
Imaris file converter 3.1	Commercial software	TIFF to IMS file converter	Bitplane	Conversion of TIFF files into IMS files	TIFF IMS
Imaris Stitcher 9.1.2	Commercial Software	2D-4D stitching software	Bitplane	Stitching of SPIM acquired datasets	IMS
Pairwise Stitching	Open-source FIJI plugin	2D-5D dataset stitcher	Preibisch et al. (Preibisch, Saalfeld and Tomancak, 2009)	Stitching of SPIM acquired 12-bit datasets	TIFF
Vessel Tools	Open-source command line tools	Vascular image data processing and analysis	Dr Gib Bogle (Kelch *et al.*, 2015)	Quantification of SPIM acquired LN HEV networks	TIFF AM

2.8.4 3D Quantification of SPIM acquired LN HEV Networks

In order to generate global 3D topological descriptors of LN HEV networks acquired by SPIM imaging, a set of command line computational tools developed by Dr Gib Bogle were implemented and further refined to process LSFM acquired datasets. These tools are freely accessible (https://github.com/gibbogle/vessel-tools) and have been previously described (Kelch *et al.*, 2015). A summary of the computational pipeline used in this work is outlined in Figure 2.1. Briefly, stitched LN HEV datasets were first converted into 8-bit files before being smoothed and segmented to a binary image using a local thresholding algorithm. By varying the threshold level according to the local average intensity, faintly stained vessel areas could be segmented. Due to inconsistent luminal HEV staining, segmented vessels often contained unlit voxels both within and along the HEV vessel wall. A vessel filling algorithm based on measuring the "insideness" of a voxel was used to fill unlit voxels found within vessels. Any remaining unlit voxels that could not be filled in this way were filled by synchronising the voxel position found in the 8-bit dataset to the segmented image and inserting voxels manually using the paint brush tool in FIJI. A pre-requisite to mapping the centre line points of any binary vessel image is that the vessel network is fully connected. Given that low order venules branch into higher order HEVs, the overall HEV network may consist of several disconnected HEV vessel networks. As a result, the largest connected objects (defined as any continuous vessel network) within the segmented image file were identified and further processed individually. The sum of all connected objects formed at least 99% of all lit voxels found in the segmented image. The centreline points of each individual vessel network were mapped (skeletonized) before being combined with the segmented image to generate a topological descriptor of the HEV vessel network. Key geometric features including the diameter and length of every individual vessel were also generated. The resulting network map could then be rendered in Amira using a colour spectrum to display the vessel diameter distribution. Statistics on individual vessel networks which make up the entire HEV network were collated in order to derive a numerical description of the overall HEV network. In order to estimate the volume of the LN, the hull tool was used to fill the HEV network in 3D with the outermost HEV vessels serving as the boundary. The total number of voxels that

made up this shape were enumerated and then multiplied by the voxel volume to derive an estimate of the LN volume.

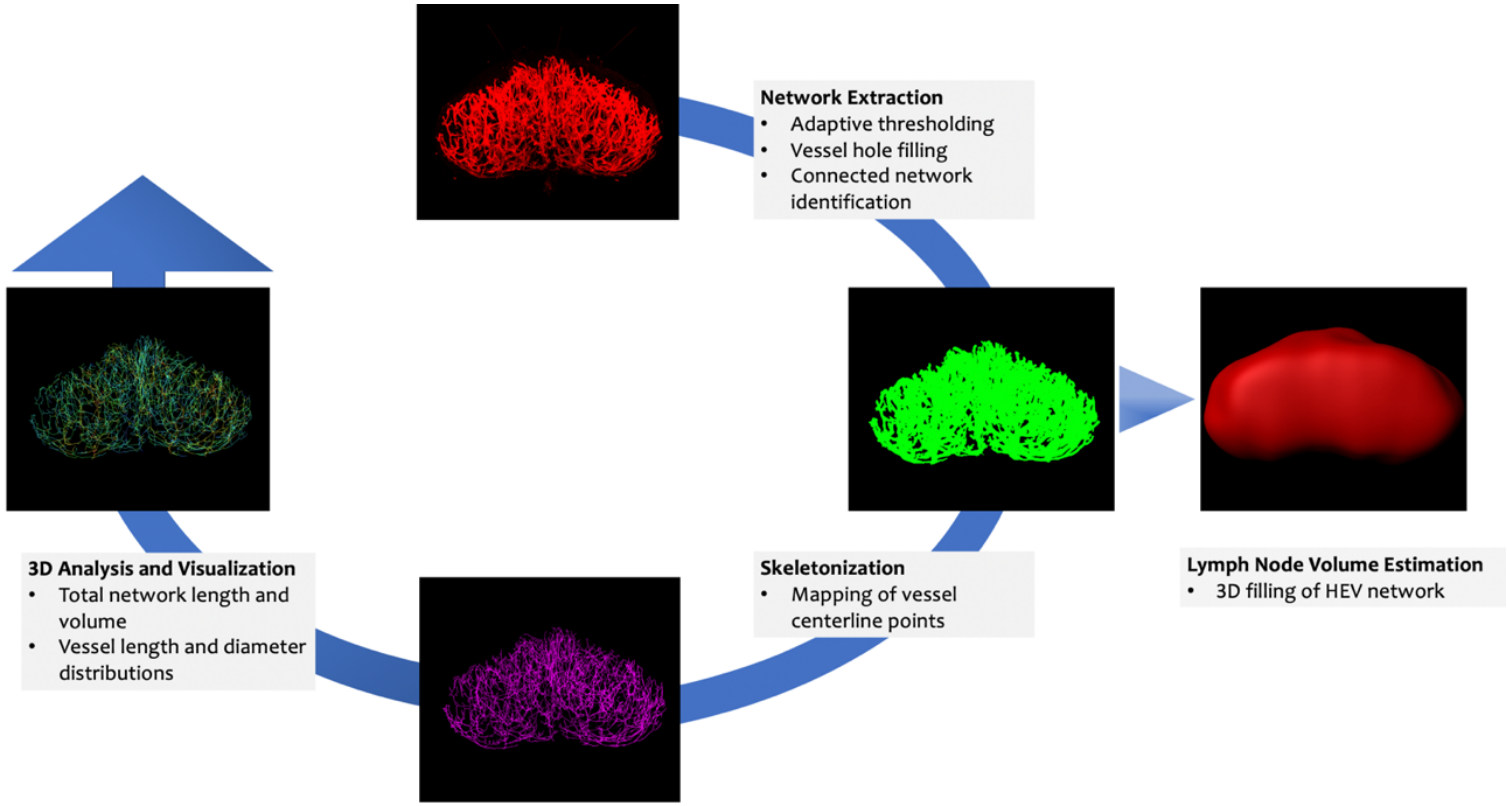

Figure 2.2 | Computational pipeline for HEV network quantification
Raw 12-bit greyscale images acquired by LSFM are converted to 8-bit images before the vessel network can be extracted. Due to staining intensity variations along the vessel endothelial wall an adaptive thresholding algorithm was employed to extract the vasculature. Any holes within vessels were filled using a 3D nearest neighbour filling algorithm which fills incompletely stained vessel walls. Remaining unlit voxels were filled manually using the paintbrush tool in FIJI. Every vessel network which is connected is identified and can subsequently be skeletonized to map the centreline points of every vessel. The volume of the tissue can be estimated by filling in 3D the entire network using the outermost vessels as a boundary. Lastly the segmented image and skeleton image are used to generate a topological descriptor which describes the entire network as a set of nodes and segments from which several numerical parameters can be extracted from including total length and volume. This network was visualized in Amira and colour coded to display the vessel diameter distribution.

2.9 Statistical Analysis

All statistical analyses were performed using Prism 7.0 (GraphPad). A P-value < 0.05 was considered significant. Details on the type of statistical tests used are shown in figure legends. The distribution of each dataset was determined using D'Agostino and Pearson, Shapiro-Wilk and Kolmogorov-Smirnov normality tests. In cases where the data was found to be normally distributed, parametric analyses using one-way ANOVA with Tukey's multiple comparison test were performed. In cases of non-normal distribution, non-parametric analyses using Kruskal-Wallis test with Dunn's multiple comparison test were performed.

3. Chapter 3

3 Results: Establishing methods for the 3D visualisation of fibrosarcoma and lymph node blood vessels using light sheet fluorescence microscopy

3.1 Introduction

Staining and imaging of thin tissue sections cannot offer a precise overview of the internal vessel structure of fibrosarcomas and LNs since the cutting plane that is used during sectioning can give rise to a high variability of observable structures particularly when such structures are asymmetrically distributed and only a limited number of sections are analysed (Kumar *et al.*, 2010). In order to comprehensively characterize the entire vasculature of fibrosarcomas and LNs a global 3D imaging approach is therefore required.

LSFM is a fluorescence-based imaging technique that utilizes a thin light sheet positioned perpendicular to the detection objective (Huisken *et al.*, 2004; Huisken and Stainier, 2009; Reynaud *et al.*, 2015). Such an orthogonal configuration of the detection and excitation axis allows for selective focal plane illumination and subsequent optical sectioning of biological specimens at high single cell resolution (Figure 3.1). 3D stacks (termed Z-stacks) can rapidly be generated by traversing the specimen across the light sheet. The first light sheet microscope ever developed with such an optical arrangement utilized sunlight to visualize gold nano-particles and was first described by Siedentopf and Zsigmondy in 1903 (Siedentopf and Zsigmondy, 1902). However, the current field of LSFM as applied to the imaging of biological specimens is largely attributed to Huskien *et al.* who in 2004 published a scientific report describing the development of a SPIM consisting of a single light sheet generating cylindrical lens coupled to a single detection objective (Huisken *et al.*, 2004). Here the potential capabilities of LSFM where showcased by performing both live-cell and fixed SPIM imaging of GFP labelled medaka embryos (Huisken *et al.*, 2004).

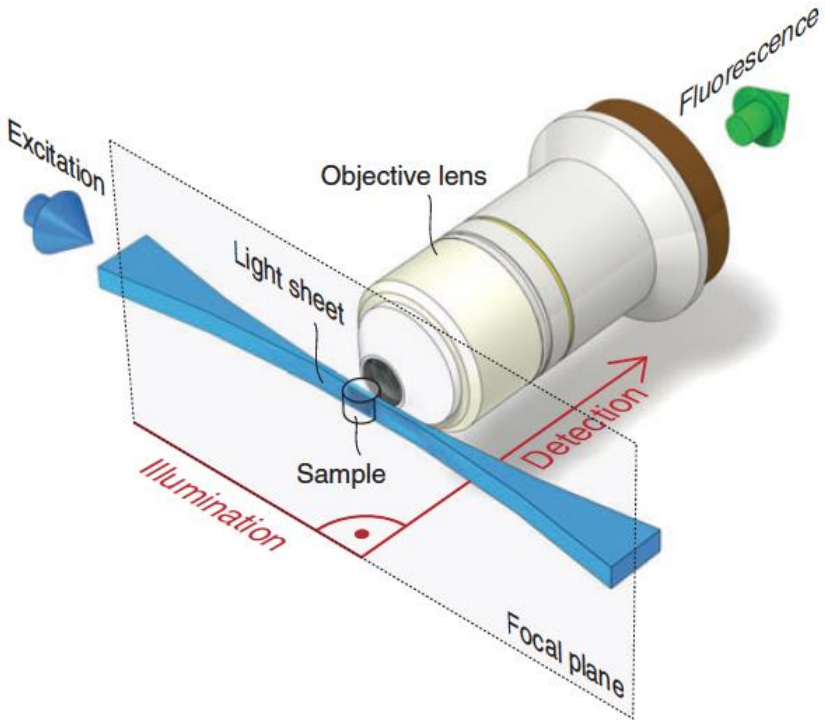

Figure 3.1 | LSFM optical arrangement.
All light sheet fluorescent microscopes selectively illuminate the volume of a sample that is found within the focal plane. This is achieved by positioning the illumination and detection axis in an orthogonal arrangement as depicted. Figure from (Huisken and Stainier, 2009).

There are several key advantages to using LSFM as opposed to other well-established fluorescent microscopy techniques such as laser scanning confocal microscopy (LSCM) in order to perform 3D imaging (Huisken and Stainier, 2009). The way in which specimens are optically sectioned in LSFM is different from that of LSCM which relies on the use of a pinhole to block out-of-focus light originating from outside the focal plane (Huisken and Stainier, 2009) (Figure 3.2). Given that there is no confinement of the detection plane in LSFM (no pinhole) a widefield detection strategy can be used to collect all light emanating from the sample at any given Z-position. This in turn results in significantly faster image acquisition. Furthermore, by selectively illuminating only the fluorophores found within the focal plane and not the entire specimen during image acquisition (which occurs in LSCM), there is also a significant reduction in photobleaching as well as phototoxicity if living samples are being imaged. It is for these reasons that LSFM was chosen over LSCM to be used in this work to image the 3D blood vessel network of fibrosarcomas and LNs. Two separate light sheet microscopes were used to achieve this. A custom built SPIM described by Abe and colleagues (Abe *et al.*, 2016) was used to image all agarose embedded specimens whilst larger fibrosarcoma specimens were imaged with the LaVision Ultramicroscope 2.

This chapter describes the optimization of *in-vivo* fluorescent labelling and optical clearing protocols that allow for a global 3D characterization of blood vessels and HEVs found in fibrosarcoma tumours and LNs.

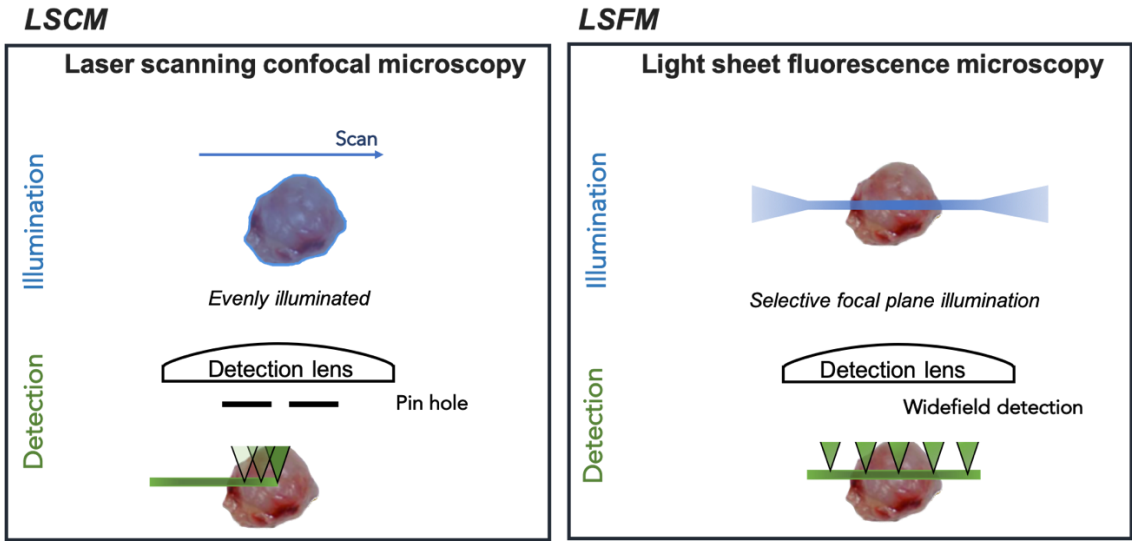

Figure 3.2 | Comparison of LSFM with LSCM.
Light sheet fluorescence microscopy (LSFM) achieves optical sectioning by selectively illuminating the focal plane. This approach allows for a widefield detection strategy and results in significantly faster imaging times. Fluorophores found outside the focal plane are not illuminated hence there is a reduction in photobleaching and phototoxicity. Laser scanning confocal microscopy (LSCM) relies on illuminating the whole specimen and blocking any out-of-focus light through the use of a pinhole. This approach leads to constant specimen excitation and as a result increased photobleaching and phototoxicity. The pinhole also restricts the detection plane leading to slower acquisition speeds. Figure adapted from (Huisken and Stainier, 2009).

3.2 Results: Blood vessel and HEV in-vivo fluorescent labelling of Fibrosarcomas and Lymph Nodes

The first experimental aim was to optimise methods for labelling the blood vasculature of fibrosarcomas and LNs. This was performed using an *in-vivo* fluorescent labelling approach. This method was chosen over whole-mount immunostaining of thick tissues given that it avoids the limitation associated with poor antibody penetration (Renier *et al.*, 2014). Indeed, using the iDISCO whole mount labelling method (Renier *et al.*, 2014), blood vessels found within deeper parts of naïve inguinal LNs could not be successfully labelled using this approach. Previous studies have shown that whole LN blood vessel and HEV networks can effectively be labelled *in-vivo* and subsequently imaged by OPT (Kumar *et al.*, 2010, 2012), SPIM (Abe *et al.*, 2016; Ozga *et al.*, 2016), extended volume confocal imaging (EVIS imaging) (Kelch *et al.*, 2015) and 2-photon microscopy (Park, Hwang and Kehrl, 2016). The intravenous injection or transcardial perfusion of fluorescently conjugated lectins as a means of labelling the blood vasculature is well described in the literature (Bies, Lehr and Woodley, 2004; Jährling, Becker and Dodt, 2009; Kelch *et al.*, 2015; Robertson *et al.*, 2015). Lectins are glycoproteins which bind with high specificity to carbohydrate components found on the endothelial plasma membrane (Bies, Lehr and Woodley, 2004). Tomato lectin derived from *Lycopersicon esculentum* specifically binds to the sugar moieties N-acetylglucosamine and N-acetyl-polyactosamine (Kawashima *et al.*, 1990; Porter, Palade and Milici, 1990) and was used in this work to label blood vessels. Whilst the IV injection of antibodies targeting the pan endothelial cell marker CD31 have been previously reported (Klingberg *et al.*, 2017) this approach only led to the faint staining of inguinal LN blood vessels and was hence not chosen to be used in this study. HEV endothelial cells express PNAd which binds to L-selectin expressed on lymphocytes (Girard, Moussion and Förster, 2012). This interaction mediates the tethering and rolling of lymphocytes across HEVs (Girard, Moussion and Förster, 2012). The anti-PNAd MECA-79 antibody binds to the 6-sulpho sialyl Lewis X epitope expressed on core 1 O-glycans which is unique to PNAds (Girard, Moussion and Förster, 2012) and was therefore used to label HEVs.

The dose of fluorescently labelled antibodies and lectins that was administered intravenously was chosen based on previous studies examining labelling of vasculature using tomato lectin (Jährling, Becker and Dodt, 2009; Robertson *et al.*, 2015) and labelling of HEVs for OPT (Kumar *et al.*, 2010, 2012), SPIM (Abe *et al.*, 2016; Ozga *et al.*, 2016) and 2-photon imaging (Park, Hwang and Kehrl, 2016). To account for any reagent loss that may occur during intravenous administration, the dose of fluorescently labelled lectin that was administered was increased from 100 µg to 150 µg. For HEV labelling, the dose of MECA-79 used was 12 µg. Tissues labelled in this way were excised and immediately fixed in 4% PFA after 12 minutes given that this is sufficient time for antibody labelling of LN HEVs to take place (Kumar *et al.*, 2010, 2012; Abe *et al.*, 2016; Ozga *et al.*, 2016). It has been empirically determined that the fluorescent signal following the intravenous injection of tomato lectin remains prominent up to 1-hour post injection in organs such as the liver and lung (Robertson *et al.*, 2015) which is well within the 12-minute time frame chosen in this study.

SLOs such as LNs are known to contain blood vessels and HEVs (Girard, Moussion and Förster, 2012) and were hence used to validate the *in-vivo* labelling procedure described above by LSCM. The blood vessel and HEV network of an inguinal LN were successfully labelled using this *in-vivo* labelling procedure (Figure 3.3 A). Subsequently the blood vessel network of a fibrosarcoma was also effectively labelled using this approach (Figure 3.3 B).

A

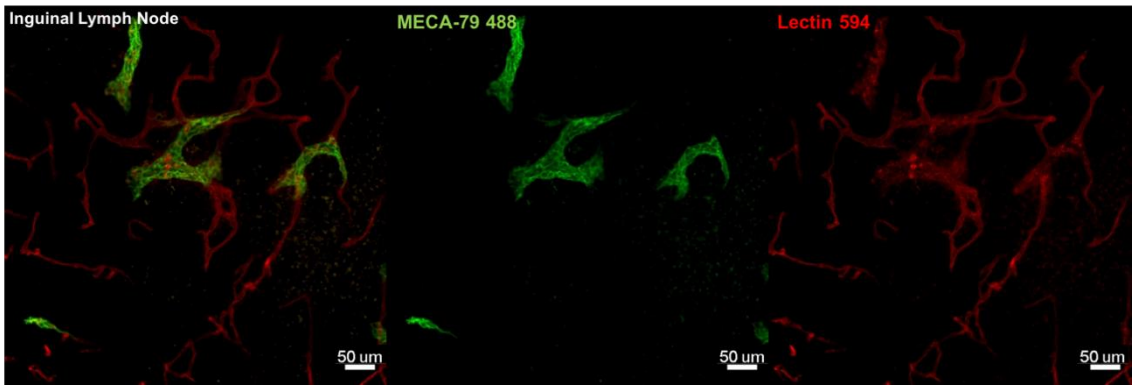

B

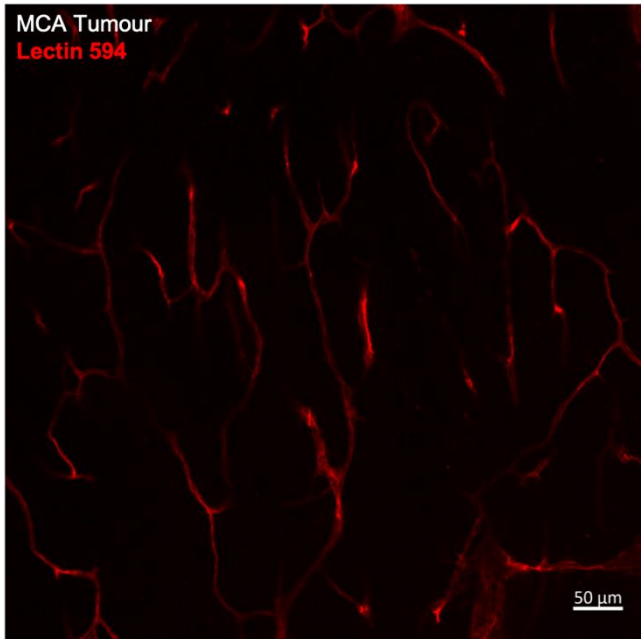

Figure 3.3 | *in-vivo* fluorescent labelling of blood vessels and HEVs.
An inguinal lymph node (**A**) was fluorescently labelled following an intravenous injection of 150 µg tomato lectin Dylight 594 to label blood vessels and 12 µg MECA-79 Alexa Fluor 488 to label HEVs. Fibrosarcoma blood vessels (**B**) were fluorescently labelled following an intravenous injection of 150 µg tomato lectin Dylight 594 and imaged using a Zeiss LSM 800 confocal microscope.

3.3 Results: Optical clearing of fibrosarcomas and lymph nodes

The second experimental aim was to optimise methods for optically clearing fibrosarcomas and LNs. Conventional fluorescence microscopy is largely restricted to the imaging of thin tissue sections which are in the order of between 10-20 microns in total thickness (Ntziachristos, 2010). This restriction in imaging depth is largely due to increasing scattering events encountered by photons as they propagate deeper through tissue (Genina, Bashkatov and Tuchin, 2010; Ntziachristos, 2010; Richardson and Lichtman, 2015). In order to resolve fluorescently labelled structures found in thicker pieces of tissue it is required that such light scattering events be reduced (Richardson and Lichtman, 2015). This can be achieved through optical clearing which can render specimens completely transparent (Erturk *et al.*, 2012; Richardson and Lichtman, 2015; Seo, Choe and Kim, 2016). Tissues are typically opaque due to the heterogeneity of light scatters present within those tissues (Richardson and Lichtman, 2015). Lipids for example have a higher refractive index than extracellular water which causes light scattering to occur (Richardson and Lichtman, 2015). By homogenising the refractive index of a specimen, light scattering is reduced and as a result tissue transparency is increased (Richardson and Lichtman, 2015). An organic solvent clearing method using methanol and BABB (1:2 ratio) was chosen for use in this work given that such solvents are considered to have strong clearing properties and are also compatible with small molecule fluorescent dyes (Seo, Choe and Kim, 2016). Furthermore, it has been reported that immunolabelled specimens stored in organic clearing solvents can retain their fluorescence over several years (Zukor, Kent and Odelberg, 2010). Lastly organic solvent clearing is very rapid and straightforward to carry out, requiring simple incubation of the specimen in a dehydrating solvent followed by incubation in a clearing solvent until full tissue transparency is achieved (Erturk *et al.*, 2012; Richardson and Lichtman, 2015; Seo, Choe and Kim, 2016). Methanol serves to remove any extracellular water and lipids whilst BABB (which has a refractive index value of 1.55) replaces water and refractive index matches any remaining dehydrated proteins (Seo, Choe and Kim, 2016). BABB clearing has effectively been applied to fluorescently labelled LNs (Kumar *et al.*, 2010, 2012; Abe *et al.*, 2016; Ozga *et al.*, 2016) as well as organs that are much larger in size such as whole brain (Dodt *et al.*, 2007; Jährling, Becker and Dodt, 2009).

For SPIM imaging it is common to embed the specimens in LMP agarose prior to tissue clearing (Huisken *et al.*, 2004; Abe *et al.*, 2016; Ozga *et al.*, 2016). Agarose embedding serves to both stabilize the specimen during image acquisition as well as to provide unobstructed light sheet access to the entire specimen. Given that LNs can effectively be imaged using the custom built SPIM described by Abe *et al.* when mounted in a cuboidal shape (Abe *et al.*, 2016), this method was also adopted for fibrosarcoma mounting. All agarose blocks were therefore cut into a cuboidal shape with the following dimensions; 8 mm x 8 mm x 25 mm. Such dimensions are imposed by the quartz cuvette into which the specimen is introduced for SPIM imaging. LNs can readily be mounted in this way whilst fibrosarcomas which have a diameter ranging from 0.8 to 1.5 cm (Hindley *et al.*, 2012) can often exceed this agarose block dimension limit. This meant that tumours had to be cut into 5 mm sized diameter pieces before being embedded and cleared in preparation for SPIM imaging.

Following agarose embedding the specimen is first dehydrated in 100% methanol. Effective dehydration is only evident once the specimen is transferred to the clearing solvent since any residual water that has not been removed can react with BABB leading to the formation of agarose block distortions (Quintana and Sharpe, 2011). Whilst LNs could effectively be dehydrated following a 24-hour incubation period in methanol as previously reported (Kumar *et al.*, 2012) (Figure 3.4 A), agarose embedded tumour blocks which are significantly larger had clear signs of agarose block distortions which would likely interfere with imaging (Figure 3.4 B). Therefore, to ensure complete dehydration, specimens were incubated for at least 3 days in methanol which was replenished after every 24 hours. Prolonged methanol dehydration prevented the formation of any agarose block distortions and complete tumour transparency was thereafter achieved following an overnight incubation in BABB (Figure 3.4 C). In some cases, fibrosarcomas were found to be filled with blood prior to being excised. Such blood-filled areas could not be made completely transparent with BABB clearing (Figure 3.4 E).

Specimens do not require prior agarose embedding in order to be imaged with the LaVision Ultramicroscope 2 (Dodt *et al.*, 2007; Jährling, Becker and Dodt,

2009; Ariel, 2018). Instead they can be introduced into the imaging chamber through the use of a sample holder. As with agarose embedded specimens, whole fibrosarcomas were effectively cleared in BABB after an overnight incubation following the previously described dehydration protocol (Figure 3.4 D).

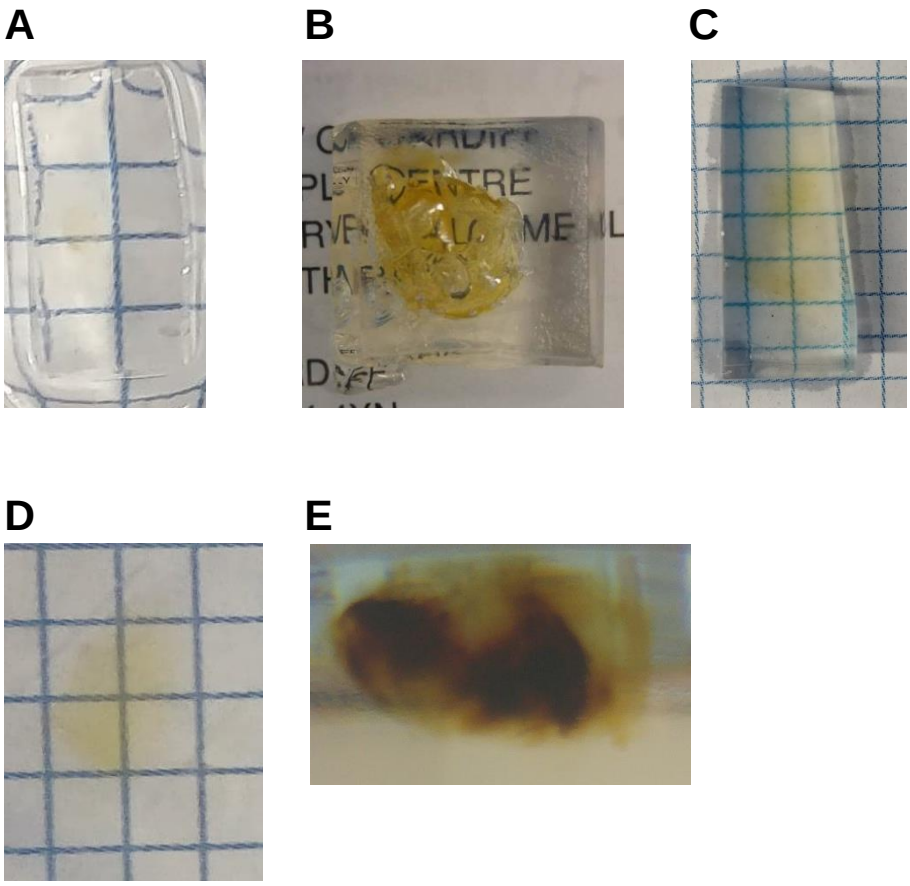

Figure 3.4 | Organic solvent-based clearing of fibrosarcomas and lymph nodes.
A tumour draining lymph node (**A**) embedded in 1.5% LMP agarose and trimmed to a cuboidal shape was dehydrated overnight in 100% methanol and effectively cleared after an overnight incubation in BABB (1:2 ratio). A 5 mm sized agarose embedded fibrosarcoma piece developed agarose block distortions after being dehydrated overnight in methanol and cleared overnight in BABB (1:2 ratio) (**B**). Dehydration in methanol for 3 days prior to BABB clearing prevented formation of agarose block distortions and enabled effective clearing (**C**). Whole fibrosarcoma effectively cleared after 3-day methanol dehydration and overnight incubation in BABB (1:2 ratio) (**D**). Blood-filled fibrosarcoma could not effectively be cleared (**E**).

3.4 Results: LSFM imaging optimization

3.4.1 Fibrosarcoma and lymph node SPIM Imaging

A custom built SPIM setup described by Abe *at al.* (Abe *et al.*, 2016) was used in this study to image agarose embedded fibrosarcomas and LNs. SPIM imaging of a dLN revealed a well-connected HEV network which formed part of a larger blood vessel network (Figures 3.5 C and D). In contrast to the high signal to noise (S/N) ratio achieved in LNs, tumours imaged by SPIM had high areas of non-specific signal on both channels (Figure 3.5 A). Furthermore, Treg replete tumours also had vessels present in the green channel detecting HEV staining. Since HEVs were not previously detected in Treg replete tumours stained and imaged by conventional 2D histology (Hindley *et al.*, 2012), it is likely that this is a result of RBC autofluorescence. Indeed, whole brain vascular networks have previously been imaged with LSFM by capturing such RBC autofluorescence on the green channel without any prior fluorescent labelling (Dodt *et al.*, 2007).

Haem is a component of RBCs that not only absorbs light but also emits fluorescence within the 488 nm and 594 nm wavelengths (Renier *et al.*, 2014). The use of fluorescent labels that emit in the far-red or near-infrared range are often used in 3D imaging to avoid such autofluorescent artefacts (Renier *et al.*, 2014). An alternative approach is to remove haem by either physical or chemical means (Susaki and Ueda, 2016). Haem can be physically removed via the transcardial perfusion of a buffer such as PBS or it can be chemically destroyed by bleaching with hydrogen peroxide (Susaki and Ueda, 2016). Given that bleaching requires simple tissue immersion and is compatible with small molecule fluorescent dyes, a bleaching protocol first described by Alanentalo *et al.* (Alanentalo *et al.*, 2006) was incorporated immediately after *in-vivo* fluorescent labelling. Additionally, the MECA-79 dose was increased from 12 µg to 50 µg to ensure complete intratumoral HEV labelling. Incubation of a blood-filled fibrosarcoma in modified Dent's bleach (composed of a 2:1:3 ratio of methanol, dimethylsulfoxide and 30% hydrogen peroxide) overnight resulted in tissue de-colourization, which is indicative of effective haem removal (Figure 3.6 A&B). Furthermore, tumours that were filled with blood prior to being excised could now be made completely transparent with BABB clearing (Figure 3.6 C). Importantly,

bleaching resulted in a significant reduction in non-specific signal across both the green and red channels and a significant improvement in the S/N ratio of the lectin signal was observed which now allowed for the visualization of the entire tumour blood vessel network (Figure 3.5 B). Similar improvements to the S/N ratio were also seen when a dLN was bleached and imaged with SPIM (Figure 3.5 D). This in accordance with the marked improvements in the S/N ratio described by Alanentalo *et al.* which allowed for the islet beta cell distribution in adult murine pancreata to be imaged by OPT (Alanentalo *et al.*, 2006).

A

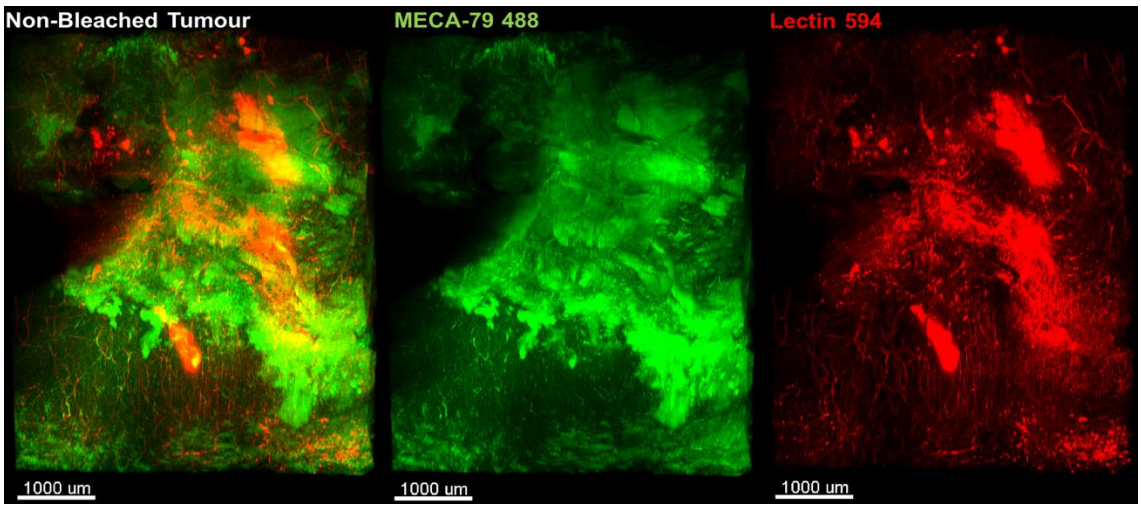
Non-Bleached Tumour
MECA-79 488
Lectin 594
1000 um
1000 um
1000 um

B

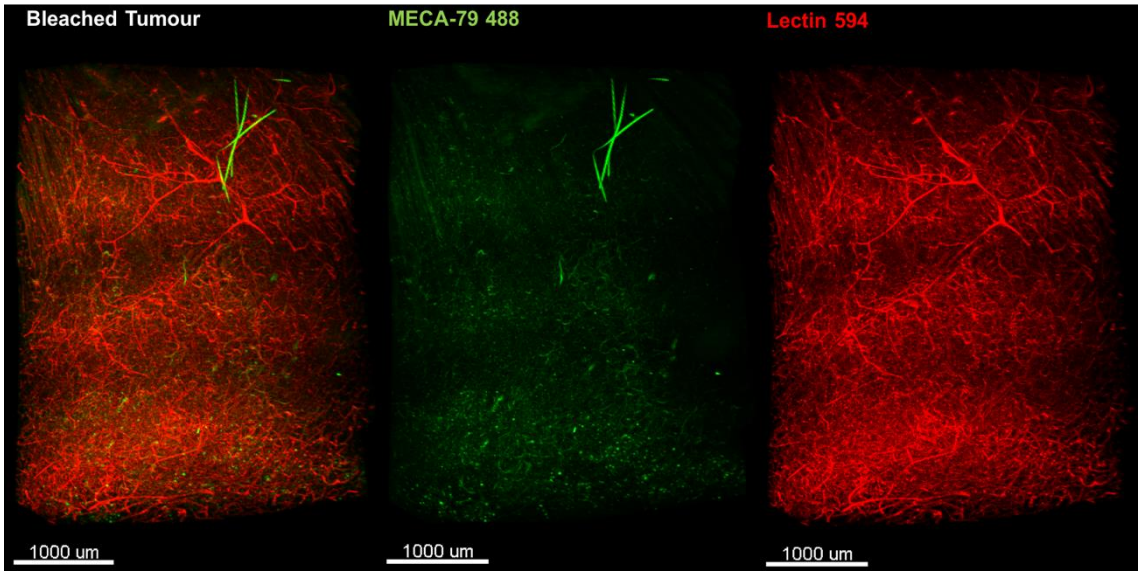
Bleached Tumour
MECA-79 488
Lectin 594
1000 um
1000 um
1000 um

C

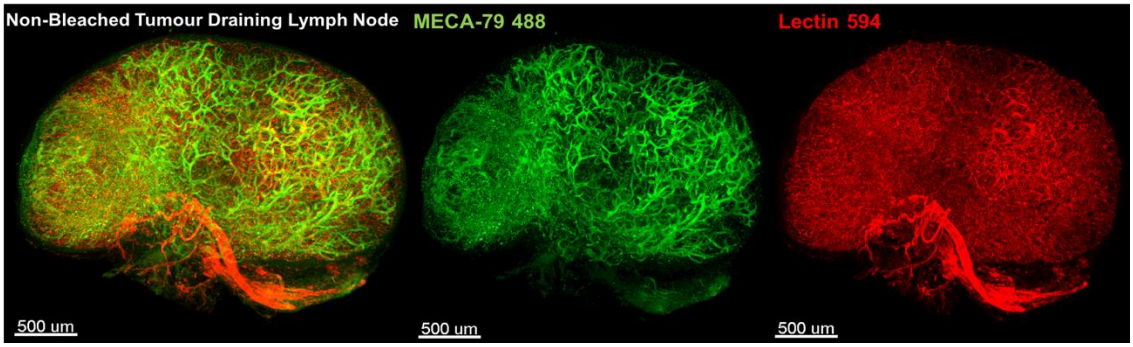

D

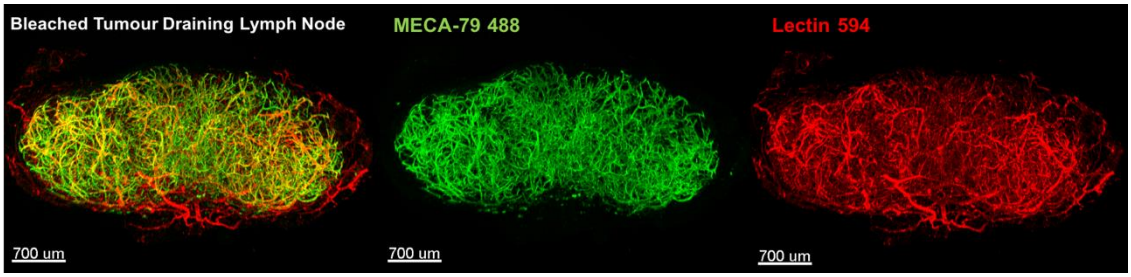

Figure 3.5 | SPIM imaging of fibrosarcomas and lymph nodes.
Volume rendering of acquired SPIM data of a Treg replete fibrosarcoma piece (**A**) and a bleached fibrosarcoma piece (**B**) is shown by displaying maximum intensity projections (MIPs) which project the highest intensity voxels along the XY viewing plane of the entire Z-stack acquired. MIPs of a tumour draining lymph node (**C**) and a bleached tumour draining lymph node (**D**) are also shown. Tumour pieces were 5 mm in diameter. Specimens were labelled *in-vivo* with an intravenous injection of 150 µg tomato lectin Dylight 594 and either 12 µg (**A** and **C**) or 50 µg (**B** and **D**) of MECA-79 AF 488.

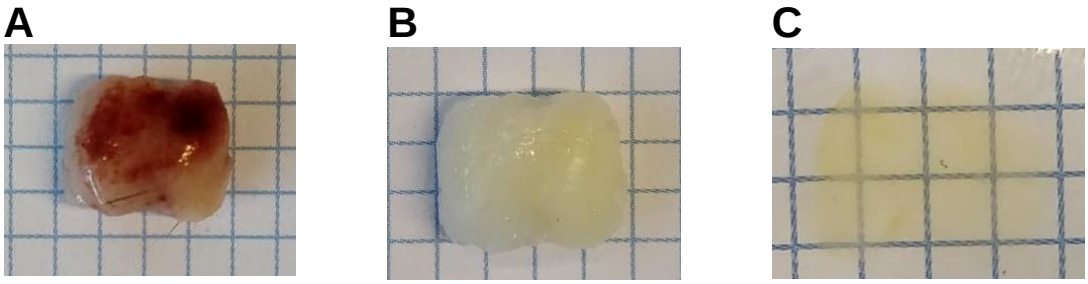

Figure 3.6 | Impact of bleaching on organic solvent-based clearing.
A blood-filled whole fibrosarcoma (**A**) was dehydrated in 100% methanol for 3 days and bleached overnight with modified Dent's bleach (**B**) and effectively optically cleared overnight in BABB (1:2 ratio) (**C**).

By limiting the thickness of the MIPs to several hundred microns, it was now possible to examine much more closely the intricate details of the inner blood vessel architecture of fibrosarcomas (Figure 3.7). Whilst the staining intensity of the MECA-79 AF 488 antibody is largely consistent across the whole HEV network (Figure 3.5 D), the tomato lectin signal shows great variability in staining intensity across the entire blood vessel network of both LNs and tumours (Figure 3.5 B&D and 3.7 A&B). Such differences in the staining patterns of tomato lectin across the vessel endothelium have previously been reported (Porter, Palade and Milici, 1990; Jährling, Becker and Dodt, 2009). These have been attributed to possible differential expression of tomato lectin binding sites across the vessel endothelium or to the method of lectin administration used (Jährling, Becker and Dodt, 2009). Whilst it has been suggested that the IV injection of tomato lectin could allow for prolonged contact of tomato lectin with its binding sites (Jährling, Becker and Dodt, 2009), in this work the IV injection of tomato lectin still led to a variable staining intensity pattern.

A

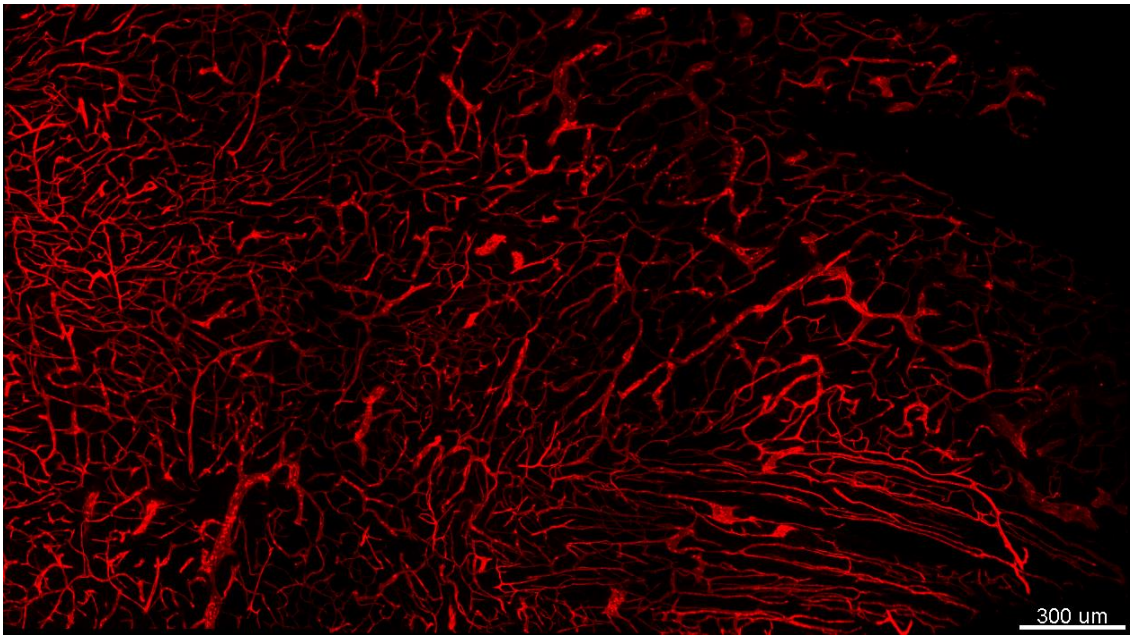

B

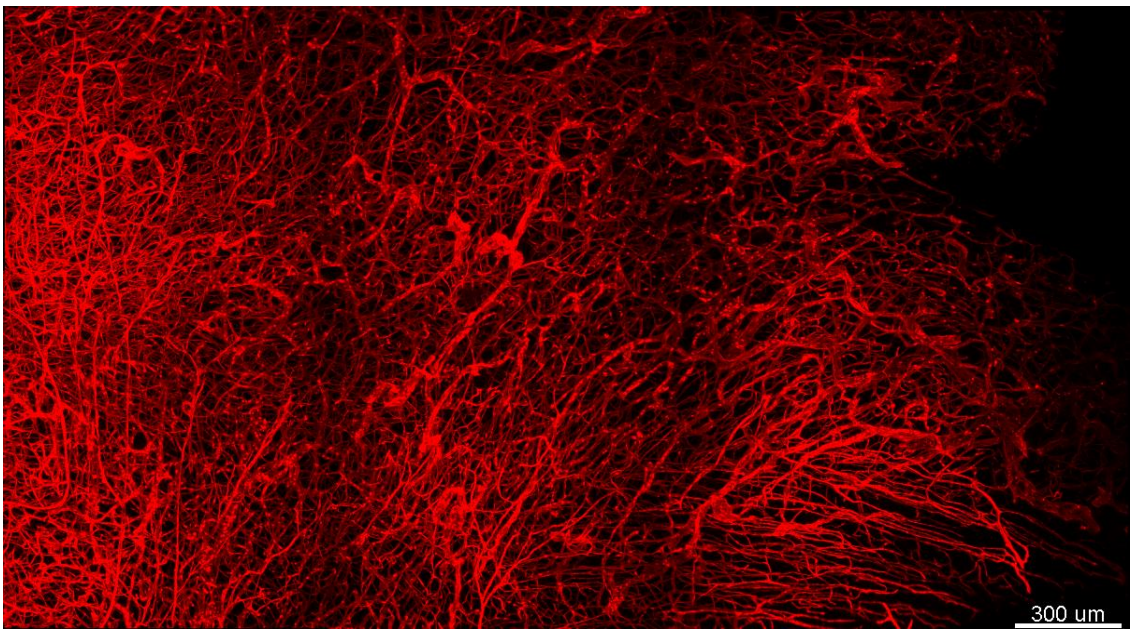

Figure 3.7 | Volume rendering of the inner blood vessel network of a Treg depleted fibrosarcoma.
Reducing the thickness of the maximum intensity projections of a 5 mm sized Treg depleted fibrosarcoma piece imaged with SPIM allows for the closer inspection of the inner blood vessel architecture. Total thickness of volume rendered is 250 µm (**A**) and 500 µm (**B**).

3.4.2 Multi-spectral Fibrosarcoma imaging

Whilst the blood vessel network could now be visualised with SPIM imaging, it was still not possible to discern RBC autofluorescence from $PNAd^+$ vessels. To overcome this, it was decided that an additional channel would be acquired. Autofluorescence was captured on the green channel given that it is known to be most prominent in the blue-green spectrum (Renier *et al.*, 2014). A further advantage of incorporating an additional channel is that the border of the specimen is delineated allowing for the overall morphology of the specimen to be examined (Dobosz *et al.*, 2014) as well as the volume to be derived by summating the total number of lit voxels that lie within that border. HEVs and blood vessels were subsequently detected on the red and far-red channels. Such multi-spectral imaging was performed on the LaVision Ultramicroscope 2 given that the custom built SPIM was not equipped with a stable far-red laser line. This allowed for the origin of the fluorescent signal to be identified since a signal found to overlap with the autofluorescence channel was deemed not to be specific. A Treg depleted tumour was treated with anti-IL-27 antibodies to promote HEV formation and imaged using this multi-spectral imaging approach (Figure 3.8). The use of anti-IL-27 antibodies as a means of promoting HEV formation is discussed in detail in Chapter 5. $PNAd^+$ vessels were now clearly distinguishable from background autofluorescence (Figure 3.8 A&B). This approach now allows for the 3D characterization of HEV networks forming in Treg depleted tumours.

A

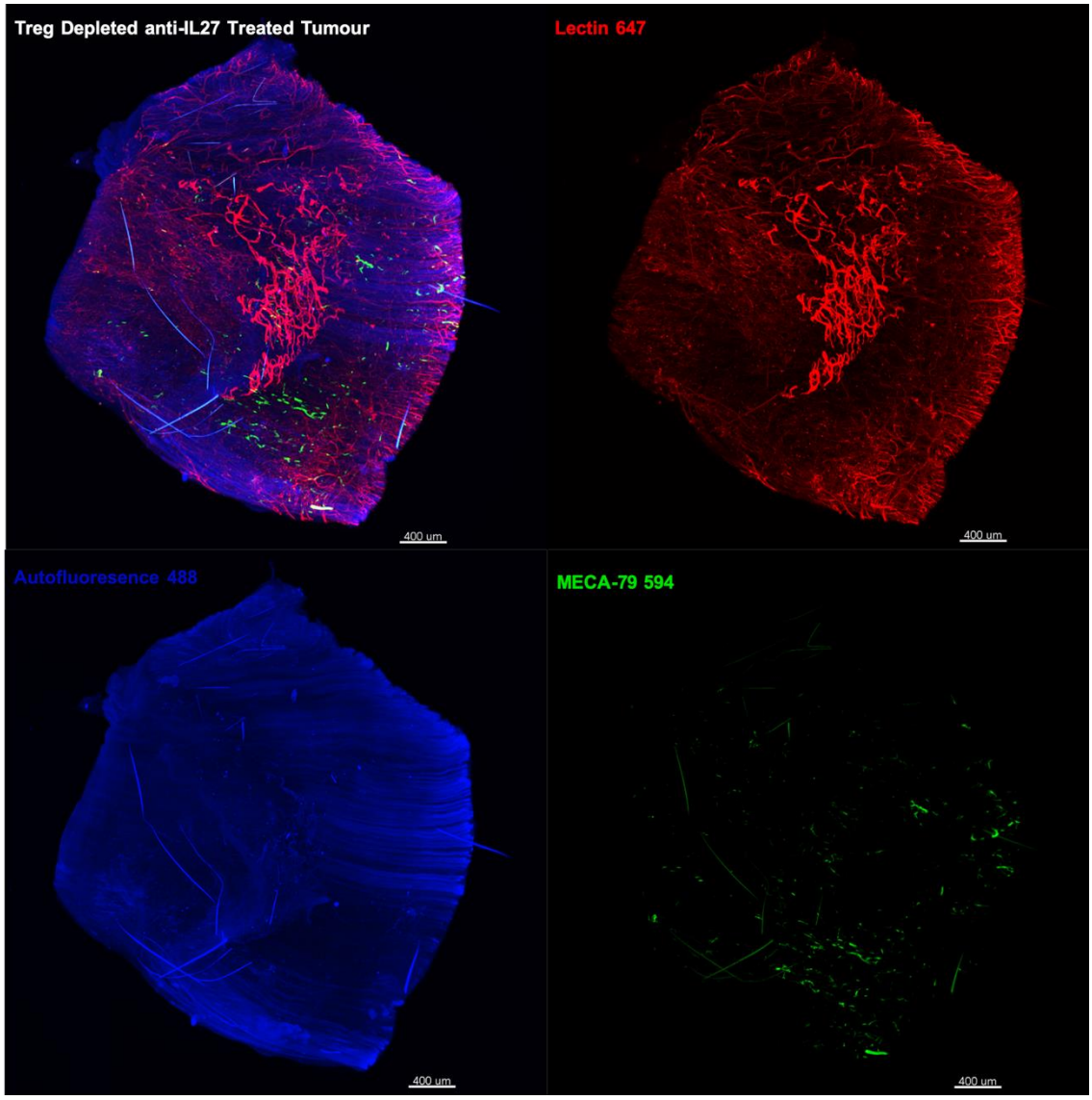
Treg Depleted anti-IL27 Treated Tumour
Lectin 647
Autofluoresence 488
MECA-79 594
400 um
400 um
400 um
400 um

B

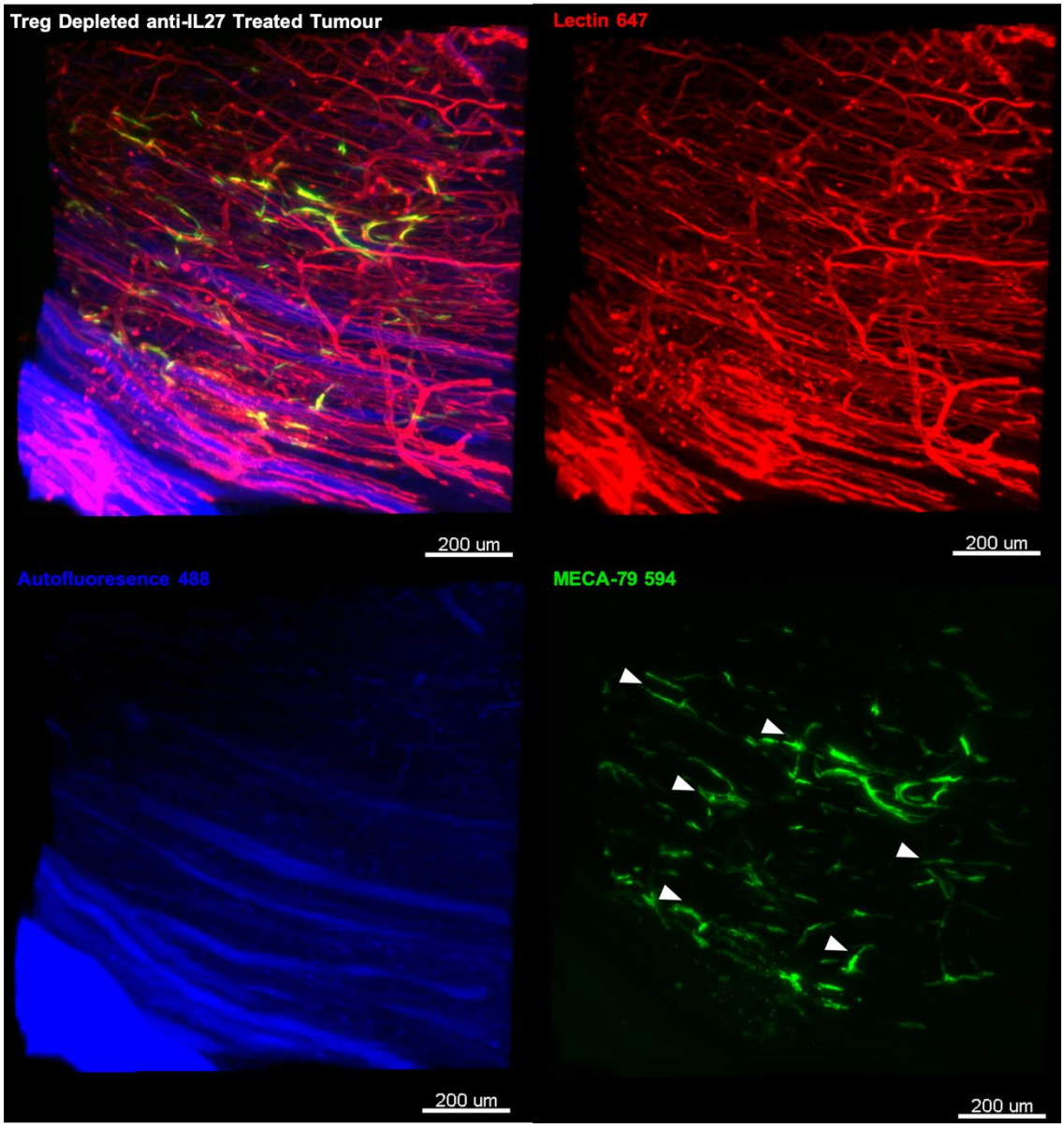

Figure 3.8 | LSFM multi-spectral imaging of a whole fibrosarcoma.
A Treg depleted and anti-IL27 treated fibrosarcoma was *in-vivo* labelled with an IV injection of 150 µg tomato lectin Dylight 647 and 50 µg MECA-79 AF 594. The whole tumour was imaged with the LaVision Ultramicroscope 2 using a 1.25x zoom factor (**A**) and 6.3x zoom factor over a region of interest with high $PNAd^+$ staining (**B**). Autofluorescence was captured on the green channel (pseudo coloured in blue). White arrowheads denote HEV specific staining which does not appear on the autofluorescence channel.

3.4.3 Optimization of LSFM imaging parameters

In comparison to the custom built SPIM which consists of a single light sheet coupled to a 5x detection objective (Abe *et al.*, 2016), the LaVision Ultramicroscope 2 is equipped with a 10x zoom optic detection objective capable of imaging specimens at different optical resolutions (Ariel, 2018). This LSFM can also utilize dual-light sheet excitation (3 light sheets from opposing sides) to provide even illumination across larger specimens (Ariel, 2018). In order to maximize the imaging time efficiency, it was decided that a zoom factor with a sufficiently large FOV encompassing as much of the specimen as possible would be used. A larger FOV would also reduce the number of overlapping XY translations required to image the whole specimen thereby allowing for faster imaging times and subsequent post image acquisition stitching (Chapter 2, Methods). To determine which optical resolution provides sufficient detail for characterizing the blood vessel network of fibrosarcomas, two different zoom factors of 0.63x and 1.25x were tested. As expected, the higher zoom factor of 1.25x was superior at providing a more detailed overview of the blood vessel network of a fibrosarcoma (Figure 3.9 A&B). This zoom factor was therefore chosen to be used in all further imaging acquisitions in order to capture the 3D vessel architecture of fibrosarcomas.

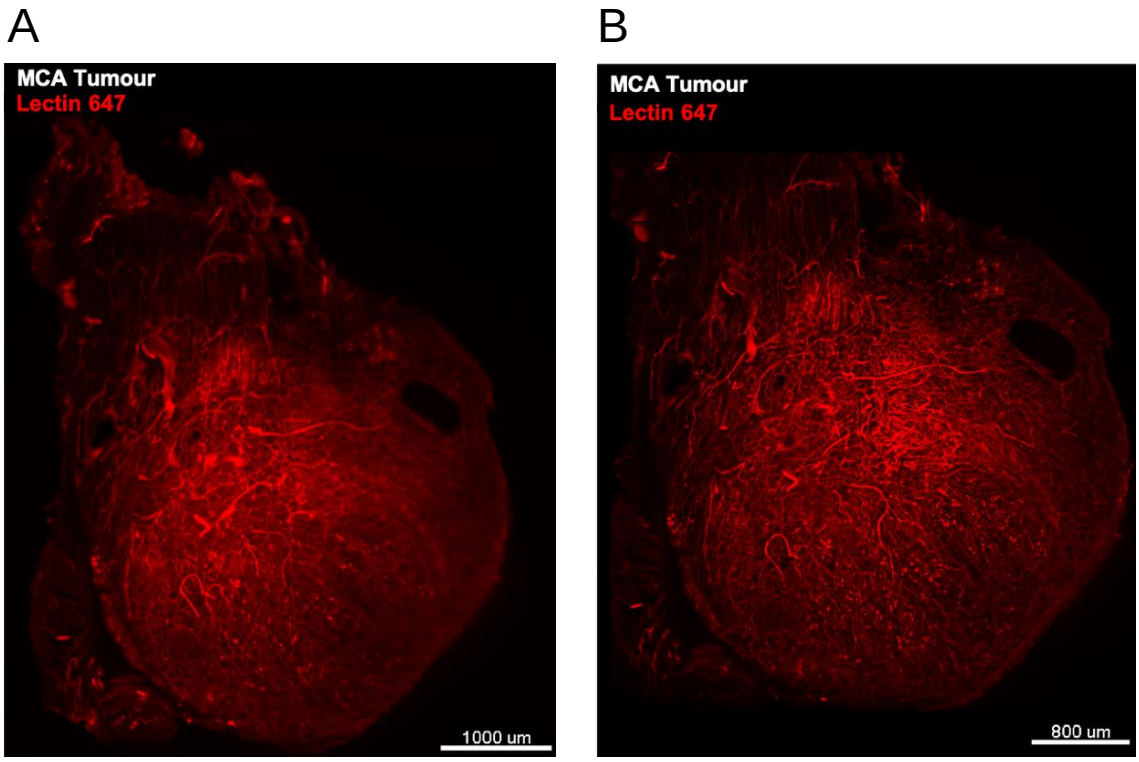

Figure 3.9 | LSFM imaging using different zoom factors.
A fibrosarcoma was intravenously labelled with 150 µg tomato lectin Dylight 647 and imaged with the LaVision Ultramicroscope 2 using either a 0.63x zoom factor (**A**) or 1.25x zoom factor (**B**). Total thickness of optical slices acquired and rendered is 100 µm.

In addition to using different zoom factors it is also possible to utilize either single or dual light sheet illumination as well as to employ dynamic focusing (Ariel, 2018). Dynamic focusing involves shifting the light sheet across the specimen in order to achieve a more even resolution across the entire FOV (Ariel, 2018). The light sheet has a Gaussian profile where the thickness of the beam is narrowest at the centre whilst becoming thicker from either side (Ariel, 2018). It is at the centre therefore that the Z-resolution is at its highest. The use of dual illumination excitation led to the acquisition of a slightly blurry image (Figure 3.10 A) whilst the use of left-handed only illumination gave a sharper image (Figure 3.10 C). Dynamic focusing did not result in a significant improvement in image quality (Figure 3.10 B). Therefore, left-handed light sheet illumination without the use of dynamic focusing was chosen for use in all further image acquisitions.

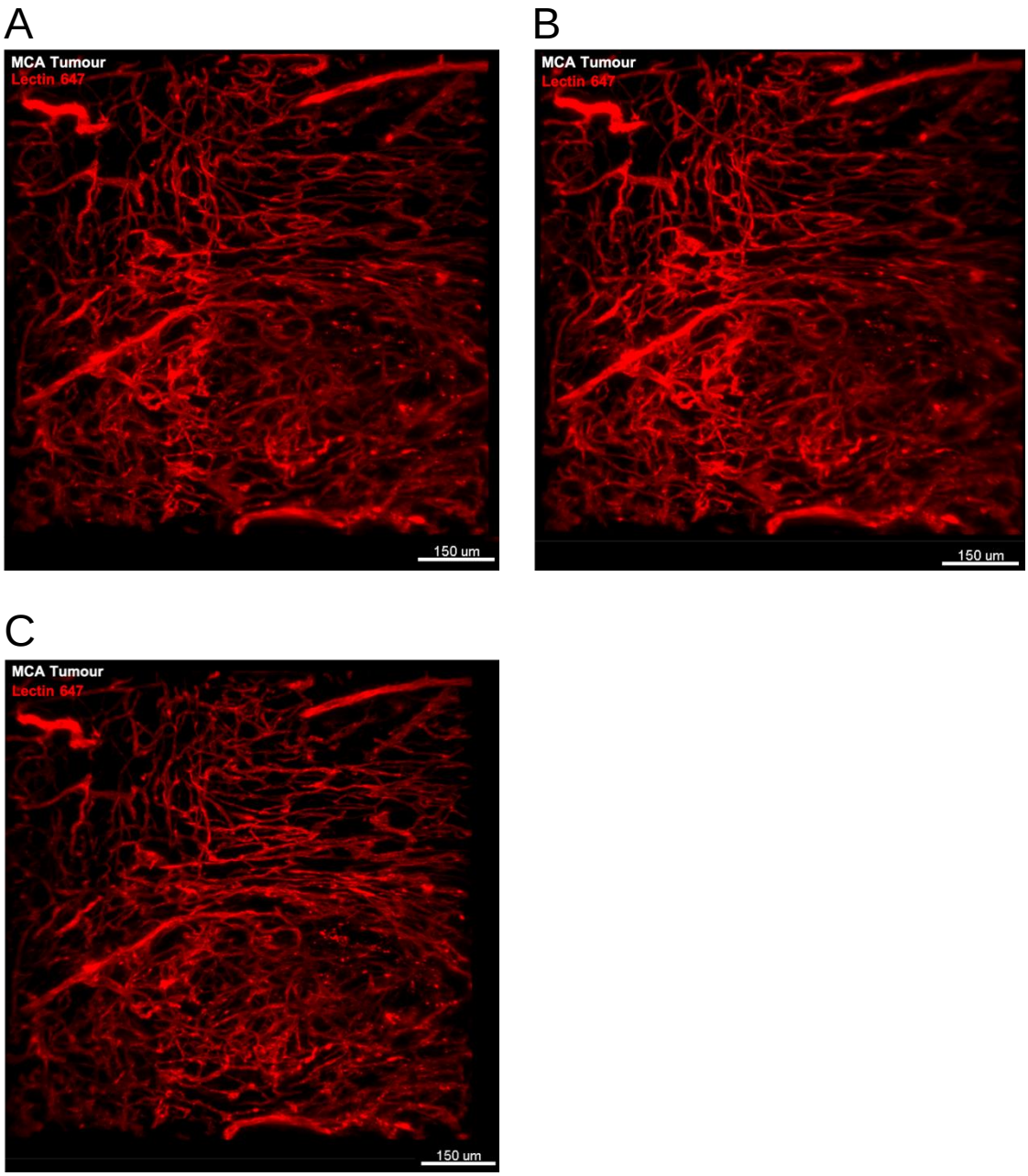

Figure 3.10 | LSFM illumination optimization.
A fibrosarcoma was intravenously labelled with 150 µg tomato lectin Dylight 647 and imaged using the LaVision Ultramicroscope 2 with a 6.3x zoom factor. The specimen was illuminated by (**A**) dual-sided light sheet excitation (**B**) with dynamic focusing or (**C**) by left hand sided light sheet excitation only (**C**). Total thickness of optical slices acquired and rendered is 100 µm.

3.5. Discussion

The ability to resolve fine blood vessel structures in thick pieces of tissue have resulted in the application of LSFM in tumour xenograft imaging (Dobosz *et al.*, 2014), small organ imaging such as LNs (Abe *et al.*, 2016; Ozga *et al.*, 2016) and even in whole organ imaging of the mouse brain (Dodt *et al.*, 2007; Jährling, Becker and Dodt, 2009; Lugo-Hernandez *et al.*, 2017). LSFM is therefore a well-suited technique for characterizing the 3D blood vessel structure of fibrosarcomas and LNs.

The incorporation of bleaching as a means of reducing autofluorescence and improving the S/N ratio was shown to be a critical step that allowed for the blood vessel and HEV network of fibrosarcomas and LNs to be visualised. Bleaching often precedes several whole mount immunostaining protocols (Alanentalo *et al.*, 2006; Renier *et al.*, 2014; Chi *et al.*, 2018) and is even an essential component of the aqueous optical clearing protocol known as Clear, Unobstructed Brain/Body Imaging Cocktails and Computational Analysis (CUBIC) (Susaki *et al.*, 2015). Indeed, haem rich tissues including blood-filled fibrosarcomas are difficult to clear without prior removal of haem (Erturk *et al.*, 2012; Renier *et al.*, 2014; Susaki and Ueda, 2016). The use of fluorescent labels that emit in the red and far-red spectrum was shown to be important, particularly in fibrosarcomas, to allow for $PNAd^{+}$ vessels to be identified.

Whilst the use of tomato lectin as a blood vessel marker gave a variable pattern of staining intensity as previously reported (Porter, Palade and Milici, 1990; Jährling, Becker and Dodt, 2009), it still permitted the examination of the 3D blood vessel network of fibrosarcomas and LNs. Such variations in staining intensity can pose problems for vessel segmentation; an image-processing step that is required prior to vessel network quantification. As described in the next chapter, a set of computational vessel tools developed by Dr Gib Bogle (Kelch *et al.*, 2015) which allow for the analysis of 8-bit greyscale 3D vessel images were purposefully designed to address such issues. More specifically the use of a local thresholding algorithm and vessel filling algorithm can be used to properly segment areas that have faint vessel labelling (Kelch *et al.*, 2015).

In conclusion using an *in-vivo* fluorescent labelling approach together with a bleaching protocol and organic solvent-based clearing method it is possible to image the 3D blood vessel and HEV network of fibrosarcomas and LNs using LSFM. It takes one week to label and clear specimens before LSFM imaging can be performed as summarised in Figure 3.11. Whilst the custom built SPIM is restricted to imaging 5 mm diameter sized fibrosarcoma pieces, the LaVision Ultramicroscope 2 can be used to image slightly larger tumour pieces (6mm in diameter).

This optimised fluorescent labelling and clearing method could now be used to image naïve, Treg depleted and tumour dLN HEVs in 3D with SPIM (Chapter 4). Furthermore, the 3D blood vessel network of fibrosarcomas as well as the characterization of HEV development following Treg depletion and HEV augmentation could now be characterised (Chapter 5).

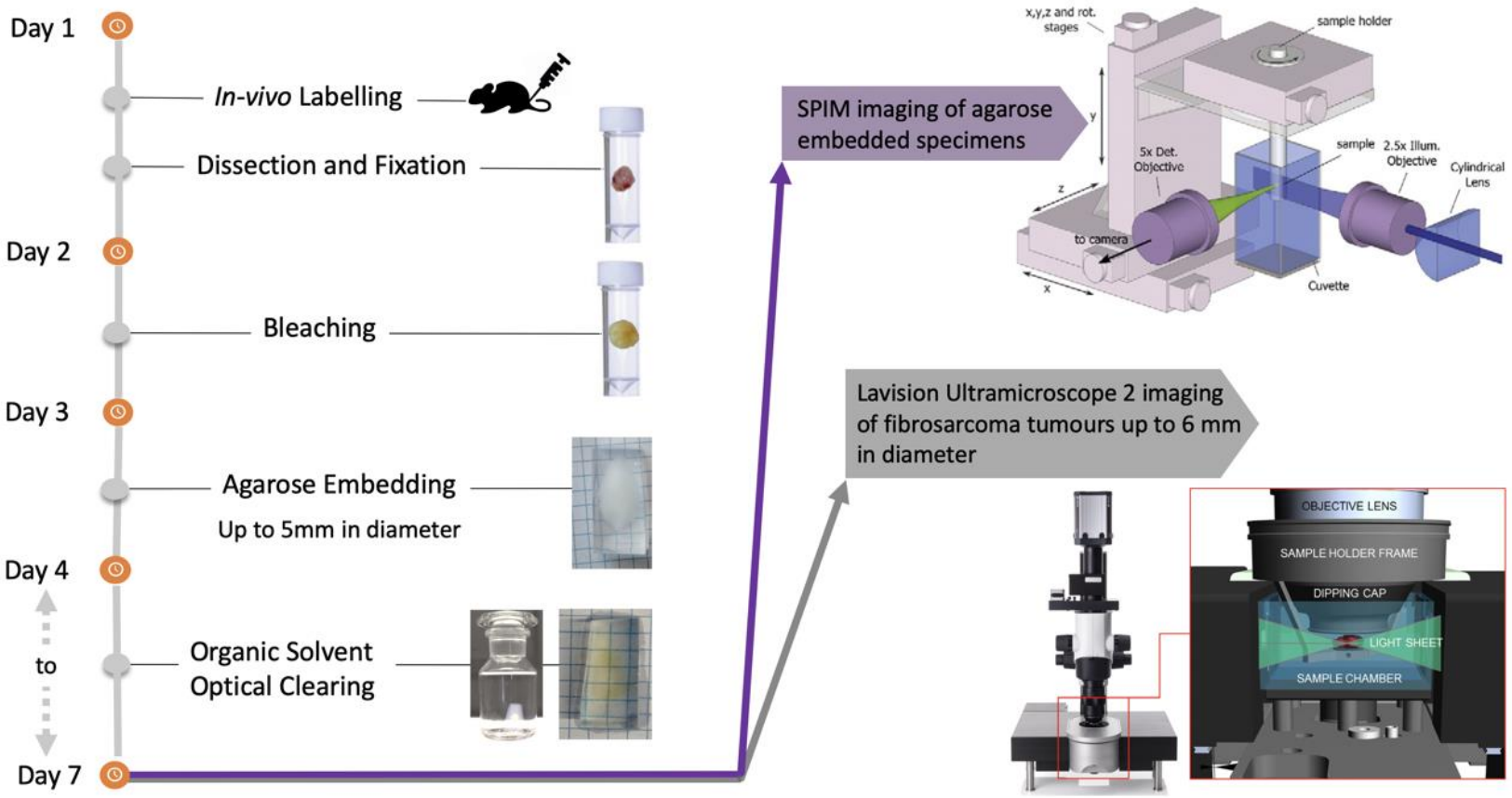

Figure 3.11 | Sample preparation workflow for LSFM imaging.
Time chart illustrating the duration of key steps required for preparing fibrosarcomas and lymph nodes for LSFM imaging. Figure adapted from (Quintana and Sharpe, 2011; Abe *et al.*, 2016).

Chapter 4

4 Results: 3-Dimensional Image Analysis of Lymph Node High Endothelial Venule Networks

4.1 Introduction

The ability to image whole blood vessel networks at micrometre resolution is readily achievable using LSFM. However, the quantitative analysis of LSFM acquired datasets remains challenging. Commercial software tools such as IMARIS filament tracer have previously been applied to LSFM datasets but analysis has largely been restricted to smaller regions of interest (ROI) (Lugo-Hernandez *et al.*, 2017; Di Giovanna *et al.*, 2018; Epah *et al.*, 2018). For example, whilst the use of gelatin hydrogel containing FITC-conjugated albumin combined with 3DISCO clearing enabled the imaging of whole murine brain blood vessel networks using LSFM, analysis utilizing IMARIS filament tracer was only restricted to a small portion of the striatum (Lugo-Hernandez *et al.*, 2017). There is therefore an unmet need for a computational pipeline that can readily process LSFM acquired datasets irrespective of the size of the vessel network.

Previous work by Kelch and colleagues described the development of a set of computational tools that allowed for the segmentation and quantification of continuous blood vessel networks found in murine lymph nodes stained with wheat germ agglutinin (WGA) and imaged by EVIS imaging (Kelch *et al.*, 2015). These vessel tools were built to process intra-luminally stained whole blood vessel networks effectively by splitting computationally intensive steps into individual tasks (Kelch *et al.*, 2015). As a result, these tools were repurposed to process LSFM datasets and were used in this work to characterize LN HEV networks imaged by SPIM.

Whilst LN HEV networks have previously been imaged by SPIM, they were not further quantified and instead used as an anatomical landmark for assessing the microenvironmental distribution of adoptively transferred T cells within the LN (Abe *et al.*, 2016). In contrast, LN HEV remodelling in the context of LCMV

infection (Kumar *et al.*, 2010), OVA/CFA immunization and autoimmune lymphadenopathy (Kumar *et al.*, 2012), has previously been globally examined using OPT and further quantified using IMARIS filament tracer. OPT is a mesoscopic imaging modality used for imaging specimens that have a diameter between 1 mm to 10 mm (Sharpe, 2004). OPT makes use of low numerical aperture (NA) objectives which provide a depth of focus (DOF) sufficient to cover 50% of the specimen (Sharpe, 2004). This in turn allows for the acquisition of 2D projections which can then be used to reconstruct the distribution of fluorescence emission (Sharpe, 2004). Whilst the use of low NA objectives allows for the rapid imaging of whole specimens, the resulting datasets are of considerably lower resolution as compared to laser scanning microscopy (Sharpe, 2004; Kumar *et al.*, 2010). Furthermore, the pre-requisite of having a DOF covering 50% of the specimen ultimately results in larger pieces of tissue having an overall lower voxel resolution. In contrast, whilst a larger number of FOVs would be required to image a larger specimen with SPIM, the resulting voxel resolution would remain constant since the lateral resolution is defined by the NA of the detection objective (as well as the wavelength of the fluorophore) and the axial resolution is governed by the minimum light sheet thickness which remains constant (Huisken and Stainier, 2009). SPIM is therefore a well-suited technique for mapping changes to LN HEVs particularly when such changes are accommodated by changes in tissue size which are known to occur following OVA/CFA immunization, Treg depletion (Kim, Rasmussen and Rudensky, 2007; Kumar *et al.*, 2012; Colbeck *et al.*, 2017), infection (Kumar *et al.*, 2010), and as a result of tumour establishment (Qian *et al.*, 2006; Maeda *et al.*, 2018).

This chapter describes the implementation of Dr Gib Bogle's computational vessel tools for quantifying lymph node HEV networks imaged by SPIM. In order to appropriately segment and quantify all LN HEV vessels, additional modifications to the tools had to be made and are described herein. The vessel tool pipeline was first used to characterize naïve LN HEV networks and subsequently to provide global topological descriptors of HEV remodelling in response to Treg depletion and fibrosarcoma establishment.

4.2 Results: LN HEV Network Analysis Computational Pipeline

The first experimental aim was to modify the vessel tools so that they could be used to segment and quantify whole LN HEV networks. Similarly to the lectin staining (Porter, Palade and Milici, 1990; Jährling, Becker and Dodt, 2009), MECA-79 exhibits a variable staining intensity pattern across the entire HEV network of lymph nodes as shown in Figure 4.1 A. Furthermore, the MECA-79 antibody only leads to the labelling of the outer vessel wall leaving several gaps/holes along the vessel wall lining and within the vessel itself. This can be seen more clearly by examining individual 5 µm thick optical cross sections (Figure 4.1 B and Figure 4.2). Such staining patterns pose problems for segmentation; a post-image acquisition processing step which generates a binary mask of the vessel network consisting of lit voxels (vessels) and non-lit voxels (background). The problem posed by the variable staining intensity pattern of MECA-79 and wheat germ agglutinin (WGA) can be resolved using the thresholding tool which sets a variable threshold level depending on the average local intensity (Kelch et al., 2015) and can readily be applied to the SPIM acquired LN HEV datasets. This variable thresholding approach combined with the use of a nearest neighbour filling algorithm and the manual addition of voxels in FIJI (Chapter 2 Methods) was sufficient to generate a binary vessel mask of the HEV network (Figure 4.1 C).

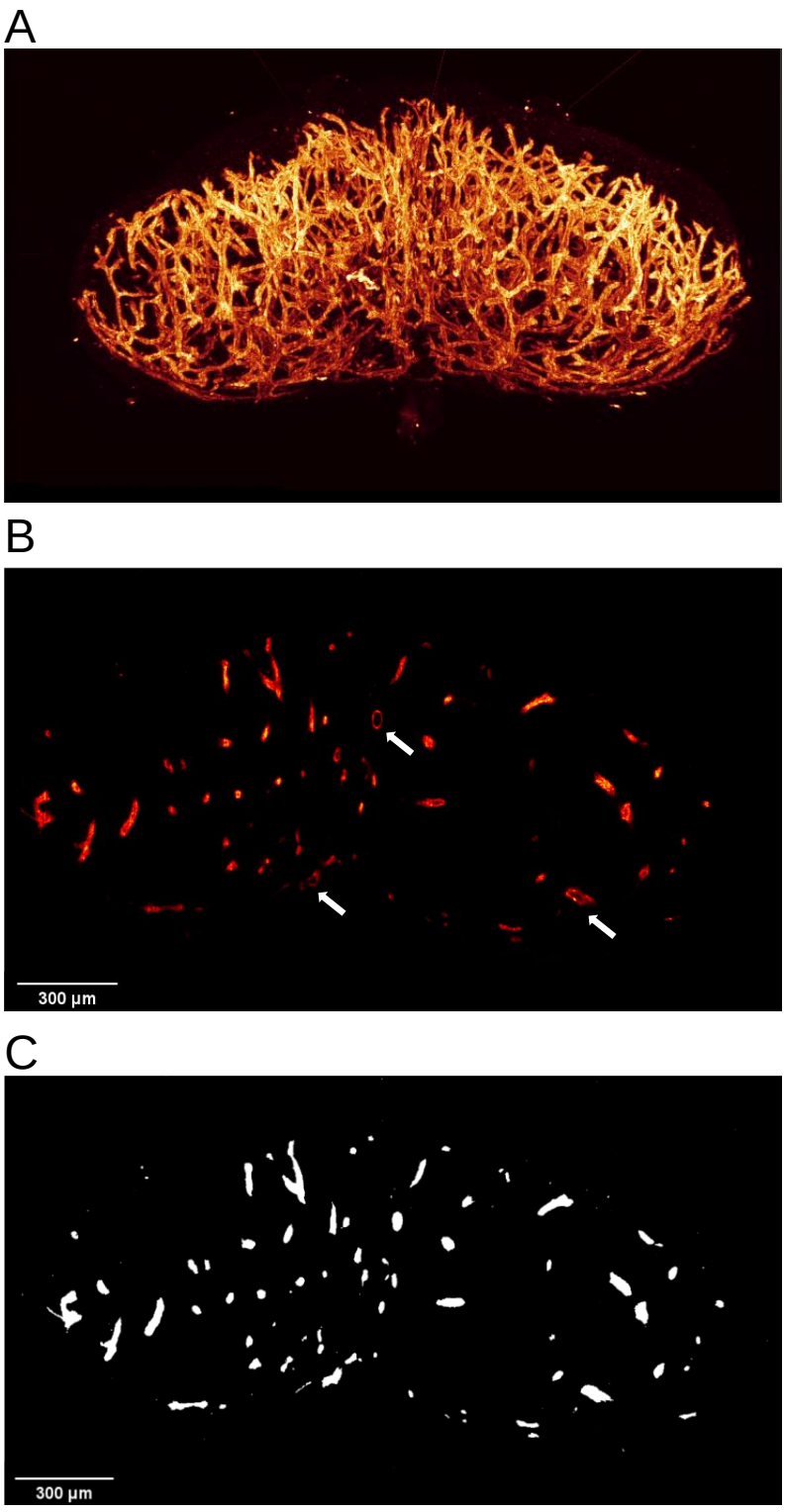

Figure 4.1 | MECA-79 Staining Pattern and HEV Segmentation.
(**A**) Maximum intensity projection of the entire HEV network of a naive inguinal lymph node labelled with 20 µg of MECA-79 594 and imaged with SPIM. (**B**) A 5 µm thick optical cross-section allows for the closer inspection of the MECA-79 staining pattern. White arrows indicate holes within or along HEV vessels. Data are colour-coded as a heatmap to display staining intensity where high intensity pixels are either white or bright yellow whilst low intensity pixels are red. (**C**) HEV network segmentation is achieved using a variable thresholding algorithm followed by the use of a nearest neighbour filling algorithm and lastly by manual insertion of voxels. Note that this approach fills previously identified holes in the HEV vessels.

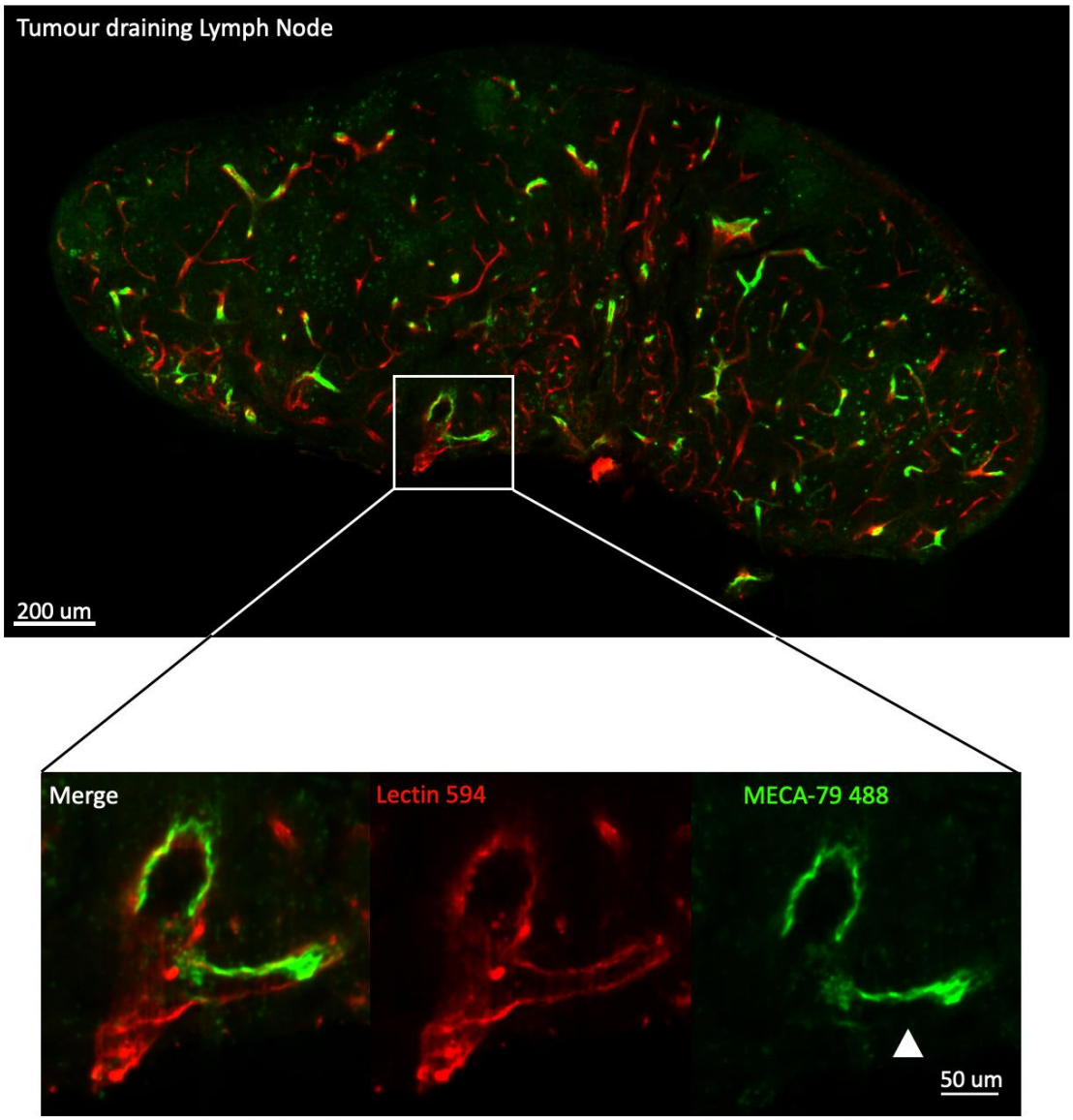

Figure 4.2 | Lectin and MECA-79 staining pattern in lymph nodes.
A 5 µm optical cross section of a fibrosarcoma draining lymph node labelled with 20 µg MECA-79 AF 488 (HEVs) and 150 µg tomato lectin Dylight 594 (blood vessels) and imaged by SPIM. Arrowhead denotes a lack of MECA-79 staining along the lining of the blood vessel wall.

The vessel tools were originally built for the purpose of quantifying a single continuous blood vessel network (Kelch *et al.*, 2015). Since HEVs branch out from low order post-capillary venules (von Andrian, 1996), this means they form discrete vessel networks that form part of the venular tree. As such, several disconnected HEVs can be found within the same LN. In order to process such disconnected vessel networks, the connect tool (a tool which detects the largest connected object within the segmented image file) had to be modified in order to be capable of identifying up to 100 largest connected objects. This modification was sufficient to allow for the identification of all HEVs that make up the entire HEV network of a LN (Figure 4.3 A&B). As such, each connected HEV network could be skeletonized and quantified separately before being visualized as a 3D model colour-coded to represent the vessel diameter (Figure 4.3 C). This computational pipeline could now be used to characterize naïve LN HEVs imaged with SPIM as well as HEV remodelling following Treg depletion and fibrosarcoma establishment.

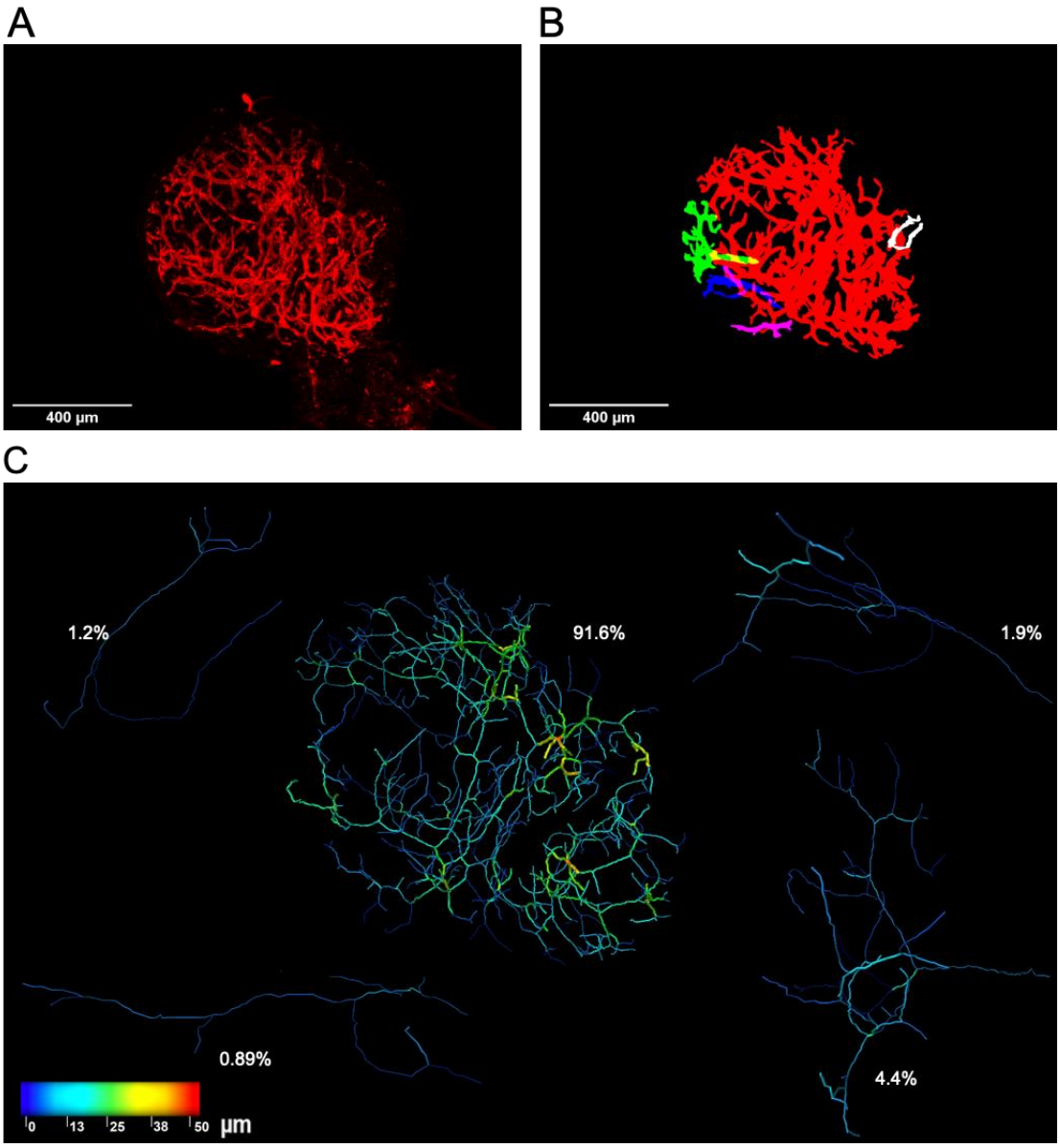

Figure 4.3 | HEV Network Identification and Quantification.
(**A**) Maximum intensity projection (MIP) of a naïve popliteal lymph node HEV network labelled with 20 µg MECA-79 594 and imaged with SPIM. (**B**) MIP of segmented HEV vessel network colour coded to represent individual PNAd$^+$ vessel networks (total number of vessel networks = 5). (**C**) Each HEV network can be rendered separately as a 3D model in Amira and colour-coded to represent the vessel diameter. Percentage of lit voxels that make up entire segmented HEV network are displayed next to each individual vessel network.

4.3 Naïve LN HEV Characterization

In order to characterize the 3D topology of LN HEVs under homeostatic conditions, both naive popliteal and inguinal LNs were labelled and imaged with SPIM (Figure 4.4 A&B). Acquired datasets were processed and analysed using the optimized computational pipeline described above. Extracted vessel parameters of individual popliteal LN HEVs and inguinal LN HEVs can be found in Table 4.1 and Table 4.2. The extracted parameters underline the complexity of the HEV network with the number of segments ranging from 836 to 1169 for popliteal LN HEVs and from 2872 to 5034 for inguinal LN HEVs. The volume estimates of popliteal and inguinal LNs are shown in Figure 4.4 C and are in close agreement with those previously reported by Kumar and colleagues, who first characterized the 3D topology of homeostatic LN HEVs by OPT (Kumar *et al.*, 2010). Similarly, a linear relationship between LN volume and total HEV length was found for both inguinal and popliteal LN HEVs (Figure 4.4 D). Importantly, the total number of branch points was found to correlate with total HEV length (Figure 4.4 E) suggesting comparable network branching structure between LNs of different sizes. These findings are in close agreement to those reported by the OPT study (Kumar *et al.*, 2010), suggesting that this is a valid approach for globally mapping LN HEVs.

Table 4.1 | Extracted popliteal LN HEV network parameters. A segment is defined as a vessel found between two branching points.

	Popliteal LN 1	Popliteal LN 2	Popliteal LN 3	Popliteal LN 4	Popliteal LN 5	Popliteal LN 6
Number of Segments	926	836	1071	1039	913	1169
Number of Branch Points	463	423	532	525	448	572
Mean Segment Diameter (μm)	18.8	24.7	20.47	16.8	18.4	16.7
Mean Segment Length (μm)	47	54.76	46.17	41.36	49.73	47.15
Network Length (cm)	4.3	4.58	4.94	4.3	4.54	5.51
Network Volume (mm^3)	0.011	0.016	0.016	0.01	0.012	0.012
Lymph Node Volume (mm^3)	0.31	0.4	0.52	0.53	0.43	0.51
Vessel Density (mm^3)	2987	2090	2059	1960	2123	2292

Table 4.2 | Extracted inguinal LN HEV network parameters. A segment is defined as a vessel found between two branching points.

	Inguinal LN 1	Inguinal LN 2	Inguinal LN 3
Number of Segments	2872	3523	5034
Number of Branch Points	1477	1429	2578
Mean Segment Diameter (μm)	30.7	26.4	25.67
Mean Segment Length (μm)	65.2	63.9	49.5
Network Length (cm)	18.73	22.53	24.91
Network Volume (mm^3)	0.137	0.12	0.131
Lymph Node Volume (mm^3)	2.6	2.47	2.89
Vessel Density (mm^3)	568	578	892

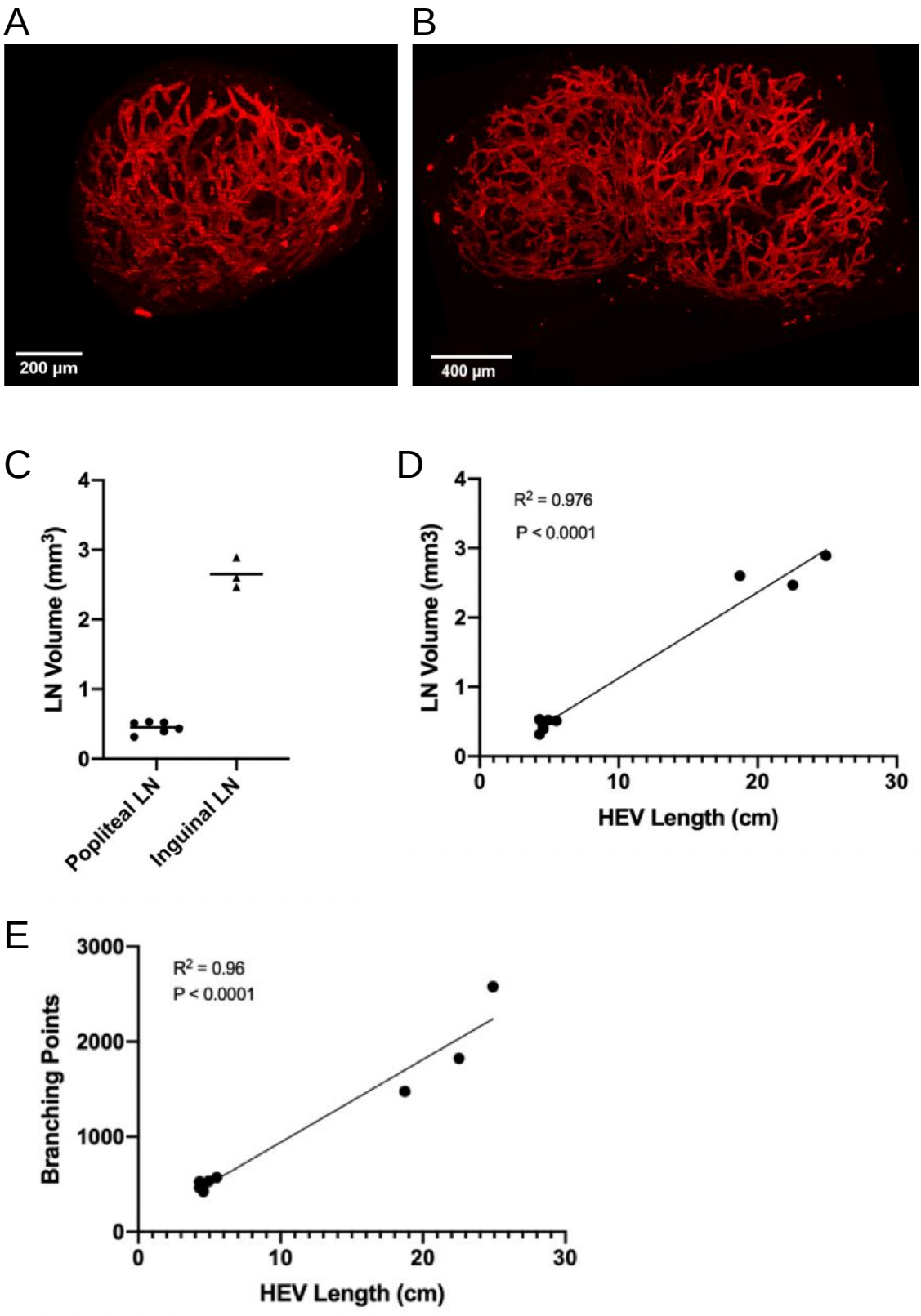

Figure 4.4 | Naïve LN HEV Characterisation.
Representative maximum intensity projections of a naïve popliteal LN HEV network (**A**) and a naïve inguinal LN HEV network (**B**) labelled with 20 µg MECA-79 594 and imaged with SPIM. (**C**) Volume estimates of naïve popliteal (n = 6) and inguinal LNs (n = 3). (**D**) Correlation between LN volume and total HEV length. (**E**) Correlation between number of branching points and total HEV length. Each symbol represents one LN. Black bars indicate the mean of each group.

The overall extent of all LN HEV networks analysed were however found to be larger in this work as compared to what has previously been reported. The average total HEV length of inguinal LN HEVs was 22.06 ± 3.12 cm which is almost twice the size reported in the OPT study (Kumar *et al.*, 2010). Furthermore, the extent of branching and the total number of HEV segments found in naïve popliteal LNs was also greater (Kumar *et al.*, 2012). Given that the LN labelling and clearing methods are comparable to those performed in the OPT study, it is possible that this difference can be attributed to the differences in resolving capability between the two imaging modalities. Furthermore, differences in infection status and cleanliness of animal facilities may lead to LN activation and an expansion of the LN HEV network. This could be experimentally tested by performing SPIM imaging and HEV quantification of LNs harvested from the same animal facility and infection status that previous groups have used (Kumar *et al.*, 2010, 2012). With regards to differences in resolving capability, it would be expected that SPIM which can achieve spatial resolutions comparable to laser scanning microscopy and which has a fixed voxel resolution regardless of tissue size would more readily detect finer vessels than OPT which achieves overall lower spatial resolutions that change according to tissue size (due to the minimum DOF requirement).

Indeed, by examining the HEV vessel length distribution across both naive popliteal and inguinal LNs (Figure 4.5 A&B) it is clear that at least 20% of HEVs have lengths that are in the order of 20 μm or less. This similarity in vessel length distribution between LNs of two different sizes reflects the ability of SPIM to consistently detect finer HEV vessels. This is in contrast to the OPT study which only showed 5% of popliteal LN HEV vessels to have total lengths less than 20 μm (Kumar *et al.*, 2012). Whilst the average HEV segment length (Figure 4.5 E) and segment length distribution (Figure 4.5 A&B) was comparable between popliteal and inguinal LNs, the HEV diameter distribution differed between the two LNs of different sizes (Figure 4.5 C&D). For popliteal LNs, HEVs with a diameter of up to 20 μm made up most of the network whilst the majority of inguinal LN HEVs consisted of vessels with a larger diameter ranging from 21-40 μm. Indeed, inguinal LN HEVs also had significantly larger diameters as compared to popliteal LN HEVs (Figure 4.5 F). This difference in vessel diameter distribution can be visualized by examining the 3D model of the LN HEV network

colour-coded to represent the vessel diameter (Figure 4.6 A&B). The average HEV diameters measured in this work, fall within the 16-55 μm HEV diameter range previously defined by Kowala and colleagues who used electron microscopy to examine the blood vessel structure of popliteal LNs (Kowala and Schoefl, 1986).

Whilst the length and diameter distributions for LNs of different anatomical size were not directly compared in the OPT study, the naïve popliteal HEV network diameter distribution was reported to consist mostly of thicker vessels ranging from 21-40 μm (Kumar *et al.*, 2012). Again, this difference can be attributed to the difference in resolving power between SPIM and OPT. Overall, 3D measurements are likely to be affected by shrinkage during sample preparation. For OPT and SPIM this occurs during BABB clearing and for EVIS imaging this occurs during resin embedding (Kelch *et al.*, 2015). However, for comparative purposes the use of SPIM and the optimized vessel tool pipeline is a valid approach for mapping global changes to LN HEVs especially given that the branching patterns between LNs of different sizes were shown to be comparable.

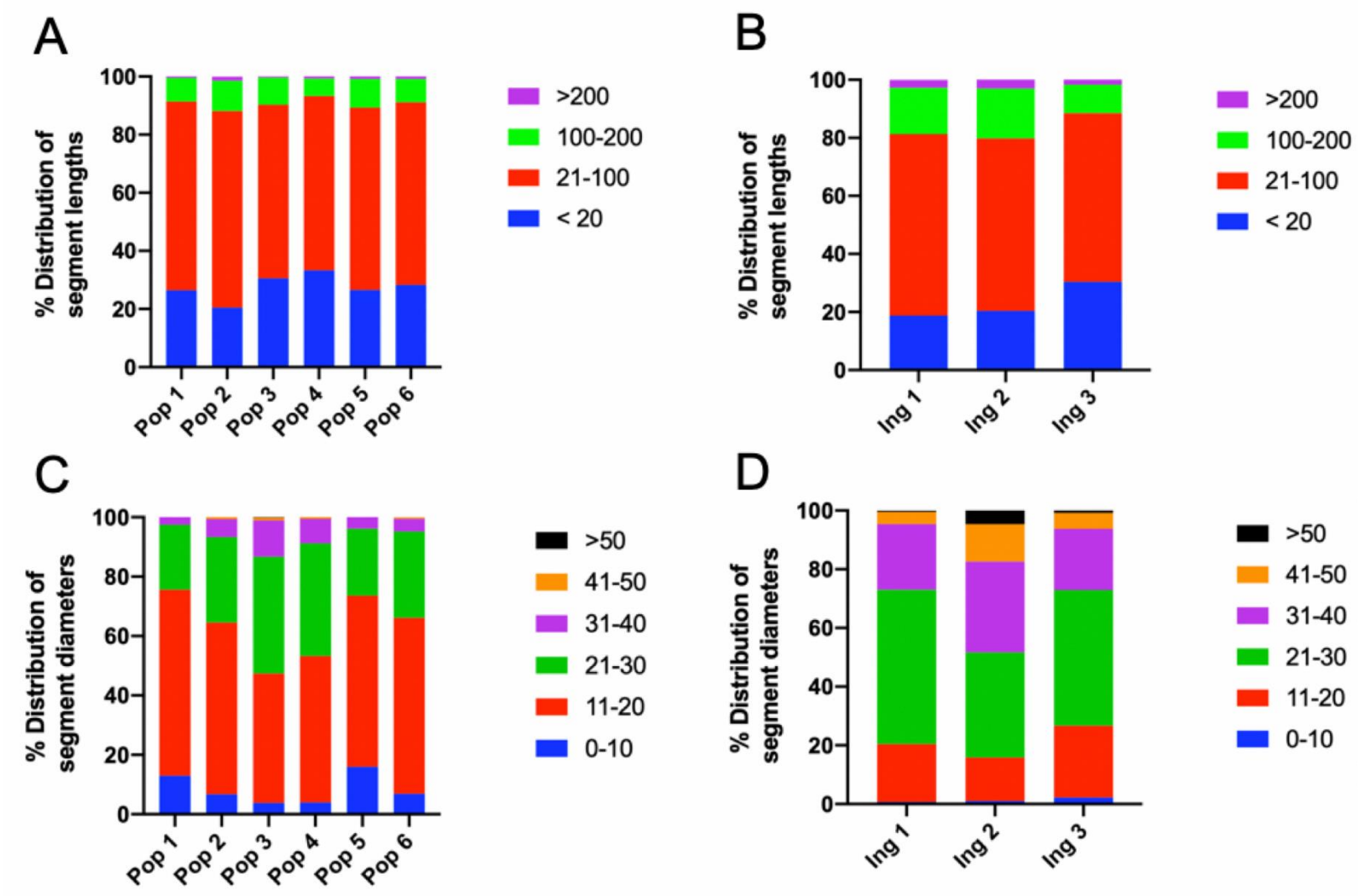
A
% Distribution of segment lengths
100
80
60
40
20
0
Pop 1
Pop 2
Pop 3
Pop 4
Pop 5
Pop 6
>200
100-200
21-100
< 20
B
% Distribution of segment lengths
Ing 1
Ing 2
Ing 3
>200
100-200
21-100
< 20
C
% Distribution of segment diameters
Pop 1
Pop 2
Pop 3
Pop 4
Pop 5
Pop 6
>50
41-50
31-40
21-30
11-20
0-10
D
% Distribution of segment diameters
Ing 1
Ing 2
Ing 3
>50
41-50
31-40
21-30
11-20
0-10

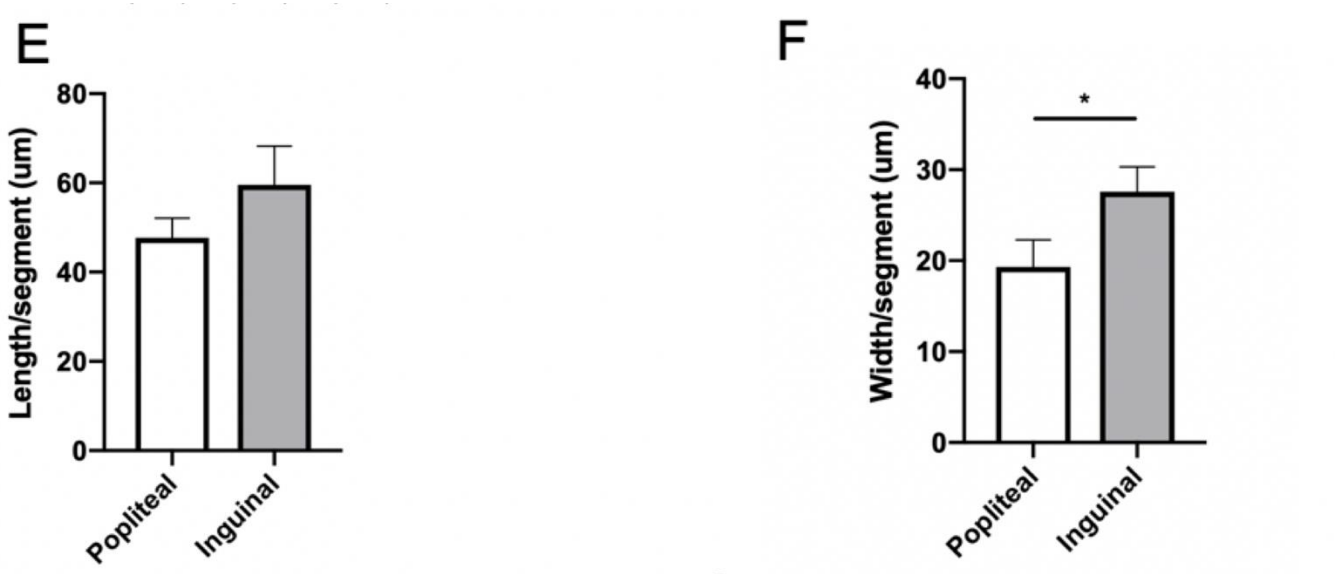

Figure 4.5 | Naïve LN HEV Length and Diameter Distribution.
Relative distribution of HEV segment lengths of individual popliteal LNs (**A**) and inguinal LNs (**B**). Lengths were divided into discrete bin (units shown are in μm) and the percentage of segments found in each bin was calculated and graphed. Relative distribution of HEV segment widths of individual popliteal LNs (**C**) and inguinal LNs (**D**). Lengths were divided into discrete bin (units are displayed in μm) and the percentage of segments found in each bin was calculated and graphed. Average segment length (**E**) and width (**F**) of inguinal (n=3) and popliteal (n=6) LN HEV segments. Popliteal LNs are abbreviated as 'Pop' and inguinal LNs are abbreviated as 'Ing'. Statistical significance was determined by Student t-test (Two tailed, *$p < 0.05$). Error bars represent standard deviations.

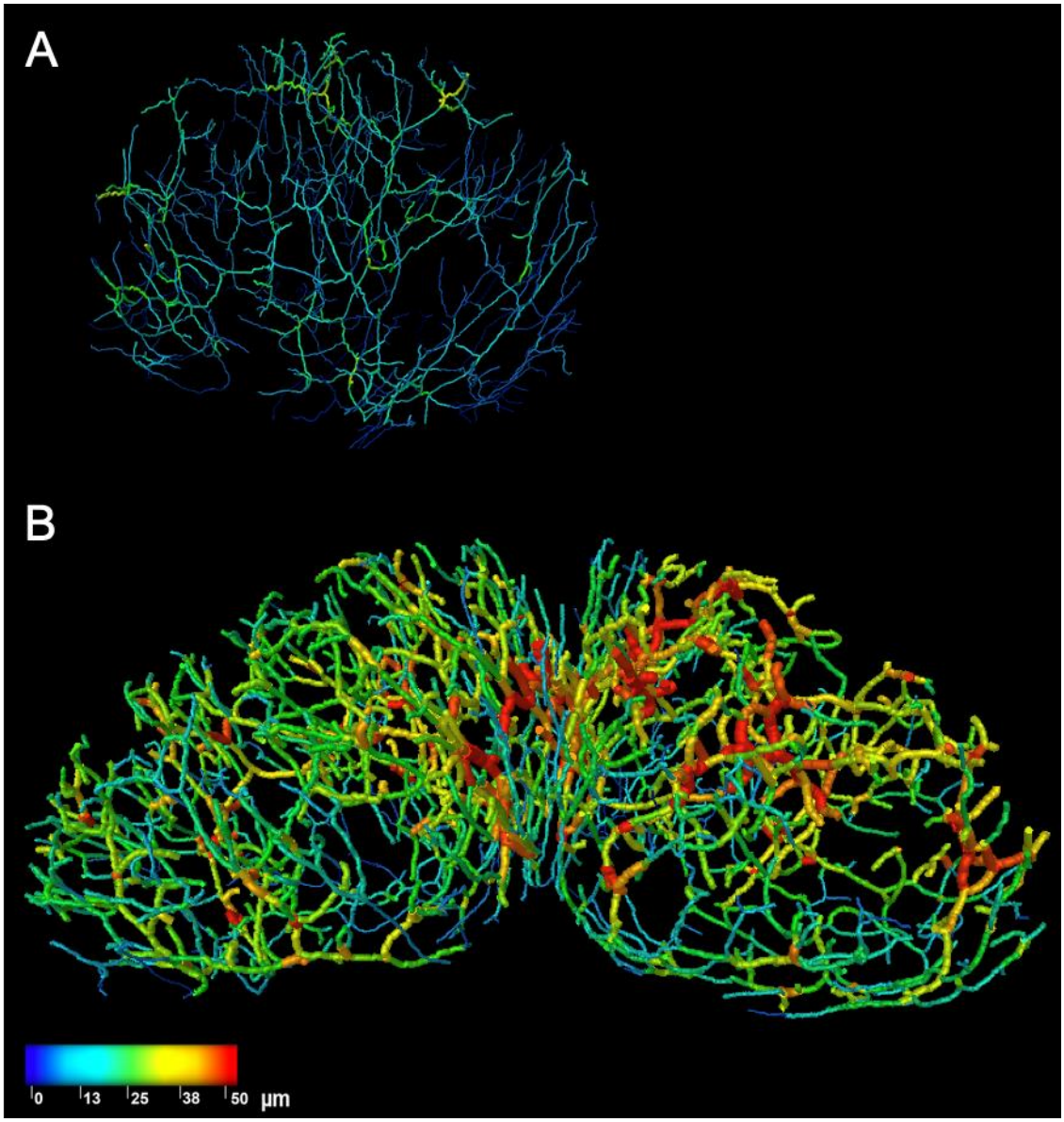

Figure 4.6 | Naïve LN HEV Vessel Diameter Distribution.
3D rendered model of naïve popliteal LN HEV sub-network (**A**) and inguinal LN HEV sub-network (**B**) generated with the vessel tools and colour-coded to represent the vessel diameter. The displayed popliteal HEV sub network formed 96% of lit voxels of the entire HEV network whilst the inguinal HEV sub network formed 97.4% of all lit voxels of the entire HEV network.

4.4 Treg depletion and LN HEV Remodelling

In order to examine global LN HEV network changes that take place following Treg depletion, Foxp3^{DTR} mice were treated with six rounds of DT and inguinal LNs were harvested and imaged with SPIM. As shown in Figure 4.7 A, a massive expansion in the LN HEV network could be observed. In order to characterize the 3D topology of LN HEVs following Treg depletion, an inguinal LN HEV network was processed using the computational pipeline described earlier. The key parameters are summarised in Table 4.3. Consistent with an increase in LN size (Kim, Rasmussen and Rudensky, 2007; Kumar *et al.*, 2012) there was roughly a 10-fold expansion in the overall LN volume. In accordance with the large HEV network expansion, there was an increase in the number of branching points as well as the total number of segments all of which are in line with the previous OPT study (Kumar *et al.*, 2012). This suggests that HEV expansion is in part the result of vessel arborization leading to the formation of new vessels. Furthermore, an approximately 6-fold increase in the total HEV length was found. A comparison of the vessel length distribution and vessel diameter distribution with naïve inguinal LN HEVs is shown in Figure 4.8 A&B. Whilst the vessel length distribution is largely comparable to that of naïve inguinal LNs, the vessel diameter distribution was altered with the majority of the network consisting of vessels with a smaller diameter of between 11-20 μm. Vessel constriction and vessel stretching may lead to a reduction in diameter as previously described (Kumar *et al.*, 2012), however a lack of any obvious changes to the vessel length distribution suggest that this is likely the result of the formation of new vessels with smaller diameters instead. Indeed, several vessels of smaller diameter can be seen in the 3D rendered model (Figure 4.7 B). Interestingly, alterations to the segment width distributions of Treg depleted popliteal LN HEVs were not previously found with OPT (Kumar *et al.*, 2012). An inability to detect vessels that have small segment widths (< 20 μm) by OPT may explain these differences. The use of a higher resolution technique such as EVIS imaging should be performed to confirm this finding. Alternatively performing OPT imaging of the same sample (previously imaged by SPIM) could reveal whether differences in the extent of the network captured hold true. Nevertheless, SPIM imaging can readily capture the global changes that are known to occur to LN HEVs following Treg depletion (Kumar *et al.*, 2012).

There are several ways by which Treg depletion may drive HEV remodelling. This includes the widespread activation of $CD4^+$ T cells as well as the accumulation and maturation of $CD11c^+$ DCs (Kim, Rasmussen and Rudensky, 2007; Lund *et al.*, 2008) both of which have important roles in mediating HEV expansion (Webster *et al.*, 2006; Chyou *et al.*, 2011). Furthermore, Tregs have also been shown to directly limit EC activation (He *et al.*, 2010; Matrougui *et al.*, 2011).

Table 4.3 | Treg depleted inguinal LN (DT LN) and fibrosarcoma draining LN (SLN) HEV network parameters. A segment is defined as a vessel found between two branching points.

	DT LN	SLN
Number of Segments	24804	14862
Number of Branch Points	12668	7840
Mean Segment Diameter (μm)	17.24	20.17
Mean Segment Length (μm)	55.3	48.5
Network Length (cm)	137.17	72.02
Network Volume (mm^3)	0.348	0.23
LN Volume (mm^3)	19.12	3.57
Vessel Density (mm^3)	1297	4163

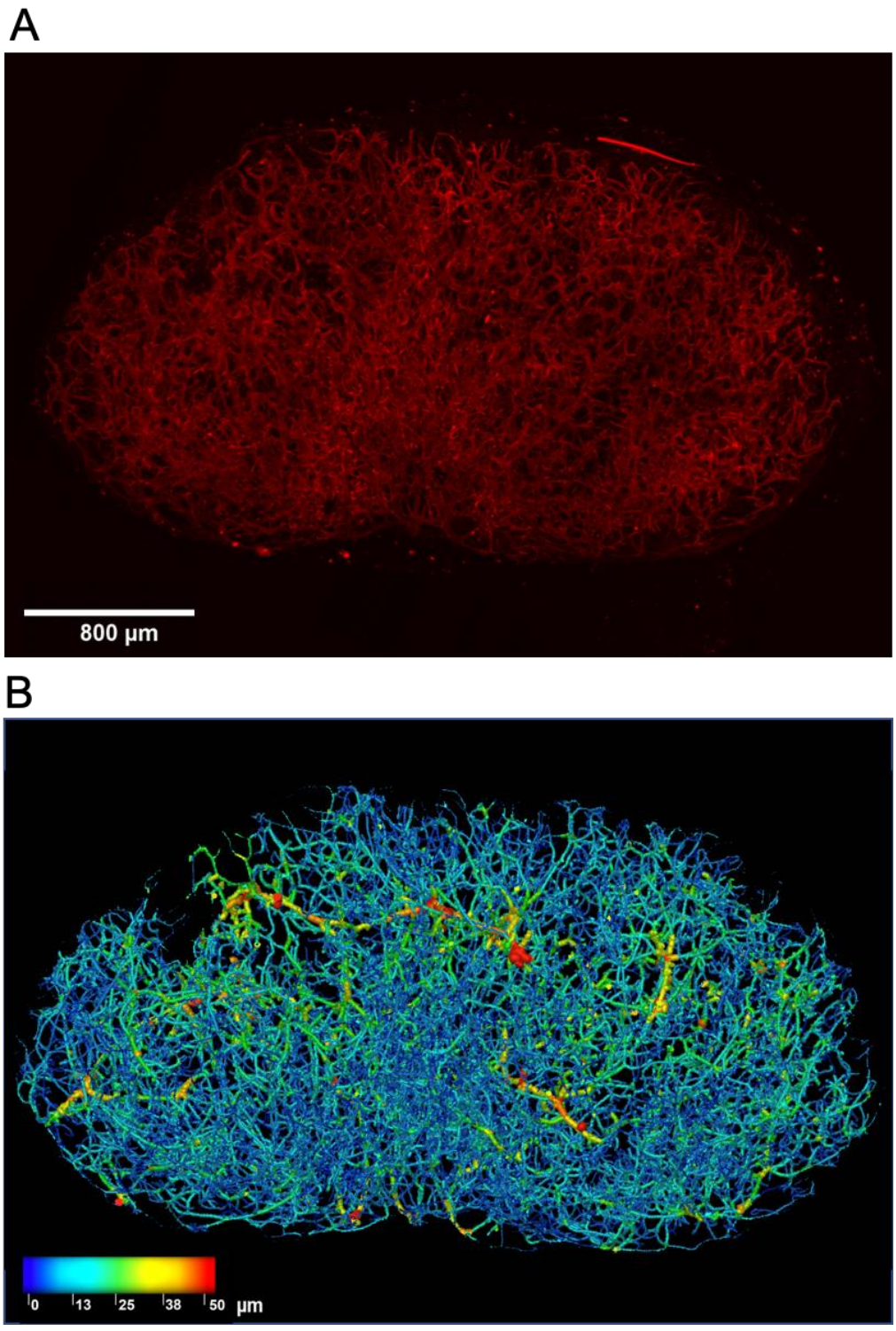

Figure 4.7 | Topological analysis of Treg depleted LN HEV Network.
(**A**) Maximum intensity projection of a Treg depleted inguinal LN (DT Ing) HEV network labelled with 20 µg MECA-79 594 and imaged with SPIM. Figure shown is the same scale as in **Figure 4.4** to allow for comparison. (**B**) 3D model of DT Ing LN HEV network colour coded to display vessel diameter in Amira. This image formed 99% of lit voxels found in the segmented image.

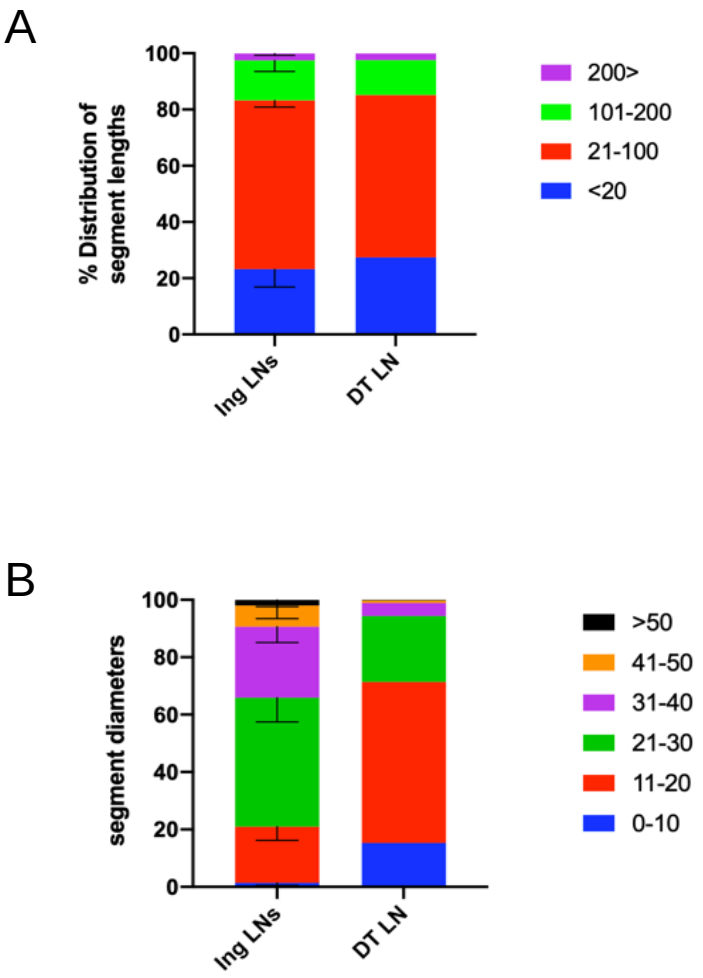

Figure 4.8 | Treg depleted LN HEV network length and diameter distributions.
Relative distribution of HEV segment lengths (**A**) and widths (**B**) of pooled naïve inguinal LNs (Ing LNs, n = 3) and a Treg depleted inguinal LN (DT LN, n = 1). Lengths were divided into discrete bin (units shown are in μm) and the percentage of segments found in each bin was calculated and graphed. Error bars represent standard deviations.

4.5 Fibrosarcoma Establishment and SLN Remodelling

The experimental aim of this section was to perform a global analysis of a fibrosarcoma draining LN HEV network in order to determine whether any tumour driven HEV remodelling takes place. Previous 2D characterizations of SLN HEVs have revealed thinning of the HEV wall and an enlargement of the lumen in axillary LNs found in human breast cancer patients (Qian *et al.*, 2006). Such changes were also recapitulated in mouse tumour models using the CNE-2, NPC and DA3 cancer cell lines (Qian *et al.*, 2006). Similar alterations to the HEV lumen as well as an increase in HEV numbers were also reported in human regional LNs derived from tongue squamous cell carcinoma (SCC) patients (Lee *et al.*, 2012) and OSCC patients (Chung *et al.*, 2012). Interestingly alterations to SLN HEVs may be model specific as structural changes to LNs draining established B16 melanoma tumours were not found (Carriere *et al.*, 2005).

In order to examine global changes that occur to a fibrosarcoma SLN HEV network, a dLN was imaged with SPIM (Figure 4.9 A) and processed using the computational pipeline. Extracted parameters are shown in Table 4.3. There was an approximately 3.5-fold increase in total HEV length. This expansion was in part the result of vessel arborization since an increase in total number of segments and branching points was also found. The segment length and width distributions (Figure 4.10 A&B) were comparable to that of a Treg depleted LN HEV network (Figure 4.8 A&B), suggesting that the establishment of a fibrosarcoma leads to the branching of small diameter vessels which in turn make up the majority of the network. In contrast to the massive LN expansion seen following Treg depletion (LN volume of 19.12 mm^3), there was only a moderate increase in LN volume (3.57 mm^3). Interestingly, the HEV vessel density was approximately 6-fold higher as compared to naïve inguinal LNs and 4-fold higher than the Treg depleted LN. Indeed, examination of the dLN HEV network (Figure 4.9 B) reveals a densely packed network consisting of mostly small (11-20 μm) diameter sized vessels. This suggests that the establishment of a fibrosarcoma leads to HEV alterations which are largely distinct from the ones described by Qian and colleagues who reported a reduction in HEV density and a dilation of the HEV lumen (Qian *et al.*, 2006).

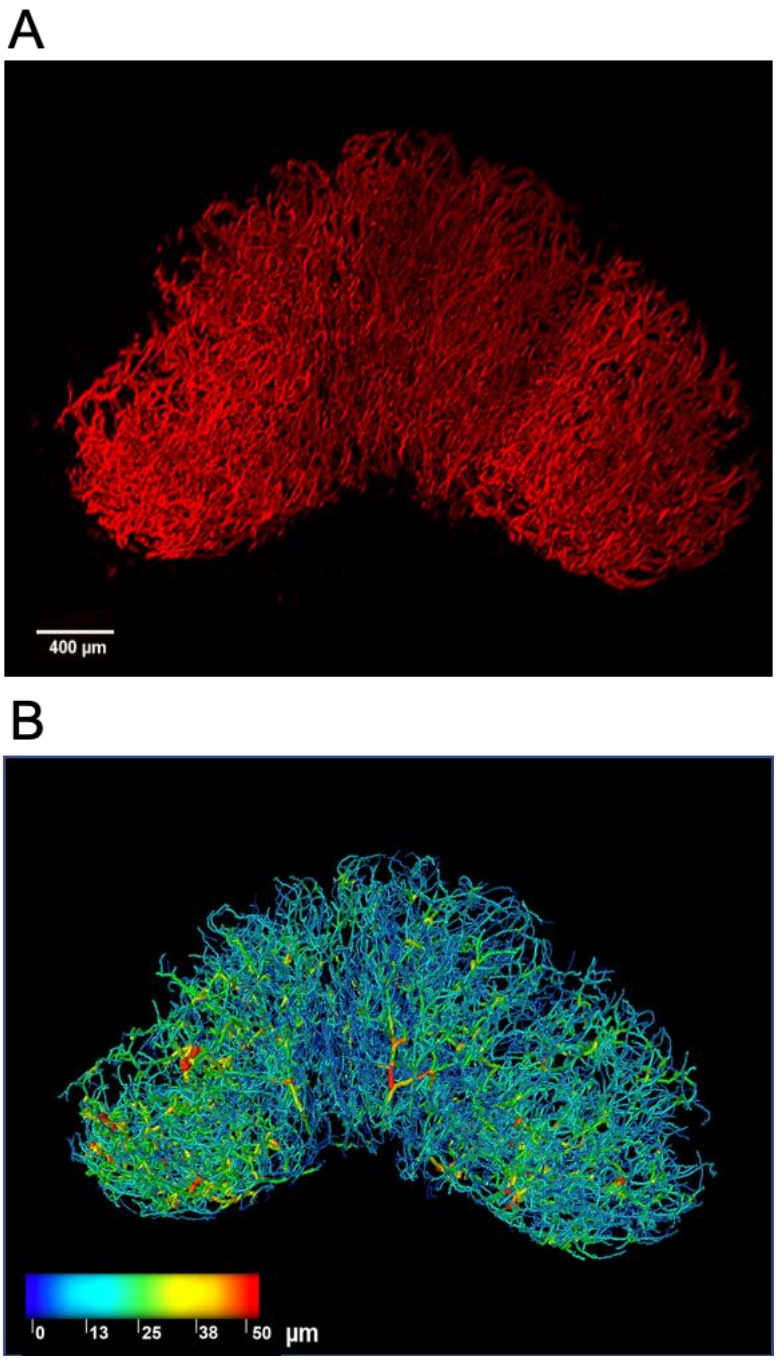

Figure 4.9 | Topological analysis of a SLN HEV network
(**A**) Maximum intensity projection of a fibrosarcoma draining inguinal LN (SLN) HEV network labelled with 20 µg MECA-79 594 and imaged with SPIM. Figure shown is the same scale as in **Figure 4.4** to allow for comparison. (**B**) 3D model of SLN HEV network colour coded to display vessel diameter in Amira. This image formed 99% of lit voxels found in the segmented image.

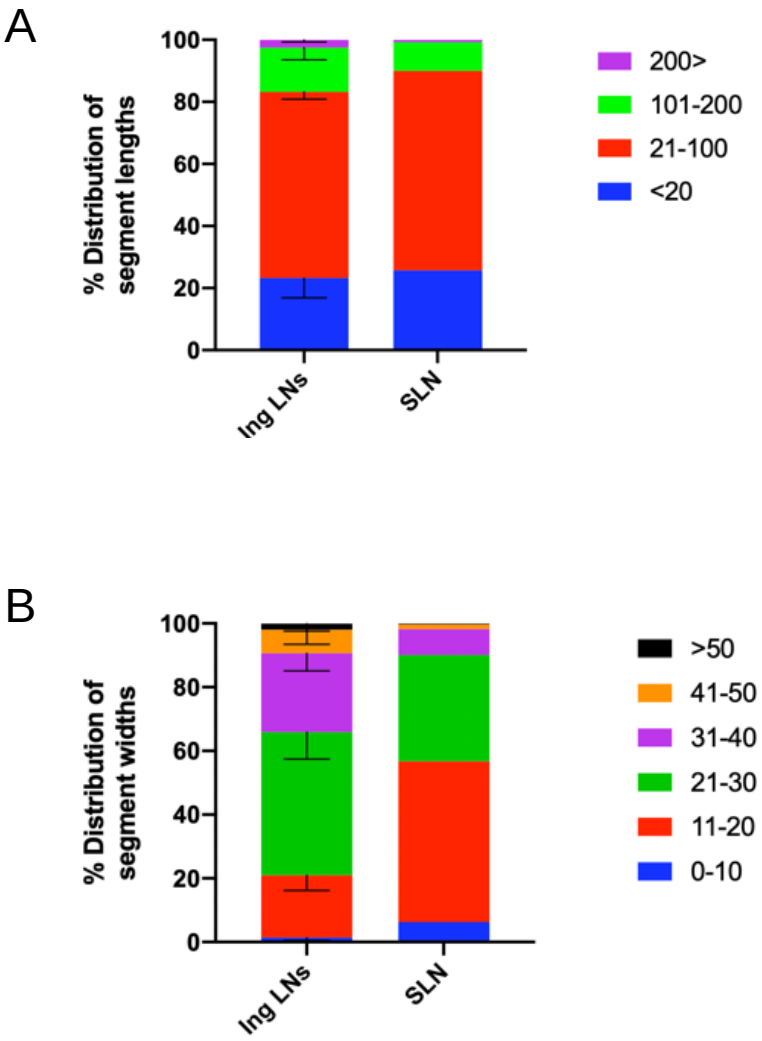

Figure 4.10 | Fibrosarcoma dLN HEV network length and diameter distributions. Relative distribution of HEV segment lengths (**A**) and widths (**B**) of pooled naïve inguinal LNs (Ing LNs, n=3) and a fibrosarcoma draining LN (SLN, n = 1). Lengths were divided into discrete bin (units shown are in μm) and the percentage of segments found in each bin was calculated and graphed. Error bars represent standard deviations.

4.6 Discussion

Topological descriptors of whole blood vessel networks acquired by LSFM can now readily be generated using the vessel tools developed by Dr Gib Bogle. The ability to identify and process several connected blood vessel networks was an important modification that allowed for the mapping of LN HEV networks. This approach could provide useful for mapping intra-tumoral HEVs which can form in isolation or as parts of TLS (Colbeck *et al.*, 2017).

Topological analysis of naïve inguinal and popliteal LNs showed comparable branching structure as previously reported by the OPT study (Kumar *et al.*, 2010) but differences in the overall extent of the networks were noted. These are likely the result of resolution differences between the two imaging modalities. This is particularly important to consider when comparing HEV remodelling captured by LSFM to other forms of LN stimulation previously characterized by OPT. The use of an HEV specific marker such as MECA-79 together with higher resolution techniques such as EVIS imaging could be performed in the future to confirm these findings.

The vessel tools were also used to characterize global HEV changes that occur following Treg depletion and establishment of a fibrosarcoma tumour, both of which led to extensive HEV expansion characterized by increased branching and formation of small (11-20 μm) diameter sized vessels. Similarities found in the segment length and width distributions may suggest shared mechanisms driving such remodelling however differences in the extent of network expansion and vessel densities were noted between the two groups. Indeed, previous OPT studies have revealed both shared and distinct features of LN HEV remodelling following LCMV infection (Kumar *et al.*, 2010), Treg depletion and OVA/CFA immunization (Kumar *et al.*, 2012).

The dLN HEV expansion was largely distinct from the one described by Qian et al. who reported a reduction in HEV density and increase in HEV diameter (Qian *et al.*, 2006). Whilst it is possible that the use of 2D sectioning and imaging techniques can lead to the sampling of rare dilated HEV that are not

representative of the rest of the HEV network (which conversely may be remodelled differently), it may be the case that the establishment and rapid growth of tumour cell lines as opposed to the development of a tumour *in situ* results in a different type of LN HEV remodelling. Furthermore, this dilated phenotype might be tumour model specific as B16-F1 draining LNs do not have any morphological alterations to their HEVs (Carriere *et al.*, 2005). Interestingly in a separate study, the use of the B16-F10 cell-line which has a higher metastatic potential than B16-F1, led to the dilated HEV phenotype and a higher quantity of HEVs (as compared to the contralateral LN) (Maeda *et al.*, 2018). HEV remodelling may be therefore be driven by tumour-secreted factors and extracellular vesicles. These have been shown to lead to the perturbation of ECs at distant sites which is one the first steps in the establishment of a pre-metastatic niche (PMN) (Peinado *et al.*, 2017). Tumour derived exosomes released by melanoma cells have been shown to home specifically to the sentinel LN, resulting in the induction of pro-angiogenic factors implicated in establishment of a PMN which supports the recruitment and growth of metastatic melanoma cells (Hood, San and Wickline, 2011). In oesophageal cancer patients, transcriptomic profiling of metastasis-free regional LNs from patients with existing metastatic nodes revealed that Dickkopf-1 (DKK1), a Wnt antagonist, was the most significantly downregulated gene as compared to regional LNs from oesophageal cancer patients without metastatic nodes (Otto *et al.*, 2014). Interestingly DKK1, which is expressed by LN vascular ECs (Otto *et al.*, 2014), has a negative effect on tumour angiogenesis (Saupe *et al.*, 2013) and perfusion (Park *et al.*, 2014). The impact of DKK1 downregulation on HEV structure/function has not yet been examined. Altered lymphatic drainage due to the establishment of a tumour may also lead to the enlarged HEV phenotype especially given the important role of the lymphatic vasculature in delivering important cues for maintaining HEV function (Liao and Ruddle, 2006). It is also possible that immune cell activation in SLNs (Maeda *et al.*, 2018) driven by tumour-derived cues could also lead to HEV remodelling. As such it would be of interest to examine and compare whether fibrosarcoma dLNs are remodelled differently based on tumour responses to Treg depletion.

Given that the vessel tools rely on user-guided processing and manual adjusting of parameters to achieve appropriate segmentation (Kelch *et al.*, 2015),

the processing of SPIM datasets with a large number of Z-stacks can be time-consuming. For Treg depleted LN HEVs there are roughly 600 Z-slices that require appropriate segmentation. Recently, machine learning approaches for automatic segmentation have been applied to whole brain vascular networks imaged by LSFM (Todorov *et al.*, 2020). In this work, automatic segmentation was found to be of similar quality to that achieved by human annotators (Todorov *et al.*, 2020). A similar approach could provide useful for the processing of several larger LN HEV datasets especially given that image segmentation is the rate limiting step of this computational pipeline.

Chapter 5

5 Results: 3-Dimensional Characterisation of Intra-tumoral High Endothelial Venule Networks

5.1 Introduction

The development of HEVs following Treg depletion in the MCA induced fibrosarcoma tumour model has been well described (Hindley *et al.*, 2012) and the main signalling pathway driving HEV formation (TNFR signalling) has also been previously elucidated (Colbeck *et al.*, 2017). However, little is known about the spatial distribution and structural organization of intra-tumoral HEV networks and how these compare to SLO such as LNs since only a 2D characterisation has so far been reported. Tumours vasculature is well recognized as being heterogenous (Nagy *et al.*, 2010; Manning *et al.*, 2013) and the average HEV area (normalised to absolute HEV number) following Treg depletion has also been shown to vary greatly (from 50 μm^2 to 450 μm^2 and above) (Colbeck *et al.*, 2017). HEVs may therefore be asymmetrically distributed and depending on the choice of cutting plane used this can result in a large variability of observable structures. Furthermore, the large size of fibrosarcomas means that several thousand 5 µm sections would need to be imaged by conventional LSCM in order to globally characterise HEV formation. Instead, the optimisation of *in-vivo* labelling, clearing and LSFM imaging protocols (Chapter 3) now allows for a whole tumour imaging approach that permits the complete characterization of HEV formation in whole fibrosarcomas.

Several studies have explored the use of HEV inducing agents in an effort to enhance lymphocyte infiltration, induce vessel normalization as well as to improve responses to checkpoint therapies all in an effort to reduce the tumour growth burden (Johansson-Percival *et al.*, 2017; He *et al.*, 2018, 2020). Importantly, in the MCA model, intratumoral HEV quantity was found to significantly correlate with both the extent of T cell infiltration and the degree of tumour control (Colbeck *et al.*, 2017). This provides a clear rationale for augmenting intra-tumoral HEVs in fibrosarcomas in order to enhance T cell

infiltration and further improve control of tumour growth. Previous 2D assessments of Treg depleted fibrosarcomas revealed no apparent distribution of HEV formation in the tumour mass (Colbeck *et al.*, 2017). 2D assessments are not sufficient to globally examine HEV distribution due to limited sampling. A global imaging approach using LSFM is warranted for confirming this pattern of distribution and is also ideally suited for characterizing any changes to HEV density, structural re-organization and distribution following HEV network expansion.

To examine whether HEV networks can be expanded, the impact of LTβR agonist administration as well as anti-IL-27 antibody treatment was examined by LSFM imaging and the effect on tumour growth rate was assessed. Signalling through the LTβR pathway has been implicated in the early development of SLOs (van de Pavert and Mebius, 2014) and importantly in the formation and maintenance of HEVs (Drayton *et al.*, 2004; Onder *et al.*, 2013). However, this pathway has also been shown to be involved in the development of HEV containing TLS at sites of chronic inflammation (Luther *et al.*, 2000; Gatumu *et al.*, 2009; Fava *et al.*, 2011) as well as the development of HEVs in cancer (Schrama *et al.*, 2001). Furthermore, human breast tumours with a high density of HEVs were also shown to have a high expression of LTβ which suggests that LTβR signalling is involved in intra-tumoral HEV formation (Martinet *et al.*, 2013). The targeted tumour delivery of LIGHT (which can signal through LTβR) also suggests that the activation of this signalling pathway may lead to the induction of intratumoral HEVs (Johansson-Percival *et al.*, 2017; He *et al.*, 2018, 2020). Interestingly, the use of an agonist anti-LTβR monoclonal antibody (CBE11) was previously found to result in increased lymphocyte infiltration and control of tumour growth in mice bearing colorectal carcinoma xenografts (Lukashev *et al.*, 2006).

IL-27 is a 2-chain cytokine composed of EBI3 and IL-27p28 subunits and acts through a heterodimer receptor consisting of IL-27Rα (WSX1) and gp130 chains which in turn signal predominantly through STAT 1 and STAT3 (Trinchieri, Pflanz and Kastelein, 2003). IL-27 is also a member of the IL-12 family; a family of dimer cytokines which may share chain components in both cytokines and receptor chains including EBI3 and gp130 (Trinchieri, Pflanz and Kastelein,

2003). IL-27 is considered a pleiotropic cytokine as it has been found to have several immune enhancing and immune regulatory functions (as discussed by Fabbi, Carbotti and Ferrini, 2017; Kourko *et al.*, 2019). IL-27 has also been shown to negatively regulate the development of ectopic lymphoid structures (ELS) in both experimental and clinical rheumatoid arthritis (RA) (Jones *et al.*, 2015). In this context, ELS were characterized by both simple T and B cell aggregates as well as more highly organized structures comprising of follicular DC (fDC) networks resembling germinal centres (GCs) (Jones *et al.*, 2015). ELS^+ RA patients were found to have increased expression of Th17/Tfh signatures (IL-17 and IL-21 transcripts) and significantly reduced IL-27 expression as compared to ELS^- patients (Jones *et al.*, 2015). Indeed, IL-27 is known to inhibit the expansion of IL-17 secreting Th17 cells (Stumhofer *et al.*, 2006) which have been implicated in supporting ELS formation and GC reactions (Peters *et al.*, 2011). $IL27ra^{-/-}$ mice developed more severe arthritis characterised by ELS formation, and higher transcripts for Th17 and Tfh cell markers (Jones *et al.*, 2015). Paradoxically, increased levels of IL-27 gene related transcripts were recently described in patients with ELS^+ Sjögren's Syndrome (SS) (Lucchesi *et al.*, 2020). However, IL-27 mediated suppression of IL-17 secretion was found to be severely impaired in these patients and associated with an aberrant IFN-γ release, suggesting defective immunoregulation by IL-27 (Lucchesi *et al.*, 2020). Importantly, in experimental sialadenitis, $IL27ra^{-/-}$ mice had abundant and larger ELS, with higher transcripts for LTβ and chemokines involved in ELS formation (including *Cxcl13* and *Ccl19*) (Lucchesi *et al.*, 2020). Expansion of ELS in $IL27ra^{-/-}$ mice was found to be mediated by IL-17 as antibody blockade of this cytokine reversed excessive GC responses and restored the cellular composition of the ELS in salivary glands (Lucchesi *et al.*, 2020). Interestingly, previous microarray transcriptional profiling of $Treg^-HEV^{hi}$ tumours (Colbeck *et al.*, 2017) revealed upregulated transcripts for IL-27 and IL-27ra. Given that IL-27 is a negative regulator of ELS formation and that heightened expression of lymphoneogenic cytokines (such as LTα and LTβ) were measured in $IL27ra^{-/-}$ mice (Jones *et al.*, 2015; Lucchesi *et al.*, 2020), the administration of anti-IL-27 antibodies as a means of augmenting HEV networks in the fibrosarcoma model was assessed.

This chapter describes the 3D characterization of HEV formation in whole fibrosarcomas following Treg depletion. The impact of LTβR agonist and anti-IL-

27 antibodies on HEV network distribution, density and tumour growth rate was also assessed. The LSFM imaging parameters that were used in this work permitted only for a qualitative characterisation of HEV density and distribution patterns. This is because the Z-resolution had to be compromised through the use of a thicker light sheet waist (25.27 μm) in order to allow for more reasonable imaging times (Chapter 2, Methods). In order to quantify whether changes to the HEV network take place and whether this is accompanied by increased T-cell infiltration following treatment with LTβR agonist and anti-IL-27 neutralizing antibodies, a conventional 2D staining and imaging approach was used as previously described (Hindley *et al.*, 2012; Colbeck *et al.*, 2017).

5.2 3D Characterisation of HEV formation in a whole Treg replete tumour

In this section the 3D distribution of pre-existing HEVs in a Treg replete tumour were examined by LSFM. Since Treg depletion has previously been found to be a prerequisite for HEV formation as assessed by 2D imaging (Hindley *et al.*, 2012), it was first important to confirm whether Treg depletion is indeed required for de novo formation of HEVs or whether pre-existing HEVs can be found in non-treated fibrosarcomas. In order to examine this, a Treg replete tumour was *in-vivo* labelled, cleared and imaged using the LaVision Ultramicroscope 2. The whole Treg replete tumour was mostly devoid of any $PNAd^+$ vessels as shown in Figure 5.1 A. However, by examining individual Z-slices it was clear that there was some PNAd specific staining present which was not detected on the autofluorescence channel (Figure 5.1 B, white arrowhead). Furthermore, the overlap of this signal with the lectin channel indicated that these were in fact blood vessels. This suggests that Treg replete tumours may present with low levels of $PNAd^+$ vessels. It is important to note however that the presence of such vessels could easily have been missed by conventional 2D imaging given that the diameter of this whole tumour was around 6 mm following BABB clearing. Furthermore, it is not uncommon for tumours to present with $PNAd^+$ vessels even in the absence of any therapeutic intervention. This has been shown to occur in several human tumours (Martinet *et al.*, 2011, 2012) as well as several murine tumour models including B16-OVA and OVA-expressing Lewis lung carcinoma tumours (Peske *et al.*, 2015). Therefore, Treg replete tumours may present with low levels of $PNAd^+$ vessels which may have previously been missed by

conventional 2D imaging. It would be of interest to determine whether PNAd$^+$ vessels are present in all or only a subset of Treg replete tumours. As described in detail previously in this thesis, depletion of Tregs results in easily detectable HEV in only a proportion of treated mice; it is possible therefore that this response arises only when PNAd (albeit at small amounts) is already present in the Treg-replete pre-treatment tumour. Presence of PNAd$^+$ blood vessels pre-treatment may be necessary to drive HEV formation following Treg depletion. Whilst LSFM can be used to address the former question, a method which allows for sequential imaging over the same vessel area within a tumour would have to be used to address the latter. An intra-vital imaging approach using surgically implanted window chambers onto solid tumours has previously been used to examine the motility and localization of adoptively transferred T cells in the same tumour lesion over the course of several days (Spranger *et al.*, 2017). This approach combined with *in-vivo* labelling and imaging of intra-tumoral HEVs prior to and following Treg depletion could be used to examine how HEV networks alter pre- and post-Treg depletion.

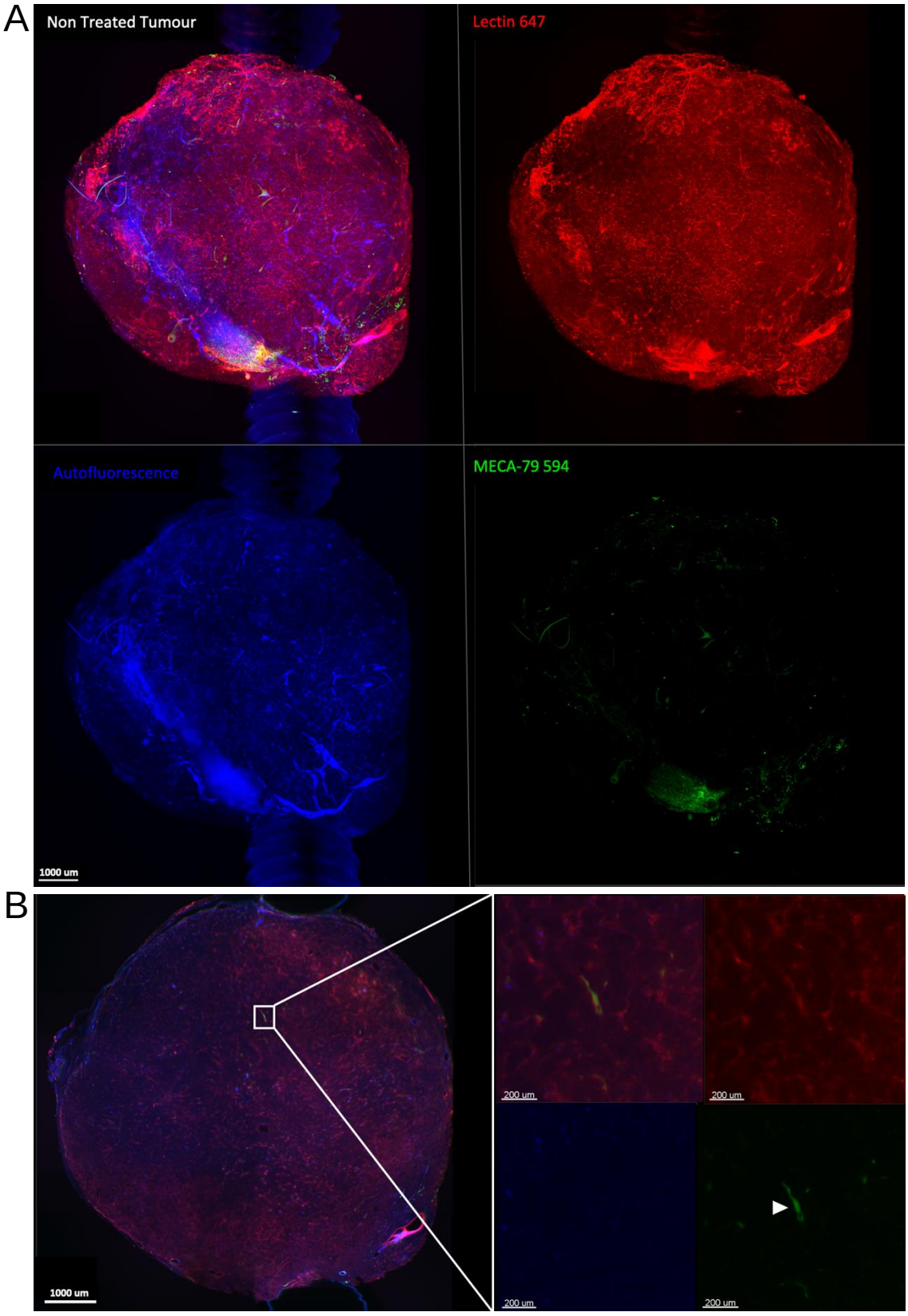

Figure 5.1 | LSFM imaging of a Treg replete fibrosarcoma.
(**A**) Maximum intensity projection (MIP) of a whole 6 mm Treg replete fibrosarcoma *in-vivo* labelled with 150 µg tomato lectin 647 and 50 µg MECA-79 594 and imaged with the LaVision Ultramicroscope 2. (**B**) Single Z-slice optical cross section reveals the presence of HEV specific staining (white arrowhead).

5.3 3D vessel architecture and HEV distribution of Treg depleted fibrosarcomas

The experimental aim of this section was to use SPIM and LSFM in order to characterise the 3D blood vessel architecture and HEV distribution of Treg depleted fibrosarcomas. Whilst the use of SPIM prevented MECA-79 specific staining from being distinguished from background autofluorescence, the high spatial resolution achieved allowed for a detailed insight into the overall blood vessel architecture. SPIM imaging of a Treg depleted fibrosarcoma tumour (imaged as three separate pieces) revealed a complex and dense blood vessel network consisting of large well separated vessels and smaller densely packed vessels (Figure 5.2 A-C). A clear separation between both vessel types was seen in the first two tumour pieces imaged by SPIM (Figure 5.2 A&B) but not in the last piece (Figure 5.2 C) suggesting intratumoral vessel heterogeneity in both vessel structure and distribution. Such intratumoral heterogeneity in vessel structure has previously been described in both murine and human urinary tumour tissue samples imaged by LSFM (Tanaka *et al.*, 2017). In this work both hypo- and hypervascular niches could be found within the same tumour piece.

Areas of continuous high signal intensity (as opposed to circular fluorescence emanating from pooled RBCs) were identified in all three tumour pieces suggesting the presence of $PNAd^+$ vessels (Figure 5.2 A-C, white arrowheads). Such vessels were not connected across the entire tumour which contrasts with the well-connected HEV network seen in SLOs such as LNs. This disconnected pattern with no apparent distribution is in line with what has previously been reported by 2D imaging (Colbeck *et al.*, 2017). Given that intra-tumoral HEV development has been shown to significantly correlate with T cell infiltration (Hindley *et al.*, 2012; Colbeck *et al.*, 2017), this suggests that well organized HEVs with distinct branching patterns (such as those seen in LNs) are not necessarily required for effective T cell infiltration. As a result, T cell trafficking kinetics via intra-tumoral HEVs may differ from that of HEVs found in SLOs. In LNs, lymphocytes have been shown to accumulate within HECs which form highly dynamic ‘pockets’ that can regulate the entry of lymphocytes into the parenchyma (Mionnet *et al.*, 2011). This rate of entry could be modulated depending upon the rate of immune cell egress from the LN (Mionnet *et al.*, 2011).

Such pockets have also been suggested to contribute to the cuboidal nature of HECs (Mionnet *et al.*, 2011). Previous LSCM analysis of Treg depleted fibrosarcomas revealed intra-tumoral $PNAd^+$ ECs do not have this cuboidal morphology (Colbeck *et al.*, 2017). As a result, T cell entry into the tumour may not be as well-regulated as it is in the LN. Furthermore, whether preferential sites along the HEV wall for T cell recruitment (termed exit ramps) exists in tumours as in the LN (Bajenoff *et al.*, 2006) is also currently not known. The functionality of intra-tumoral HEVs thereby remains to be determined by intravital 2-photon imaging as it is still possible that HEVs are only a by-product of an effective T cell response (Colbeck *et al.*, 2017).

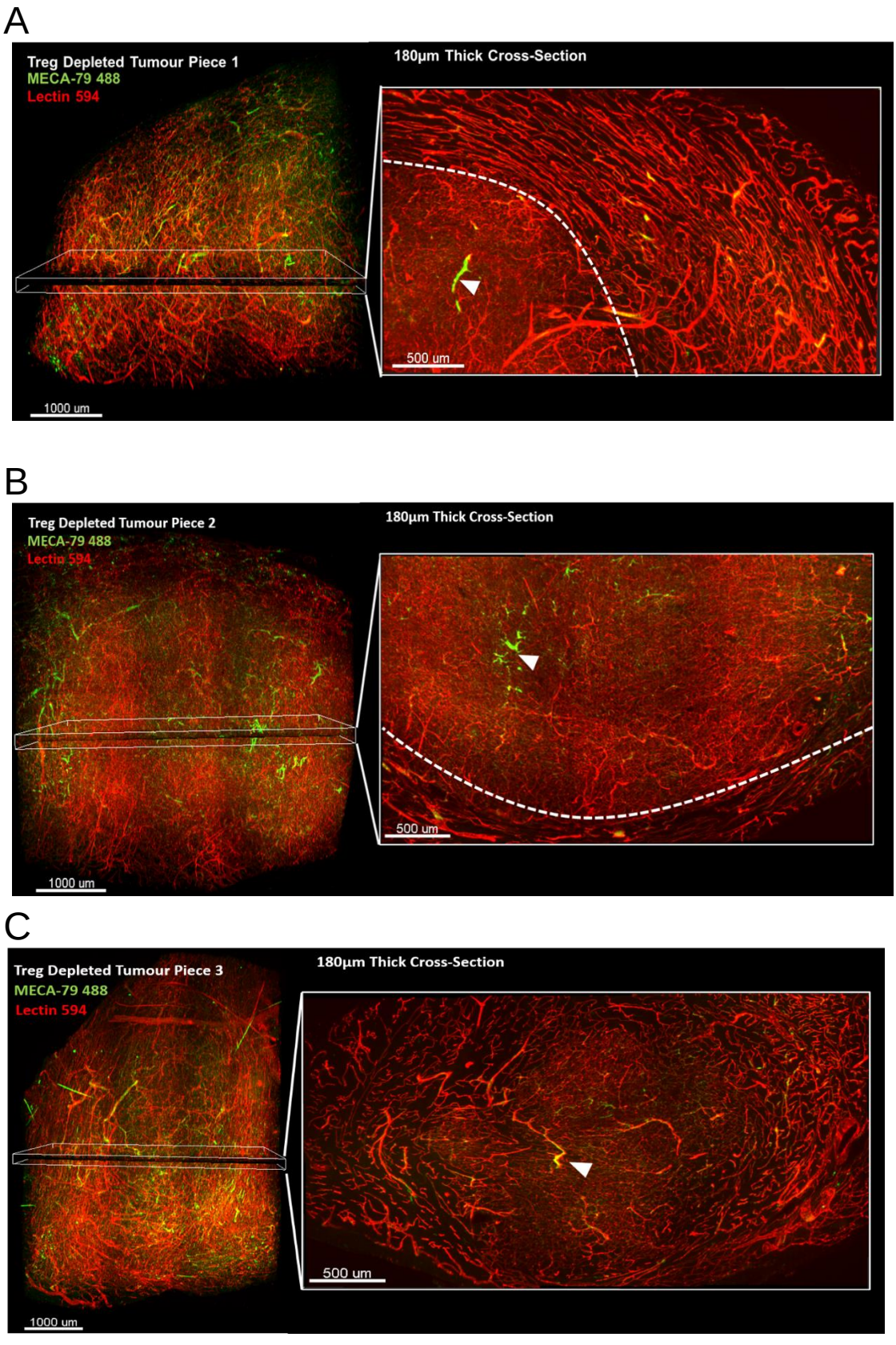

Figure 5.2 | 3D vessel architecture of a Treg depleted fibrosarcomca imaged with SPIM. (**A, B, C**) Maximum intensity projection of a Treg depleted MCA tumour labelled *in-vivo* with 150 µg tomato lectin 594 and 50 µg MECA-79 488 and imaged with SPIM. The tumour was cut into three pieces and imaged separately. Z-depth of optical cross sections is 180 µm. Dotted line shows separation between dense small vessels and large well separated vessels. White arrowheads denote putative HEV^{+} vessels identified on the basis of continuous fluorescence as opposed to circular fluorescence emanating from red blood cells.

In order to specifically examine the global distribution of intra-tumoral $PNAd^+$ vessels, two whole Treg depleted tumours were *in-vivo* labelled, cleared and imaged using the LaVision Ultramicroscope 2. As shown in Figure 5.3 B, HEVs could now specifically be distinguished from background autofluorescence. The development of HEVs following Treg depletion was previously found to result in significantly lower growth rates as compared to Treg replete and Treg depleted HEV^- tumours (Hindley *et al.*, 2012). In accordance with this finding, 3D imaging of a Treg depleted regressor tumour revealed the formation of extensive $PNAd^+$ vessels (Figure 5.3 B). Here, regressor status was based on the growth rate value (Figure 5.3 A) which was found to be comparable to growth rates of $Treg^-HEV^+$ tumours as previously described (Hindley *et al.*, 2012). A similar pattern of disconnected $PNAd^+$ vessels was identified which was again distinct from the organised network seen in LNs (Figure 5.3 B). In contrast to this, imaging of a non-regressor Treg depleted tumour revealed only a single branching vessel positive for MECA-79 staining (Figure 5.3 C, white arrow ahead). Clear differences in the extent of the HEV network between the regressor tumour and the Treg replete tumour further suggests that this is a valid approach to mapping HEV formation in whole tumours.

A

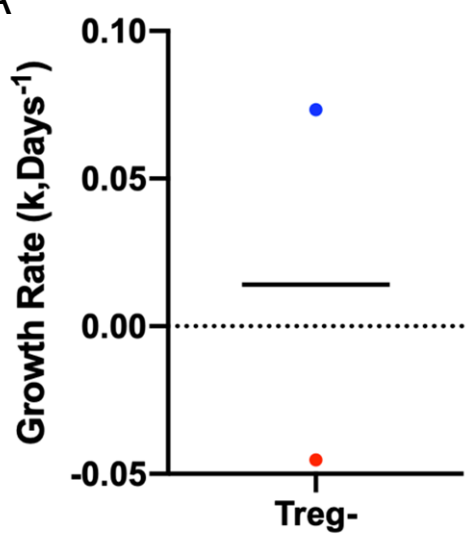
0.10
0.05
0.00
-0.05
Growth Rate (k,Days-1)
Treg-

B

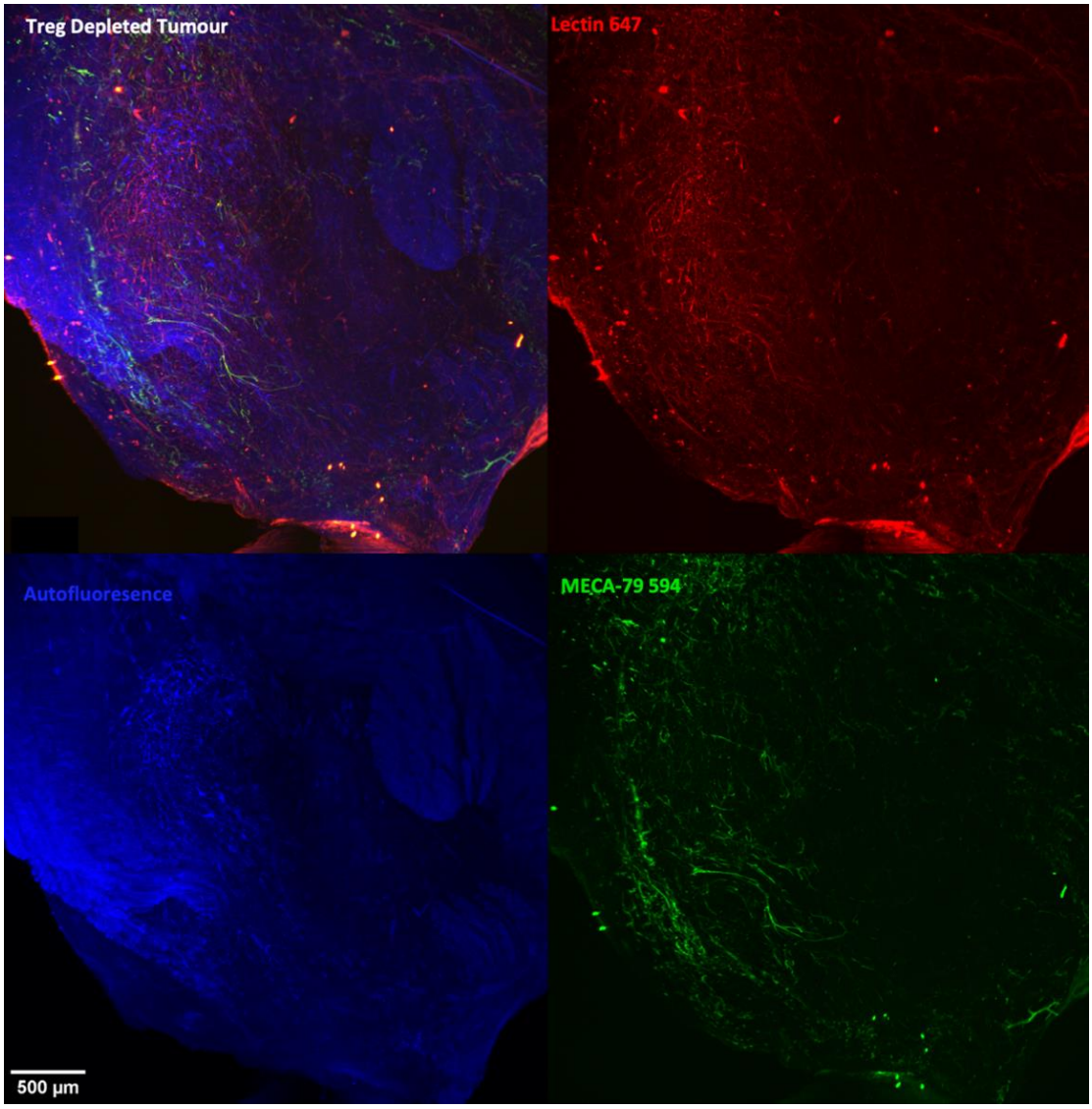
Treg Depleted Tumour
Lectin 647
Autofluoresence
MECA-79 594
500 µm

C

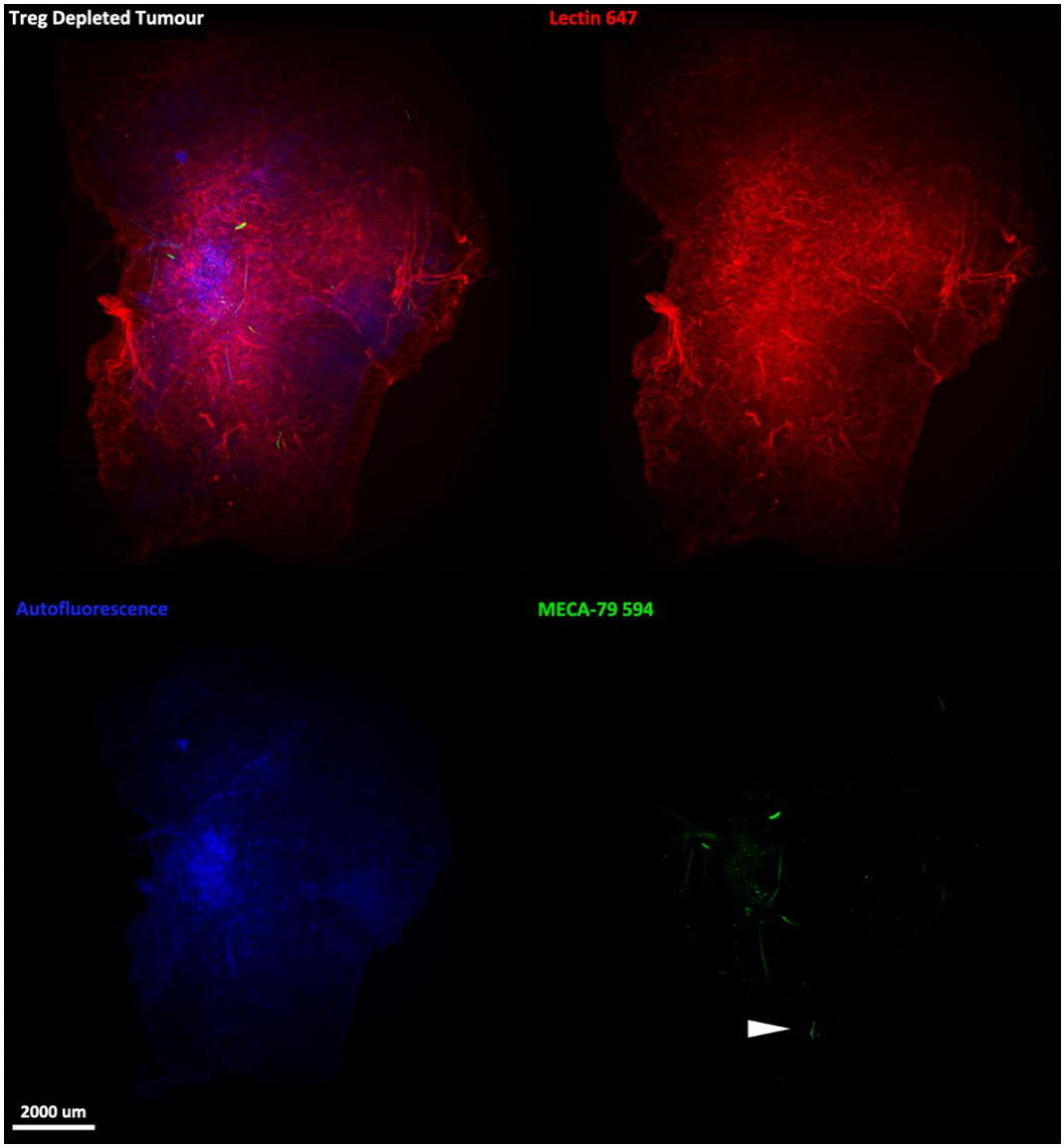

Figure 5.3 | LSFM imaging of Treg depleted fibrosarcomas.
(**A**) Growth rate values (k, per day) of a regressor (red) and non-regressor (blue) Treg depleted fibrosarcoma imaged by LSFM. Maximum intensity projections (MIPs) of regressor (**B**) and non-regressor (**C**) Treg depleted fibrosaromcas *in-vivo* labelled with 150 µg lectin 647 and 50 µg MECA-79 594 and imaged with the LaVision Ultramicroscope 2. White arrowhead in (**C**) denotes single branching vessel positive for HEV specific staining.

Closer inspection of the intra-tumoral HEV structure of the regressor tumour (Figure 5.4 B) revealed HEVs of varying lengths and structural organization. Dense clusters of $PNAd^+$ vessels could be identified as well as several $PNAd^+$ vessels that were well separated but did not form extensive networks. In addition, several isolated $PNAd^+$ vessels could also be identified (Figure 5.4 B, white arrowheads). Whilst a higher density of HEVs may suggest more extensive branching, it is important to note that the current Z-resolution does not permit for a comprehensive characterisation of HEV network connectivity. This is because vessels found connected in the XY plane may either be directly joined together (due to branching) or they may be an overlap of intersecting vessels found at separate Z-depths. In areas of dense $PNAd^+$ vessel clustering, it is not possible to distinguish between the two cases at the current Z-resolution. Nevertheless, examination of orthogonal views can offer insights into how aggregates of $PNAd^+$ vessels are distributed across the entire volume of the tumour and how this may change following HEV augmentation. Therefore, in order to examine the global distribution pattern of HEVs found in the regressor tumour, MIPs of orthogonal views were projected and examined (Figure 5.4 A). The majority of $PNAd^+$ vessels were localized to the outermost edges of the tumour with the centre of the tumour being largely devoid of any PNAd staining. This asymmetric distribution and varied density of $PNAd^+$ vessels reiterate the importance of taking a global imaging approach since depending upon which cutting plane had been chosen for 2D sectioning there would have been a great variation in observable structures. Future LSFM imaging with the use of a thinner light sheet will be required to determine the extent of intratumoral HEV network connectivity. Further to this, intra vital imaging could be used to ascertain whether a certain type of structural organization of intra-tumoral HEVs is more effective at T cell recruitment.

A

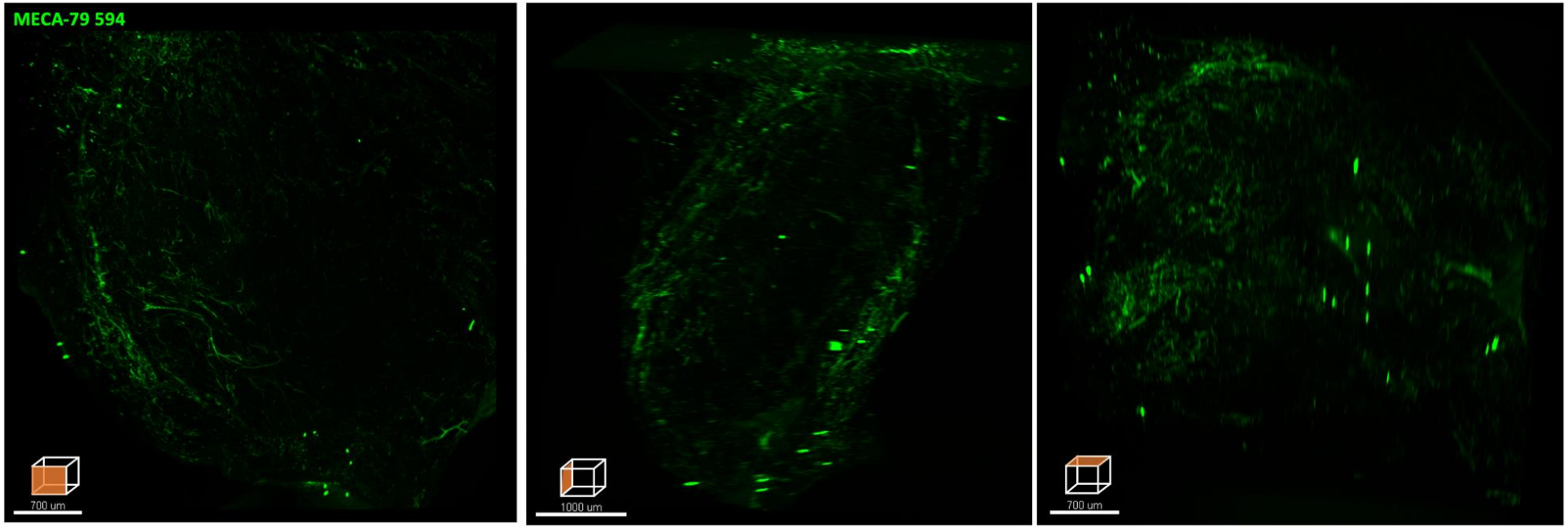

B

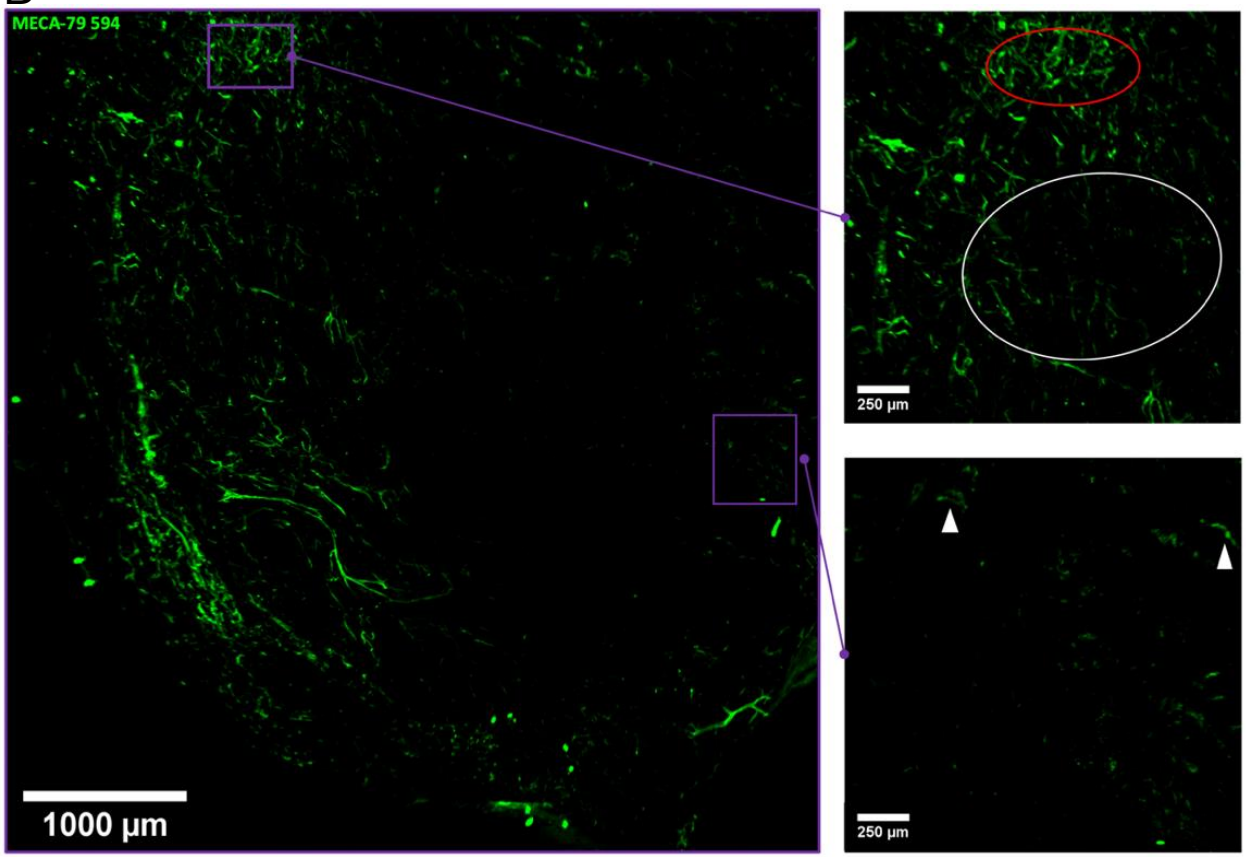

Figure 5.4 | Structural organization and global distribution of intra-tumoral HEVs in a Treg depleted fibrosarcoma.
(A) Maximum intensity projections (MIPs) of orthogonal views of a Treg depleted regressor tumour (same as in **Figure 5.3 B**) allow for the examination of the intra-tumoral HEV distribution. **(B)** MIPs of digitally zoomed XY view allows for a closer inspection of the structural organization of HEVs. Areas circled in red indicate dense PNAd$^+$ vessel clusters whose connectivity cannot be established at current Z-resolution. Areas circled in white indicate well separated PNAd$^+$ vessels that are not well connected. White arrowheads indicate isolated PNAd$^+$ vessels.

Whilst responders have previously been distinguished from non-responders by the presence of HEVs and a significantly higher number of TILs as compared to non-responders (Hindley *et al.*, 2012), the large size of fibrosarcomas precluded the use of whole mount staining techniques readily applicable to smaller organs such as LNs (Kumar *et al.*, 2010) for whole tumour lymphocyte labelling. Instead, the use of fluorescent reporter mice such as CD2–DsRed mice (Veiga-Fernandes *et al.*, 2007) could be used in the future to confirm this association and to further examine the distribution of T cells in relation to HEV formation. This is particularly important as it would not only confirm the association between the extent of HEV formation and extent of T cell infiltration but would also allow for determining whether HEV augmentation (following LTβR agonist and/or anti-IL-27 administration) results in a larger influx of T cells in comparison to Treg depletion alone. However, a clearing protocol other than BABB which is known to rapidly quench fluorescent protein signal (Erturk *et al.*, 2012; Abe *et al.*, 2016) will have to be used. Several fluorescent protein compatible clearing techniques have been described including organic solvent based techniques such as ECi (Klingberg *et al.*, 2017) and uDISCO clearing (Pan *et al.*, 2016) both of which are compatible with the LaVision Ultramicroscope 2.

5.4 3D examination of intra-tumoral HEV development following LTβR agonist administration and anti-IL-27 antibodies

In this section, the impact of LTβR agonist and anti-IL-27 antibody administration (either as single agents or in combination with Treg depletion) on global intra-tumoral HEV formation was assessed by LSFM. Changes to the global distribution pattern and any changes to HEV density were qualitatively examined. As shown in Figure 5.5 and Figure 5.7 A-C, combinatory DT and LTβR agonist treatment led to the formation of several dense clusters of $PNAd^+$ vessels in both tumours examined by LSFM. Such clusters were much more extensive in comparison to the Treg depleted regressor and examination of orthogonal views revealed that they were not restricted to the outermost edges but instead occupied much larger volumes which extended into deeper parts of the tumour (Figure 5.6 A and Figure 5.8 A-C). The overall density and volumetric size of such clusters was also heterogenous. Differences in density and structural organization of intratumoral HEVs could also be seen by closer inspection of

digitally zoomed XY views of the MECA-79 channel (Figure 5.6 B and Figure 5.9 A-C). A whole LTβR agonist Ab-treated and Treg depleted tumour had a structural organization of HEVs consisting of dense clusters of $PNAd^+$ vessels (whose connectivity cannot be established at the current Z-resolution) as well as smaller aggregates of $PNAd^+$ vessels that were not well connected and that did not form extensive branching networks (Figure 5.6 B). There were also parts of the tumour where several isolated $PNAd^+$ vessels could also be identified (Figure 5.6 B, white arrowheads). This pattern, whilst similar to that observed in tumours only depleted of Tregs (Figure 5.4 B), implies that addition of the LTβR agonist antibody promotes more extensive organisation of the HEV network. Two separate pieces of the same LTβR agonist antibody treated and Treg depleted tumour also had a similar structural organization (Figures 5.9 A&C). In the third piece however, there were extensive $PNAd^+$ clusters of varying density (Figure 5.9 B) that occupied almost the entire volume of the tumour piece (Figure 5.8 B, orthogonal views). isolated $PNAd^+$ vessels could also be found in this tumour piece as well (Figure 5.9 B, white arrowheads). It would be of interest to determine whether dense clusters of $PNAd^+$ vessels are the result of a well-connected branching network, several branching networks or a collection of vessels with few branching numbers that are found in close proximity. As mentioned previously it is not possible to distinguish between these cases at the current Z-resolution. If differences in the extent of HEV network connectivity are found in future LSFM studies, then the functional significance of such structures could be examined directly by intra-vital imaging. Whether T-cells preferentially accumulate around certain types of HEVs also remains to be determined by LSFM imaging of tumours with fluorescently labelled T cells.

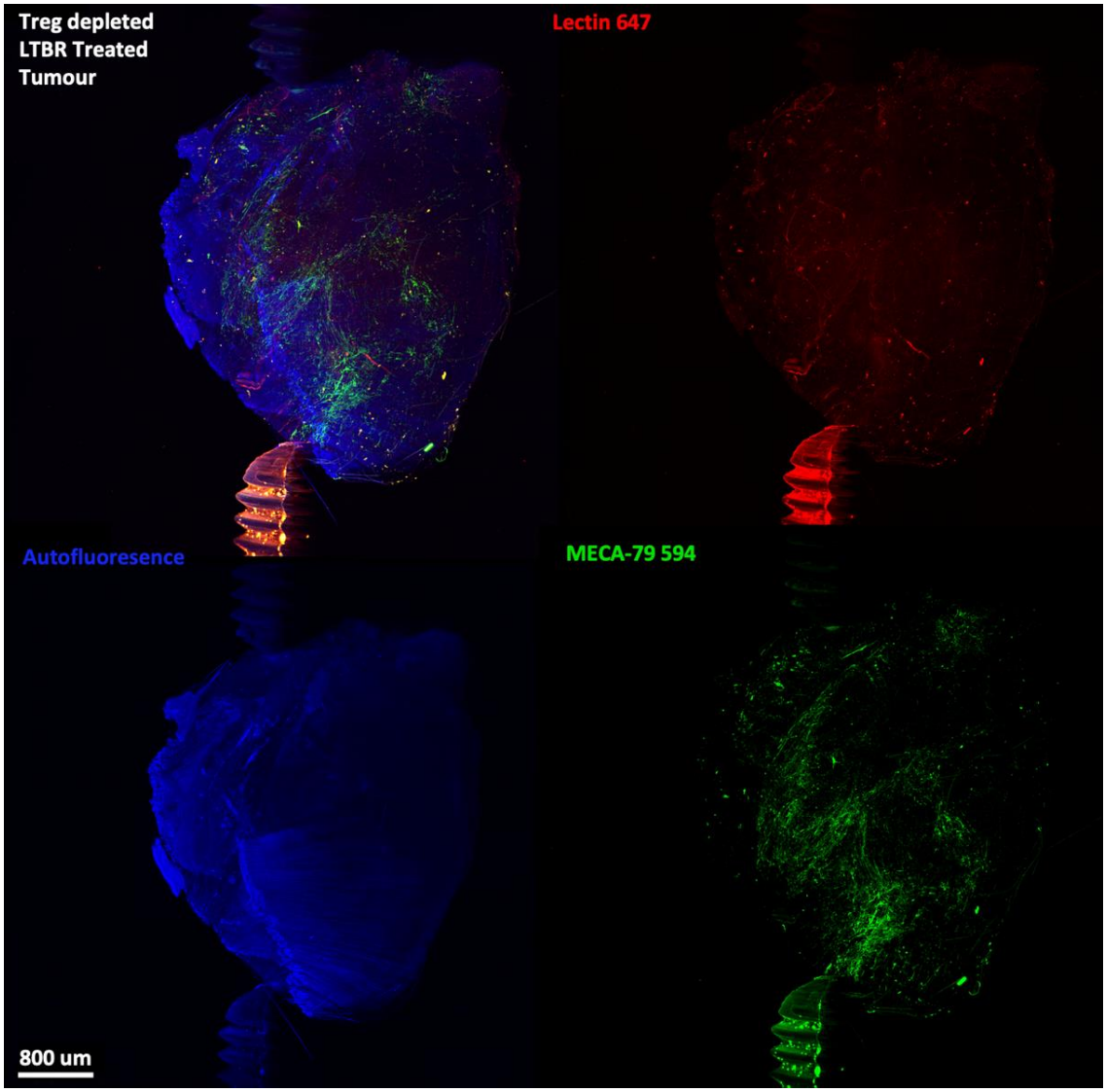

Figure 5.5 | LSFM imaging of a whole Treg depleted and LTβR agonist treated fibrosarcoma.
Maximum intensity projections (MIPs) of a Treg depleted and LTβR agonist treated fibrosarcoma labelled with 150 µg lectin 647 and 50 µg MECA-79 594 and imaged with the LaVision Ultramicroscope 2.

A

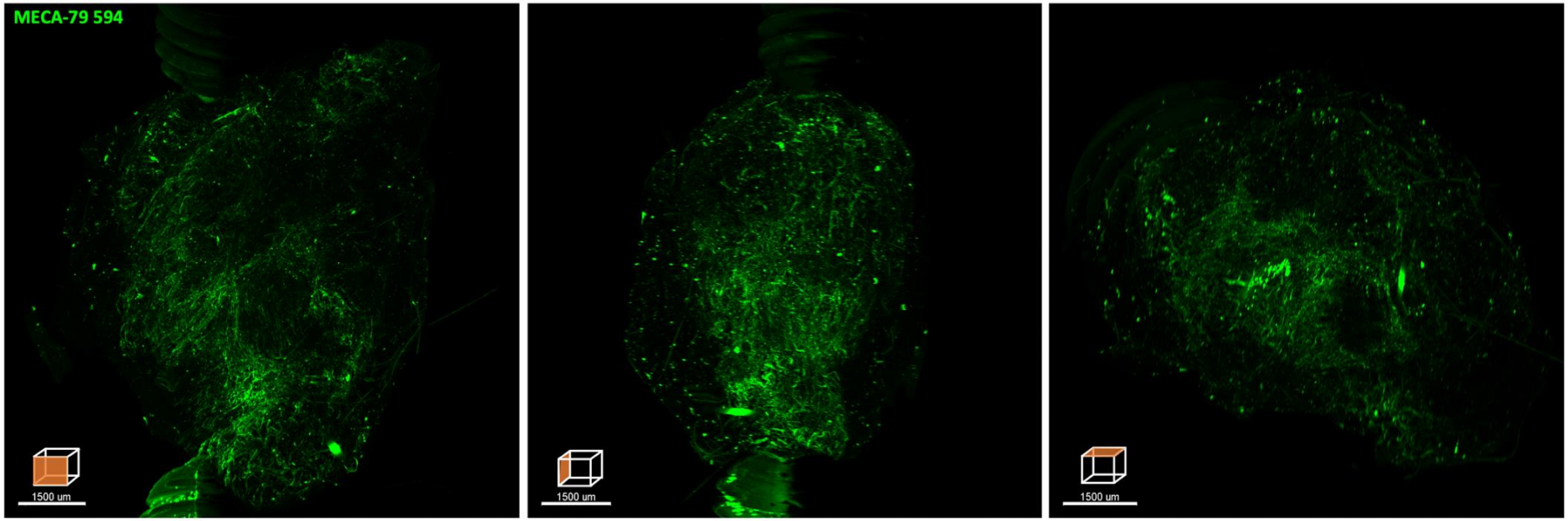

B

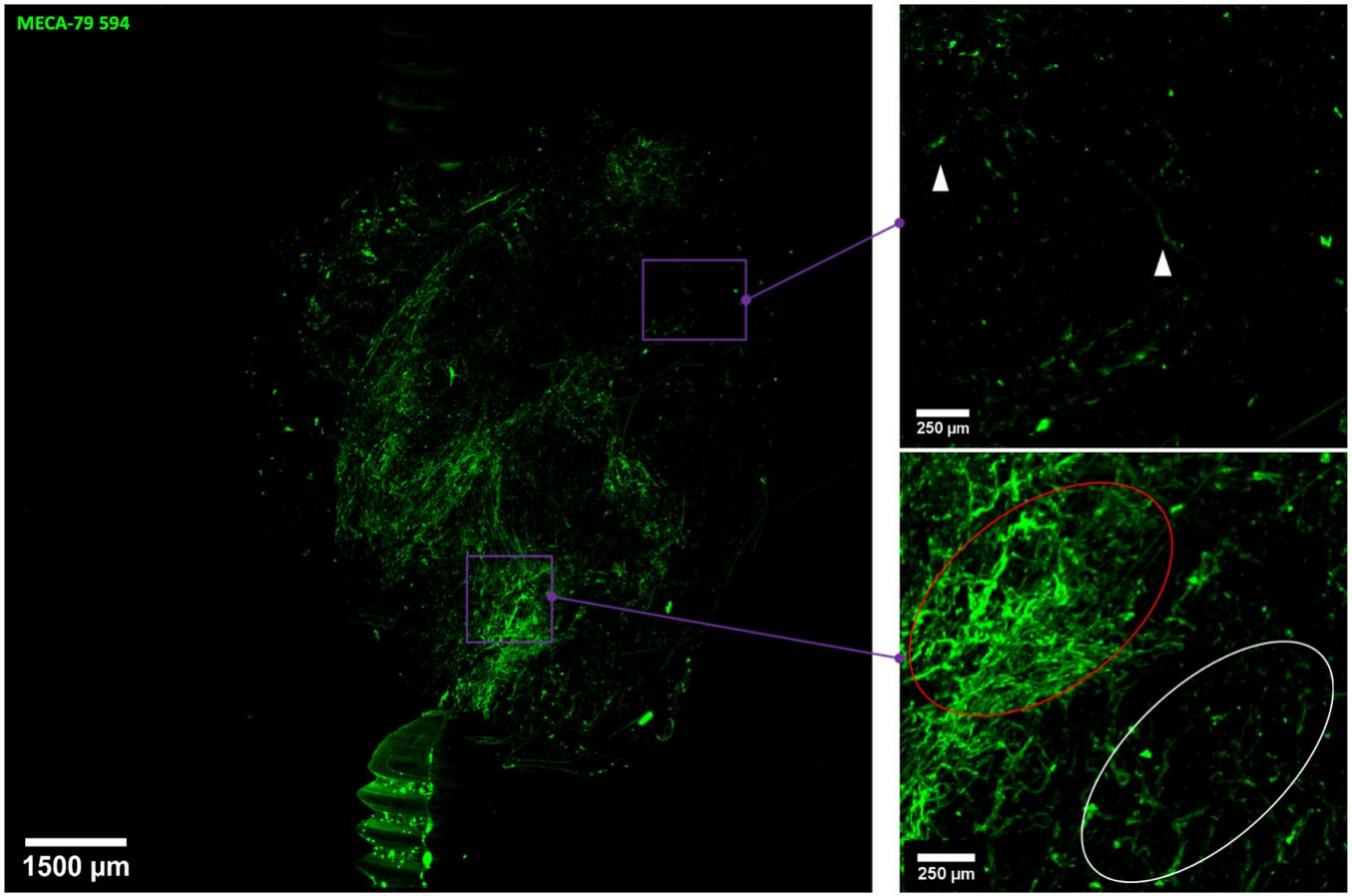

Figure 5.6 | Structural organization and global distribution of intra-tumoral HEVs in a Treg depleted and LTβR agonist treated fibrosarcoma.
(A) Maximum intensity projections (MIPs) of orthogonal views reveal the global distribution of intratumoral HEVs in a Treg depleted and LTβR agonist treated fibrosarcoma (same as in **Figure 5.5**). (**B**) MIPs of digitally zoomed XY view allows for a closer inspection of the structural organization of HEVs. Areas circled in red indicate dense PNAd$^+$ vessel clusters whose connectivity cannot be established at current Z-resolution. Areas circled in white indicate well separated PNAd$^+$ vessels that are not well connected. White arrowheads indicate isolated PNAd$^+$ vessels.

A

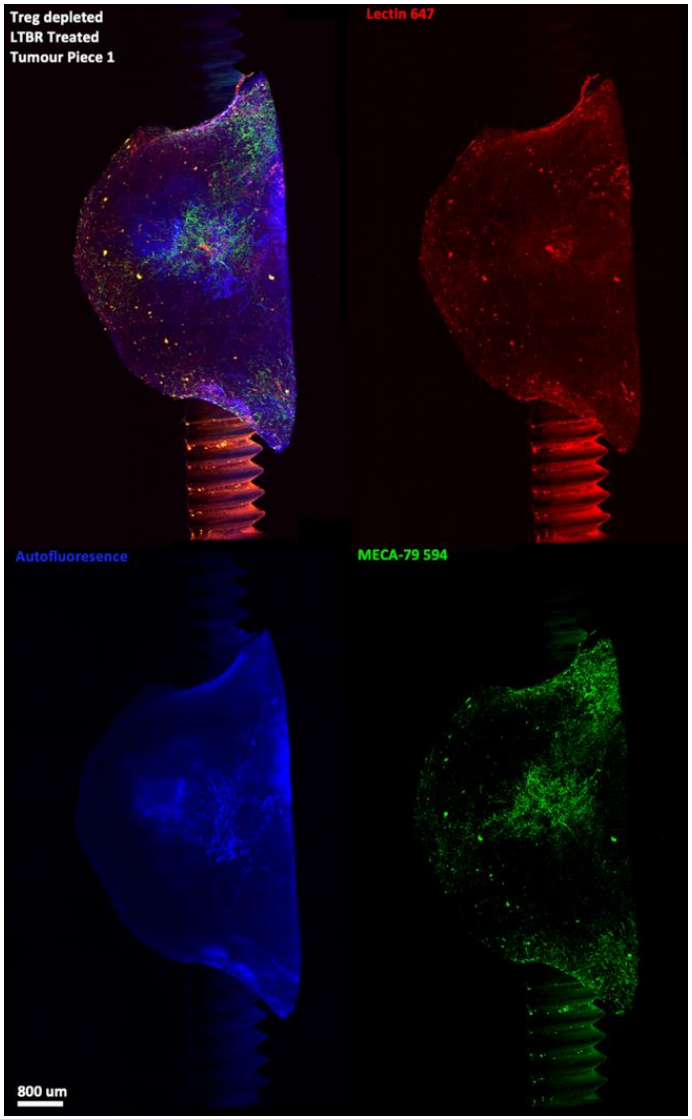
Treg depleted
LTBR Treated
Tumour Piece 1
Lectin 647
Autofluoresence
MECA-79 594
800 um

B

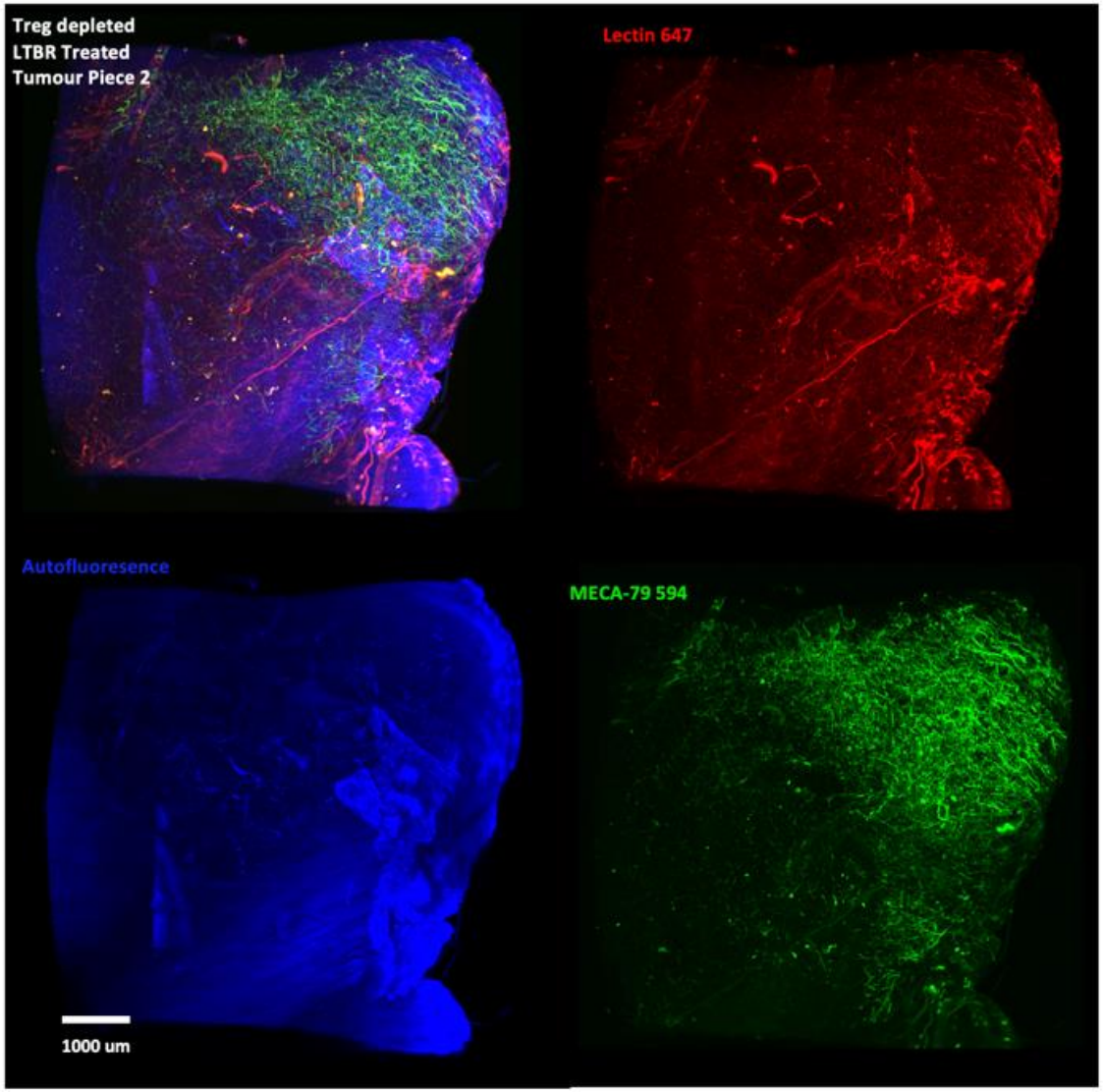
Treg depleted
LTBR Treated
Tumour Piece 2
Lectin 647
Autofluoresence
MECA-79 594
1000 um

C

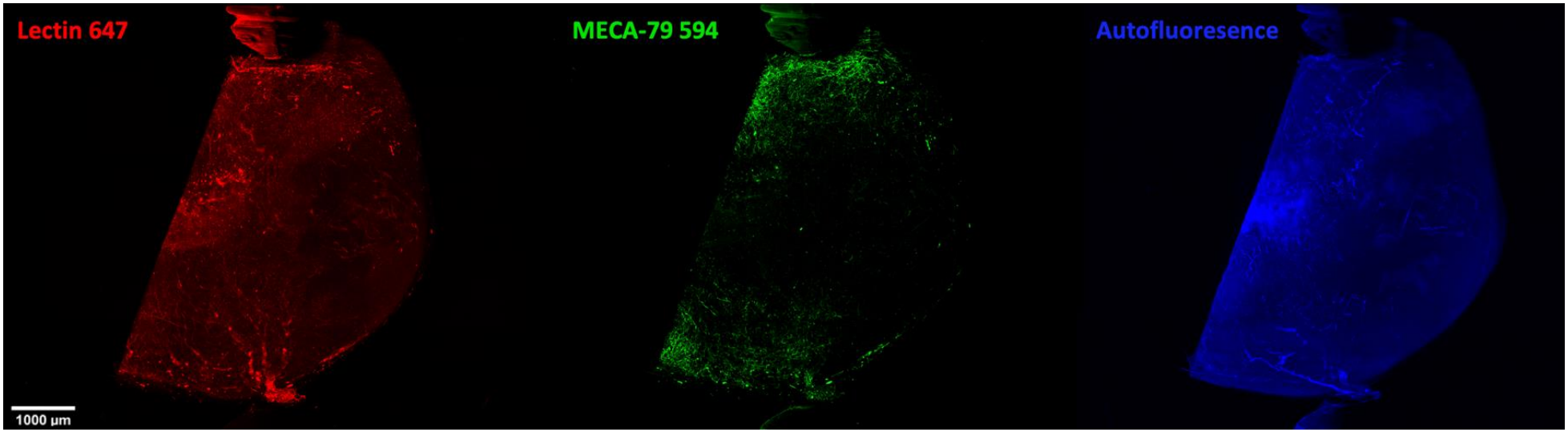

Figure 5.7 | LSFM imaging of a Treg depleted and LTβR agonist treated fibrosarcoma.
Maximum intensity projections (MIPs) of a Treg depleted and LTβR agonist treated fibrosarcoma labelled with 150 µg tomato lectin 647 and 50 µg MECA79 594 and imaged with the LaVision Ultramicroscope 2. Tumour was cut into three separate pieces (**A**,**B**,**C**) which were imaged separately.

A

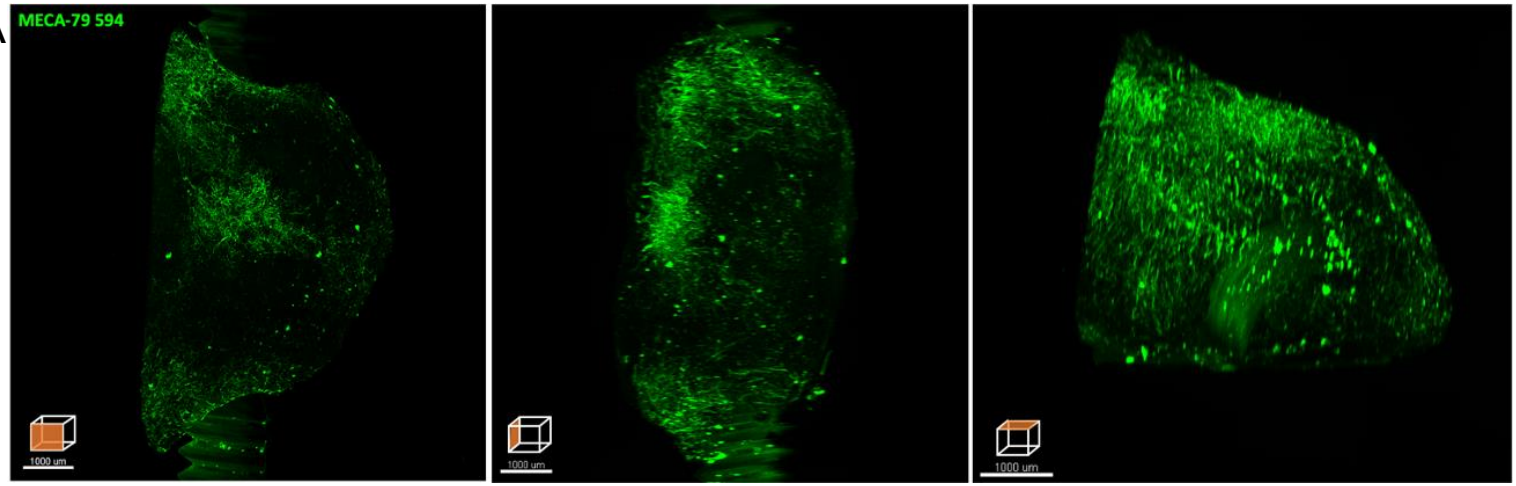
MECA-79 594
1000 um
1000 um
1000 um

B

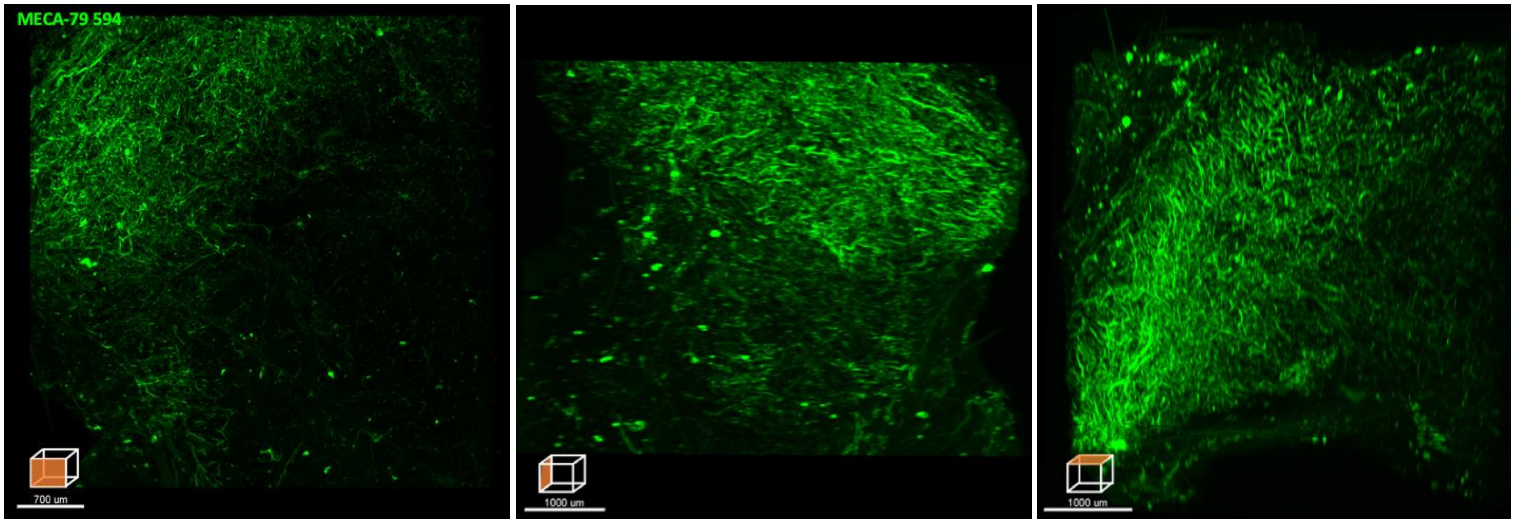
MECA-79 594
700 um
1000 um
1000 um

C

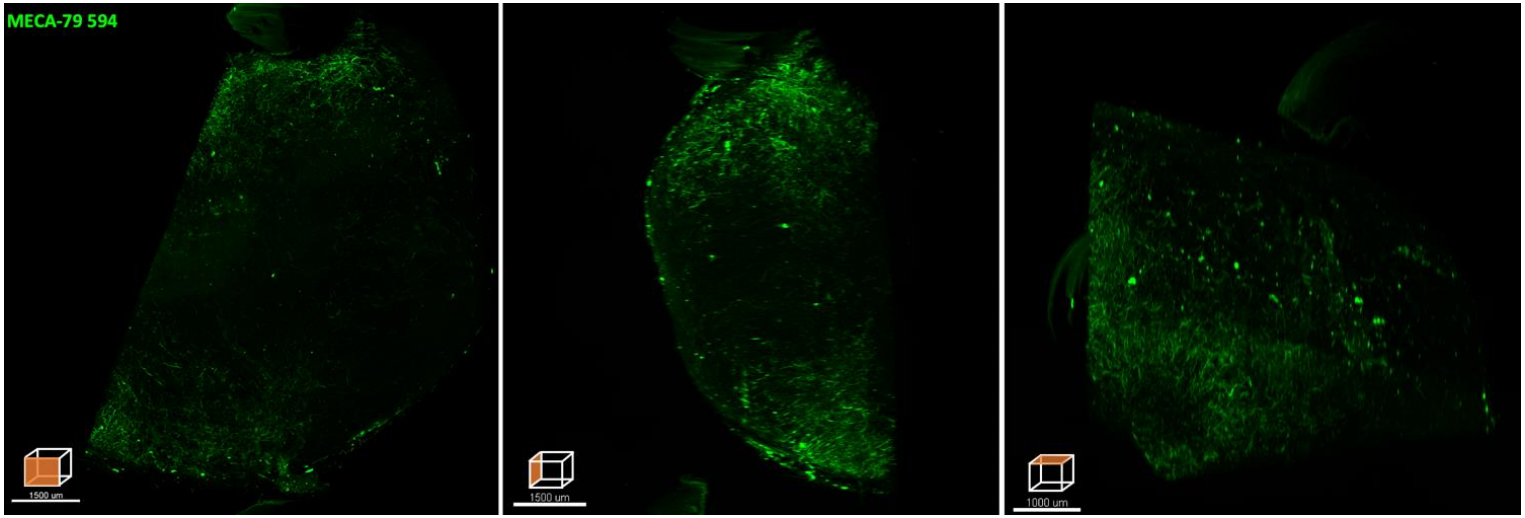

Figure 5.8 | Global distribution of intra-tumoral HEVs in a Treg depleted and LTβR agonist treated fibrosarcoma.
Maximum intensity projections (MIPs) of orthogonal views of a Treg depleted and LTβR agonist tumour (same as in **Figure 5.7**) cut and imaged in three separate pieces (**A**,**B**,**C**) allows for the examination of the intra-tumoral HEV distribution.

A

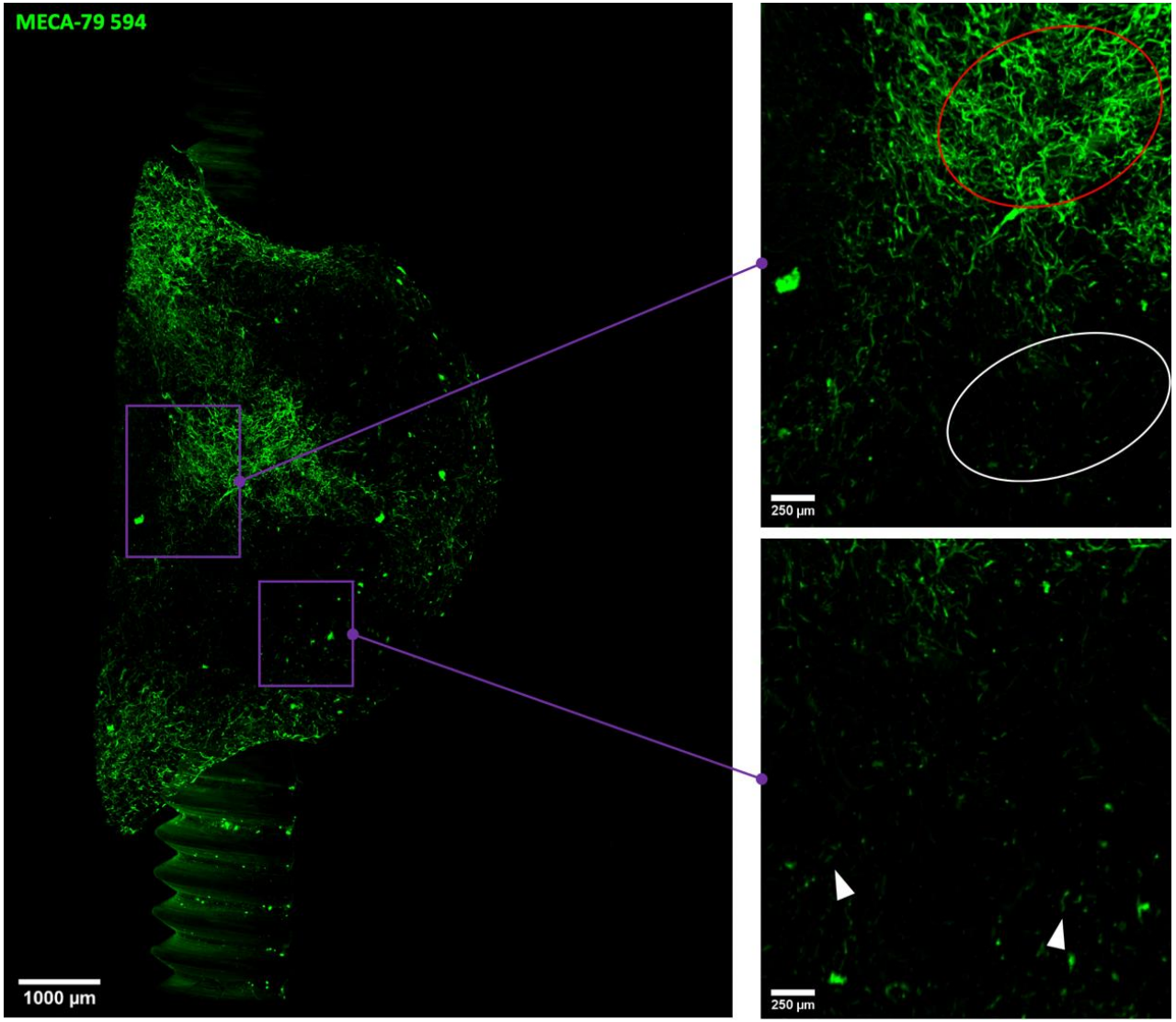

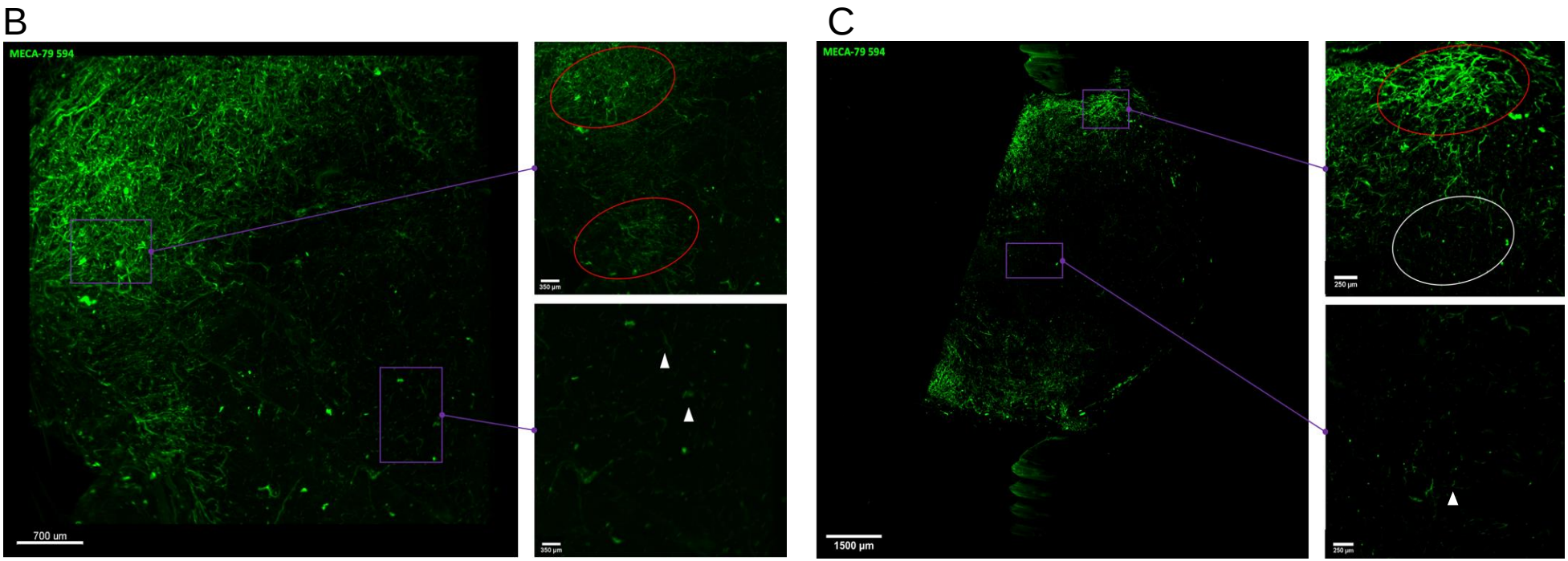

Figure 5.9 | Structural organization of intra-tumoral HEVs in a Treg depleted and LTβR agonist treated fibrosarcoma.
Maximum intensity projections (MIPs) of digitally zoomed XY views of three separate pieces (**A**,**B**,**C**) of a Treg depleted and LTβR treated fibrosarcoma (same as in **Figure 5.7**) allows for a closer inspection of the structural organization of HEVs. Areas circled in red indicate dense PNAd$^+$ vessel clusters whose connectivity cannot be established at current Z-resolution. Areas circled in white indicate well separated PNAd$^+$ vessels that are not well connected. White arrowheads indicate isolated PNAd$^+$ vessels.

Combinatory treatment with neutralizing anti-IL-27 antibodies and Treg depletion resulted in the formation of several dense clusters of PNAd$^+$ vessels (Figure 5.10). Examination of orthogonal MIPs (Figure 5.11 A), revealed that these clusters occupied almost the entire volume of the tumour which suggests extensive intra-tumoral HEV expansion. This is in contrast to LTβR agonist and Treg depleted tumours where large volumes of the tumour were still largely devoid of PNAd$^+$ staining (Figure 5.6 A and Figure 5.8 A&C). Closer examination of the HEV network also revealed several smaller aggregates of PNAd$^+$ vessels that were not well connected (Figure 5.11 B). Isolated PNAd$^+$ vessels could also be found (Figure 5.11 B, white arrowheads). As with LTβR agonist treated and Treg depleted tumours, it would also be of interest to determine the extent of network connectivity and whether this differs between the two treatment groups at a higher Z-resolution. LSFM imaging with a thinner light sheet waist can be used to address these questions in the future. 2-photon imaging is warranted for examining whether more organized branching structures lead to more effective recruitment of T cells. Complementary to this, LSFM imaging and quantification of intra tumoral T-cells will show whether augmented HEVs support a higher influx of T cells. It would also be of interest to determine whether these agents expand existing PNAd$^+$ vessels and/or whether they induce de novo HEV neogenesis. Several PNAd$^+$ vessels that were not directly connected could be identified in both treatment conditions which is suggestive of de novo HEV formation.

The future use of a thinner light sheet waist thickness (of 5 µm), would permit for a numerical characterisation of intra-tumoral HEV development using the optimised LSFM vessel tools. This would allow for a quantitative approach to mapping intra-tumoral HEVs. Further to this, individual vessel lengths and diameters could be measured, and overall network connectivity could be derived. Whether the proportion of vessels that are PNAd$^+$ is increased following HEV augmentation could also be determined and expressed as a percentage of the entire tumour blood vessel network as has previously been done for putative HEVs in a mesenteric LN (Kelch *et al.*, 2015). This approach would be useful for comparing the extent of HEV network expansion between different treatment groups. Insights into whether specific types of HEVs are associated with a larger influx of immune cells could be examined by computing spatial distances between T cells and specific types of HEVs (delineated for example on the basis

of branching number or relative density). A similar approach has previously been used to determine the spatial localization of DCs, which lack key factors for intranodal positioning, in relation to the nearest point in the HEV network (Mayer *et al.*, 2012).

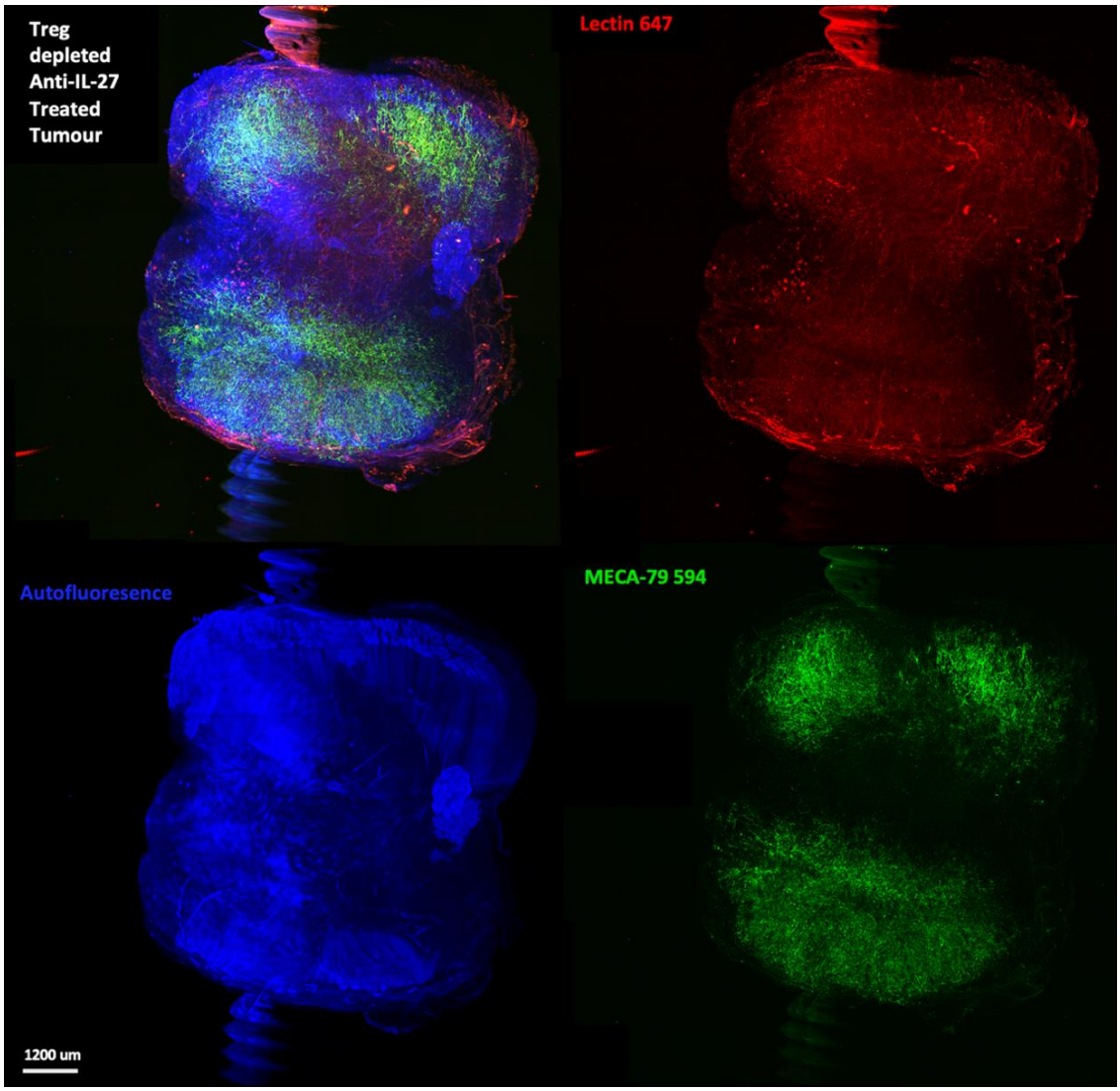

Figure 5.10 | LSFM imaging of a Treg depleted and anti-IL-27 treated fibrosarcoma. Maximum intensity projection (MIP) of a whole Treg depleted and anti-IL-27 antibody treated fibrosarcoma *in-vivo* labelled with 150 µg tomato lectin 647 and 50 µg MECA-79 594 and imaged with the LaVision Ultramicroscope 2.

A

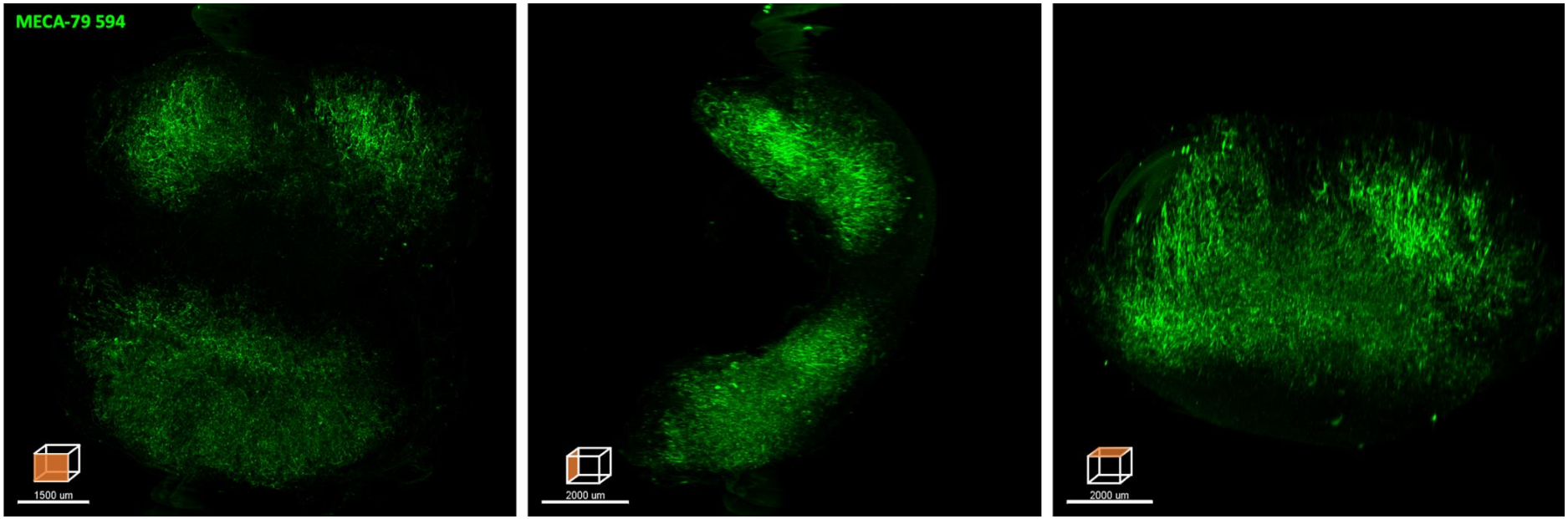

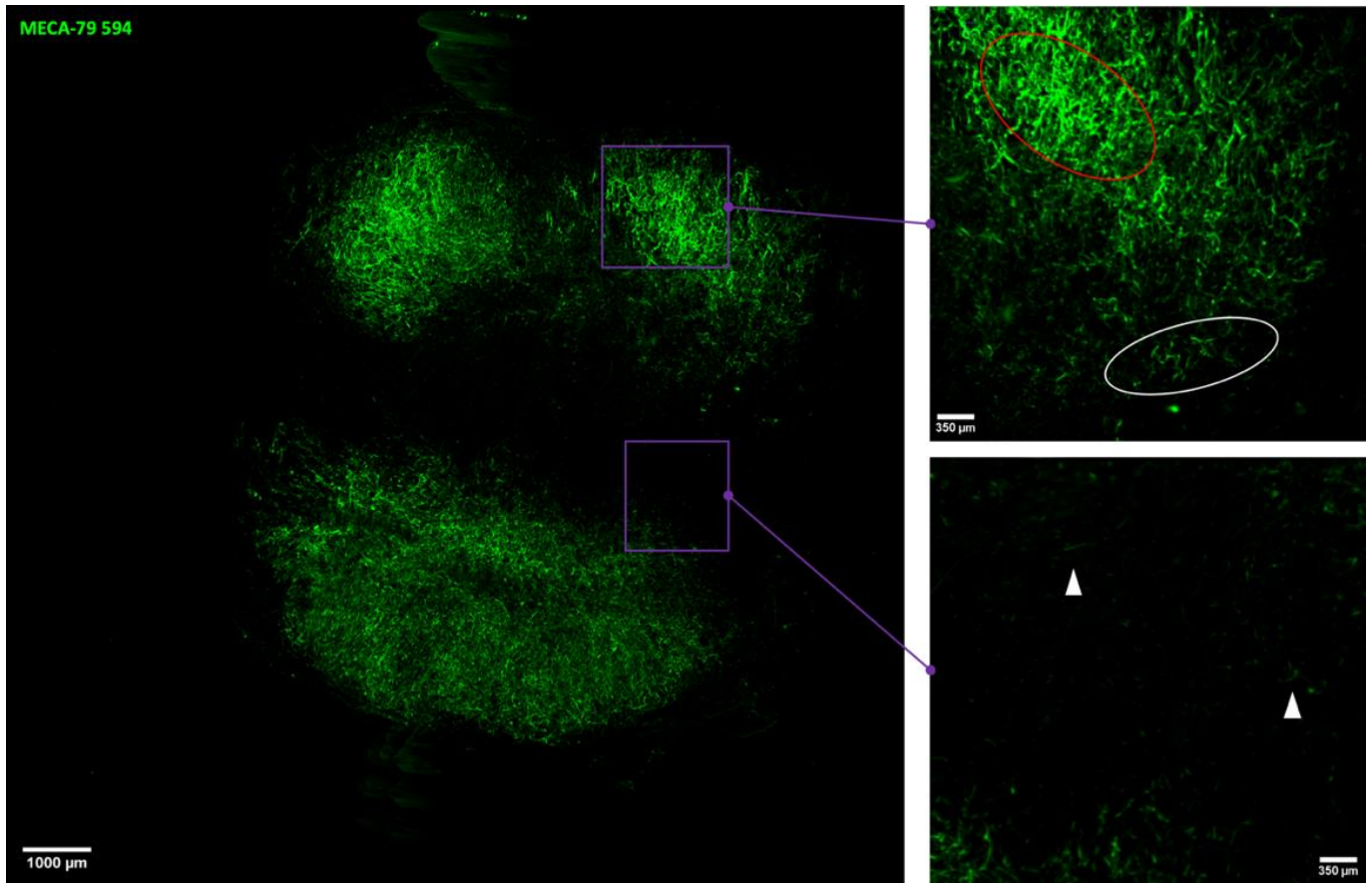

Figure 5.11 | Structural organization and global distribution of intra-tumoral HEVs in a Treg depleted and anti-IL-27 treated fibrosarcoma.
(**A**) Maximum intensity projections (MIPs) of orthogonal views of a Treg depleted and anti-IL-27 treated fibrosarcoma (same as in **Figure 5.10**) reveal the global distribution of intratumoral HEVs. (**B**) MIPs of digitally zoomed XY view allow for a closer inspection of the structural organization of HEVs. Areas circled in red indicate dense PNAd$^+$ vessel clusters whose connectivity cannot be established at current Z-resolution. Areas circled in white indicate well separated PNAd$^+$ vessels that are not well connected. White arrowheads indicate isolated PNAd$^+$ vessels.

5.5 2D examination of intra-tumoral HEV formation following LTβR agonist administration and anti-IL-27 antibody treatment

This section describes the use of conventional staining and 2D imaging techniques to assess the impact of LTβR agonist and anti-IL-27 antibody treatment on HEV formation. In order to quantify changes to the HEV network, a method previously developed and described by Dr Emily Colbeck was used (Colbeck, 2015). This approach allowed for the extraction of several numerical parameters relating to HEV formation including HEV density, average HEV area and total HEV area which were then compared across the different treatment groups. As shown in Figure 5.12 A&C administration of LTβR agonist to Treg replete mice resulted in the formation of $PNAd^+$ vessels in 7/8 treated mice which is consistent with previous reports (Colbeck *et al.*, 2017). Administration of LTβR agonist to Treg depleted mice also resulted in $PNAd^+$ vessel formation in 7/7 mice that were treated (Figure 5.12 B&C). Whilst there was a trend for increased total HEV area (Figure 5.12 C) in this group compared to Treg depletion alone (ns P = >0.9999) and in Treg replete mice treated with LTβR agonist (ns P = 0.1224), this did not reach statistical significance. There were no statistically significant differences in HEV density between the three treatment groups as shown in Figure 5.12 D. However, in comparison to Treg depleted mice, Treg replete (**P = 0.0052) and Treg depleted (*** P = 0.0009) mice treated with LTβR agonist had significantly larger average HEV areas (Figure 5.12 E). Taken together, this suggests that LTβR agonist treatment alone or in combination with Treg depletion leads to an increase in average HEV area but not to an increase in HEV density.

A

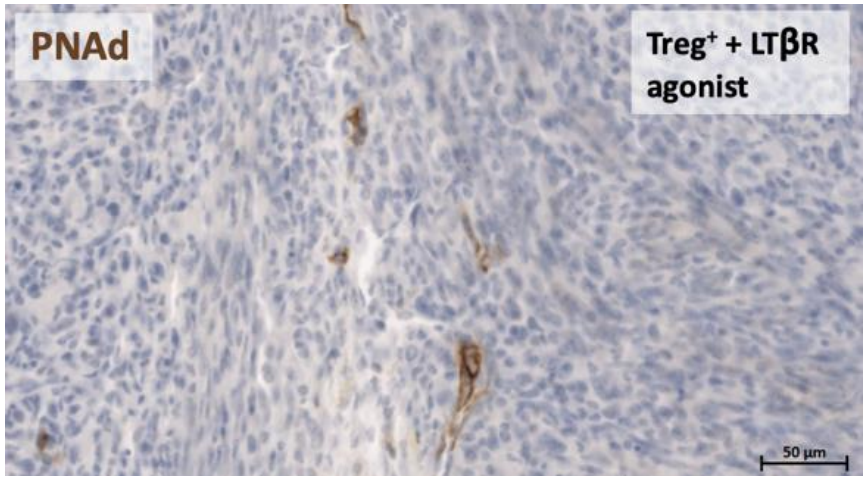
PNAd
Treg+ + LTβR agonist
50 µm

B

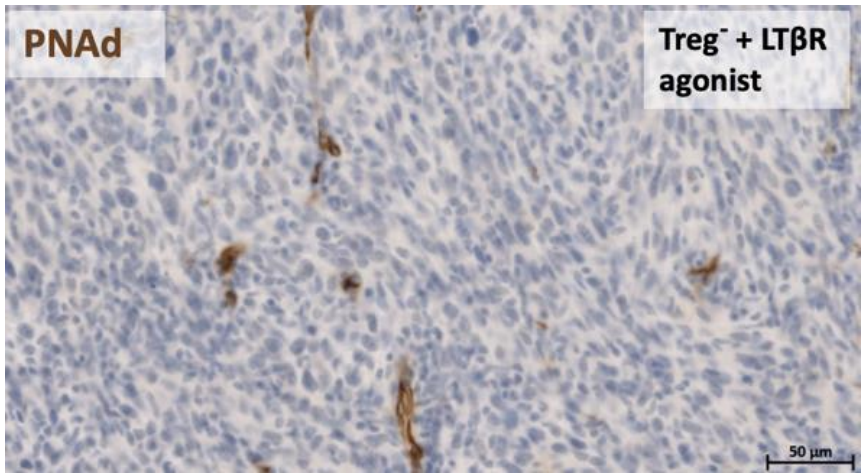
PNAd
Treg- + LTβR agonist
50 µm

C

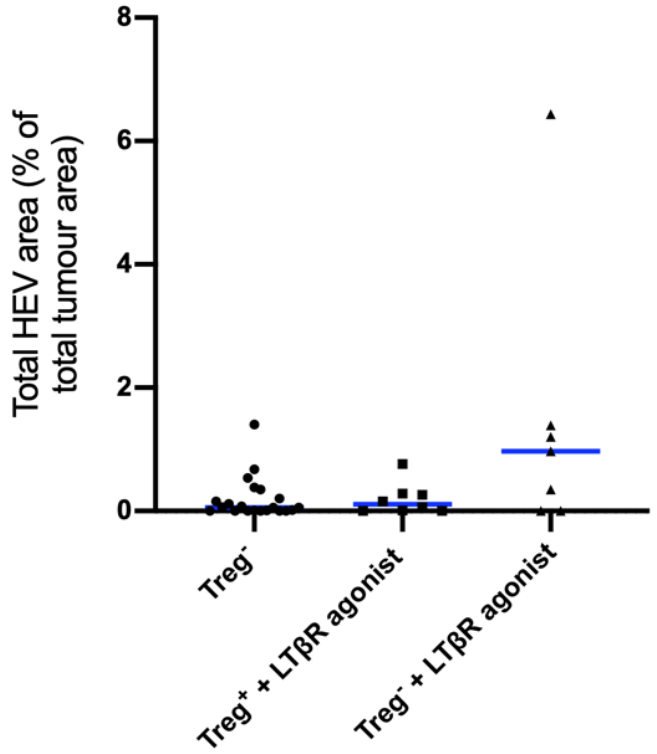
Total HEV area (% of total tumour area)
8
6
4
2
0
Treg-
Treg+ + LTβR agonist
Treg- + LTβR agonist

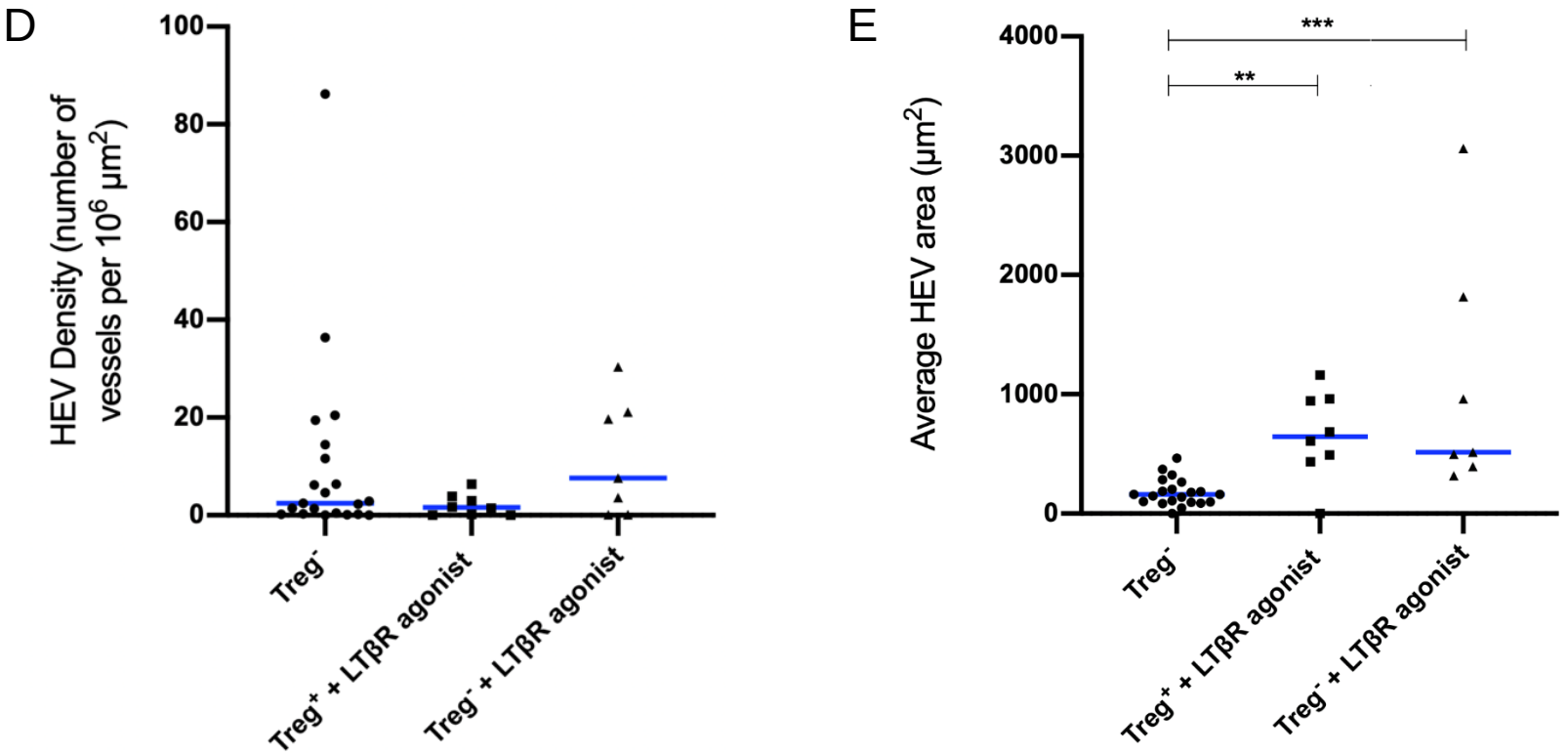

Figure 5.12 | Impact of LTβR agonist treatment on intra-tumoral HEV formation.
Representative microscopy images of HEVs in a (**A**) $Treg^+$ + LTβR agonist treated tumour and (**B**) $Treg^-$ + LTβR agonist treated tumour. HEVs were stained using the MECA-79 antibody and detected using DAB chromagen. Sections were counterstained by haematoxylin. Quantitative HEV measurements for $Treg^-$ (n=21) $Foxp3^{DTR}$ animals, $Treg^+$ and LTβR agonist treated (n = 8) $Foxp3^{DTR}$ animals and $Treg^-$ and LTβR agonist treated (n = 7) $Foxp3^{DTR}$ animals are also shown. (**C**) Total HEV area was measured as a percentage of the total tumour area. (**D**) HEV density was calculated per unit area of tumour (10^6 µm^2) and (**E**) the average HEV vessel area (µm^2). Statistical significance was determined by Kruskal-Wallis test with Dunn's multiple comparison test. (**, P< 0.01, ***, P<0.001).

Administration of neutralizing anti-IL27 antibodies to Treg replete mice resulted in the formation of $PNAd^+$ vessels in 3/7 mice that were treated (Figure 5.13 A&C). Whilst a larger sample size will be required to confirm whether roughly 50% of anti-IL-27 treated mice develop HEVs, it does raise the possibility that similar factors may dictate whether HEVs form following Treg depletion and treatment with anti-IL-27 neutralizing antibodies. Consistent with this possibility, treatment of Treg depleted mice with anti-IL-27 antibodies resulted in the formation of HEVs in 5/9 treated mice (Figure 5.13 B&C). As shown in Figure 5.13 C, there was a trend for increased total HEV area in this group compared to Treg depletion alone (ns P = >0.9999) and to Treg replete mice treated with anti-IL-27 antibodies (ns P = 0.1773) however this did not reach statistical significance. Furthermore, Treg replete mice treated with anti-IL-27 antibodies had significantly lower HEV densities as compared to Treg depleted mice (*P = 0.0227) (Figure 5.13 D). As with LTβR agonist treatment, the administration of anti-IL-27 antibodies to Treg depleted mice did not lead to significantly higher HEV densities as compared to Treg depletion alone (ns P = 0.8030) (Figure 5.13 D). Whilst there was a trend for larger average HEV areas in Treg depleted mice treated with anti-IL-27 antibodies as compared to Treg depleted only (ns P = >0.9999) and Treg replete mice treated with anti-IL-27 antibodies (ns P = 0.6851) (Figure 5.13 E), this did not reach statistical significance. A larger sample size will be required to confirm these findings in the future. It is interesting to note that this trend in increased HEV area was not observed in Treg replete mice treated with anti-IL-27 antibodies (Figure 5.13 E), suggesting Treg depletion is required for such changes to take place.

Given that the average HEV area varied between 396 μm^2 and 3060 μm^2 for Treg depleted mice treated with LTβR agonist (Figure 5.12 E) and between 887 μm^2 and 5130 μm^2 in Treg depleted mice treated with anti-IL-27 antibodies (Figure 5.13 E) it would be important to confirm these findings in whole tumours using a 3D imaging approach. As described earlier, a 2D sectioning and imaging approach can give rise to a high variability of observable structures particularly when such structures are asymmetrically distributed. Furthermore, this approach cannot be used to generate global descriptors of intratumoral HEV formation.

A

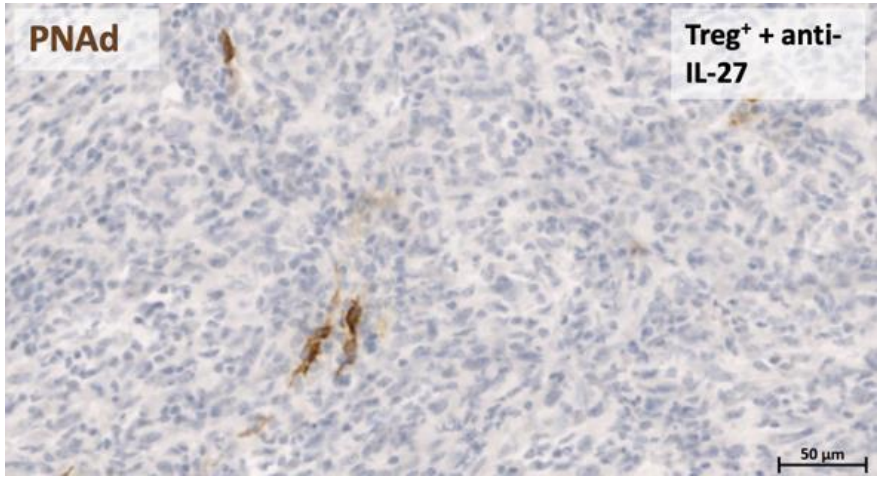
PNAd
Treg+ + anti-IL-27
50 µm

B

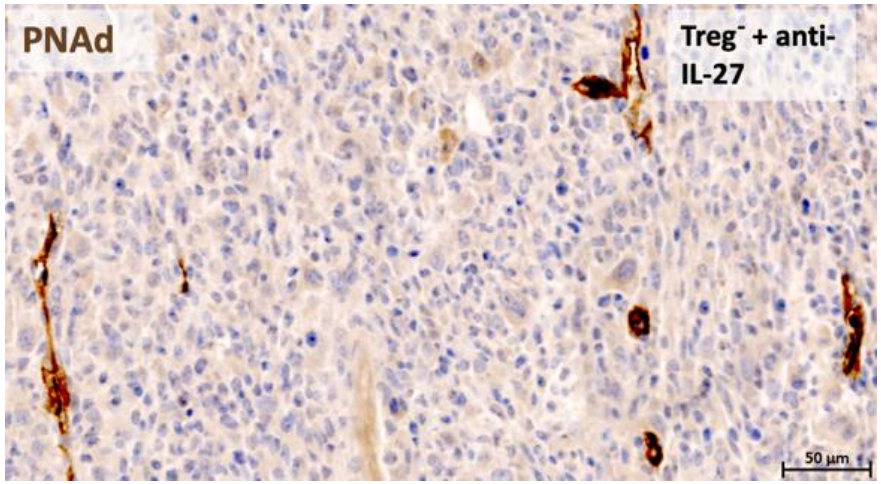
PNAd
Treg- + anti-IL-27
50 µm

C

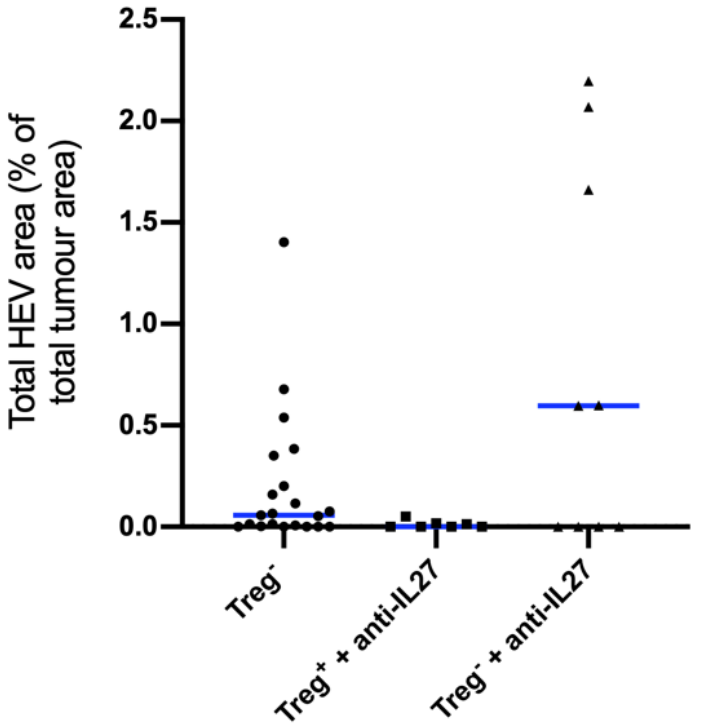
Total HEV area (% of total tumour area)
2.5
2.0
1.5
1.0
0.5
0.0
Treg-
Treg+ + anti-IL27
Treg- + anti-IL27

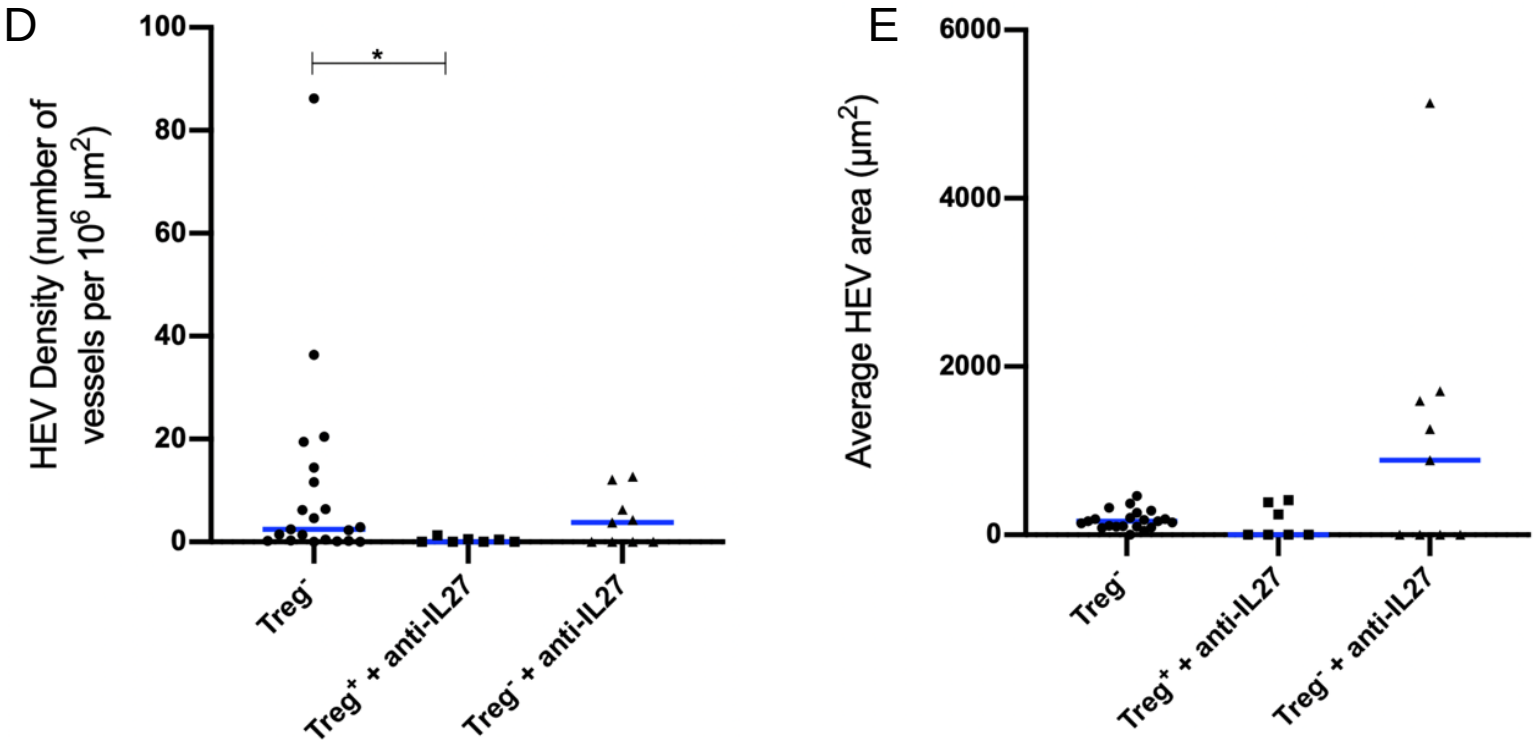

Figure 5.13 | Impact of anti-IL-27 antibody treatment on intra-tumoral HEV formation.
Representative microscopy images of HEVs in a (**A**) $Treg^+$ + anti-IL-27 antibody treated tumour and (**B**) $Treg^-$ + anti-IL-27 antibody treated tumour. HEVs were stained using the MECA-79 antibody and detected using DAB chromagen. Sections were counterstained by haematoxylin. Quantitative HEV measurements for $Treg^-$ (n=21) $Foxp3^{DTR}$ animals, $Treg^+$ and anti-IL-27 antibody treated (n = 7) $Foxp3^{DTR}$ animals and $Treg^-$ and anti-IL-27 antibody treated (n = 9) $Foxp3^{DTR}$ animals are also shown. (**C**) Total HEV area was measured as a percentage of the total tumour area. (**D**) HEV density was calculated per unit area of tumour (10^6 μm^2) and (**E**) the average HEV vessel area (μm^2). Statistical significance was determined by Kruskal-Wallis test with Dunn's multiple comparison test. (*, $P < 0.05$).

5.6 Impact of LTβR agonist and anti-IL-27 antibodies on fibrosarcoma growth rate and extent of T-cell infiltration

In this section the impact of LTβR agonist administration and anti-IL-27 antibody administration, either alone or in combination with Treg depletion, on fibrosarcoma growth rate were assessed. A 2D staining and imaging approach was also used to determine whether such treatments lead to a higher infiltration of T-cells. As shown in Figure 5.14 the administration of LTβR agonist alone did not result in significantly lower tumour growth rates as compared to Treg replete tumours (ns P = 0.8006) which is consistent with previous findings (Colbeck *et al.*, 2017). When administered to Treg depleted mice, there was a significant reduction in tumour growth rate relative to Treg replete tumours (**P = 0.0059). However, the combinatory use of these agents did not improve control of tumour growth as there was no statistically significant difference between $Treg^-$ vs $Treg^-$ and LTβR agonist treated tumours (ns P = 0.6364).

LTβR agonist treatment alone was found not to increase the extent of T-cell infiltration consistent with previous findings (Colbeck *et al.*, 2017), since the CD4 counts were significantly lower than those found in $Treg^-HEV^{hi}$ tumours (****P = <0.0001) and not significantly different from those found in Treg replete (ns P = >0.9999) tumours as shown in Figure 5.15 A. In addition, the CD8 T cell counts were significantly lower as compared to $Treg^-HEV^{hi}$ (****P = <0.0001) and not significantly different to Treg replete tumours (ns P = >0.9999) as shown in Figure 5.15 B. Similarly, whilst Treg depleted and LTβR agonist treated mice had significantly higher CD4 counts than Treg replete and LTβR agonist treated mice (**P = 0.0063) there were no statistically significant differences in comparison to Treg replete (ns P = 0.7829), $Treg^-HEV^{hi}$ (ns P = > 0.9999) or $Treg^-HEV^{lo}$ tumours (ns P = 0.7040) (Figure 5.15 A). Whilst the CD8 counts were significantly higher in comparison to Treg replete tumours (**P = 0.0056) and $Treg^-HEV^{lo}$ (*P = 0.0134) they were not significantly different from $Treg^-HEV^{hi}$ (ns P = >0.9999) tumours (Figure 5.15 B), suggesting overall that the use of LTβR agonist either alone or in combination with Treg depletion does not lead to an increase in T-cell infiltration.

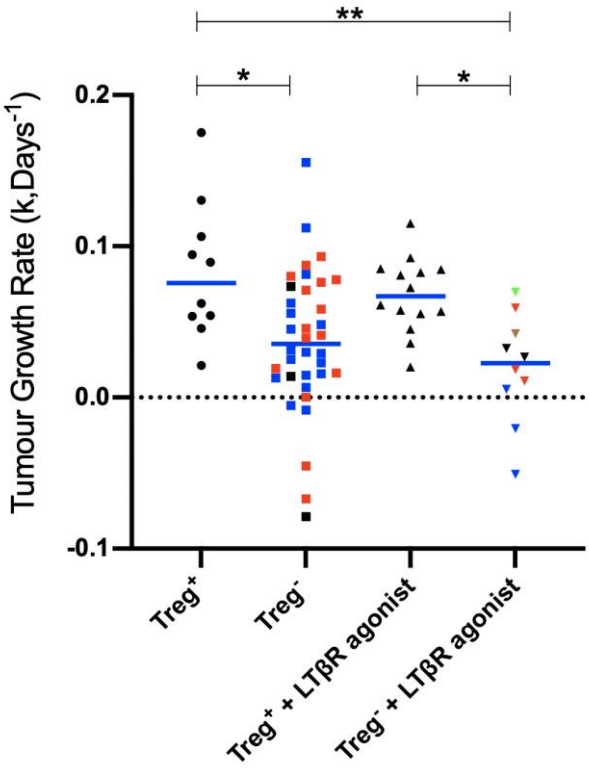

Figure 5.14 | Impact of LTβR agonist treatment on fibrosarcoma growth rate.
Tumour growth rates (k, per day) for $Treg^{+}$ (n = 10) $Foxp3^{DTR}$ animals, $Treg^{-}$ (n = 36) $Foxp3^{DTR}$ animals, $Treg^{+}$ and LTβR agonist treated (n = 14) $Foxp3^{DTR}$ animals and $Treg^{-}$ and LTβR agonist treated (n = 10) $Foxp3^{DTR}$ animals. Using the median of total HEV area as a cut off value, individual data points are also displayed as HEV^{high} (blue) or HEV^{low} (red). Datapoint in brown corresponds to sample imaged in **Figure 5.5** and datapoint in green corresponds to sample imaged in **Figure 5.7**. Statistical significance was determined by one-way ANOVA with Tukey's multiple comparison test. (*, P< 0.05, **, P< 0.01).

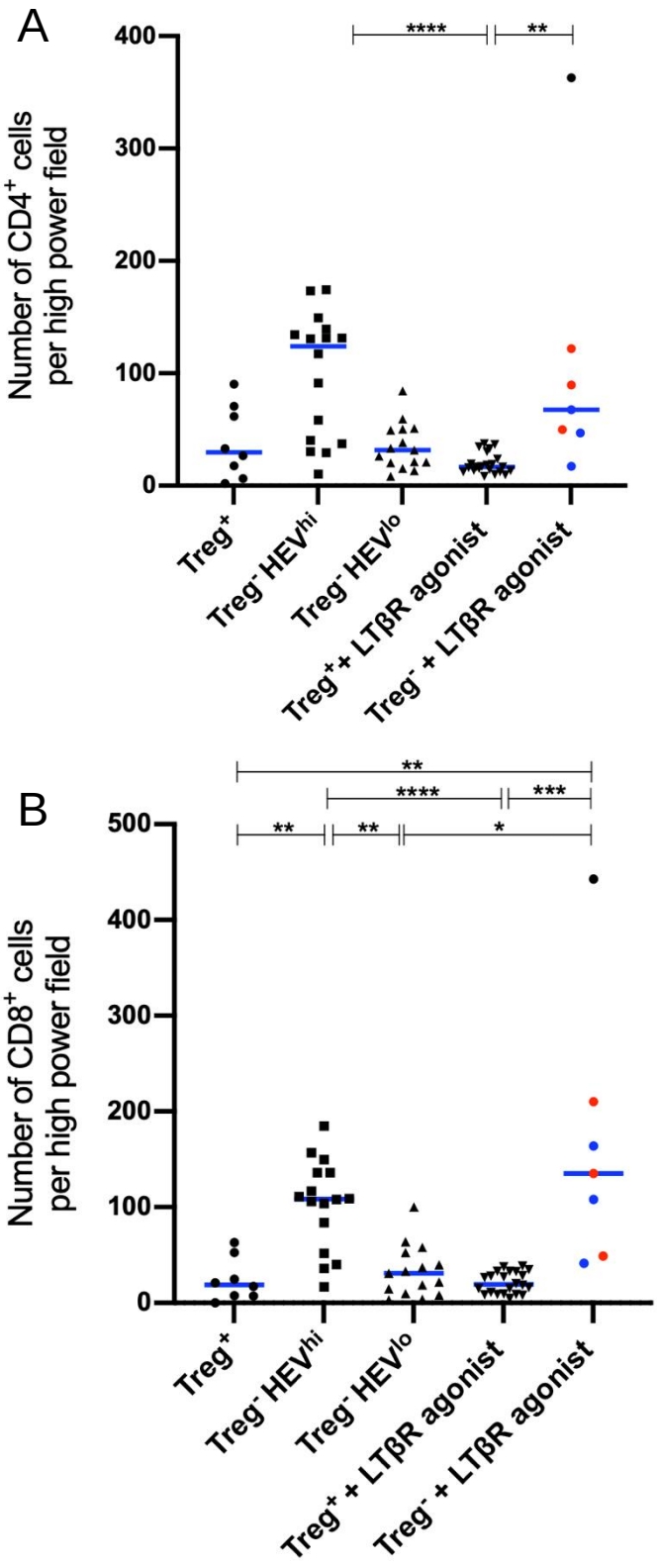

Figure 5.15 | Impact of LTβR treatment on intra-tumoral T-cell infiltration
(**A**) Number of $CD4^+$ T-cells and (**B**) $CD8^+$ T-cells per high power field view for $Treg^+$ (n = 8) $Foxp3^{DTR}$ animals, $Treg^-HEV^{hi}$ (n = 16) $Foxp3^{DTR}$ animals, $Treg^-HEV^{lo}$(n = 15), Treg+ and LTβR agonist treated (n = 22) $Foxp3^{DTR}$ animals and Treg- and LTβR agonist treated (n = 7) $Foxp3^{DTR}$ animals. Using the median of total HEV area as a cut off value, individual data points are also displayed as HEV^{high} (blue) or HEV^{low} (red). Statistical significance was determined by Kruskal-Wallis test with Dunn's multiple comparison test. (*, P< 0.05, **, P<0.01, ***, P<0.001, ****, P<0.0001).

As shown in Figure 5.16 treatment with IL-27 alone did not improve control of tumour growth relative to Treg replete tumours (ns P = >0.9999). Interestingly, the combined use of anti-IL-27 and Treg depletion seemed to abrogate control of tumour growth as there was no significant difference between combinatory treatment vs Treg replete tumours (ns P = 0.9485) whilst a significantly higher tumour growth rate in comparison to Treg depletion alone was found (*P = 0.0392). Treg replete mice treated with anti-IL-27 antibodies were found not to have a higher number of infiltrating T cells as the $CD4^+$ T cell counts were significantly lower than $Treg^-HEV^{hi}$ tumours (*P = 0.0106) and not significantly different from Treg replete tumours (ns P = >0.9999) (Figure 5.17 A). Similarly, there were no significant differences between the $CD8^+$ T cell counts in Treg replete mice treated with anti-IL-27 and Treg replete tumours (ns P = >0.9999) as shown in Figure 5.17 B. Treg depleted mice treated with anti-IL-27 did not have significantly different $CD4^+$ T cell counts as compared to Treg replete mice (ns P = 0.2911) as shown in Figure 5.17 A. Whilst the $CD8^+$ T cell counts in this group were significantly higher as compared to Treg replete mice (**P = 0.0048) and $Treg^-HEV^{lo}$ tumours (**P = 0.0058) they were not significantly different from $Treg^-HEV^{hi}$ tumours (ns P = >0.9999) as shown in Figure 5.17 B. Overall this suggests that the use of neutralizing anti-IL-27 antibodies either alone or in combination with Treg depletion does not lead to an increase in T cell infiltration.

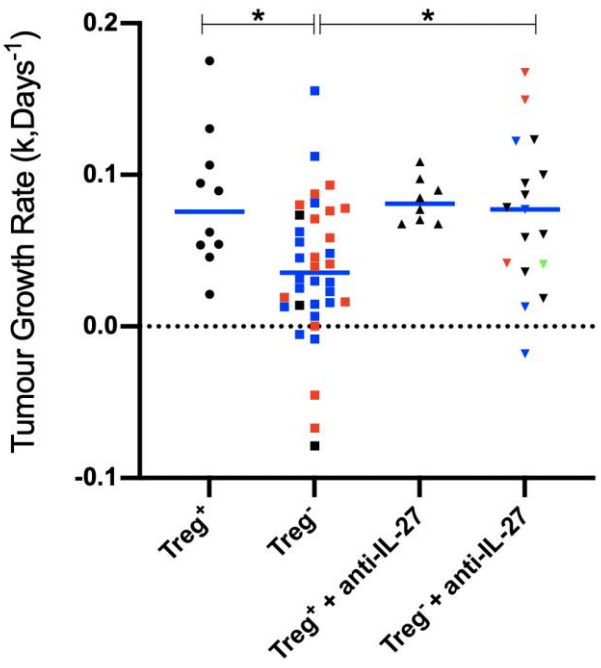

Figure 5.16 | Impact of anti-IL-27 antibody administration on fibrosarcoma growth rate. Tumour growth rates (k,per day) for $Treg^{+}$ (n = 10) $Foxp3^{DTR}$ animals, $Treg^{-}$ (n = 36) $Foxp3^{DTR}$ animals, $Treg^{+}$ and anti-IL-27 antibody treated (n = 8) $Foxp3^{DTR}$ animals and $Treg^{-}$ and anti-IL-27 antibody treated (n = 17) $Foxp3^{DTR}$ animals. Using the median of total HEV area as a cut off value, individual data points are also displayed as HEV^{high} (blue) or HEV^{low} (red). Data point in green corresponds to sample imaged in **Figure 5.10**. Statistical significance was determined by one-way ANOVA with Tukey's multiple comparison test. (*, $P < 0.05$).

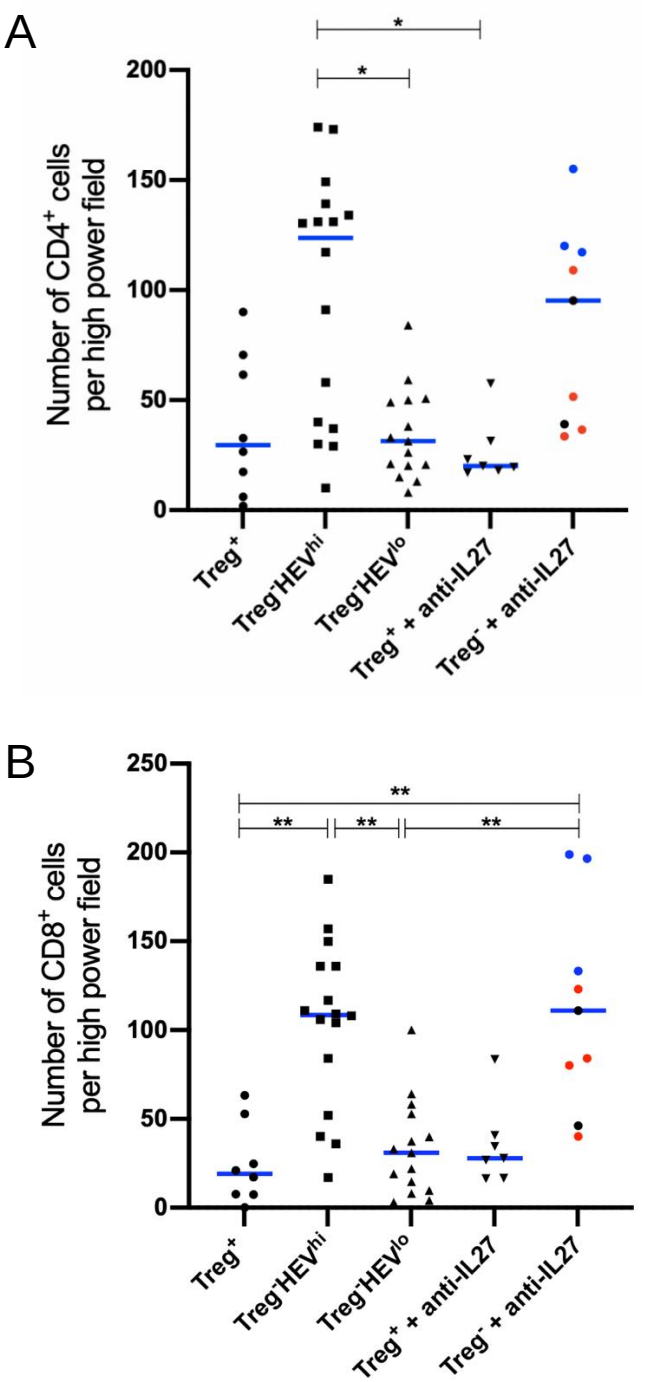

Figure 5.17 | Impact of anti-IL-27 antibody treatment on intra-tumoral T-cell infiltration. (**A**) Number of $CD4^+$ T-cells and (**B**) $CD8^+$ T-cells per high power field view for $Treg^+$ (n = 8) $Foxp3^{DTR}$ animals, $Treg^-HEV^{hi}$ (n = 16) $Foxp3^{DTR}$ animals, $Treg^-HEV^{lo}$(n = 15), $Treg^+$ and anti-IL-27 treated (n = 7) $Foxp3^{DTR}$ animals and $Treg^-$ and anti-IL-27 treated (n = 9) $Foxp3^{DTR}$ animals. Using the median of total HEV area as a cut off value, individual data points are also displayed as HEV^{high} (blue) or HEV^{low} (red). Statistical significance was determined by Kruskal-Wallis test with Dunn's multiple comparison test. (*, P< 0.05, **, P<0.01).

An increase in tumour size following combinatory Treg depletion and anti-IL-27 antibody treatment may not necessarily reflect abrogated control of tumour growth. Given the clear extensive expansion in $PNAd^+$ vessels (Figure 5.10 and Figure 5.11 A&B), it is possible that this leads to a higher influx of immune cells which in turn drives the expansion of the tumour. Whilst 2D imaging did not reveal an increase in the extent of T-cell infiltration (Figure 5.17 A&B), it would be important to examine this by 3D imaging particularly given the large variability in HEV structures seen using this approach (Figure 5.13 C-E). Furthermore, different types of structural HEV organizations were identified by LSFM imaging (Figure 5.11 B) which in turn could reflect HEVs of differing immune cell recruiting capabilities or efficiencies. Prior to increasing the n number for 3D imaging, it would be important to perform further sectioning, staining and 2D analysis of the same FFPE tumour tissue to confirm the findings presented above. This approach could readily be performed on existing tissues and would provide further confidence that the use of these agents does not lead to an increase in influx of immune cells.

In addition to the vascular expansion that occurs following LN stimulation, LNs also greatly expand in size as a result of an increased influx of immune cells (Anderson, Anderson and Wyllie, 1975; Liao and Ruddle, 2006; Qian *et al.*, 2006; Kumar *et al.*, 2010, 2012). LN hypertrophy following CFA immunization has also been shown to be mediated by LIGHT which in turn was found to be required for the influx of T cells and peripheral DCs into LNs (Zhu *et al.*, 2011). Furthermore, immune-related increases in tumour size and even number of lesions following immunotherapy have been documented in the clinic as a result of immune cell infiltration or inflammatory edema (as discussed by Chai *et al.*, 2019). This recognition of tumour pseudoprogression in response to cellular or checkpoint immunotherapies, is reflected by recent developments of immune specific criteria for assessing clinical responses to immunotherapy (as discussed by Chai *et al.*, 2019). It would therefore be important to determine, ideally by LSFM, whether there is indeed a larger influx of immune cells following the establishment of more extensive HEV networks.

Alternatively, there may be an impairment in anti-tumour immunity which might be explained by the well-established immune enhancing activities of IL-27

(as discussed by Fabbi, Carbotti and Ferrini, 2017; Kourko *et al.*, 2019). For example, IL-27 has been shown to mediate Th1 polarization and IFN-γ production in naïve $CD4^+$ T cells (Pflanz *et al.*, 2002; Takeda *et al.*, 2003). IL-27 also stimulates $CD8^+$ T cell proliferation and release of effector molecules including IFN-γ, granzyme B and Eomesodermin (Schneider *et al.*, 2011). Furthermore, potent anti-tumour activity has also been demonstrated using a TBJ neuroblastoma cell line engineered to overexpress IL-27 (Salcedo *et al.*, 2004). In this work CTL generation, proliferation and effector function were increased resulting in complete durable remission in >90% of mice bearing tumours (Salcedo *et al.*, 2004). With particular relevance to this work, IL27ra deficient mice bearing MCA induced fibrosarcomas had accelerated tumour growth and development as well as decreased IFN- γ production by CD4 and CD8 T cells (Natividad *et al.*, 2013). Therefore, a lack of IL-27 signalling even in the absence of Tregs may prevent control of tumour growth. However, it is important to note that administration of anti-IL-27 as a single agent did not accelerate tumour growth (Figure 5.16) since Treg replete tumours had comparable growth rates to anti-IL-27 only treated tumours.

5.7 Discussion

LSFM imaging of fibrosarcomas revealed the presence of complex and heterogenous vessel networks with areas of both hypo and hyper-vascular niches. Consistent with previous reports (Hindley *et al.*, 2012; Colbeck *et al.*, 2017) HEVs were more extensive in a Treg depleted regressor than a non-regressor. In contrast to SLOs such as LNs, HEVs were found to be heterogeneously distributed and were not well connected across the entire tumour. The identification of several pre-existing $PNAd^+$ vessels in a Treg replete tumour suggests Treg depletion may not be required for de novo HEV neogenesis. A larger sample number of Treg replete tumours will need to be imaged in order to confirm this finding.

The use of LTβR agonist in combination with Treg depletion was found to boost HEV network formation however this did not result in an improvement in control of tumour growth relative to Treg depletion alone. A 2D imaging approach revealed significant increases in total HEV area suggesting this treatment expands intra-tumoral HEVs. In order to examine the functional consequences of such changes an intra-vital imaging approach could be used to compare the trafficking efficiency of lymphocytes within HEVs that form in Treg depleted tumours as compared to those which form following treatment with LTβR agonist. 2D staining and imaging did not reveal an increase in T cell infiltration suggesting such increases in intra-tumoral HEV areas do not lead to enhanced T cell trafficking. Increases in HEV area have previously been documented in murine and human sentinel LN HEVs (Qian *et al.*, 2006; Chung *et al.*, 2012; Lee *et al.*, 2012; Shen *et al.*, 2014). Given that such changes have been associated with worse prognosis (Lee *et al.*, 2012) it would be important to examine whether in tumours this leads to an increase in tumour cell dissemination efficiency. Whilst CD2-DsRed mice can readily be used to examine lymphocyte recruitment by intra-tumoral HEVs using 2-photon microscopy, tracking tumour cell dissemination via HEVs in the MCA model is challenging. This is largely because MCA induced fibrosarcomas develop *in-situ* which precludes the use of fluorescent reporter genes that have previously been used to track tumour cell migration (Brown *et al.*, 2018; Pereira *et al.*, 2018). Cell lines derived from primary MCA-tumours have previously been established and even genetically

manipulated to silence expression of tenascin (TNC) using a targeted shRNA approach (Pires *et al.*, 2020). Whilst these cell lines were even labelled with GFP to confirm transfection with shTNC, the tumours which formed all responded to Treg depletion (Pires *et al.*, 2020) suggesting this approach does not fully recapitulate the responses seen in the MCA model. Importantly HEVs could not be identified by IHC staining in the cell line tumours following Treg depletion (unpublished observations by Dr Ana Pires) suggesting this approach cannot be used to examine the impact of HEV inducing agents or to further assess the functional implications of HEV expansion. The impact of LTβR agonist should therefore be examined on other well-established tumour cell lines providing they are amenable to such therapeutic approaches. As mentioned earlier, HEV augmentation using LIGHT has previously been examined using various well established cell lines including Lewis lung carcinoma and B16-F10 melanoma (He *et al.*, 2020) however the impact on tumour cell dissemination has not yet been assessed.

3D imaging revealed that the administration of anti-IL-27 antibodies in combination with Treg depletion also led to the formation of extensive and dense $PNAd^{+}$ vessels. Whether such vessels display similar network branching structures to LTβR and DT treated tumours or even LN HEVs will need to be confirmed by LSFM imaging with the use of a thinner light sheet waist. IL-27 is a negative regulator of IL-17; a cytokine that has been implicated in ELS formation (Peters *et al.*, 2011). Furthermore lymphoid tissue inducer (LTi) cells which are involved in the development of lymphoid tissue through lymphotoxin production (De Togni *et al.*, 2014) have also been shown to produce abundant amounts of IL-17 (Takatori *et al.*, 2009). Therefore, it is possible that a lack of inhibitory function over IL-17 production may explain the more extensive HEVs seen by 3D imaging of a Treg depleted and anti-IL-27 treated tumour. Furthermore, in experimental sialadenitis, IL-17 blockade in $IL27ra^{-/-}$ mice was shown to significantly reduce genes involved in ELS formation including LTβ (Lucchesi *et al.*, 2020) further supporting the role of IL-17 in controlling aspects of lymphoid like tissue development. It would therefore be of interest to perform microarray and/or RNA sequencing analysis of Treg depleted tumours treated with anti-IL-27 antibodies as has previously been done for Treg replete and depleted tumours (Hindley *et al.*, 2012) in order to examine whether Th17 transcripts are indeed

upregulated. It is also possible that IL-27 deficiency has a direct impact on intra-tumoral HEV structure/function given that IL-27 has also been shown to negatively regulate angiogenesis (Zorzoli *et al.*, 2012; Fink *et al.*, 2019). The use of IL-27ra$^{-/-}$ mice in a mouse model of mammary carcinoma led to increased EC proliferation, migration and sprouting leading to the formation of immature leaky vessels with poor pericyte coverage (Fink *et al.*, 2019). It would therefore be important to determine the direct impact of IL-27 deficiency on tumour ECs which express PNAd. Whilst HEV networks were found to be much more extensive, combinatory anti-IL-27 antibody treatment and Treg depletion abrogated control of tumour growth. This may be a consequence of a lack of immune enhancing and direct anti-tumour effects of IL-27 (as discussed by Fabbi, Carbotti and Ferrini, 2017; Kourko *et al.*, 2019). Indeed, Natividad and colleagues have previously demonstrated that MCA induced fibrosarcomas emerge earlier and with faster growth rate kinetics in IL27ra$^{-/-}$ mice (Natividad *et al.*, 2013). This in turn was accompanied by a reduction in IFN-γ production by CD4 and CD8 T cells as well as an enhanced generation of Tregs (Natividad *et al.*, 2013).

Whilst an increase in the extent of T-cell infiltration may drive tumour expansion, a 2D assessment did not reveal a higher number of infiltrating T cells following treatment of Treg depleted mice with anti-IL-27 antibodies. In order to exclude the possibility that only a subset of HEVs which form following HEV augmentation are indeed functional, it would be important to characterize both the distribution and extent of T cell infiltration using the 3D imaging techniques described in this thesis. The use of LSFM imaging and tumour bearing mice that express an appropriate fluorescent protein marker on T cells (such as CD2–DsRed mice) could be used in the future to examine this, especially given that single cell populations have successfully been resolved by LSFM (Mayer *et al.*, 2012; Abe *et al.*, 2016) and further quantified in large tumour pieces (Tanaka *et al.*, 2017).

An important limitation in this work was the use of a thick 25.27 µm light sheet waist which precluded the resolution of vessels smaller than 25.27 µm in the Z-dimension including the separation of vessels found within a 25.27 µm or smaller gap. This in turn did not allow for the characterisation of intra-tumoral HEV branching patterns as well as the use of Dr Gib Bogle's optimized vessel

tools for generating intra-tumoral HEV topological descriptors. An imaging approach using a thinner light sheet waist comparable to SPIM (5 μm) could be performed in the future but this would require the collection of more images in order to achieve sufficient sampling. Nevertheless, the clear qualitative differences in HEV formation between regressors, non-regressors and a Treg replete tumour suggests this to be a valid approach to qualitatively examining HEV distribution and density patterns. The clear qualitative differences in extent and distribution of intra-tumoral HEV networks following treatment with LTβR agonist and anti-IL-27 antibodies further support this notion.

Chapter 6

6 Final Discussion

6.1 LSFM imaging and 3D analysis of fibrosarcoma and LN blood vessel and HEV networks

The first aim of this PhD thesis was to optimize fluorescent labelling, clearing and LSFM imaging protocols that allow for a global 3D characterization of blood vessels and HEVs found in LNs and fibrosarcoma tumours. Chapter 3 describes how large murine fibrosarcomas are readily amenable to BABB organic solvent clearing and that in combination with *in-vivo* labelling and autofluorescence reducing protocols, it is now possible to resolve entire intra-tumoral blood vessel and HEV structures using LSFM. Furthermore, it was also shown that the same optimized labelling and clearing protocols can be used to image entire blood vessel and HEV networks found in LNs.

The second aim of this PhD project was to further develop, implement and validate 3D vessel quantification tools that could be used to generate topological descriptors of continuous blood vessel networks acquired by LSFM imaging. Chapter 4 describes the main modifications that were made to process discrete vessel networks acquired by LSFM imaging. By increasing the number of objects that the connect tool could identify, it was possible to fully segment both inguinal and popliteal LN HEV networks. These optimized tools were subsequently validated by processing naïve popliteal and inguinal LN HEV networks acquired by SPIM. Naïve LN HEVs were found to have consistent branching network structures across different LN sizes which is in line with previous studies that used OPT (Kumar *et al.*, 2010, 2012). Whilst differences in the overall extent of the network were noted in this study as compared to the aforementioned studies, it would be important to determine whether this is a result of differences in the overall resolving capabilities between the two imaging modalities. This could be experimentally tested by imaging the same *in-vivo* labelled and cleared LN sample by both OPT and LSFM followed by performing the same quantitative

analysis described herein. The optimized and validated vessel tools were then used to explore the impact of both Treg depletion and the presence of a fibrosarcoma tumour on the draining LN HEV network. Widespread changes to the structural organization of LN HEVs were documented in both instances and characterized by an expansion of small (11-20 µm) diameter sized HEVs.

The third aim of this study was to examine the global distribution and structural organization of intra-tumoral HEVs using LSFM imaging. In Chapter 5, 3D imaging of a Treg depleted regressor tumour revealed several dense clusters of HEVs as well as several well separated $PNAd^{+}$ vessels that were not well connected. Such vessels were heterogeneously distributed and localized mainly to the outermost edges of the tumour. The functional relevance of different structural HEV organizations has yet to be uncovered. Such questions pertaining to the functionality of intra-tumoral HEVs could be addressed using a combination of both intra-vital and LSFM imaging. Whilst intra-tumoral HEVs have previously been found to be in close proximity to the immune cell infiltrate by 2D staining (Hindley *et al.*, 2012; Colbeck *et al.*, 2017) their ability to directly recruit T-cells has not yet been examined. Fibrosarcomas derived from CD2-DsRED mice could be imaged by 2-photon microscopy in order to determine whether T-cells are indeed actively recruited by intra-tumoral HEVs. Complementary LSFM imaging using a Z resolution that is sufficient to characterize the extent of HEV network connectivity could in turn be used to examine the T-cell distribution in relation to specific types of HEV organizational patterns as previously described (Mayer *et al.*, 2012).

6.2 Imaging approaches to characterize intra-tumoral HEV formation

Before this study, assessments of intratumoural HEVs was performed by 2D staining. Using this methods, HEV were not observed in Treg-replete tumours leading to the conclusion that Treg depletion is a pre-requisite for the development of intra-tumoral HEVs (Hindley *et al.*, 2012; Colbeck *et al.*, 2017). However, in this study, the use of LSFM imaging which is a much more comprehensive imaging technique showed that a non-treated fibrosarcoma contained a small proportion of blood vessels that stained positive for PNAd. Whilst this finding will have to be confirmed using a larger sample number, it does

raise the possibility that HEVs are present pre-treatment at least in some tumours. It is even possible that their presence may dictate whether or not a fibrosarcoma develops a more significant HEV network following Treg depletion, that is associated with T cell infiltration and tumour control. Thus, Treg depletion may drive the expansion of pre-existing $PNAd^+$ vessels or lead to the *de novo* formation of HEVs, or even a combination of both. Such questions pertaining to HEV neogenesis and expansion could be further addressed using intra-vital imaging techniques that allow for repeated imaging across the same tumour lesion over an extended period of time. The use of implanted window chambers as previously described (Spranger *et al.*, 2017) could be adapted to the MCA model in order to examine this. Multicolored fate-mapping systems which involve the labelling of a single cell population with different colours to allow for the tracking of individual cells and their progeny over time and space have previously been used to track the behaviour of blood endothelial cells during LN expansion (Mondor *et al.*, 2016). This approach could also be used to determine whether different ECs found within the tumour have an equal propensity to differentiate into HEVs. Examination of the $PNAd^+$ EC colour composition would also provide clues as to whether a specific circulating endothelial cell progenitor cell leads to the formation of $PNAd^+$ vessels as previously suggested (Ager and May, 2015). In order to gain a better understanding of how HEVs arise, transcriptional profiling of tumour $PNAd^-$ ECs, LN HECs and tumour $PNAd^+$ ECs should be performed. Computational methods such as velocyto could be used to predict the future state of cells (thereby inferring their origin) based on changes in the transcriptional rate of genes (as estimated from the ratio of unsliced to spliced reads) (La Manno *et al.*, 2018). Since it has previously been shown (Colbeck *et al.*, 2017) and subsequently confirmed by LSFM imaging that only a subset of tumour blood vessels express PNAd, transcriptional profiling may lead to the identification of immunosuppressive molecules that prevent HEV formation.

6.3 Imaging approaches to uncover differential responses to Treg depletion

An important unanswered question which remains is why responses to Treg depletion only leads to the formation of HEVs in approximately 50% of treated mice despite profound increases in systemic T cell activation in all treated mice

(Hindley *et al.*, 2012). Previous unpublished data from the lab revealed low levels of angiogenesis-related gene transcripts which distinguished HEV^+ from HEV^- tumours of Treg depleted mice. These included gene transcripts associated with arterial specification such as Notch4, Dll4, Jag2 and Hes1 which have previously been shown to distinguish capillary ECs from HECs (Lee *et al.*, 2014; Brulois *et al.*, 2020). Furthermore, a mixed angiogenic genetic signature was observed in Treg replete mice. Taken together this suggests that the extent of angiogenic activity pre-treatment may dictate whether tumours can develop HEV after Treg depletion. In order to examine this further an LSFM imaging approach combined with the optimized vessel tool pipeline described in Chapter 4 of this thesis, could be used to extract and compare whole vascular profiles of Treg replete, HEV^+ and HEV^- tumours. Should this work reveal that high angiogenic activity prevents the formation of HEVs, then the judicious use of anti-angiogenic agents to normalize the vasculature prior to Treg depletion could be further explored. Indeed, vessel normalization through the use of anti-angiogenic therapy has been shown to be required for the development of HEVs following combinatory treatment with anti PD-L1 in murine models of breast and pancreatic neuroendocrine mouse tumours (Allen *et al.*, 2017).

Examination of the lymphatic vasculature in this context should also be performed. Afferent lymph has been shown to be important in maintaining HEVs in LNs (Hendriks and Eestermans, 1983; Liao and Ruddle, 2006) and their development in tumours may be important for intra-tumoral HEV formation and function. Indeed, functional afferent lymphatic vessels have already been described in MCA induced fibrosarcomas previously by our lab (Ondondo *et al.*, 2014). Importantly, robust staining for the lymphatic vessel marker LYVE-1 and expression of the chemokine CCL21 was recently shown in responder tumours suggesting improved functionality of lymphatic vessels in comparison to non-responder and non-treated tumours (Pires *et al.*, 2020). Therefore, it is possible that the presence of functional afferent-like lymphatics may be an essential prerequisite to HEV development. To date only a 2D assessment of lymphatic vessels has been performed and a global analysis is currently lacking. As such, the LaVision Ultramicroscope 2 could be used to examine this as it is equipped with a near infra-red laser line which further expands the number of fluorescent markers that can be imaged in the same tumour. Ultimately HEVs, T cells, blood

vessels and lymphatic vessels could be imaged simultaneously. Such imaging could be used to define the global distribution and structural organization of lymphatic vessel networks across whole tumours and to further examine whether intra-tumoral HEV formation and function (as assessed by the spatial distribution of T-cells in relation to the nearest $PNAd^+$ vessels) is dependent on the presence of intra-tumoral lymphatic vessels. Information gained from such studies may guide the development of novel immunotherapies which could focus on improving lymphatic vessel function for HEV induction.

Local factors within the TME prior to Treg depletion may also impinge on the ability of tumours to form HEVs. Differential signalling in pathways that are associated with impaired anti-tumour immune responses and immune cell exclusion such as WNT-β-catenin signalling (Spranger, Bao and Gajewski, 2015; Spranger and Gajewski, 2018b) or TGF-β signalling (Mariathasan *et al.*, 2018) may dictate whether or not HEVs can form. In addition, tumour immunogenicity may be an important factor that dictates response to Treg depletion as previously suggested (Pires *et al.*, 2020). Indeed, somatic mutational heterogeneity in MCA induced sarcomas was recently demonstrated by whole exosome sequencing (Lee *et al.*, 2019). Furthermore, a link between the mutational landscape of a tumour and TCR expansion was recently demonstrated by Joshi and colleagues (Joshi *et al.*, 2019). In this work the selective expansion of TCR sequences was found to correlate with the number of non-synonymous mutations at the same sites (Joshi *et al.*, 2019).

6.4 Intra-tumoral HEV expansion implications for T cell recruitment and tumour cell dissemination

The ability of LTβR agonist and anti-IL-27 neutralizing antibodies to augment intra-tumoral HEVs, enhance the extent of T-cell infiltration and further improve control of tumour growth was assessed as described in Chapter 5 of this thesis. A qualitative examination of LSFM imaging data revealed increases in the density of HEV networks in both LTβR agonist and anti-IL-27 neutralizing antibody treated tumours as compared to Treg depletion alone. Such networks occupied much larger volumes suggesting a change in the global distribution of HEVs as well. Despite such profound changes to the density and global

distribution of intra-tumoral HEVs, there were no increases in the extent of T cell infiltration (as revealed by 2D imaging) or an improvement in control of tumour growth. In fact, combinatory Treg depletion and treatment with anti-IL-27 antibodies led to an abrogated control of tumour growth. This could be the result of a lack of immune enhancing and/or direct anti-tumour effects of IL-27 (as discussed by Fabbi, Carbotti and Ferrini, 2017; Kourko *et al.*, 2019). Nevertheless, it is still not clear why HEV augmentation did not lead to an increase in the extent of T cell infiltration. These results reiterate the need to examine whether intra-tumoral HEVs are indeed functional and not simply bystanders of an active immune response (as discussed by Colbeck *et al.*, 2017). With this in mind, a key next experiment to determine directly the functionality of intra-tumoral HEVs in fibrosarcomas is 2-photon imaging to visualise T cell transmigration across intra-tumoral HEVs.

The results of several pre-clinical studies point to HEV induction as an effective component of cancer therapy (Allen *et al.*, 2017; Johansson-Percival *et al.*, 2017; He *et al.*, 2018, 2020). However, the findings described above raises concern that this may not always be the case, even suggesting that HEV can have a potentially detrimental functional impact. Indeed, there is evidence that intra-tumoral HEVs may be associated with worse prognosis (Shen *et al.*, 2014). In oral and pharyngeal squamous cell carcinoma (OPSCC), two types of HEV were identified: a classical HEV phenotype associated with lymphocyte infiltrate, and an HEV-like phenotype characterised by thin-walled, dilated lumens containing RBCs, which were not associated with lymphocyte infiltrate but found adjacent to tumour cell clusters (Shen *et al.*, 2014). A higher density of HEV-like vessels in the primary tumour was found to be associated with LN metastasis (Shen *et al.*, 2014) further supporting the need to examine intra-tumoral HEVs as a site for tumour cell dissemination. There is limited evidence to support the metastatic potential of MCA induced fibrosarcomas including a paper by Wexler and Rosenberg in 1979 which showed that 75% of tumour bearing mice had lung metastases present 50 days post amputation of the tumour bearing leg (Wexler and Rosenberg, 1979). Furthermore, unpublished preliminary data generated by a postdoctoral research associate in our lab Dr Ana Pires has shown that fibroblast like cells could more readily be cultured from the dLNs and ndLNs of non-responder tumours as compared to non-treated tumours (Pires, 2020,

unpublished data). Whilst these are preliminary findings, they support the metastatic potential of MCA induced fibrosarcomas and indicate that tumour cells originating from non-responder tumours are more invasive and more likely to migrate to distant sites. Nevertheless, it is challenging to use the MCA model to examine tumour cell dissemination as fluorescent reporter genes cannot be implemented to track tumour cell migration.

The 4T1 breast cancer model however provides a good alternative to investigate whether intra-tumoral HEVs in their basal state disseminate tumour cells and whether treatment with HEV augmenting agents further enhances this dissemination. This is because 4T1 tumours have previously been shown to present with low levels of HEVs pre-treatment and to be responsive to HEV induction and expansion upon treatment with the phosphoinositide 3-kinase δ (PI3Kδ) inhibitor (PI-3065) which reduces the number and function of Tregs (Lauder *et al.*, 2020). Furthermore, 4T1 cells expressing the mCherry fluorescent marker have been shown to migrate and intravasate to LN HEVs (Brown *et al.*, 2018). The time taken for intravasation to take place coincided with the detection of 4T1 cells within the systemic blood circulation suggesting 4T1 cells can actively be disseminated by basal HEVs (Brown *et al.*, 2018). Intra vital imaging could therefore be used to directly assess whether intra-tumoral HEVs disseminate fluorescently labelled 4T1 cells and luciferase expressing 4T1 cells could be further used to assess the impact of HEV augmenting agents on overall metastatic burden by bioluminescence imaging of isolated lungs as previously described (Brown *et al.*, 2018).

LSFM imaging could also be used to investigate the extent and localization of tumour cell dissemination in an unbiased manner by resolving single tumour cells within the whole mouse body. Recent developments in the field of tissue clearing such as the development of uDISCO clearing by the Erturk group first allowed for the visualization of the intact mouse nervous system by inducing shrinkage of the entire mouse body by up to 65% in volume (Pan *et al.*, 2016). The same group later described the development of vDISCO which combines pressure-driven, nanobody-based whole-body immunolabeling to boost fluorescent protein signals with existing clearing protocols including CUBIC and 3DISCO to achieve efficient clearing of bone and skin in order to image the entire

intact mouse body (Cai *et al.*, 2019). With direct relevance to cancer research, vDISCO was used to examine the spatial distribution, size and shape of metastases in 5 different mouse models of cancer at a single cell level (Pan *et al.*, 2019). The systemic distribution and impact of therapeutic monoclonal antibodies was also examined (Pan *et al.*, 2019). Several challenges exist with implementing this technique in routine pre-clinical cancer research. At present, manually re-positioning of the mouse body inside the imaging chamber is required in order to image different parts of the body (Cai *et al.*, 2019). Advancements in light sheet microscopes that allow for the imaging of the entire mouse body in one imaging session would significantly simplify data processing and 3D reconstruction (Cai *et al.*, 2019) and may further encourage the implementation of this technique.

6.5 Sentinel LN HEV remodelling and impact of HEV augmenting agents on SLOs

In Chapter 4, it was shown that the establishment of a non-treated tumour led to widespread changes to the sentinel LN HEV network which was characterized by the extensive expansion of small diameter sized HEVs. Given that non-responder tumours may be more invasive it would be important to determine whether this is accompanied by distinct changes to the sentinel LN HEV network. Indeed, it is possible that non-responder dLNs exhibit the sentinel LN HEV phenotype which is characterized by a dilated lumen with or without the presence of RBCs (Qian *et al.*, 2006; Chung *et al.*, 2012; Shen *et al.*, 2014; Maeda *et al.*, 2018). This is important as the SLN HEV phenotype has been shown to be associated with a worse prognosis (Lee *et al.*, 2012). Therefore, whether fibrosarcoma dLN HEVs are differentially remodelled by non-treated, non-responder and responder tumours could be examined in the future by LSFM imaging. This work may further implicate HEVs as an important dissemination route for metastatic spread and provide further evidence that this role may be impacted by the type of response generated following Treg depletion.

It is also important to address the functional impact HEV augmenting agents have on SLOs such as LNs. In Chapter 5, LTβR agonist treatment either with or without Treg depletion was found to lead to an increase in average HEV area

which bears resemblance to the dilated sentinel LN HEV phenotype. The impact of this treatment on LN HEVs has not yet been examined and warrants further investigation. Therefore the functional relevance of sentinel LN HEV remodelling and impact of HEV augmenting agents could be explored using 2-photon imaging and CD2-DsRed mice (to examine the impact on T cell trafficking efficiency) or using mice bearing fluorescently labelled tumours that allow for tumour cell migration tracking using 2-photon microscopy as discussed earlier. If such changes are indeed found to be detrimental to either the ability of a LN to initiate immune responses or found to enhance tumour cell dissemination leading to an increased metastatic burden, then tumour targeted delivery of such agents using VTPs should be explored. Indeed, the aformentioned LIGHT-VTP therapy utilized the CGKRK pentapeptide to home LIGHT specifically to GBM vessels (He *et al.*, 2018). CGKRK has also been shown to targets vessels in mouse models of breast cancer (Agemy *et al.*, 2013) and epidermal carcinogenesis (Hoffman *et al.*, 2003). CGKRK reportedly binds to heparan sulfate (Hoffman *et al.*, 2003) and the mitochondrial p32 protein which is expressed on the cell surface of activated endothelial cells (Agemy *et al.*, 2013).

6.6 LSFM imaging in Cancer Research and Diagnosis

Recent work by Uhlen and colleagues has demonstrated FFPE human tumour biopsies could readily be deparaffinized, rehydrated, whole mount stained and optically cleared using iDISCO (Tanaka *et al.*, 2017). The development of the diagnosing immunolabelled paraffin-embedded cleared organs (DIPCO) pipeline is important as it demonstrated that LSFM imaging could be performed on existing tumour sample collections (Tanaka *et al.*, 2017). This study also revealed substantial 3D heterogeneity of stained markers across different tumour regions (Tanaka *et al.*, 2017) suggesting rare tumour cell or immune cell populations that would otherwise be missed by conventional 2D staining can readily be detected by LSFM imaging. Furthermore, certain structural and heterogeneity features measured in 3D were found to correlate better with tumour staging than standard 2D staining parameters (Tanaka *et al.*, 2017). Overall, this approach will further increase the accuracy of cancer diagnosis and may provide useful in cases where the identification of single tumour cells that metastasize to LNs or other distant metastatic sites is important (as discussed by Garvalov and

Ertürk, 2017). Although advantageous, the implementation of LSFM in routine clinical diagnosis is currently met with several challenges including cost of current commercial light sheet microscopes and analysis software as well as time consuming labelling and clearing protocols (Tanaka *et al.*, 2017).

6.7 Final Conclusion

In conclusion, this thesis describes how *in-vivo* labelling, organic solvent optical clearing and autofluorescence reducing protocols were successfully optimized and used to characterize the 3D global distribution of intra-tumoral HEVs in a Treg replete tumour and following Treg depletion and HEV augmentation. Further to this, a set of open-source command line vessel tracing tools developed by Dr Gib Bogle were further optimized to process LSFM acquired datasets. These tools can now readily be applied to any blood vessel network captured by LSFM including spatially separated vessels which form discrete networks within a larger blood vessel network. The imaging methods and analysis tools described herein can be used to address several outstanding questions that have been raised both in this work and by others (as discussed by Milutinovic *et al.*, 2020). This includes uncovering how sentinel LN HEVs are remodelled in 3D, the mechanisms driving such remodelling and whether this ultimately leads to impaired immune activation and more effective dissemination of tumour cells in comparison to basal LN HEVs. The impact of HEV-inducing therapies on LN HEV networks and how this affects their role as both regulators of immunity and sites for tumour cell dissemination can now also be addressed. Whether intratumoral HEVs are capable of disseminating tumour cells should also be examined. This work will further our current understanding of the dual roles of HEVs in cancer and immunity (summarised in Figure 6.1) and inform the design of novel cancer therapies that aim to promote immune activation whilst simultaneously limiting cancer cell dissemination.

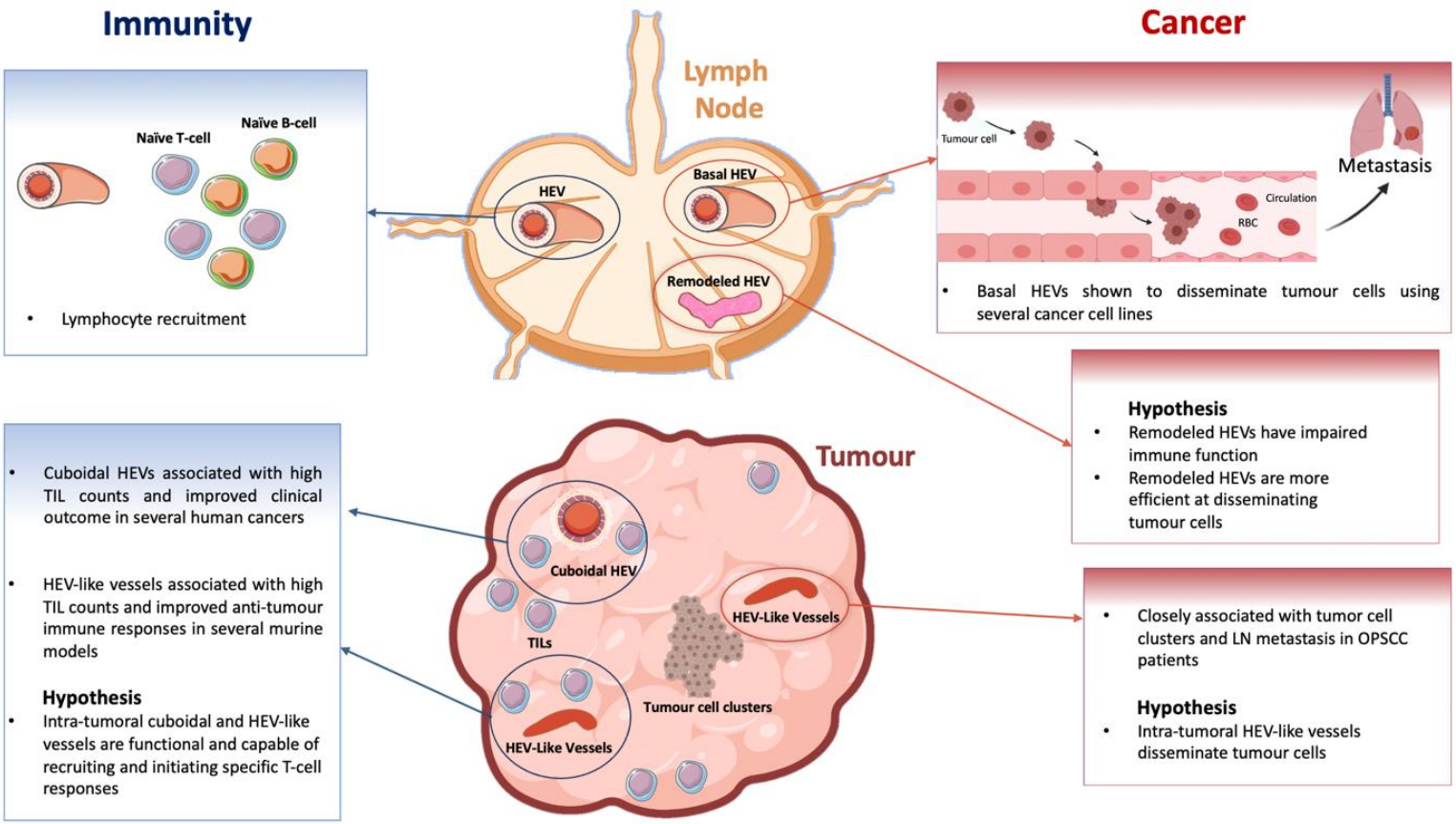

Figure 6.1 | Dual roles of HEV in cancer progression and immunity.
The dual roles of HEVs as initiators of immunity and as a major site for tumour cell dissemination in both lymph nodes and tumours is summarised. Whilst lymphocyte recruitment and tumour cell dissemination via basal HEVs has been demonstrated via 2-photon imaging, the functional role of remodelled HEVs in the lymph node has yet to be determined. Similarly, whilst intra-tumoral HEVs have been associated with high TIL counts as well as LN metastasis in OPSCC patients, their functional role has not been directly examined by intra-vital imaging

Appendix

Supplementary Figures

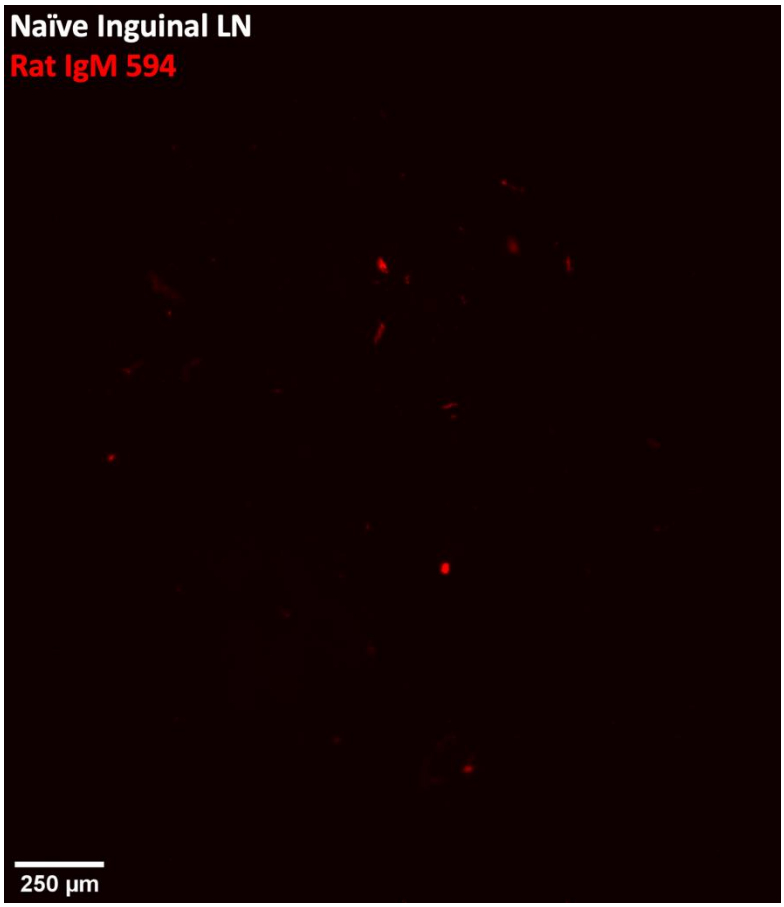

Supplementary Figure 1.
Isotype control staining for 3D lymph node HEV network characterization. A naive inguinal lymph node was *in-vivo* labelled with 20 µg rat IgM 594 and imaged by SPIM.

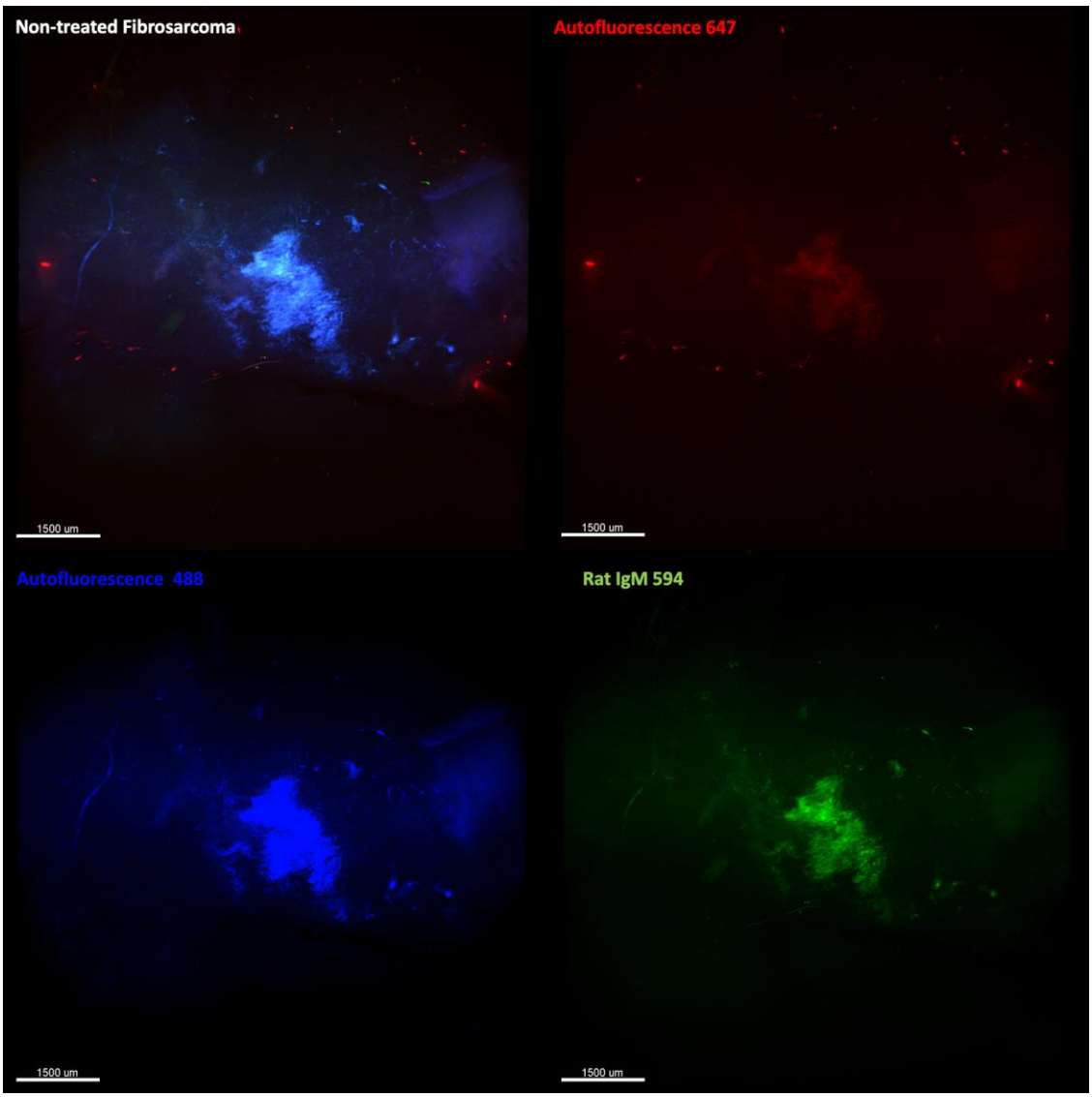

Supplementary Figure 2.
Isotype control staining for 3D HEV network characterization in fibrosarcomas. A non-treated fibrosarcoma was *in-vivo* labelled with 50 µg rat IgM 594 and imaged using the LaVision Ultramicroscope 2.

References

Abe, J. *et al.* (2016) 'Light sheet fluorescence microscopy for in situ cell interaction analysis in mouse lymph nodes.', *Journal of immunological methods*. Netherlands, 431, pp. 1–10. doi: 10.1016/j.jim.2016.01.015.

Acton, S. E. *et al.* (2012) 'Podoplanin-rich stromal networks induce dendritic cell motility via activation of the C-type lectin receptor CLEC-2.', *Immunity*. United States, 37(2), pp. 276–289. doi: 10.1016/j.immuni.2012.05.022.

Acton, S. E. *et al.* (2014) 'Dendritic cells control fibroblastic reticular network tension and lymph node expansion.', *Nature*. England, 514(7523), pp. 498–502. doi: 10.1038/nature13814.

Agemy, L. *et al.* (2013) 'Proapoptotic peptide-mediated cancer therapy targeted to cell surface p32.', *Molecular therapy : the journal of the American Society of Gene Therapy*. United States, 21(12), pp. 2195–2204. doi: 10.1038/mt.2013.191.

Ager, A. (2017) 'High Endothelial Venules and Other Blood Vessels: Critical Regulators of Lymphoid Organ Development and Function.', *Frontiers in immunology*. Switzerland, 8, p. 45. doi: 10.3389/fimmu.2017.00045.

Ager, A. and May, M. J. (2015) 'Understanding high endothelial venules: Lessons for cancer immunology.', *Oncoimmunology*. United States, 4(6), p. e1008791. doi: 10.1080/2162402X.2015.1008791.

Alanentalo, T. *et al.* (2006) 'Tomographic molecular imaging and 3D quantification within adult mouse organs', *Nature Methods*. Nature Publishing Group, 4, p. 31. Available at: https://doi.org/10.1038/nmeth985.

Allen, E. *et al.* (2017) 'Combined antiangiogenic and anti – PD-L1 therapy stimulates tumor immunity through HEV formation', 1(April).

Aloisi, F. and Pujol-Borrell, R. (2006) 'Lymphoid neogenesis in chronic inflammatory diseases.', *Nature reviews. Immunology*. England, 6(3), pp. 205–217. doi: 10.1038/nri1786.

Altmann, D. M. (2018) 'A Nobel Prize-worthy pursuit: cancer immunology and harnessing immunity to tumour neoantigens.', *Immunology*. England, pp. 283–284. doi: 10.1111/imm.13008.

Anderson, N. D., Anderson, A. O. and Wyllie, R. G. (1975) 'Microvascular changes in lymph nodes draining skin allografts.', *The American journal of pathology*. United States, 81(1), pp. 131–160.

von Andrian, U. H. (1996) 'Intravital microscopy of the peripheral lymph node microcirculation in mice.', *Microcirculation (New York, N.Y. : 1994)*. United States, 3(3), pp. 287–300. doi: 10.3109/10739689609148303.

von Andrian, U. H. and Mempel, T. R. (2003) 'Homing and cellular traffic in lymph nodes.', *Nature reviews. Immunology*. England, 3(11), pp. 867–878. doi: 10.1038/nri1222.

Andtbacka, R. H. I. *et al.* (2015) 'Talimogene Laherparepvec Improves Durable Response Rate in Patients With Advanced Melanoma.', *Journal of clinical oncology : official journal of the American Society of Clinical Oncology*. United States, 33(25), pp. 2780–2788. doi: 10.1200/JCO.2014.58.3377.

Angeli, V. *et al.* (2006) 'B cell-driven lymphangiogenesis in inflamed lymph nodes enhances dendritic cell mobilization.', *Immunity*. United States, 24(2), pp. 203–215. doi: 10.1016/j.immuni.2006.01.003.

Ariel, P. (2018) *UltraMicroscope II – A User Guide*, *UltraMicroscope II – A User Guide*. University of North Carolina at Chapel Hill, University Libraries. doi: 10.17615/C69M15.

Ayers, M. *et al.* (2017) 'IFN-γ-related mRNA profile predicts clinical response to PD-1 blockade', *The Journal of clinical investigation*. 2017/06/26. American Society for Clinical Investigation, 127(8), pp. 2930–2940. doi: 10.1172/JCI91190.

Bahmani, B. *et al.* (2018) 'Ectopic high endothelial venules in pancreatic ductal adenocarcinoma: A unique site for targeted delivery.', *EBioMedicine*. Netherlands, 38, pp. 79–88. doi: 10.1016/j.ebiom.2018.11.030.

Bajenoff, M. *et al.* (2006) 'Stromal cell networks regulate lymphocyte entry, migration, and territoriality in lymph nodes.', *Immunity*. United States, 25(6), pp. 989–1001. doi: 10.1016/j.immuni.2006.10.011.

Batchelor, T. T. *et al.* (2010) 'Phase II study of cediranib, an oral pan-vascular endothelial growth factor receptor tyrosine kinase inhibitor, in patients with recurrent glioblastoma.', *Journal of clinical oncology : official journal of the American Society of Clinical Oncology*. United States, 28(17), pp. 2817–2823. doi: 10.1200/JCO.2009.26.3988.

Benahmed, F. *et al.* (2014) 'Multiple CD11c+ cells collaboratively express IL-1beta to modulate stromal vascular endothelial growth factor and lymph node vascular-stromal growth.', *Journal of immunology (Baltimore, Md. : 1950)*. United States, 192(9), pp. 4153–4163. doi: 10.4049/jimmunol.1301765.

Bies, C., Lehr, C.-M. and Woodley, J. F. (2004) 'Lectin-mediated drug targeting: history and applications.', *Advanced drug delivery reviews*. Netherlands, 56(4), pp. 425–435. doi: 10.1016/j.addr.2003.10.030.

van den Broek, M. E. *et al.* (1996) 'Decreased tumor surveillance in perforin-deficient mice', *The Journal of experimental medicine*. The Rockefeller University Press, 184(5), pp. 1781–1790. doi: 10.1084/jem.184.5.1781.

Brown, M. *et al.* (2018) 'Lymph node blood vessels provide exit routes for metastatic tumor cell dissemination in mice.', *Science (New York, N.Y.)*. United States, 359(6382), pp. 1408–1411. doi: 10.1126/science.aal3662.

Browning, J. L. *et al.* (2005) 'Lymphotoxin-beta receptor signaling is required for the homeostatic control of HEV differentiation and function.', *Immunity*. United States, 23(5), pp. 539–550. doi: 10.1016/j.immuni.2005.10.002.

van der Bruggen, P. *et al.* (1991) 'A gene encoding an antigen recognized by cytolytic T lymphocytes on a human melanoma', *Science*, 254(5038), pp. 1643 LP – 1647. doi: 10.1126/science.1840703.

Brulois, K. *et al.* (2020) 'A molecular map of murine lymph node blood vascular endothelium at single cell resolution.', *Nature communications*, 11(1), p. 3798. doi: 10.1038/s41467-020-17291-5.

Buckanovich, R. J. *et al.* (2008) 'Endothelin B receptor mediates the endothelial barrier to T cell homing to tumors and disables immune therapy.', *Nature medicine*. United States, 14(1), pp. 28–36. doi: 10.1038/nm1699.

Burnet, M. (1957) 'Cancer—A Biological Approach', *British Medical Journal*, 1(5022), pp. 779 LP – 786. doi: 10.1136/bmj.1.5022.779.

Burton, J. B. *et al.* (2008) 'Suppression of prostate cancer nodal and systemic metastasis by blockade of the lymphangiogenic axis.', *Cancer research*. United States, 68(19), pp. 7828–7837. doi: 10.1158/0008-5472.CAN-08-1488.

Cabrita, R. *et al.* (2020) 'Tertiary lymphoid structures improve immunotherapy and survival in melanoma.', *Nature*. England, 577(7791), pp. 561–565. doi: 10.1038/s41586-019-1914-8.

Cai, R. *et al.* (2019) 'Panoptic imaging of transparent mice reveals whole-body neuronal projections and skull-meninges connections.', *Nature neuroscience*, 22(2), pp. 317–327. doi: 10.1038/s41593-018-0301-3.

Calon, A. *et al.* (2015) 'Stromal gene expression defines poor-prognosis subtypes in colorectal cancer.', *Nature genetics*. United States, 47(4), pp. 320–329. doi: 10.1038/ng.3225.

Cancer Research UK, https://www.cancerresearchuk.org/about-cancer/what-is-cancer, Accessed November 2020

Carlsen, H. S. *et al.* (2005) 'Disparate lymphoid chemokine expression in mice and men: no evidence of CCL21 synthesis by human high endothelial venules.', *Blood*. United States, 106(2), pp. 444–446. doi: 10.1182/blood-2004-11-4353.

Di Caro, G. *et al.* (2014) 'Occurrence of tertiary lymphoid tissue is associated with T-cell infiltration and predicts better prognosis in early-stage colorectal cancers.', *Clinical cancer research : an official journal of the American Association for Cancer Research*. United States, 20(8), pp. 2147–2158. doi: 10.1158/1078-0432.CCR-13-2590.

Carriere, V. *et al.* (2005) 'Cancer cells regulate lymphocyte recruitment and leukocyte-endothelium interactions in the tumor-draining lymph node.', *Cancer research*. United States, 65(24), pp. 11639–11648. doi: 10.1158/0008-5472.CAN-05-1190.

Chae, S.-S. *et al.* (2010) 'Angiopoietin-2 interferes with anti-VEGFR2-induced vessel normalization and survival benefit in mice bearing gliomas.', *Clinical*

cancer research : an official journal of the American Association for Cancer Research. United States, 16(14), pp. 3618–3627. doi: 10.1158/1078-0432.CCR-09-3073.

Chai, L. F. *et al.* (2019) 'Challenges in assessing solid tumor responses to immunotherapy.', *Cancer gene therapy*. England. doi: 10.1038/s41417-019-0155-1.

Chen, Z. *et al.* (2005) 'Down-regulation of vascular endothelial cell growth factor-C expression using small interfering RNA vectors in mammary tumors inhibits tumor lymphangiogenesis and spontaneous metastasis and enhances survival.', *Cancer research*. United States, 65(19), pp. 9004–9011. doi: 10.1158/0008-5472.CAN-05-0885.

Chesney, J. *et al.* (2018) 'Randomized, Open-Label Phase II Study Evaluating the Efficacy and Safety of Talimogene Laherparepvec in Combination With Ipilimumab Versus Ipilimumab Alone in Patients With Advanced, Unresectable Melanoma.', *Journal of clinical oncology : official journal of the American Society of Clinical Oncology*. United States, 36(17), pp. 1658–1667. doi: 10.1200/JCO.2017.73.7379.

Chi, J. *et al.* (2018) 'Adipo-Clear: A Tissue Clearing Method for Three-Dimensional Imaging of Adipose Tissue.', *Journal of visualized experiments : JoVE*. United States, (137). doi: 10.3791/58271.

Chiang, C. L.-L., Kandalaft, L. E. and Coukos, G. (2011) 'Adjuvants for enhancing the immunogenicity of whole tumor cell vaccines.', *International reviews of immunology*. England, 30(2–3), pp. 150–182. doi: 10.3109/08830185.2011.572210.

Chung, M. K. *et al.* (2012) 'Lymphatic vessels and high endothelial venules are increased in the sentinel lymph nodes of patients with oral squamous cell carcinoma before the arrival of tumor cells.', *Annals of surgical oncology*. United States, 19(5), pp. 1595–1601. doi: 10.1245/s10434-011-2154-9.

Chyou, S. *et al.* (2008) 'Fibroblast-type reticular stromal cells regulate the lymph node vasculature.', *Journal of immunology (Baltimore, Md. : 1950)*. United States, 181(6), pp. 3887–3896. doi: 10.4049/jimmunol.181.6.3887.

Chyou, S. *et al.* (2011) 'Coordinated regulation of lymph node vascular-stromal growth first by CD11c+ cells and then by T and B cells.', *Journal of immunology (Baltimore, Md.: 1950)*. United States, 187(11), pp. 5558–5567. doi: 10.4049/jimmunol.1101724.

Chyou, S. *et al.* (2012) 'Normalization of the lymph node T cell stromal microenvironment in lpr/lpr mice is associated with SU5416-induced reduction in autoantibodies.', *PloS one*. United States, 7(3), p. e32828. doi: 10.1371/journal.pone.0032828.

Clarke, M. *et al.* (2005) 'Effects of radiotherapy and of differences in the extent of surgery for early breast cancer on local recurrence and 15-year survival: an overview of the randomised trials.', *Lancet (London, England)*. England,

366(9503), pp. 2087–2106. doi: 10.1016/S0140-6736(05)67887-7.

Colbeck, E. (2015) *Mechanisms of Foxp3+ Regulatory T cell enrichment and High Endothelial Venule formation in tumours*. Cardiff University.

Colbeck, Emily Jayne *et al.* (2017) 'Tertiary Lymphoid Structures in Cancer: Drivers of Antitumor Immunity, Immunosuppression, or Bystander Sentinels in Disease?', *Frontiers in immunology*. Switzerland, 8, p. 1830. doi: 10.3389/fimmu.2017.01830.

Colbeck, Emily J *et al.* (2017) 'Treg Depletion Licenses T Cell-Driven HEV Neogenesis and Promotes Tumor Destruction.', *Cancer immunology research*. United States, 5(11), pp. 1005–1015. doi: 10.1158/2326-6066.CIR-17-0131.

Cupedo, T. *et al.* (2004) 'Presumptive lymph node organizers are differentially represented in developing mesenteric and peripheral nodes.', *Journal of immunology (Baltimore, Md. : 1950)*. United States, 173(5), pp. 2968–2975. doi: 10.4049/jimmunol.173.5.2968.

Darvin, P. *et al.* (2018) 'Immune checkpoint inhibitors: recent progress and potential biomarkers.', *Experimental & molecular medicine*. United States, 50(12), p. 165. doi: 10.1038/s12276-018-0191-1.

Dasoveanu, D. C. *et al.* (2016) 'Regulation of Lymph Node Vascular-Stromal Compartment by Dendritic Cells.', *Trends in immunology*. England, 37(11), pp. 764–777. doi: 10.1016/j.it.2016.08.013.

Diacovo, T. G. *et al.* (1998) 'Circulating activated platelets reconstitute lymphocyte homing and immunity in L-selectin-deficient mice.', *The Journal of experimental medicine*. United States, 187(2), pp. 197–204. doi: 10.1084/jem.187.2.197.

Dighe, A. S. *et al.* (1994) 'Enhanced in vivo growth and resistance to rejection of tumor cells expressing dominant negative IFN gamma receptors.', *Immunity*. United States, 1(6), pp. 447–456. doi: 10.1016/1074-7613(94)90087-6.

Dirkx, A. E. M. *et al.* (2003) 'Tumor angiogenesis modulates leukocyte-vessel wall interactions in vivo by reducing endothelial adhesion molecule expression.', *Cancer research*. United States, 63(9), pp. 2322–2329.

Dobosz, M. *et al.* (2014) 'Multispectral fluorescence ultramicroscopy: three-dimensional visualization and automatic quantification of tumor morphology, drug penetration, and antiangiogenic treatment response.', *Neoplasia (New York, N.Y.)*. United States, 16(1), pp. 1–13.

Dodt, H.-U. *et al.* (2007) 'Ultramicroscopy: three-dimensional visualization of neuronal networks in the whole mouse brain', *Nature Methods*. Nature Publishing Group, 4, p. 331. Available at: https://doi.org/10.1038/nmeth1036.

Dougan, M., Dranoff, G. and Dougan, S. K. (2019) 'Cancer Immunotherapy: Beyond Checkpoint Blockade', *Annual Review of Cancer Biology*. Annual Reviews, 3(1), pp. 55–75. doi: 10.1146/annurev-cancerbio-030518-055552.

Drayton, D. L. *et al.* (2004) 'IκB Kinase Complex α Kinase Activity Controls Chemokine and High Endothelial Venule Gene Expression in Lymph Nodes and Nasal-Associated Lymphoid Tissue', *The Journal of Immunology*, 173(10), pp. 6161 LP – 6168. doi: 10.4049/jimmunol.173.10.6161.

Dunn, G. P. *et al.* (2002) 'Cancer immunoediting: from immunosurveillance to tumor escape.', *Nature immunology*. United States, 3(11), pp. 991–998. doi: 10.1038/ni1102-991.

Engberg, H. *et al.* (2016) 'Cancer risk and mortality after kidney transplantation: a population-based study on differences between Danish centres using standard immunosuppression with and without glucocorticoids', *Nephrology Dialysis Transplantation*, 31(12), pp. 2149–2156. doi: 10.1093/ndt/gfw304.

Epah, J. *et al.* (2018) '3D Imaging and Quantitative Analysis of Vascular Networks: A Comparison of Ultramicroscopy and Micro-Computed Tomography.', *Theranostics*. Australia, 8(8), pp. 2117–2133. doi: 10.7150/thno.22610.

Erturk, A. *et al.* (2012) 'Three-dimensional imaging of solvent-cleared organs using 3DISCO.', *Nature protocols*. England, 7(11), pp. 1983–1995. doi: 10.1038/nprot.2012.119.

Fabbi, M., Carbotti, G. and Ferrini, S. (2017) 'Dual Roles of IL-27 in Cancer Biology and Immunotherapy.', *Mediators of inflammation*. United States, 2017, p. 3958069. doi: 10.1155/2017/3958069.

Farnsworth, R. H. *et al.* (2011) 'A role for bone morphogenetic protein-4 in lymph node vascular remodeling and primary tumor growth.', *Cancer research*. United States, 71(20), pp. 6547–6557. doi: 10.1158/0008-5472.CAN-11-0200.

Fava, R. A. *et al.* (2011) 'Lymphotoxin-beta receptor blockade reduces CXCL13 in lacrimal glands and improves corneal integrity in the NOD model of Sjogren's syndrome.', *Arthritis research & therapy*. England, 13(6), p. R182. doi: 10.1186/ar3507.

Feig, C. *et al.* (2013) 'Targeting CXCL12 from FAP-expressing carcinoma-associated fibroblasts synergizes with anti-PD-L1 immunotherapy in pancreatic cancer.', *Proceedings of the National Academy of Sciences of the United States of America*. United States, 110(50), pp. 20212–20217. doi: 10.1073/pnas.1320318110.

Fink, A. F. *et al.* (2019) 'IL27Rα Deficiency Alters Endothelial Cell Function and Subverts Tumor Angiogenesis in Mammary Carcinoma', *Frontiers in oncology*. Frontiers Media S.A., 9, p. 1022. doi: 10.3389/fonc.2019.01022.

Fletcher, A. L., Acton, S. E. and Knoblich, K. (2015) 'Lymph node fibroblastic reticular cells in health and disease.', *Nature reviews. Immunology*. England, 15(6), pp. 350–361. doi: 10.1038/nri3846.

Freeman, G. J. *et al.* (2000) 'Engagement of the PD-1 immunoinhibitory receptor by a novel B7 family member leads to negative regulation of lymphocyte

activation.', *The Journal of experimental medicine*. United States, 192(7), pp. 1027–1034. doi: 10.1084/jem.192.7.1027.

Fuertes, M. B. *et al.* (2011) 'Host type I IFN signals are required for antitumor CD8+ T cell responses through CD8{alpha}+ dendritic cells.', *The Journal of experimental medicine*. United States, 208(10), pp. 2005–2016. doi: 10.1084/jem.20101159.

Gabrilovich, D. I. *et al.* (1996) 'Production of vascular endothelial growth factor by human tumors inhibits the functional maturation of dendritic cells.', *Nature medicine*. United States, 2(10), pp. 1096–1103. doi: 10.1038/nm1096-1096.

Gajewski, T., Meng, Y. and Harlin, H. (2007) 'Chemokines expressed in melanoma metastases associated with T cell infiltration', *Journal of Clinical Oncology*. American Society of Clinical Oncology, 25(18_suppl), p. 8501. doi: 10.1200/jco.2007.25.18_suppl.8501.

Gallimore, A. and Godkin, A. (2008) 'Regulatory T cells and tumour immunity - observations in mice and men', *Immunology*. 2007/12/07. Blackwell Science Inc, 123(2), pp. 157–163. doi: 10.1111/j.1365-2567.2007.02748.x.

Galon, J. *et al.* (2006) 'Type, density, and location of immune cells within human colorectal tumors predict clinical outcome.', *Science (New York, N.Y.)*. United States, 313(5795), pp. 1960–1964. doi: 10.1126/science.1129139.

Ganesh, S. *et al.* (2018) 'RNAi-Mediated β-Catenin Inhibition Promotes T Cell Infiltration and Antitumor Activity in Combination with Immune Checkpoint Blockade', *Molecular Therapy*, 26(11), pp. 2567–2579. doi: https://doi.org/10.1016/j.ymthe.2018.09.005.

Gao, J. *et al.* (2016) 'Loss of IFN-gamma Pathway Genes in Tumor Cells as a Mechanism of Resistance to Anti-CTLA-4 Therapy.', *Cell*. United States, 167(2), pp. 397-404.e9. doi: 10.1016/j.cell.2016.08.069.

Garvalov, B. K. and Ertürk, A. (2017) 'Seeing whole-tumour heterogeneity.', *Nature biomedical engineering*. England, 1(10), pp. 772–774. doi: 10.1038/s41551-017-0150-5.

Gatumu, M. K. *et al.* (2009) 'Blockade of lymphotoxin-beta receptor signaling reduces aspects of Sjogren's syndrome in salivary glands of non-obese diabetic mice.', *Arthritis research & therapy*. England, 11(1), p. R24. doi: 10.1186/ar2617.

Genina, E. A., Bashkatov, A. N. and Tuchin, V. V (2010) 'Tissue optical immersion clearing.', *Expert review of medical devices*. England, 7(6), pp. 825–842. doi: 10.1586/erd.10.50.

Di Giovanna, A. P. *et al.* (2018) 'Whole-Brain Vasculature Reconstruction at the Single Capillary Level.', *Scientific reports*. England, 8(1), p. 12573. doi: 10.1038/s41598-018-30533-3.

Girard, J.-P., Moussion, C. and Förster, R. (2012) 'HEVs, lymphatics and

homeostatic immune cell trafficking in lymph nodes', *Nature Reviews Immunology*. Nature Publishing Group, a division of Macmillan Publishers Limited. All Rights Reserved., 12, p. 762. Available at: https://doi.org/10.1038/nri3298.

Greenwald, R. J., Freeman, G. J. and Sharpe, A. H. (2005) 'The B7 family revisited.', *Annual review of immunology*. United States, 23, pp. 515–548. doi: 10.1146/annurev.immunol.23.021704.115611.

Hacohen, N. *et al.* (2013) 'Getting personal with neoantigen-based therapeutic cancer vaccines', *Cancer immunology research*. 2013/04/07, 1(1), pp. 11–15. doi: 10.1158/2326-6066.CIR-13-0022.

Hamid, O. *et al.* (2013) 'Safety and Tumor Responses with Lambrolizumab (Anti–PD-1) in Melanoma', *New England Journal of Medicine*. Massachusetts Medical Society, 369(2), pp. 134–144. doi: 10.1056/NEJMoa1305133.

Hanahan, D. and Weinberg, R. A. (2000) 'The hallmarks of cancer.', *Cell*. United States, 100(1), pp. 57–70. doi: 10.1016/s0092-8674(00)81683-9.

Hanahan, D. and Weinberg, R. A. (2011) 'Hallmarks of cancer: the next generation.', *Cell*. United States, 144(5), pp. 646–674. doi: 10.1016/j.cell.2011.02.013.

Harlin, H. *et al.* (2009) 'Chemokine expression in melanoma metastases associated with CD8+ T-cell recruitment.', *Cancer research*. United States, 69(7), pp. 3077–3085. doi: 10.1158/0008-5472.CAN-08-2281.

Hay, J. B. and Hobbs, B. B. (1977) 'The flow of blood to lymph nodes and its relation to lymphocyte traffic and the immune response.', *The Journal of experimental medicine*. United States, 145(1), pp. 31–44. doi: 10.1084/jem.145.1.31.

Hayasaka, H. *et al.* (2010) 'Neogenesis and development of the high endothelial venules that mediate lymphocyte trafficking.', *Cancer science*. England, 101(11), pp. 2302–2308. doi: 10.1111/j.1349-7006.2010.01687.x.

He, B. *et al.* (2018) 'Vascular targeting of LIGHT normalizes blood vessels in primary brain cancer and induces intratumoural high endothelial venules.', *The Journal of pathology*. England, 245(2), pp. 209–221. doi: 10.1002/path.5080.

He, B. *et al.* (2020) 'Remodeling of Metastatic Vasculature Reduces Lung Colonization and Sensitizes Overt Metastases to Immunotherapy.', *Cell reports*. United States, 30(3), pp. 714-724.e5. doi: 10.1016/j.celrep.2019.12.013.

He, S. *et al.* (2010) 'CD4+CD25+Foxp3+ regulatory T cells protect the proinflammatory activation of human umbilical vein endothelial cells.', *Arteriosclerosis, thrombosis, and vascular biology*. United States, 30(12), pp. 2621–2630. doi: 10.1161/ATVBAHA.110.210492.

Helmink, B. A. *et al.* (2020) 'B cells and tertiary lymphoid structures promote immunotherapy response.', *Nature*. England, 577(7791), pp. 549–555. doi:

10.1038/s41586-019-1922-8.

Hendriks, H. R. and Eestermans, I. L. (1983) 'Disappearance and reappearance of high endothelial venules and immigrating lymphocytes in lymph nodes deprived of afferent lymphatic vessels: a possible regulatory role of macrophages in lymphocyte migration.', *European journal of immunology*. Germany, 13(8), pp. 663–669. doi: 10.1002/eji.1830130811.

Herman, P. G., Yamamoto, I. and Mellins, H. Z. (1972) 'Blood microcirculation in the lymph node during the primary immune response', *The Journal of experimental medicine*. The Rockefeller University Press, 136(4), pp. 697–714. doi: 10.1084/jem.136.4.697.

Herzog, B. H. *et al.* (2013) 'Podoplanin maintains high endothelial venule integrity by interacting with platelet CLEC-2.', *Nature*. England, 502(7469), pp. 105–109. doi: 10.1038/nature12501.

Higano, C. S. *et al.* (2009) 'Integrated data from 2 randomized, double-blind, placebo-controlled, phase 3 trials of active cellular immunotherapy with sipuleucel-T in advanced prostate cancer.', *Cancer*. United States, 115(16), pp. 3670–3679. doi: 10.1002/cncr.24429.

Hildner, K. *et al.* (2008) 'Batf3 deficiency reveals a critical role for CD8alpha+ dendritic cells in cytotoxic T cell immunity', *Science (New York, N.Y.)*, 322(5904), pp. 1097–1100. doi: 10.1126/science.1164206.

Hindley, J. P. *et al.* (2012) 'T-cell trafficking facilitated by high endothelial venules is required for tumor control after regulatory T-cell depletion.', *Cancer research*. United States, 72(21), pp. 5473–5482. doi: 10.1158/0008-5472.CAN-12-1912.

Hinrichs, C. S. and Rosenberg, S. A. (2014) 'Exploiting the curative potential of adoptive T-cell therapy for cancer.', *Immunological reviews*. England, 257(1), pp. 56–71. doi: 10.1111/imr.12132.

Hodi, F. S. *et al.* (2010) 'Improved survival with ipilimumab in patients with metastatic melanoma.', *The New England journal of medicine*. United States, 363(8), pp. 711–723. doi: 10.1056/NEJMoa1003466.

Hoffman, J. A. *et al.* (2003) 'Progressive vascular changes in a transgenic mouse model of squamous cell carcinoma.', *Cancer cell*. United States, 4(5), pp. 383–391. doi: 10.1016/s1535-6108(03)00273-3.

Hollingsworth, R. E. and Jansen, K. (2019) 'Turning the corner on therapeutic cancer vaccines', *npj Vaccines*, 4(1), p. 7. doi: 10.1038/s41541-019-0103-y.

Hood, J. L., San, R. S. and Wickline, S. A. (2011) 'Exosomes released by melanoma cells prepare sentinel lymph nodes for tumor metastasis.', *Cancer research*. United States, 71(11), pp. 3792–3801. doi: 10.1158/0008-5472.CAN-10-4455.

Horl, D. *et al.* (2019) 'BigStitcher: reconstructing high-resolution image datasets of cleared and expanded samples.', *Nature methods*. United States, 16(9), pp. 870–874. doi: 10.1038/s41592-019-0501-0.

Huang, Y. *et al.* (2012) 'Vascular normalizing doses of antiangiogenic treatment reprogram the immunosuppressive tumor microenvironment and enhance immunotherapy.', *Proceedings of the National Academy of Sciences of the United States of America*. United States, 109(43), pp. 17561–17566. doi: 10.1073/pnas.1215397109.

Huisken, J. *et al.* (2004) 'Optical Sectioning Deep Inside Live Embryos by Selective Plane Illumination Microscopy', *Science*, 305(5686), pp. 1007 LP – 1009. doi: 10.1126/science.1100035.

Huisken, J. and Stainier, D. Y. R. (2009) 'Selective plane illumination microscopy techniques in developmental biology.', *Development (Cambridge, England)*. England, 136(12), pp. 1963–1975. doi: 10.1242/dev.022426.

Hurwitz, H. *et al.* (2004) 'Bevacizumab plus irinotecan, fluorouracil, and leucovorin for metastatic colorectal cancer.', *The New England journal of medicine*. United States, 350(23), pp. 2335–2342. doi: 10.1056/NEJMoa032691.

Jährling, N., Becker, K. and Dodt, H.-U. (2009) '3D-reconstruction of blood vessels by ultramicroscopy', *Organogenesis*. Landes Bioscience, 5(4), pp. 227–230. Available at: https://www.ncbi.nlm.nih.gov/pubmed/20539742.

Jain, R. K. (2005) 'Normalization of tumor vasculature: an emerging concept in antiangiogenic therapy.', *Science (New York, N.Y.)*. United States, 307(5706), pp. 58–62. doi: 10.1126/science.1104819.

Jain, R. K. (2014) 'Antiangiogenesis strategies revisited: from starving tumors to alleviating hypoxia.', *Cancer cell*. United States, 26(5), pp. 605–622. doi: 10.1016/j.ccell.2014.10.006.

Jatoi, I. *et al.* (1999) 'Significance of axillary lymph node metastasis in primary breast cancer.', *Journal of clinical oncology : official journal of the American Society of Clinical Oncology*. United States, 17(8), pp. 2334–2340. doi: 10.1200/JCO.1999.17.8.2334.

Ji, R.-R. *et al.* (2012) 'An immune-active tumor microenvironment favors clinical response to ipilimumab.', *Cancer immunology, immunotherapy : CII*. Germany, 61(7), pp. 1019–1031. doi: 10.1007/s00262-011-1172-6.

Johansson-Percival, A. *et al.* (2017) 'De novo induction of intratumoral lymphoid structures and vessel normalization enhances immunotherapy in resistant tumors.', *Nature immunology*. United States, 18(11), pp. 1207–1217. doi: 10.1038/ni.3836.

Jones, G. W. *et al.* (2015) 'Interleukin-27 inhibits ectopic lymphoid-like structure development in early inflammatory arthritis.', *The Journal of experimental medicine*. United States, 212(11), pp. 1793–1802. doi: 10.1084/jem.20132307.

Joshi, K. *et al.* (2019) 'Spatial heterogeneity of the T cell receptor repertoire reflects the mutational landscape in lung cancer.', *Nature medicine*, 25(10), pp. 1549–1559. doi: 10.1038/s41591-019-0592-2.

Joshi, N. S. *et al.* (2015) 'Regulatory T Cells in Tumor-Associated Tertiary Lymphoid Structures Suppress Anti-tumor T Cell Responses.', *Immunity*. United States, 43(3), pp. 579–590. doi: 10.1016/j.immuni.2015.08.006.

Joyce, J. A. and Fearon, D. T. (2015) 'T cell exclusion, immune privilege, and the tumor microenvironment.', *Science (New York, N.Y.)*. United States, 348(6230), pp. 74–80. doi: 10.1126/science.aaa6204.

Kantarjian, H. *et al.* (2017) 'Blinatumomab versus Chemotherapy for Advanced Acute Lymphoblastic Leukemia.', *The New England journal of medicine*. United States, 376(9), pp. 836–847. doi: 10.1056/NEJMoa1609783.

Kaplan, D. H. *et al.* (1998) 'Demonstration of an interferon gamma-dependent tumor surveillance system in immunocompetent mice.', *Proceedings of the National Academy of Sciences of the United States of America*. United States, 95(13), pp. 7556–7561. doi: 10.1073/pnas.95.13.7556.

Kaufman, H. L. *et al.* (2018) 'Updated efficacy of avelumab in patients with previously treated metastatic Merkel cell carcinoma after >/=1 year of follow-up: JAVELIN Merkel 200, a phase 2 clinical trial.', *Journal for immunotherapy of cancer*. England, 6(1), p. 7. doi: 10.1186/s40425-017-0310-x.

Kawashima, H. *et al.* (1990) 'Carbohydrate binding specificities of several poly-N-acetyllactosamine-binding lectins.', *Glycoconjugate journal*. United States, 7(4), pp. 323–334.

Kelch, I. D. *et al.* (2015) 'Organ-wide 3D-imaging and topological analysis of the continuous microvascular network in a murine lymph node.', *Scientific reports*. England, 5, p. 16534. doi: 10.1038/srep16534.

Kim, J. M., Rasmussen, J. P. and Rudensky, A. Y. (2007) 'Regulatory T cells prevent catastrophic autoimmunity throughout the lifespan of mice.', *Nature immunology*. United States, 8(2), pp. 191–197. doi: 10.1038/ni1428.

Klingberg, A. *et al.* (2017) 'Fully Automated Evaluation of Total Glomerular Number and Capillary Tuft Size in Nephritic Kidneys Using Lightsheet Microscopy.', *Journal of the American Society of Nephrology : JASN*. United States, 28(2), pp. 452–459. doi: 10.1681/ASN.2016020232.

Koebel, C. M. *et al.* (2007) 'Adaptive immunity maintains occult cancer in an equilibrium state.', *Nature*. England, 450(7171), pp. 903–907. doi: 10.1038/nature06309.

Kourko, O. *et al.* (2019) 'IL-27, IL-30, and IL-35: A Cytokine Triumvirate in Cancer', *Frontiers in oncology*. Frontiers Media S.A., 9, p. 969. doi: 10.3389/fonc.2019.00969.

Kowala, M. C. and Schoefl, G. I. (1986) 'The popliteal lymph node of the mouse: internal architecture, vascular distribution and lymphatic supply.', *Journal of anatomy*. England, 148, pp. 25–46.

Kratz, A. *et al.* (1996) 'Chronic inflammation caused by lymphotoxin is lymphoid

neogenesis.', *The Journal of experimental medicine*. United States, 183(4), pp. 1461–1472. doi: 10.1084/jem.183.4.1461.

Kruger, S. *et al.* (2019) 'Advances in cancer immunotherapy 2019 – latest trends', *Journal of Experimental & Clinical Cancer Research*, 38(1), p. 268. doi: 10.1186/s13046-019-1266-0.

Krummel, M. F. and Allison, J. P. (1995) 'CD28 and CTLA-4 have opposing effects on the response of T cells to stimulation.', *The Journal of experimental medicine*. United States, 182(2), pp. 459–465. doi: 10.1084/jem.182.2.459.

Kumar, V. *et al.* (2010) 'Global lymphoid tissue remodeling during a viral infection is orchestrated by a B cell-lymphotoxin-dependent pathway.', *Blood*. United States, 115(23), pp. 4725–4733. doi: 10.1182/blood-2009-10-250118.

Kumar, V. *et al.* (2012) 'Optical projection tomography reveals dynamics of HEV growth after immunization with protein plus CFA and features shared with HEVs in acute autoinflammatory lymphadenopathy', *Frontiers in immunology*. Frontiers Research Foundation, 3, p. 282. doi: 10.3389/fimmu.2012.00282.

Kuwabara, S. *et al.* (2019) 'Prognostic relevance of tertiary lymphoid organs following neoadjuvant chemoradiotherapy in pancreatic ductal adenocarcinoma.', *Cancer science*, 110(6), pp. 1853–1862. doi: 10.1111/cas.14023.

Lacorre, D.-A. *et al.* (2004) 'Plasticity of endothelial cells: rapid dedifferentiation of freshly isolated high endothelial venule endothelial cells outside the lymphoid tissue microenvironment.', *Blood*. United States, 103(11), pp. 4164–4172. doi: 10.1182/blood-2003-10-3537.

Lauder, S. N. *et al.* (2020) 'Enhanced antitumor immunity through sequential targeting of PI3Kδ and LAG3.', *Journal for immunotherapy of cancer*, 8(2). doi: 10.1136/jitc-2020-000693.

Leach, D. R., Krummel, M. F. and Allison, J. P. (1996) 'Enhancement of antitumor immunity by CTLA-4 blockade.', *Science (New York, N.Y.)*. United States, 271(5256), pp. 1734–1736. doi: 10.1126/science.271.5256.1734.

Lee, C.-L. *et al.* (2019) 'Mutational landscape in genetically engineered, carcinogen-induced, and radiation-induced mouse sarcoma.', *JCI insight*, 4(13). doi: 10.1172/jci.insight.128698.

Lee, M. *et al.* (2014) 'Transcriptional programs of lymphoid tissue capillary and high endothelium reveal control mechanisms for lymphocyte homing.', *Nature immunology*.
United States, 15(10), pp. 982–995. doi: 10.1038/ni.2983.

Lee, S. Y. *et al.* (2012) '2011 Young Surgeon's Award Winner: high endothelial venules: a novel prognostic marker in cancer metastasis and the missing link?', *Annals of the Academy of Medicine, Singapore*. Singapore, 41(1), pp. 21–28.

Liang, J. J. *et al.* (2010) 'High levels of expression of human stromal cell-derived

factor-1 are associated with worse prognosis in patients with stage II pancreatic ductal adenocarcinoma.', *Cancer epidemiology, biomarkers & prevention : a publication of the American Association for Cancer Research, cosponsored by the American Society of Preventive Oncology*. United States, 19(10), pp. 2598–2604. doi: 10.1158/1055-9965.EPI-10-0405.

Liao, S. and Ruddle, N. H. (2006) 'Synchrony of high endothelial venules and lymphatic vessels revealed by immunization.', *Journal of immunology (Baltimore, Md. : 1950)*. United States, 177(5), pp. 3369–3379. doi: 10.4049/jimmunol.177.5.3369.

Link, A. *et al.* (2007) 'Fibroblastic reticular cells in lymph nodes regulate the homeostasis of naive T cells.', *Nature immunology*. United States, 8(11), pp. 1255–1265. doi: 10.1038/ni1513.

Lucchesi, D. *et al.* (2020) 'Impaired IL-27 Mediated Control of CD4+ T Cell Function Impacts on Ectopic Lymphoid Structure Formation in Patients with Sjögren's Syndrome', *Arthritis & Rheumatology*. John Wiley & Sons, Ltd, n/a(n/a). doi: 10.1002/art.41289.

Lugo-Hernandez, E. *et al.* (2017) '3D visualization and quantification of microvessels in the whole ischemic mouse brain using solvent-based clearing and light sheet microscopy', *Journal of Cerebral Blood Flow & Metabolism*. SAGE Publications Ltd STM, 37(10), pp. 3355–3367. doi: 10.1177/0271678X17698970.

Lukashev, M. *et al.* (2006) 'Targeting the lymphotoxin-beta receptor with agonist antibodies as a potential cancer therapy.', *Cancer research*. United States, 66(19), pp. 9617–9624. doi: 10.1158/0008-5472.CAN-06-0217.

Luke, J. J. *et al.* (2019) 'WNT/beta-catenin Pathway Activation Correlates with Immune Exclusion across Human Cancers.', *Clinical cancer research : an official journal of the American Association for Cancer Research*. United States, 25(10), pp. 3074–3083. doi: 10.1158/1078-0432.CCR-18-1942.

Lund, J. M. *et al.* (2008) 'Coordination of early protective immunity to viral infection by regulatory T cells.', *Science (New York, N.Y.)*. United States, 320(5880), pp. 1220–1224. doi: 10.1126/science.1155209.

Luther, S. A. *et al.* (2000) 'BLC expression in pancreatic islets causes B cell recruitment and lymphotoxin-dependent lymphoid neogenesis.', *Immunity*. United States, 12(5), pp. 471–481. doi: 10.1016/s1074-7613(00)80199-5.

Maeda, T. *et al.* (2018) 'Immune-mediated antitumor effect of a transplanted lymph node.', *International journal of cancer*. United States, 143(5), pp. 1224–1235. doi: 10.1002/ijc.31414.

Makkouk, A. and Weiner, G. J. (2015) 'Cancer immunotherapy and breaking immune tolerance: new approaches to an old challenge.', *Cancer research*. United States, 75(1), pp. 5–10. doi: 10.1158/0008-5472.CAN-14-2538.

Mandelboim, O. *et al.* (1994) 'CTL induction by a tumour-associated antigen

octapeptide derived from a murine lung carcinoma.', *Nature*. England, 369(6475), pp. 67–71. doi: 10.1038/369067a0.

Manning, C. S. *et al.* (2013) 'Intravital imaging reveals conversion between distinct tumor vascular morphologies and localized vascular response to Sunitinib', *IntraVital*. Taylor & Francis, 2(1), p. e24790. doi: 10.4161/intv.24790.

La Manno, G. *et al.* (2018) 'RNA velocity of single cells.', *Nature*, 560(7719), pp. 494–498. doi: 10.1038/s41586-018-0414-6.

Mariathasan, S. *et al.* (2018) 'TGFβ attenuates tumour response to PD-L1 blockade by contributing to exclusion of T cells', *Nature*, 554(7693), pp. 544–548. doi: 10.1038/nature25501.

Martin, J. D., Seano, G. and Jain, R. K. (2019) 'Normalizing Function of Tumor Vessels: Progress, Opportunities, and Challenges.', *Annual review of physiology*. United States, 81, pp. 505–534. doi: 10.1146/annurev-physiol-020518-114700.

Martinet, L. *et al.* (2011) 'Human solid tumors contain high endothelial venules: association with T- and B-lymphocyte infiltration and favorable prognosis in breast cancer.', *Cancer research*. United States, 71(17), pp. 5678–5687. doi: 10.1158/0008-5472.CAN-11-0431.

Martinet, L. *et al.* (2012) 'High endothelial venules (HEVs) in human melanoma lesions: Major gateways for tumor-infiltrating lymphocytes.', *Oncoimmunology*, 1(6), pp. 829–839. doi: 10.4161/onci.20492.

Martinet, L. *et al.* (2013) 'High endothelial venule blood vessels for tumor-infiltrating lymphocytes are associated with lymphotoxin beta-producing dendritic cells in human breast cancer.', *Journal of immunology (Baltimore, Md. : 1950)*. United States, 191(4), pp. 2001–2008. doi: 10.4049/jimmunol.1300872.

Matrougui, K. *et al.* (2011) 'Natural regulatory T cells control coronary arteriolar endothelial dysfunction in hypertensive mice.', *The American journal of pathology*. United States, 178(1), pp. 434–441. doi: 10.1016/j.ajpath.2010.11.034.

Maude, S. L. *et al.* (2018) 'Tisagenlecleucel in Children and Young Adults with B-Cell Lymphoblastic Leukemia.', *The New England journal of medicine*. United States, 378(5), pp. 439–448. doi: 10.1056/NEJMoa1709866.

Mayer, J. *et al.* (2012) 'Quantitative measurements in 3-dimensional datasets of mouse lymph nodes resolve organ-wide functional dependencies.', *Computational and mathematical methods in medicine*, 2012, p. 128431. doi: 10.1155/2012/128431.

Mebius, R. E. *et al.* (1996) 'A developmental switch in lymphocyte homing receptor and endothelial vascular addressin expression regulates lymphocyte homing and permits CD4+ CD3- cells to colonize lymph nodes.', *Proceedings of the National Academy of Sciences of the United States of America*. United States, 93(20), pp. 11019–11024. doi: 10.1073/pnas.93.20.11019.

Mellman, I. *et al.* (2016) 'De-Risking Immunotherapy: Report of a Consensus Workshop of the Cancer Immunotherapy Consortium of the Cancer Research Institute.', *Cancer immunology research*. United States, 4(4), pp. 279–288. doi: 10.1158/2326-6066.CIR-16-0045.

Milutinovic, S. *et al.* (2020) 'The Dual Role of High Endothelial Venules in Cancer Progression versus Immunity.', *Trends in cancer*. United States. doi: 10.1016/j.trecan.2020.10.001.

Mionnet, C. *et al.* (2011) 'High endothelial venules as traffic control points maintaining lymphocyte population homeostasis in lymph nodes.', *Blood*, 118(23), pp. 6115–6122. doi: 10.1182/blood-2011-07-367409.

Mittal, D. *et al.* (2014) 'New insights into cancer immunoediting and its three component phases--elimination, equilibrium and escape.', *Current opinion in immunology*. England, 27, pp. 16–25. doi: 10.1016/j.coi.2014.01.004.

Miyasaka, M. and Tanaka, T. (2004) 'Lymphocyte trafficking across high endothelial venules: dogmas and enigmas.', *Nature reviews. Immunology*. England, 4(5), pp. 360–370. doi: 10.1038/nri1354.

Mohammed, R. A. A. *et al.* (2007) 'Improved methods of detection of lymphovascular invasion demonstrate that it is the predominant method of vascular invasion in breast cancer and has important clinical consequences.', *The American journal of surgical pathology*. United States, 31(12), pp. 1825–1833. doi: 10.1097/PAS.0b013e31806841f6.

Mondor, I. *et al.* (2016) 'Clonal Proliferation and Stochastic Pruning Orchestrate Lymph Node Vasculature Remodeling.', *Immunity*. United States, 45(4), pp. 877–888. doi: 10.1016/j.immuni.2016.09.017.

Motz, G. T. *et al.* (2014) 'Tumor endothelium FasL establishes a selective immune barrier promoting tolerance in tumors.', *Nature medicine*. United States, 20(6), pp. 607–615. doi: 10.1038/nm.3541.

Moussion, C. and Girard, J.-P. (2011) 'Dendritic cells control lymphocyte entry to lymph nodes through high endothelial venules.', *Nature*. England, 479(7374), pp. 542–546. doi: 10.1038/nature10540.

Mumprecht, V., Roudnicky, F. and Detmar, M. (2012) 'Inflammation-induced lymph node lymphangiogenesis is reversible.', *The American journal of pathology*. United States, 180(3), pp. 874–879. doi: 10.1016/j.ajpath.2011.11.010.

Nagy, J. A. *et al.* (2010) 'Heterogeneity of the tumor vasculature', *Seminars in thrombosis and hemostasis*. 2010/05/20, 36(3), pp. 321–331. doi: 10.1055/s-0030-1253454.

Naito, Y. *et al.* (1998) 'CD8+ T cells infiltrated within cancer cell nests as a prognostic factor in human colorectal cancer.', *Cancer research*. United States, 58(16), pp. 3491–3494.

Nathanson, S. D. *et al.* (2010) 'The role of lymph node metastasis in the systemic dissemination of breast cancer', *Indian journal of surgical oncology*. 2011/03/29. Springer-Verlag, 1(4), pp. 313–322. doi: 10.1007/s13193-011-0063-9.

Natividad, K. D. T. *et al.* (2013) 'Interleukin-27 signaling promotes immunity against endogenously arising murine tumors', *PloS one*. 2013/03/12. Public Library of Science, 8(3), pp. e57469–e57469. doi: 10.1371/journal.pone.0057469.

Neyt, K. *et al.* (2012) 'Tertiary lymphoid organs in infection and autoimmunity.', *Trends in immunology*. England, 33(6), pp. 297–305. doi: 10.1016/j.it.2012.04.006.

Ntziachristos, V. (2010) 'Going deeper than microscopy: the optical imaging frontier in biology.', *Nature methods*. United States, 7(8), pp. 603–614. doi: 10.1038/nmeth.1483.

Oldstone, M. B. A. (2016) 'An Odyssey to Viral Pathogenesis.', *Annual review of pathology*. United States, 11, pp. 1–19. doi: 10.1146/annurev-pathol-012615-044107.

Onder, L. *et al.* (2013) 'Endothelial cell-specific lymphotoxin-beta receptor signaling is critical for lymph node and high endothelial venule formation.', *The Journal of experimental medicine*. United States, 210(3), pp. 465–473. doi: 10.1084/jem.20121462.

Ondondo, B. *et al.* (2014) 'Progression of carcinogen-induced fibrosarcomas is associated with the accumulation of naïve CD4+ T cells via blood vessels and lymphatics.', *International journal of cancer*, 134(9), pp. 2156–2167. doi: 10.1002/ijc.28556.

Ott, P. A. *et al.* (2017) 'An immunogenic personal neoantigen vaccine for patients with melanoma', *Nature*, 547(7662), pp. 217–221. doi: 10.1038/nature22991.

Otto, B. *et al.* (2014) 'Molecular changes in pre-metastatic lymph nodes of esophageal cancer patients', *PloS one*. Public Library of Science, 9(7), pp. e102552–e102552. doi: 10.1371/journal.pone.0102552.

Ozga, A. J. *et al.* (2016) 'pMHC affinity controls duration of CD8+ T cell-DC interactions and imprints timing of effector differentiation versus expansion.', *The Journal of experimental medicine*. United States, 213(12), pp. 2811–2829. doi: 10.1084/jem.20160206.

Pages, F. *et al.* (2005) 'Effector memory T cells, early metastasis, and survival in colorectal cancer.', *The New England journal of medicine*. United States, 353(25), pp. 2654–2666. doi: 10.1056/NEJMoa051424.

Pages, F. *et al.* (2009) 'In situ cytotoxic and memory T cells predict outcome in patients with early-stage colorectal cancer.', *Journal of clinical oncology : official journal of the American Society of Clinical Oncology*. United States, 27(35), pp. 5944–5951. doi: 10.1200/JCO.2008.19.6147.

Pages, F. *et al.* (2010) 'Immune infiltration in human tumors: a prognostic factor

that should not be ignored.', *Oncogene*. England, 29(8), pp. 1093–1102. doi: 10.1038/onc.2009.416.

Pan, C. *et al.* (2016) 'Shrinkage-mediated imaging of entire organs and organisms using uDISCO.', *Nature methods*. United States, 13(10), pp. 859–867. doi: 10.1038/nmeth.3964.

Pan, C. *et al.* (2019) 'Deep Learning Reveals Cancer Metastasis and Therapeutic Antibody Targeting in the Entire Body.', *Cell*. United States, 179(7), pp. 1661-1676.e19. doi: 10.1016/j.cell.2019.11.013.

Park, C., Hwang, I.-Y. and Kehrl, J. H. (2016) 'Intravital Two-Photon Imaging of Lymphocytes Crossing High Endothelial Venules and Cortical Lymphatics in the Inguinal Lymph Node.', *Methods in molecular biology (Clifton, N.J.)*. United States, 1407, pp. 195–206. doi: 10.1007/978-1-4939-3480-5_15.

Park, H. *et al.* (2014) 'Distinct roles of DKK1 and DKK2 in tumor angiogenesis.', *Angiogenesis*, 17(1), pp. 221–234. doi: 10.1007/s10456-013-9390-5.

van de Pavert, S. A. and Mebius, R. E. (2014) 'Development of secondary lymphoid organs in relation to lymphatic vasculature.', *Advances in anatomy, embryology, and cell biology*. Germany, 214, pp. 81–91. doi: 10.1007/978-3-7091-1646-3_7.

Peinado, H. *et al.* (2017) 'Pre-metastatic niches: organ-specific homes for metastases', *Nature Reviews Cancer*, 17(5), pp. 302–317. doi: 10.1038/nrc.2017.6.

Pereira, E. R. *et al.* (2018) 'Lymph node metastases can invade local blood vessels, exit the node, and colonize distant organs in mice.', *Science (New York, N.Y.)*. United States, 359(6382), pp. 1403–1407. doi: 10.1126/science.aal3622.

Peske, J. D. *et al.* (2015) 'Effector lymphocyte-induced lymph node-like vasculature enables naive T-cell entry into tumours and enhanced anti-tumour immunity.', *Nature communications*. England, 6, p. 7114. doi: 10.1038/ncomms8114.

Peters, A. *et al.* (2011) 'Th17 cells induce ectopic lymphoid follicles in central nervous system tissue inflammation.', *Immunity*. United States, 35(6), pp. 986–996. doi: 10.1016/j.immuni.2011.10.015.

Peterson, T. E. *et al.* (2016) 'Dual inhibition of Ang-2 and VEGF receptors normalizes tumor vasculature and prolongs survival in glioblastoma by altering macrophages.', *Proceedings of the National Academy of Sciences of the United States of America*. United States, 113(16), pp. 4470–4475. doi: 10.1073/pnas.1525349113.

Pfeiffer, F. *et al.* (2008) 'Distinct molecular composition of blood and lymphatic vascular endothelial cell junctions establishes specific functional barriers within the peripheral lymph node.', *European journal of immunology*. Germany, 38(8), pp. 2142–2155. doi: 10.1002/eji.200838140.

Pflanz, S. *et al.* (2002) 'IL-27, a heterodimeric cytokine composed of EBI3 and p28 protein, induces proliferation of naive CD4+ T cells.', *Immunity*. United States, 16(6), pp. 779–790. doi: 10.1016/s1074-7613(02)00324-2.

Pires, A. (2020) *Exploring the reciprocal relationship between the immune system and the tumour microenvironment.* Cardiff University.

Pires, A. *et al.* (2020) 'Immune Remodelling of the Extracellular Matrix Drives Loss of Cancer Stem Cells and Tumor Rejection.', *Cancer immunology research*. United States. doi: 10.1158/2326-6066.CIR-20-0070.

Poortmans, P. M. *et al.* (2015) 'Internal Mammary and Medial Supraclavicular Irradiation in Breast Cancer', *New England Journal of Medicine*. Massachusetts Medical Society, 373(4), pp. 317–327. doi: 10.1056/NEJMoa1415369.

Porter, G. A., Palade, G. E. and Milici, A. J. (1990) 'Differential binding of the lectins Griffonia simplicifolia I and Lycopersicon esculentum to microvascular endothelium: organ-specific localization and partial glycoprotein characterization.', *European journal of cell biology*. Germany, 51(1), pp. 85–95.

Preibisch, S., Saalfeld, S. and Tomancak, P. (2009) 'Globally optimal stitching of tiled 3D microscopic image acquisitions', *Bioinformatics (Oxford, England)*. 2009/04/03. Oxford University Press, 25(11), pp. 1463–1465. doi: 10.1093/bioinformatics/btp184.

Qian, C.-N. *et al.* (2006) 'Preparing the "soil": the primary tumor induces vasculature reorganization in the sentinel lymph node before the arrival of metastatic cancer cells.', *Cancer research*. United States, 66(21), pp. 10365–10376. doi: 10.1158/0008-5472.CAN-06-2977.

Qian, C.-N., Resau, J. H. and Teh, B. T. (2007) 'Prospects for vasculature reorganization in sentinel lymph nodes.', *Cell cycle (Georgetown, Tex.)*. United States, 6(5), pp. 514–517. doi: 10.4161/cc.6.5.3931.

Quintana, L. and Sharpe, J. (2011) 'Preparation of mouse embryos for optical projection tomography imaging.', *Cold Spring Harbor protocols*. United States, 2011(6), pp. 664–669. doi: 10.1101/pdb.prot5639.

Renier, N. *et al.* (2014) 'iDISCO: a simple, rapid method to immunolabel large tissue samples for volume imaging.', *Cell*. United States, 159(4), pp. 896–910. doi: 10.1016/j.cell.2014.10.010.

Reynaud, E. G. *et al.* (2015) 'Guide to light-sheet microscopy for adventurous biologists.', *Nature methods*. United States, 12(1), pp. 30–34. doi: 10.1038/nmeth.3222.

Richardson, D. S. and Lichtman, J. W. (2015) 'Clarifying Tissue Clearing', *Cell*, 162(2), pp. 246–257. doi: 10.1016/j.cell.2015.06.067.

Rigamonti, N. *et al.* (2014) 'Role of angiopoietin-2 in adaptive tumor resistance to VEGF signaling blockade.', *Cell reports*. United States, 8(3), pp. 696–706. doi: 10.1016/j.celrep.2014.06.059.

Rivera, L. B. and Bergers, G. (2015) ‘Tumor angiogenesis, from foe to friend’, *Science*, 349(6249), pp. 694 LP – 695. doi: 10.1126/science.aad0862.

Robert, C. *et al.* (2011) ‘Ipilimumab plus Dacarbazine for Previously Untreated Metastatic Melanoma’, *New England Journal of Medicine*. Massachusetts Medical Society, 364(26), pp. 2517–2526. doi: 10.1056/NEJMoa1104621.

Robert, C., Ribas, A., *et al.* (2014) ‘Anti-programmed-death-receptor-1 treatment with pembrolizumab in ipilimumab-refractory advanced melanoma: a randomised dose-comparison cohort of a phase 1 trial.’, *Lancet (London, England)*. England, 384(9948), pp. 1109–1117. doi: 10.1016/S0140-6736(14)60958-2.

Robert, C., Long, G. V, *et al.* (2014) ‘Nivolumab in Previously Untreated Melanoma without BRAF Mutation’, *New England Journal of Medicine*. Massachusetts Medical Society, 372(4), pp. 320–330. doi: 10.1056/NEJMoa1412082.

Roberts, E. W. *et al.* (2013) ‘Depletion of stromal cells expressing fibroblast activation protein-alpha from skeletal muscle and bone marrow results in cachexia and anemia.’, *The Journal of experimental medicine*. United States, 210(6), pp. 1137–1151. doi: 10.1084/jem.20122344.

Roberts, N. *et al.* (2006) ‘Inhibition of VEGFR-3 activation with the antagonistic antibody more potently suppresses lymph node and distant metastases than inactivation of VEGFR-2.’, *Cancer research*. United States, 66(5), pp. 2650–2657. doi: 10.1158/0008-5472.CAN-05-1843.

Robertson, R. T. *et al.* (2015) ‘Use of labeled tomato lectin for imaging vasculature structures.’, *Histochemistry and cell biology*. Germany, 143(2), pp. 225–234. doi: 10.1007/s00418-014-1301-3.

Rooney, M. S. *et al.* (2015) ‘Molecular and genetic properties of tumors associated with local immune cytolytic activity.’, *Cell*. United States, 160(1–2), pp. 48–61. doi: 10.1016/j.cell.2014.12.033.

Sade-Feldman, M. *et al.* (2017) ‘Resistance to checkpoint blockade therapy through inactivation of antigen presentation.’, *Nature communications*. England, 8(1), p. 1136. doi: 10.1038/s41467-017-01062-w.

Sahin, U. *et al.* (2017) ‘Personalized RNA mutanome vaccines mobilize poly-specific therapeutic immunity against cancer’, *Nature*, 547(7662), pp. 222–226. doi: 10.1038/nature23003.

Salcedo, R. *et al.* (2004) ‘IL-27 mediates complete regression of orthotopic primary and metastatic murine neuroblastoma tumors: role for CD8+ T cells.’, *Journal of immunology (Baltimore, Md. : 1950)*. United States, 173(12), pp. 7170–7182. doi: 10.4049/jimmunol.173.12.7170.

Salmon, H. *et al.* (2012) ‘Matrix architecture defines the preferential localization and migration of T cells into the stroma of human lung tumors.’, *The Journal of clinical investigation*. United States, 122(3), pp. 899–910. doi: 10.1172/JCI45817.

Samimi, M. (2019) ‘Immune Checkpoint Inhibitors and Beyond: An Overview of Immune-Based Therapies in Merkel Cell Carcinoma.’, *American journal of clinical dermatology*. New Zealand, 20(3), pp. 391–407. doi: 10.1007/s40257-019-00427-9.

Saupe, F. *et al.* (2013) ‘Tenascin-C downregulates wnt inhibitor dickkopf-1, promoting tumorigenesis in a neuroendocrine tumor model.’, *Cell reports*. United States, 5(2), pp. 482–492. doi: 10.1016/j.celrep.2013.09.014.

Sautes-Fridman, C. *et al.* (2019) ‘Tertiary lymphoid structures in the era of cancer immunotherapy.’, *Nature reviews. Cancer*. England, 19(6), pp. 307–325. doi: 10.1038/s41568-019-0144-6.

Schadendorf, D. *et al.* (2015) ‘Pooled Analysis of Long-Term Survival Data From Phase II and Phase III Trials of Ipilimumab in Unresectable or Metastatic Melanoma.’, *Journal of clinical oncology : official journal of the American Society of Clinical Oncology*. United States, 33(17), pp. 1889–1894. doi: 10.1200/JCO.2014.56.2736.

Schmittnaegel, M. *et al.* (2017) ‘Dual angiopoietin-2 and VEGFA inhibition elicits antitumor immunity that is enhanced by PD-1 checkpoint blockade.’, *Science translational medicine*. United States, 9(385). doi: 10.1126/scitranslmed.aak9670.

Schmittnaegel, M. and De Palma, M. (2017) ‘Reprogramming Tumor Blood Vessels for Enhancing Immunotherapy.’, *Trends in cancer*. United States, 3(12), pp. 809–812. doi: 10.1016/j.trecan.2017.10.002.

Schneider, R. *et al.* (2011) ‘IL-27 increases the proliferation and effector functions of human naive CD8+ T lymphocytes and promotes their development into Tc1 cells.’, *European journal of immunology*. Germany, 41(1), pp. 47–59. doi: 10.1002/eji.201040804.

Schrama, D. *et al.* (2001) ‘Targeting of lymphotoxin-alpha to the tumor elicits an efficient immune response associated with induction of peripheral lymphoid-like tissue.’, *Immunity*. United States, 14(2), pp. 111–121. doi: 10.1016/s1074-7613(01)00094-2.

Schrama, D. *et al.* (2008) ‘Immunological tumor destruction in a murine melanoma model by targeted LTalpha independent of secondary lymphoid tissue.’, *Cancer immunology, immunotherapy : CII*. Germany, 57(1), pp. 85–95. doi: 10.1007/s00262-007-0352-x.

Schreiber, R. D., Old, L. J. and Smyth, M. J. (2011) ‘Cancer Immunoediting: Integrating Immunity’s Roles in Cancer Suppression and Promotion’, *Science*, 331(6024), pp. 1565 LP – 1570. doi: 10.1126/science.1203486.

Schumacher, T. N. and Schreiber, R. D. (2015) ‘Neoantigens in cancer immunotherapy.’, *Science (New York, N.Y.)*. United States, 348(6230), pp. 69–74. doi: 10.1126/science.aaa4971.

Seo, J., Choe, M. and Kim, S.-Y. (2016) ‘Clearing and Labeling Techniques for Large-Scale Biological Tissues.’, *Molecules and cells*. Korea (South), 39(6), pp. 439–446. doi: 10.14348/molcells.2016.0088.

Shankaran, V. *et al.* (2001) ‘IFNgamma and lymphocytes prevent primary tumour development and shape tumour immunogenicity.’, *Nature*. England, 410(6832), pp. 1107–1111. doi: 10.1038/35074122.

Sharma, P. and Allison, J. P. (2015) ‘The future of immune checkpoint therapy.’, *Science (New York, N.Y.)*. United States, 348(6230), pp. 56–61. doi: 10.1126/science.aaa8172.

Sharpe, J. (2004) ‘Optical projection tomography.’, *Annual review of biomedical engineering*. United States, 6, pp. 209–228. doi: 10.1146/annurev.bioeng.6.040803.140210.

Shen, H. *et al.* (2014) ‘Alterations of high endothelial venules in primary and metastatic tumors are correlated with lymph node metastasis of oral and pharyngeal carcinoma.’, *Cancer biology & therapy*, 15(3), pp. 342–349. doi: 10.4161/cbt.27328.

Shields, J. D. *et al.* (2010) ‘Induction of lymphoidlike stroma and immune escape by tumors that express the chemokine CCL21.’, *Science (New York, N.Y.)*. United States, 328(5979), pp. 749–752. doi: 10.1126/science.1185837.

Shinkai, Y. *et al.* (1992) ‘RAG-2-deficient mice lack mature lymphocytes owing to inability to initiate V(D)J rearrangement.’, *Cell*. United States, 68(5), pp. 855–867. doi: 10.1016/0092-8674(92)90029-c.

Shrimali, R. K. *et al.* (2010) ‘Antiangiogenic agents can increase lymphocyte infiltration into tumor and enhance the effectiveness of adoptive immunotherapy of cancer.’, *Cancer research*. United States, 70(15), pp. 6171–6180. doi: 10.1158/0008-5472.CAN-10-0153.

Siedentopf, H. and Zsigmondy, R. (1902) ‘Uber Sichtbarmachung und Größenbestimmung ultramikoskopischer Teilchen, mit besonderer Anwendung auf Goldrubingläser’, *Annalen der Physik*. John Wiley & Sons, Ltd, 315(1), pp. 1–39. doi: 10.1002/andp.19023150102.

Small, E. J. *et al.* (2006) ‘Placebo-controlled phase III trial of immunologic therapy with sipuleucel-T (APC8015) in patients with metastatic, asymptomatic hormone refractory prostate cancer.’, *Journal of clinical oncology : official journal of the American Society of Clinical Oncology*. United States, 24(19), pp. 3089–3094. doi: 10.1200/JCO.2005.04.5252.

Soderberg, K. A. *et al.* (2005) ‘Innate control of adaptive immunity via remodeling of lymph node feed arteriole.’, *Proceedings of the National Academy of Sciences of the United States of America*. United States, 102(45), pp. 16315–16320. doi: 10.1073/pnas.0506190102.

Sporn, M. B. (1996) ‘The war on cancer.’, *Lancet (London, England)*. England, 347(9012), pp. 1377–1381. doi: 10.1016/s0140-6736(96)91015-6.

Spranger, S. *et al.* (2016) 'Density of immunogenic antigens does not explain the presence or absence of the T-cell-inflamed tumor microenvironment in melanoma.', *Proceedings of the National Academy of Sciences of the United States of America*. United States, 113(48), pp. E7759–E7768. doi: 10.1073/pnas.1609376113.

Spranger, S. *et al.* (2017) 'Tumor-Residing Batf3 Dendritic Cells Are Required for Effector T Cell Trafficking and Adoptive T Cell Therapy.', *Cancer cell*. United States, 31(5), pp. 711-723.e4. doi: 10.1016/j.ccell.2017.04.003.

Spranger, S., Bao, R. and Gajewski, T. F. (2015) 'Melanoma-intrinsic β-catenin signalling prevents anti-tumour immunity', *Nature*, 523(7559), pp. 231–235. doi: 10.1038/nature14404.

Spranger, S. and Gajewski, T. F. (2018a) 'Impact of oncogenic pathways on evasion of antitumour immune responses.', *Nature reviews. Cancer*. England, 18(3), pp. 139–147. doi: 10.1038/nrc.2017.117.

Spranger, S. and Gajewski, T. F. (2018b) 'Mechanisms of Tumor Cell–Intrinsic Immune Evasion', *Annual Review of Cancer Biology*. Annual Reviews, 2(1), pp. 213–228. doi: 10.1146/annurev-cancerbio-030617-050606.

Street, S. E., Cretney, E. and Smyth, M. J. (2001) 'Perforin and interferon-gamma activities independently control tumor initiation, growth, and metastasis.', *Blood*. United States, 97(1), pp. 192–197. doi: 10.1182/blood.v97.1.192.

Stumhofer, J. S. *et al.* (2006) 'Interleukin 27 negatively regulates the development of interleukin 17-producing T helper cells during chronic inflammation of the central nervous system.', *Nature immunology*. United States, 7(9), pp. 937–945. doi: 10.1038/ni1376.

Stutman, O. (1975) 'Immunodepression and malignancy.', *Advances in cancer research*. United States, 22, pp. 261–422. doi: 10.1016/s0065-230x(08)60179-7.

Susaki, E. A. *et al.* (2015) 'Advanced CUBIC protocols for whole-brain and whole-body clearing and imaging', *Nature Protocols*. Nature Publishing Group, 10(11), pp. 1709–1727. doi: 10.1038/nprot.2015.085.

Susaki, E. A. and Ueda, H. R. (2016) 'Whole-body and Whole-Organ Clearing and Imaging Techniques with Single-Cell Resolution: Toward Organism-Level Systems Biology in Mammals.', *Cell chemical biology*. United States, 23(1), pp. 137–157. doi: 10.1016/j.chembiol.2015.11.009.

Takatori, H. *et al.* (2009) 'Lymphoid tissue inducer-like cells are an innate source of IL-17 and IL-22.', *The Journal of experimental medicine*. United States, 206(1), pp. 35–41. doi: 10.1084/jem.20072713.

Takeda, A. *et al.* (2003) 'Cutting edge: role of IL-27/WSX-1 signaling for induction of T-bet through activation of STAT1 during initial Th1 commitment.', *Journal of immunology (Baltimore, Md. : 1950)*. United States, 170(10), pp. 4886–4890. doi: 10.4049/jimmunol.170.10.4886.

Tanaka, N. *et al.* (2017) 'Whole-tissue biopsy phenotyping of three-dimensional tumours reveals patterns of cancer heterogeneity', *Nature Biomedical Engineering*, 1(10), pp. 796–806. doi: 10.1038/s41551-017-0139-0.

Tang, H. *et al.* (2016) 'Facilitating T Cell Infiltration in Tumor Microenvironment Overcomes Resistance to PD-L1 Blockade.', *Cancer cell*. United States, 29(3), pp. 285–296. doi: 10.1016/j.ccell.2016.02.004.

Tauriello, D. V. F. *et al.* (2018) 'TGFbeta drives immune evasion in genetically reconstituted colon cancer metastasis.', *Nature*. England, 554(7693), pp. 538–543. doi: 10.1038/nature25492.

Teng, M. W. L. *et al.* (2012) 'Opposing roles for IL-23 and IL-12 in maintaining occult cancer in an equilibrium state.', *Cancer research*. United States, 72(16), pp. 3987–3996. doi: 10.1158/0008-5472.CAN-12-1337.

Thomé, R. (1898) 'Endothelien als Phagocyten (aus den Lymphdrüsen von Macacus cynomolgus)', *Archiv für mikroskopische Anatomie*, 52(4), pp. 820–842. doi: 10.1007/BF02977038.

Todorov, M. I. *et al.* (2020) 'Machine learning analysis of whole mouse brain vasculature.', *Nature methods*. United States, 17(4), pp. 442–449. doi: 10.1038/s41592-020-0792-1.

De Togni, P. *et al.* (2014) 'Pillars article: Abnormal development of peripheral lymphoid organs in mice deficient in lymphotoxin. Science. 1994. 264: 703-707.', *Journal of immunology (Baltimore, Md. : 1950)*. United States, 192(5), pp. 2010–2014.

Topalian, S. L. *et al.* (2012) 'Safety, activity, and immune correlates of anti-PD-1 antibody in cancer.', *The New England journal of medicine*. United States, 366(26), pp. 2443–2454. doi: 10.1056/NEJMoa1200690.

Townsend, S. E. and Allison, J. P. (1993) 'Tumor rejection after direct costimulation of CD8+ T cells by B7-transfected melanoma cells', *Science*, 259(5093), pp. 368 LP – 370. doi: 10.1126/science.7678351.

Trinchieri, G., Pflanz, S. and Kastelein, R. A. (2003) 'The IL-12 family of heterodimeric cytokines: new players in the regulation of T cell responses.', *Immunity*. United States, 19(5), pp. 641–644. doi: 10.1016/s1074-7613(03)00296-6.

Tumeh, P. C. *et al.* (2014) 'PD-1 blockade induces responses by inhibiting adaptive immune resistance.', *Nature*. England, 515(7528), pp. 568–571. doi: 10.1038/nature13954.

Tzeng, T.-C. *et al.* (2010) 'CD11c(hi) dendritic cells regulate the re-establishment of vascular quiescence and stabilization after immune stimulation of lymph nodes.', *Journal of immunology (Baltimore, Md. : 1950)*. United States, 184(8), pp. 4247–4257. doi: 10.4049/jimmunol.0902914.

Vacchelli, E. *et al.* (2013) 'Trial Watch', *OncoImmunology*. Taylor & Francis, 2(5),

p. e24238. doi: 10.4161/onci.24238.

Veerman, K. *et al.* (2019) 'Single-Cell Analysis Reveals Heterogeneity of High Endothelial Venules and Different Regulation of Genes Controlling Lymphocyte Entry to Lymph Nodes', *Cell Reports*, 26(11), pp. 3116-3131.e5. doi: https://doi.org/10.1016/j.celrep.2019.02.042.

Veiga-Fernandes, H. *et al.* (2007) 'Tyrosine kinase receptor RET is a key regulator of Peyer's patch organogenesis.', *Nature*. England, 446(7135), pp. 547–551. doi: 10.1038/nature05597.

Walunas, T. L. *et al.* (1994) 'CTLA-4 can function as a negative regulator of T cell activation.', *Immunity*. United States, 1(5), pp. 405–413. doi: 10.1016/1074-7613(94)90071-x.

Warnock, R. A. *et al.* (1998) 'Molecular mechanisms of lymphocyte homing to peripheral lymph nodes.', *The Journal of experimental medicine*. United States, 187(2), pp. 205–216. doi: 10.1084/jem.187.2.205.

Webster, B. *et al.* (2006) 'Regulation of lymph node vascular growth by dendritic cells.', *The Journal of experimental medicine*. United States, 203(8), pp. 1903–1913. doi: 10.1084/jem.20052272.

Wexler, H. and Rosenberg, S. A. (1979) 'Pulmonary metastases from autochthonous 3-methylcholanthrene-induced murine tumors.', *Journal of the National Cancer Institute*. United States, 63(6), pp. 1393–1395.

Whelan, T. J. *et al.* (2015) 'Regional Nodal Irradiation in Early-Stage Breast Cancer.', *The New England journal of medicine*. United States, 373(4), pp. 307–316. doi: 10.1056/NEJMoa1415340.

Wirsing, A. M. *et al.* (2016) 'Presence of tumour high-endothelial venules is an independent positive prognostic factor and stratifies patients with advanced-stage oral squamous cell carcinoma.', *Tumour biology : the journal of the International Society for Oncodevelopmental Biology and Medicine*. United States, 37(2), pp. 2449–2459. doi: 10.1007/s13277-015-4036-4.

Wolchok, J. D. *et al.* (2013) 'Nivolumab plus Ipilimumab in Advanced Melanoma', *New England Journal of Medicine*. Massachusetts Medical Society, 369(2), pp. 122–133. doi: 10.1056/NEJMoa1302369.

World Health Organisation, https://www.who.int/health-topics/cancer, Accessed November 2020.

Zang, X. *et al.* (2010) 'Tumor associated endothelial expression of B7-H3 predicts survival in ovarian carcinomas.', *Modern pathology : an official journal of the United States and Canadian Academy of Pathology, Inc*. United States, 23(8), pp. 1104–1112. doi: 10.1038/modpathol.2010.95.

Zanotti, L. *et al.* (2016) 'Mouse mesenchymal stem cells inhibit high endothelial cell activation and lymphocyte homing to lymph nodes by releasing TIMP-1', *Leukemia*, 30(5), pp. 1143–1154. doi: 10.1038/leu.2016.33.

Zaretsky, J. M. *et al.* (2016) 'Mutations Associated with Acquired Resistance to PD-1 Blockade in Melanoma.', *The New England journal of medicine*. United States, 375(9), pp. 819–829. doi: 10.1056/NEJMoa1604958.

Zeng, Y. *et al.* (2019) 'Dual blockade of CXCL12-CXCR4 and PD-1-PD-L1 pathways prolongs survival of ovarian tumor-bearing mice by prevention of immunosuppression in the tumor microenvironment.', *FASEB journal : official publication of the Federation of American Societies for Experimental Biology*. United States, 33(5), pp. 6596–6608. doi: 10.1096/fj.201802067RR.

Zhu, M. *et al.* (2011) 'LIGHT regulates inflamed draining lymph node hypertrophy', *Journal of immunology (Baltimore, Md. : 1950)*. 2011/05/13, 186(12), pp. 7156–7163. doi: 10.4049/jimmunol.1002097.

Zorzoli, A. *et al.* (2012) 'Interleukin-27 inhibits the growth of pediatric acute myeloid leukemia in NOD/SCID/Il2rg-/- mice.', *Clinical cancer research : an official journal of the American Association for Cancer Research*. United States, 18(6), pp. 1630–1640. doi: 10.1158/1078-0432.CCR-11-2432.

Zukor, K. A., Kent, D. T. and Odelberg, S. J. (2010) 'Fluorescent whole-mount method for visualizing three-dimensional relationships in intact and regenerating adult newt spinal cords.', *Developmental dynamics : an official publication of the American Association of Anatomists*. United States, 239(11), pp. 3048–3057. doi: 10.1002/dvdy.22441.